Translational and Molecular Imaging Institute

TMII

MSSM

Mount Sinai School of Medicine

Program Book

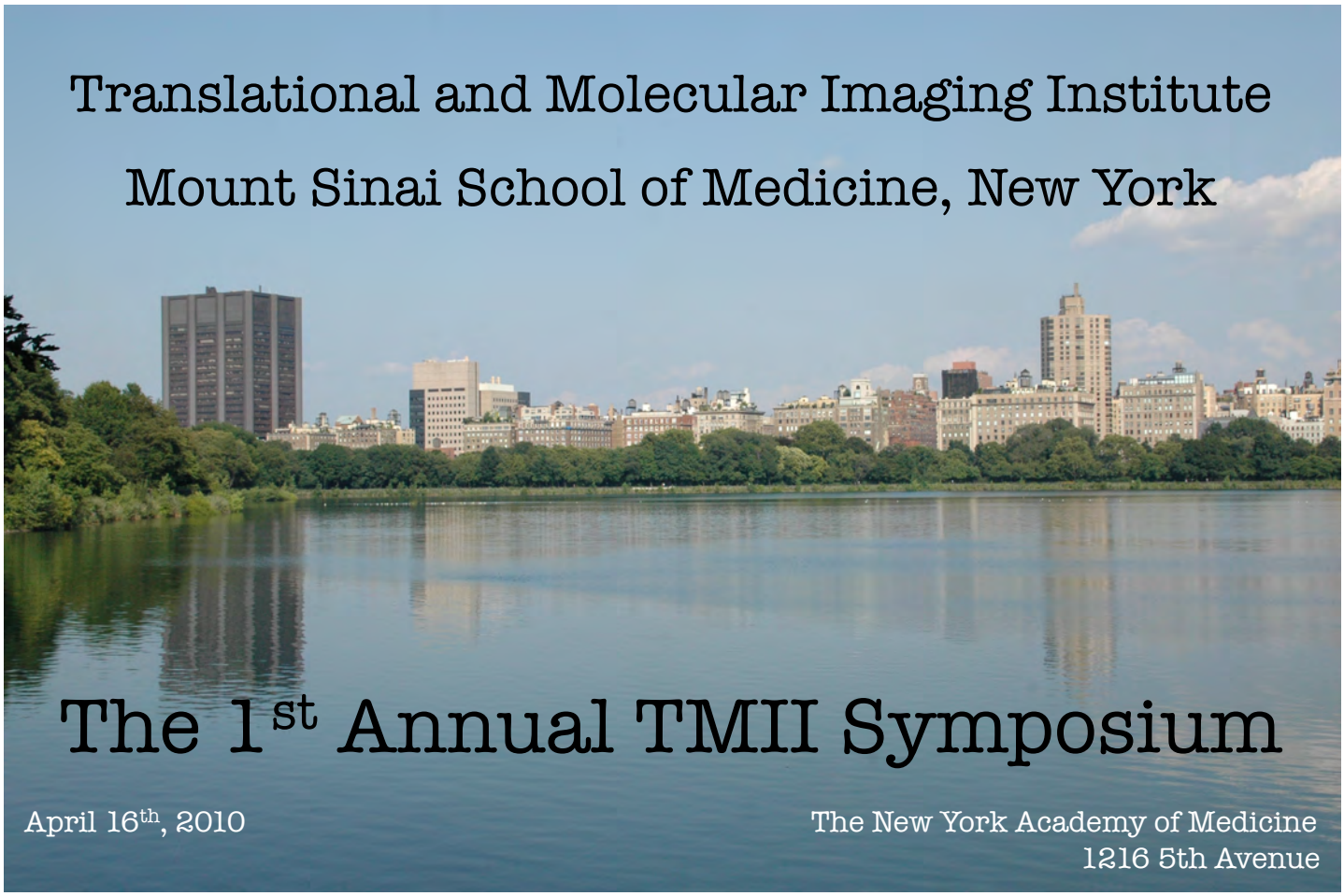

Content

Message from the Institute Director and the Dean of Mount Sinai

Translational and Molecular Imaging Institute

TMII

MSSM

Mount Sinai School of Medicine

It is with great enthusiasm and pride that we introduce the establishment of the Translational and Molecular Imaging Institute (TMII) and the 1st Annual TMII Symposium. The formation of three focused Programs (Cardiovascular Imaging Program, Neuro Imaging Program and Nanomedicine Program) and the Cell Tracking Core will shape TMII's vibrant translational research environment for the Mount Sinai Medical Center and its community at large.

The TMII symposium is intended to offer some snapshots of translational imaging research at Mount Sinai and other institutions in and outside the New York metropolitan area.

The TMII team and the Mount Sinai School of Medicine have carefully worked to organize this new symposium, and we look forward to familiarizing you with our Institute and its research endeavors. We encourage you to review the Program Book, which, in addition to providing abstracts and the program summary, includes additional information regarding the speakers as well as the activities, facilities and faculty members at our Institute and Mount Sinai's efforts in translational research.

Welcome to New York and Mount Sinai.

Zahi A. Fayad, Ph.D.

TMII director
Professor of Radiology
Professor of Medicine

Dennis S. Charney, MD

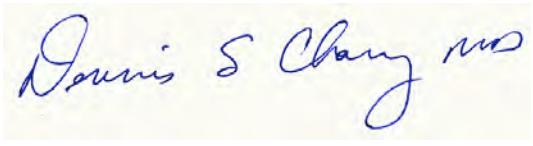

Anne and Joel Ehrenkranz Dean,
Mount Sinai School of Medicine
Executive Vice President for Academic Affairs, The Mount Sinai Medical Center

1216 Fifth Avenue
New York, NY 10029
(212) 822-7200

Hosack Hall -HH

President's Gallery - PG

Reception Room 1 - R1

Translational and Molecular Imaging Institute

TMII

MSSM

Mount Sinai School of Medicine

7:00-8:00	Registration/ Breakfast	Presenter	Moderator	PG
8:00 -8:15	Opening Remarks-Dr. Fayad	Zahi A. Fayad, PhD		HH
8:15-8:30	Opening Remarks-Dr. Charney	Dean Dennis Charney, MD		HH
8:30 -9:30	Keynote speaker	Valentin Fuster, MD, PhD (MSSM)		HH
	Session I		Zahi A. Fayad, PhD	
9:30-10:15	Cardiac	Joseph Wu, MD, PhD (Stanford)		HH
10:15-10:30	Cardiac selected abstract	David Cormode, PhD (MSSM)		HH
10:30-11:00	BREAK/POSTERS		Venkatesh Mani, PhD	PG
	Session II		Cheuk Tang, PhD	
11:00-11:45	Neuro	John Gore, PhD (Vanderbilt)		HH
11:45-12:00	Neuro selected abstract	Lazar Fleysher, PhD (NYU)		HH
12:00-1:00	LUNCH			RM-20
	Session III		Burton Drayer, MD	
1:00-1:15	Pilot Project	MaryAnn Mclaughlin, MD (MSSM)		HH
1:15-1:30	Pilot Project	Dara Dickstein, PhD (MSSM)		HH
	Session IV		Willem Mulder, PhD	
1:30-2:15	Nanomedicine	Daniel Anderson, PhD (MIT)		HH
2:15-2:30	Nanomedicine-selected abstract	Balaji Sitharaman, PhD (Stony Brook)		HH
2:30-3:00	BREAK/POSTERS		Bachir Taouli, MD	PG
	Session V		Karen Saebo, PhD	
3:00-3:45	Cancer	Peter Choyke, MD (NIH)		HH
3:45-4:00	Cancer-selected abstract	Giselle Suero Abreu (NYU)		HH
4:00-4:30	Closing Remarks	Burton Drayer, MD (MSSM)		HH
4:30-6:30	RECEPTION			PG

Biographies from invited speakers

Zahi A. Fayad, Ph.D.

Director Translational and Molecular Institute, Mount Sinai School of Medicine

Biography

Dr. Fayad serves as Professor of Radiology and Medicine (Cardiology) at the Mount Sinai School of Medicine. He is the Director of the Translational and Molecular Imaging Institute, Director and Founder of the Eva and Morris Feld Imaging Science Laboratories at the Mount Sinai School of Medicine. Dr. Fayad is one of the world's leaders in the development and use of multimodality cardiovascular imaging including, cardiovascular magnetic resonance (CMR), computed tomography (CT), and positron emission tomography (PET), and molecular imaging to study cardiovascular disease. His recent focus has been on the noninvasive assessment of atherosclerosis. He is also involved in the development of novel methods for targeted drug delivery to improve the treatment of atherosclerosis. He holds 8 US and Worldwide patents in the field of imaging. He has authored more than 200 peer-reviewed publications, 50 book chapters, and over 400 meeting presentations.

Dr. Fayad had his trainings at the Johns Hopkins University (Nitish Thakor, Elliott McVeight, Elias Zerhouni and William Brody) and at the University of Pennsylvania (Leon Axel). From 1996 to 1997 he was junior faculty in the Department of Radiology and the University of Pennsylvania. In 1997 he joined the faculty at Mount Sinai School of Medicine. Dr. Fayad is the recipient of multiple prestigious awards. In 2007 he was the given the John Paul II Medal from Krakow, Poland in recognition for the potential of his work on humankind. As a teacher and mentor, Dr. Fayad has been also extremely successful. He has trained over 30 postdoctoral fellows, clinical fellows and students. His trainees have received major awards, fellowships, and positions in academia and industry. In 2008 he received the Outstanding Teacher Award from the International Society of Magnetic Resonance in Medicine (ISMRM) for his teaching on cardiovascular imaging and molecular imaging. Recently, in 2009 he was awarded the title of Honorary Professor in Nanomedicine at Aarhus University in Denmark.

Dennis S. Charney, M.D.

Dean, Mount Sinai School of Medicine

Biography

The arrival of Dennis S. Charney, MD, at Mount Sinai in 2004 signaled a new era of innovation in research, education, and clinical care. Since joining the faculty, he has established a culture of excellence that has elevated Mount Sinai School of Medicine to among the top medical schools in the nation.

With an emphasis on translational research, Dr. Charney has accelerated the pace of change at Mount Sinai, streamlined collaboration across disciplines, and facilitated the integration of research, clinical care, and educational innovation. These efforts have produced remarkable results. Mount Sinai School of Medicine now ranks 18th in National Institutes of Health (NIH) funding and in the past four years, its position in U.S. News & World Report has risen from 32 to 22.

A leading investigator on neurobiology and the treatment of mood and anxiety disorders, Dr. Charney has made fundamental contributions to the understanding of neural circuits and neurochemistry related to human anxiety, fear, and mood. He has pioneered research related to the psychobiological mechanisms of human resilience to stress. In addition, his research team has made major contributions to the discovery of novel and more effective treatments for mood and anxiety disorders.

A prolific author, Dr. Charney has written more than 700 publications, including groundbreaking scientific papers, chapters, and books. His scientific research has been honored by every major award in his field.

Valentin Fuster, M.D. Ph.D.

Director of Mount Sinai Heart, Mount Sinai School of Medicine

Biography

Dr. Fuster serves The Mount Sinai Medical Center as Director of Mount Sinai Heart, the Zena and Michael A. Wiener Cardiovascular Institute and the Marie-Josee and Henry R. Kravis Center for Cardiovascular Health. He is also the Richard Gorlin, MD/Heart Research Foundation Professor, Mount Sinai School of Medicine.

After receiving his medical degree from Barcelona University and completing an internship at Hospital Clinic in Barcelona, Dr. Fuster spent several years at the Mayo Clinic, first as a resident and later as Professor of Medicine and Consultant in Cardiology. In 1981, he came to Mount Sinai School of Medicine as head of Cardiology. From 1991 to 1994, he was Mallinckrodt Professor of Medicine at Harvard Medical School and Chief of Cardiology at the Massachusetts General Hospital. He returned to Mount Sinai in 1994 as Director of the Zena and Michael A. Wiener Cardiovascular Institute and most recently, he has been named the Director of the Mount Sinai Heart.

Among the seemingly countless awards and positions of distinction that he holds are Past President of the American Heart Association, Immediate Past President of the World Heart Federation, a member of the Institute of Medicine of the National Academy of Sciences, a former member of the National Heart, Lung and Blood Institute Advisory Council, and former Chairman of the Fellowship Training Directors Program of the American College of Cardiology. Seventeen distinguished universities throughout the world have granted him honoris causa. Dr. Fuster is the President of Science of the Centro Nacional de Investigaciones Cardiovasculares Carlos III (CNIC) in Madrid, Spain.

Dr. Fuster is the recipient of three major ongoing NIH grants. He has published more than 500 articles on the subjects of coronary artery disease, atherosclerosis and thrombosis, and he has become the lead Editor of two major textbooks on cardiology, 'The Heart' (previously edited by Dr. J. Willis Hurst) and "Atherothrombosis and Coronary Artery Disease" (with Dr. Eric Topol and Dr. Elizabeth Nabel). Dr. Fuster has been appointed Editor-in-Chief of the Nature journal that focuses on cardiovascular medicine.

Joseph Wu, M.D., Ph.D.
Department of Medicine and Department of Radiology, Stanford School of Medicine

Biography
Joseph Wu, M.D., Ph.D. is an assistant professor in the Department of Medicine (Cardiology) and Department of Radiology at the Stanford School of Medicine. Dr. Wu received his M.D. from the Yale School of Medicine. He completed his cardiology fellowship training followed by a PhD in molecular pharmacology at UCLA. Dr. Wu's lab works on biological mechanisms of adult stem cells, embryonic stem cells, and induced pluripotent stem cells. The lab uses a combination of gene profiling, tissue engineering, physiological testing, and molecular imaging technologies to better understand stem cell biology in vitro and in vivo. For adult stem cells, we are interested in monitoring stem cell survival, proliferation, and differentiation. For ESC, we are currently studying their tumorigenicity, immunogenicity, and differentiation. For iPSC, we are working on novel derivation techniques. We also work on development of novel vectors and therapeutic genes for cardiovascular gene therapy applications.

Abstract Cardiac Imaging Presentation by Joseph Wu
Coronary artery disease is the number one cause of morbidity and mortality in the Western world. In recent years, stem cell therapy has shown exciting promise for treatment of ischemic heart disease and others. However, the understanding of stem cell biology is in its infancy. Nevertheless, multiple human studies have been initiated in recent years. My talk will focus on the promises and limitations of using adult stem cells for cardiovascular regeneration. The second half will focus on how imaging technologies have been used to shed important insights into the biology of pluripotent stem cells (e.g., differentiation, tumorigenicity, and immunogenicity). Sample references are highlighted below as well.

1) van der Bogt K et al. Circulation 2008;118:S121-S129.
2) Swijnenburg RJ et al. PNAS 2008;105(35):12991-2996.
3) Li Z et al. JACC 2009;53(14):1229-40.
4) Sun N et al. PNAS 2009;106:15720-15725.
5) Jia F et al. Nature Methods 2010;7(3):197-9.

John C. Gore, Ph.D.
Director, Vanderbilt University Institute of Imaging Science

Biography
John C. Gore, Ph.D., is Director of the Institute of Imaging Science and Chancellor's University Professor of Radiology and Radiological Sciences, Biomedical Engineering, Physics and Astronomy, and Molecular Physiology and Biophysics at Vanderbilt University. Dr. Gore obtained his Ph.D. in Physics at the University of London in the UK in 1976 and has been an active leader in imaging research and applications for over 30 years. He also holds a degree in Law. He is an elected fellow of the American Institute of Medical and Biological Engineering, the International Society for Magnetic Resonance in Medicine (ISMRM), and the Institute of Physics (UK). In 2004 Dr. Gore was awarded the Gold Medal of the ISMRM for his contributions to the field of magnetic resonance imaging. He has served twice as a trustee of the ISMRM and is editor-in-chief of the journal *Magnetic Resonance Imaging*. He founded the pioneering MRI research program at Hammersmith Hospital in the UK in the late 1970's prior to establishing and directing the MRI research program at Yale University from 1982-2002. He has published over 400 original papers and contributions within the medical imaging field. His research interests include the development and application of imaging methods for understanding tissue physiology and structure, molecular imaging and functional brain imaging.

Abstract Neuro Imaging Presentation by John C. Gore

Opportunities and Challenges of Ultra-High Field MRI and MRS

The development and applications to human subjects of magnetic resonance imaging systems at fields of 7 Tesla and above provide many new opportunities for clinical applications and neuroscience. The increased signal strength at higher fields enables higher resolution images to be acquired, which provides new insights into the structural anatomy of the brain. Specific contrast mechanisms such as those originating from the susceptibility of blood and the influence of oxygen (such as the BOLD effect) are enhanced at higher field, permitting functional brain mapping to be performed with greater sensitivity and spatial resolution. Appropriate high field techniques can provide more precise measurements of functional connectivity and temporal processing in the brain. High resolution spectroscopy also benefits from the greater spectral dispersion at high fields, so that measurements of brain metabolites and neurotransmitters can be made with greater accuracy. These benefits have been realized in several studies of brain structure, function and pathology, including higher resolution mapping of visual and sensorimotor cortex and functional studies of neural connectivity. They also have shown considerable promise for clinical studies of diseases such as multiple sclerosis and Parkinson's disease, where the sensitivity to brain iron and higher spatial resolution images allows detection of pathological changes with increased sensitivity. However, high field MR imaging is also affected by technical limitations and artifacts that require additional research and development. For example, macroscopic field variations caused by inhomogeneities of magnetic susceptibility within the body can degrade spectra and introduce image distortions. Moreover, the performance of radiofrequency (RF) coils is also affected at higher fields, and it is more difficult to create uniform RF fields within large objects. These challenges are being met using various technical innovations such as dynamic shimming, the use of parallel arrays of coils, novel spectral-spatial excitation methods, novel pulse sequences and post-acquisition digital processing. In combination these efforts promise to allow ultra-high field imaging and spectroscopy to achieve their full potential.

Daniel Anderson, Ph.D.
Koch Institute for Integrative Cancer Research, MIT

Biography
Dr. Daniel G. Anderson is appointed at the David H. Koch Institute for Integrative Cancer Research at the Massachusetts Institute of Technology. He received his PhD in molecular genetics from the University of California at Davis. At MIT, he pioneered the use of robotic methods for the development of smart biomaterials for drug delivery and tissue engineering. He has developed methods allowing rapid synthesis, formulation, analysis, and biological testing of large libraries of biomaterials for use in medical devices, cell therapy and drug delivery. In particular, the advanced drug delivery systems he has developed provide new methods for nanoparticulate and microparticulate drug delivery, non-viral gene therapy, siRNA delivery, and vaccines. His work has resulted in the publication of over 120 papers, patents and patent applications. These patents have led to a number of licenses to pharmaceutical, chemical and biotechnology companies.

Abstract Nanomedicine Imaging Presentation by Daniel G. Anderson

High throughput approaches to drug delivery and tissue engineering

High throughput, combinatorial approaches have revolutionized small molecule drug discovery. Here we describe our work on high throughput methods for creating and screening biomaterials for drug delivery and tissue engineering. We have developed automated methods allowing for rapid nanoliter scale synthesis of 1000's of biomaterials, as well as the testing of their chemical, material, and biological properties. These methods have also been applied towards the development of new methods to control stem cell behavior, as well as vehicles for drug delivery. In particular, these combinatorial libraries of polymers and lipidoids have yielded new approaches for microparticulate drug delivery, non-viral gene therapy, siRNA delivery, and vaccines.

Peter L. Choyke, M.D.

Molecular Imaging Program, Center for Cancer Research, NCI

Biography

Dr. Choyke obtained his medical degree from Jefferson Medical College and completed his residency in Diagnostic Radiology at Yale-New Haven Hospital. Following an imaging fellowship at the University of Pennsylvania he joined the faculty of Georgetown University and soon thereafter the Diagnostic Radiology Department, Clinical Center, NIH. In June 2004 he started the Molecular Imaging Program within the Center for Cancer Research, NCI.

His research interests include translation of molecular imaging methods into the clinic including MRI, optical and Radionuclide/PET methods. His research includes novel methods of detecting ovarian cancer metastases, lymphangiogenesis, multi-targeted epithelial growth factor (HER1, HER2) imaging, prostate cancer detection, angiogenesis imaging and exploration of unique animal models of cancer.

Burton Drayer, M.D.

Chair of the Department of Radiology, Mount Sinai School of Medicine

Biography

Dr. Drayer is executive vice-president for Risk at The Mount Sinai Medical Center and the Dr. Charles M. and Marilyn Newman Professor and chair of the Department of Radiology (1995-present). He also served as president of The Mount Sinai Hospital from November 2003 to September 2008.

Dr. Drayer received his undergraduate degree in political science from the University of Pennsylvania in Philadelphia. In 1971, he received his medical degree from the Finch University of Health Sciences/The Chicago Medical School and went on to complete an internship and neurology residency at the University of Vermont in Burlington. Dr. Drayer served his radiology residency followed by a neuroradiology fellowship at the University of Pittsburgh. Dr. Drayer's academic appointments began in 1977 at the University of Pittsburgh Health Center. From 1979 to 1986, Dr. Drayer was at Duke University Medical Center in Durham, N.C., where he became professor of radiology and assistant professor of medicine (neurology). In 1986, he was appointed chair of the Division of Neuroimaging Research-Education at the Barrow Neurological Institute in Phoenix, where he remained until 1995. Dr. Drayer then moved to The Mount Sinai Medical Center.

Since 1979, Dr. Drayer has authored or coauthored nearly 200 journal articles, 41 book chapters and two books and is a sought-after lecturer both nation-ally and internationally, giving over 200 invited lectures and speeches. Dr. Drayer's many awards and honors include the Cornelius G. Dyke Award from the American Society of Neuroradiology and the Distinguished Service Award from the American Board of Radiology. He was elected to the RSNA Board of Directors in December 2003 and has acted as liaison for the annual meeting and technology and served as board chairman in 2009. He is president elect of the RSNA for 2010 and will be president of the RSNA in 2011.

Abstracts selected for oral presentation

Multi-color computed tomography for plaque characterization in atherosclerosis

David P. Cormode,[1] Ewald Roessl,[2] Axel Thran,[2] Denis van Loo,[3] Torjus Skajaa,[1,4] Ronald E. Gordon,[1] Jens-Peter Schlomka,[2] Valentin Fuster,[1] Edward A. Fisher,[5] Willem J. M. Mulder,[1] Roland Proksa,[2] Zahi A. Fayad[1]

1 – Mount Sinai School of Medicine, 2 – Philips Research Europe, 3- University of Ghent, 4 - Aarhus University, 5 – New York University

Introduction - Spectral computed tomography (CT) is a new imaging technique that can distinguish different materials by analysis of their X-ray absorption at different wavelengths. In CT imaging of atherosclerosis, it is valuable to identify iodine and calcifications. Lately, gold nanoparticles have been proposed as contrast agents for CT and exhibit excellent properties for macrophage targeting. Our objective, therefore, was to investigate the potential of spectral CT to distinguish iodine and gold contrast agents from each other as well as soft tissue and bone tissue, for the purpose of multicolor imaging of atherosclerotic plaque composition.

Methods - We synthesized a macrophage targeted, fluorescently labeled gold nanoparticle (AuHDL), while vascular phase iodine contrast agents were commercially sourced. Phantom imaging was performed using water or meat as a matrix, with calcium phosphate simulating bone and calcifications. The apoE knockout mouse was used as model of atherosclerosis. These mice were injected with gold nanoparticles, followed by iodine contrast agents at 24 hours and then imaged. Wild-type mice were used as controls. Aortic sections from these mice were imaged using confocal microscopy and transmission electron microscopy.

Results and Discussion - Phantom imaging showed that the spectral CT system could distinguish gold, iodine, bone/calcifications and soft tissue simultaneously. Importantly, in apoE knockout mice spectral CT allowed multicolor visualization of gold, iodine bone and tissue (A). We observed gold uptake by aortic plaques to extensively occur in the aorta by spectral CT and nanoCT (B). TEM imaging and confocal microscopy of aortic sections confirmed that the gold particles localized in macrophages (C).

Conclusion - Spectral CT married with carefully chosen contrast agents can provide valuable and unique information on atherosclerotic plaque composition.

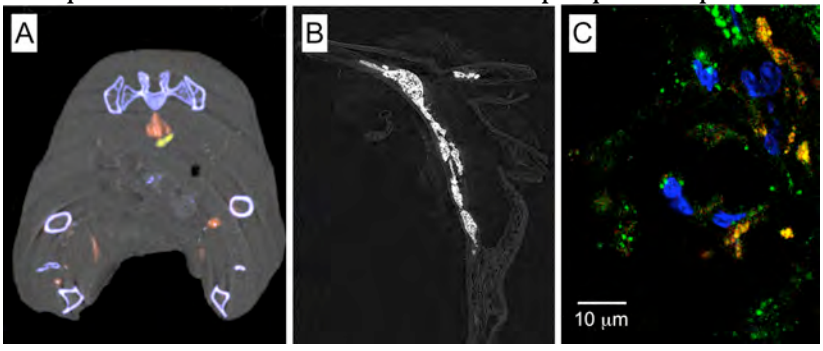

Figure 1 A) Spectral CT image of a mouse where gold is shown as yellow, iodine as red and bone as blue. B) NanoCT image of the aortic arch. C) Confocal microscopy image of an aorta section showing macrophage specificity of Au-HDL.

Intra-cellular Sodium fraction in the human brain at 7T in-vivo.

L. Fleysher[1], N. Oesingmann[2], R. Brown[3], G. Wiggins[3], D. Sodickson[4], M. Inglese[5]

1. Department of Radiology, NYU School of Medicine, New York, New York 2. Siemens Medical Solutions USA, Inc. 3. Department of Radiology and Center for Biomedical Imaging, NYU School of Medicine, New York, New York 4. Departments of Radiology, Physiology and Neuroscience, NYU School of Medicine, New York, New York 5. Departments of Radiology and Neurology, NYU School of Medicine, New York, New York

Abstract

Single quantum and triple-quantum sodium imaging is used to obtain the intracellular sodium fraction (ISF) and intracellular concentration from the human brain in-vivo.

Introduction

Sodium MRI is a useful technique in the studies of several neurological disorders including tumors, stroke [1] and Alzheimer's disease [2]. While the extracellular sodium concentration remains relatively constant as long as there is adequate tissue perfusion, the intracellular sodium density may provide information about cellular and metabolic integrity and ion homeostasis. The two compartments can be differentiated with the help of TQF sodium imaging [3,4].

Methods

Six healthy volunteers (2 older (mean age 66.5+/-0.7) and 4 younger (mean age 27.5+/-1.3)) were recruited for the study. The study was approved by the local IRB and informed consent was obtained from all subjects. Experiments were performed on a 7T whole-body MAGNETOM scanner (Siemens Healthcare, Germany) with a custom-built dual-tuned TX/RX $^{1}H/^{23}Na$ head coil [5]. ISF protocol was based on [6]. Acquisition parameters for the 12-step B0-corrected TQF imaging [6] were 240x240x240 mm^3 FOV with 30x30x24 encoding matrix; TR=150ms, TE=6.8ms, FA=90^0 and τ_1=6.8ms τ_2=150μs.

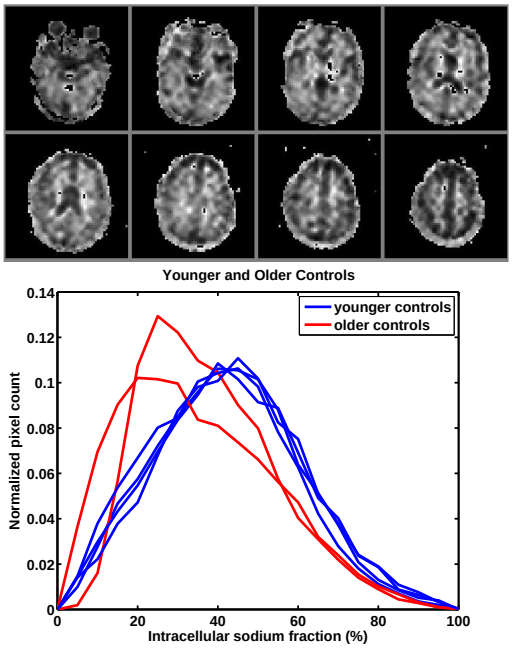

Figure 2: Quantitative map of the intracellular sodium fraction from a volunteer (top) and the histograms of the intracellular fraction across the brain in each of the three volunteers (bottom).

Results and Conclusion

Several contiguous axial slices of the ISF maps from a young volunteer are shown in Figure 1, along with histograms of ISF across the brain in each volunteer. The images reveal that the mean ISF in the young brain is 43%. This is in a good agreement with the predicted values between 26% and 57% [7]. Assuming 25 mM [8] average brain tissue TSC, the average intracellular sodium concentration is 11mM which is in good agreement with previous reports of 10-15 mM [7]. It is remarkable to note that the ISF distributions form the younger volunteers are quite close to each possibly due to similarities of the younger healthy human brains. It is also expected that ISF in the healthy brain tissue will decrease with age. This effect is caused by shrinkage of the brain cells and cell degeneration. Our data show a similar trend, as the ISF distributions for the older volunteers indicate lower intracellular content (shifted to the left) compared to their younger counterparts.

Acknowledgments: This study was supported in part by R01 NS051623.

References: 1. Thulborn, el. al. Neuroimaging Clin N Am 15:639, 2005. **2.** Mellon, et.al. AJNR Am J Neuroradiol. 30:978, 2009. **3.** Jaccard, et. al. J Chem Phys 85:6282, 1986. **4.** Hancu, et. al. Magn Reson Med 42:1146, 1999.**5.** Wiggins, at. al. ISMRM 2010 **6.** Fleysher, et. al. ISMRM 2010. **7.** Ouwerkerk, et. al. Radiology 227:529, 2003. **8.** Inglese, et. al. Brain 2010 in press.

GCO#08-1323
Effect of Fine Particulate Matter Exposure
On Carotid Neovascularization Using DCE-MRI
PI: Mary Ann McLaughlin, MD, MPH

PROGRESS REPORT

Traditional risk factors for CVD include lifestyle (smoking, physical inactivity, stress, diet) serum lipids, gender, race, age and family history. These risk factors, however, do not fully explain the etiology or incidence of CVD. Exposure to inhaled particulate matter (PM) has been investigated as an additional risk factor for cardiovascular disease (CVD).
There is evidence that PM exposure may hasten the development of atherosclerosis. One major clinical interest in atherosclerosis is the presence and extent of neoangiogenesis and inflammation in atherosclerotic plaques. This can be considered a marker of risk associated with the lesion. Calcagno et. al. investigated the use of two imaging techniques, including digital contrast enhanced MRI, to quantify inflammation expressed as plaque neovessels content in a rabbit model of atherosclerosis. The use of non-invasive imaging modalities could be proposed in a clinical setting to complimentarily evaluate prognosis and treatment of atherosclerotic plaques.

This study aims to evaluate the effect of particulate matter exposure on carotid atherosclerosis using dynamic contrast enhanced MRI (DCE-MRI) and to correlate the area under the signal intensity curve (AUC) results obtained from DCE-MRI with coronary artery calcium score (CACS), ankle brachial index (ABI) and peripheral arterial tonometry (PAT) index.

The number of subjects to be enrolled with funding from this study is 54.

From the time of final IRB approval (1/14/2009) to this date, we have enrolled a total of 37 subjects. Although IRB approval was obtained in January, 2009, the MRI machine was not calibrated for our use until May 2009. In addition, the MRI machine will not be available for 8 weeks (11/09 to 1/10) due to enhancement/construction of the equipment.

Out of the 37 subjects enrolled, 22 have completed the study, 13 were screen failures and 2 are still in the process of completing the study. Out of the 13 screen failures, 3 had glomerular filtration rate (GFR) that did not meet the study criterion; and 10 were due to the MRI exclusion checklist: 8 were claustrophobic, 1 was due to a metal tissue marker; and 1 had reactive airway dysfunction syndrome.

Recent studies have yielded the same information as initially submitted and no relevant recent literature can be added as of now. No findings can be reported for now as recruitment and data collection is still going on. An interim analysis will be done in December 2009.

The Mount Sinai IRB has determined that this research continues to involve GREATER THAN minimal risk. No new risk factors have been identified in the course of the study.

The Mount Sinai IRB has approved continuation (no-cost extension) of this study from 12/16/2009 to 12/15/2010.

Enrollment was temporarily stopped on the second week of November due to enhancement/construction of the MRI machine but will resume by the second week of January as this is the target date for the completion of the construction.

Tracking Changes in Spine Morphology in Alzheimer's using High Resolution Imaging

PI: ***Dara Dickstein, Ph.D***

Summary of Progress from Previous Funding period:

The proposed project was designed to assess the morphological attributes that contribute to neurodegeneration and synaptic dysfunction using rigorous quantitative morphologic approaches. The hypotheses to be tested were: 1) both Aβ and hyperphosphorylated tau leads to progressive changes in the morphology of neurons, resulting in reduced complexity of dendritic arborization, reduced number of spines and altered spine morphology and volume; 2) the different protein conformations contained within Aβ plaques and NFTs will affect spines and dendritic morphometric parameters in pyramidal neurons at specific and progressive stages of disease pathology. For Specific Aim 1, we completed detailed quantitative analysis of the effect of Aβ accumulation on morphologic alterations in neurons and spines in Tg2576 APP model mice. While no differences were seen between Tg mice and wild-type at 9 months of age, significant apical atrophy was observed at 24 months of age. Moreover, significant differences in apical dendritic length and complexity were observed during disease progression with little to no change in the basal dendrites. When assessing the distribution of spine types and volumes there was a significant shifts toward thin, less stable spines in 24 month old mice compared to 9 month old mice, and thin spines were larger in old animals. The shift towards the thin, less stable spines observed suggests that older, more severely affected animals, have fewer functionally stable spines and can account for the cognitive impairment observed in AD. We have also reported a detailed quantitative analysis of the effect of hyperphosphorylated tau on morphologic alterations in neurons and spines in htau mice. We found that there was a decrease in apical dendritic arbor length between 3 and 6 month old mice; however no significant differences were observed in basal arbor length or branching pattern. In contrast, there was an increase in apical dendritic arbor length and complexity in 12 month old mice compared to the other age groups. Upon analysis of spine density and morphology, we have observed an increase with age of mushroom (i.e., more stable) spines overall, however, htau mice had fewer mushroom spines then wild-type; however, the volume of mushroom spines decreased from 3 to 6 months and increased from 6 to 12 months. The findings above suggest that tau-related pathology induces morphological alterations in apical dendrites. This increase in complexity and branching in 12 month mice and the increase of volume of mushroom spines may represent compensatory mechanisms in the remaining intact neurons. Such irregularities in apical dendrites may result in the deterioration of neuronal function observed in AD and shed light on the mechanistic relationship between synaptic integrity and cognitive decline. We are pursuing our effort to quantify these same attributes in the TgCRND8 AD model mouse. To date we have data from 3 and 6 month old mice, however, we need to increase the number of mice per age group and as such are still blinded to the genotypes of the mice for which we have data.

In the context of Specific Aim 2, we have continued our analysis in the amyloid and tau transgenic mouse models to assess the effect of different protein conformations on neuron and spine morphology.

This study involved the use of luminescent conjugated oligothiophenes (LCO) probes in conjunction with intracellular injections of Lucifer yellow and subsequent 3D reconstruction. We had initially started the study using the LCO probe FTAA that had been used in previous studies. In the past year, a better, smaller, more discerning, and quantifiable luminescent-conjugated thiophene polymer (LCP), polythiophene acetic acid (PTAA), has been produced. We have now begun to use this LCO and have optimized its staining and imaging parameters for all three mouse models. With these parameters optimized we will now be able to assess how the different protein conformations contained within Aβ plaques and NFTs will affect spines and dendritic morphometric characteristics.

List of Publications:

Dickstein, D.L., Brautigam, H., Evans, Z.A., and Hof, P.R. Changes in dendritic complexity and synaptic density during the progression of Alzheiemer's disease. (in preparation).

Dickstein, D. L., Brautigam, H, Stockton, S.D., Schmeidler, J., and Hof, P.R. Changes in dendritic complexity and spine morphology in a transgenic mouse expressing human wild-type tau. ***Brain Structure and function.*** (in revision).

Luebke, J.I., Weaver, C., Rocher, A.B., Rodriguez, A., Crimins, J.L., Dickstein, D.L., Wearne, S.L., and Hof, P.R. Dendritic vulnerability in Alzheimer's disease and aging: insights from analyses of cortical pyramidal neurons in transgenic mice and non-human primate models. ***Brain Structure and Function.*** (accepted).

Elder, G, Gama Sosa, M.A., De Gasperi, R., Dickstein, D.L., and Hof, P.R. Presenilin transgenic mice as Model's of Alzheimer's disease. ***Brain Structure and Function.*** (accepted).

Åslund, A., Sigurdson, C.J., Grathwohl, S., Bolmont, T., **Dickstein, D.L.,** Glimsdal, E., Klingstedt, T., Prokop, S., Lindgren, M., Konradsson, P., HoltzmanD.M., Hof, P.R., Heppner, F.L., Gandy, S., Hammarström, P., Jucker, M., Aguzzi, A., and Nilsson, K.P.R. Novel pentameric thiophene derivatives for in vitro and in vivo optical imaging of a plethora of protein aggregates in cerebral amyloidoses (2009) ***ACS Chemical Biology***. 4(8):673-84

Toward Gadolinium-single walled carbon nanotube-based cellular magnetic resonance imaging contrast agents: In vitro cytotoxicity and phantom MRI studies

Pramod Avti,* Henry Bryant[†], Youssef Wadghiri,# Joseph Frank[†], Kenneth Shroyer*, Balaji Sitharaman*

*Departments of Biomedical Engineering and Pathology, Stony Brook University, Stony Brook, NY 11794; [†]Frank Laboratory, Radiology and Imaging Sciences, Clinical Center, National Institutes of Health, Bethesda, MD 20892, [#]Department of Radiology, NY School of Medicine, NY 10016

Introduction: Gadolinium (Gd)-based compounds are widely used as clinical contrast agents (CAs) for magnetic resonance imaging (MRI). Gd, as a free ion, is extremely toxic [1]. Typically, the toxicity of Gd as a free ion is sequestered by coordinating Gd with multidentate ligands (chelates) [1]. A recent approach to sequester the toxicity involves encapsulation of Gd within single walled carbon nanotubes (Gd-SWCNTs) [2]. In this work, we present the *in vitro* cytotoxicity and MRI of the Gd-SWCNTs towards their development as novel nanosystems for cellular MRI.

Methods: The synthesis method involves chemical vapor deposition (CVD) of carbon feedstock on lanthanoid nanoparticles prepared by a block copolymer templating technique [2]. The Gd-SWCNTs were water-solubilized by dispersing them in N-(Carbonyl-methoxypolyethyleneglycol-5000)-1,2 distearoyl-sn-glycero-3-phosphoethanol amine (DSPE-PEG). NIH 3T3 cells were treated with the water soluble Gd-SWCNT for 12, 24 and 48 hrs. Transmission Electron Microscope operating at 80 keV was used to take the images of 75 nm thick cell histology sections. The toxicity profile was analyzed using cell viability, lactate dehydrogenase, micronuclei formation by staining with acridine orange, changes in the cell cycle (propidium iodide staining) and apoptosis (FITC-annexin-V vs propidium iodide) by flow cytometry. Phantom MRI studies were performed on a 3T Philips MR scanner.

Results & discussion: The Gd-SWCNTs at high concentrations up to 25µg/ml did not show any significant cytotoxicity profiles up to 48 hours (**Figure 1**). TEM showed that these nanoparticles are efficiently translocated into the cellular vacuoles (**Figure 2**). Cytotoxicity analysis using Trypan blue exclusion and live/dead cell assay using Calcein/EthD showed no significant changes in the cell viability in the concentration range of 7ng - 10µg/ml and decreased the viability by 10 – 15% in the concentrations range of 50-100µg/ml up to 48 hrs. Lactate dehydrogenase, a cytoplasmic enzyme marker, is released during cytotoxic agent's treatment and reflects the membrane damage. Lactate dehydrogenase (LDH) assay showed no significant changes up to 25µg/ml of Gd-SWNCT treatment for 48 hrs. This indicates that the gadonanotubes do not cause membrane damage at 25µg/ml concentration. Further, the ability of these nanotubes to disturb the cellular homeostasis leading to apoptosis (programmed cell death) was performed by analyzing annexin-v binding to phosphatidyl serine (PS) (a preapoptotic condition) and caspase-3 activity (point of no return). Externalization of PS to the outer leaflet of plasma membrane is a pre-apoptotic condition. The inability of gadonanotubes at concentrations 25µg/ml to externalize PS and increase caspase-3 activity shows their cellular non-toxic effects. To overcome any cytotoxic conditions the cells regulate the cell cycle to trigger the survival signals. Gadonanotubes treated up to 25µg/ml did not alter the normal cycle and maintained the cellular homeostasis up to 24hrs. MRI relaxivities (an important measure of efficacy) of the Gd-

SWCNTs at 1.5 T were 126 $mM^{-1}s^{-1}$; 25 fold greater than the current, clinically used Gd^{3+} based contrast agent Magnevist. (4.5 $mM^{-1}s^{-1}$). Representative T_1 weighted MRI images of the water soluble Gd-SWCNT in 4% gelatin (4 grams of gelatine in 100 grams of water) and a control (4% gelatin) are shown in **Figure 3**. At 0.22 mM concentration, Gd-SWCNTs showed significant enhancements (SNR > 100) compared to pure water.

Conclusion: In conclusion, MRI phantom studies on the Gd-SWCNT show extremely large signal enhancement with intensities up to 100-150 times larger than pure water at modest concentrations of gadolinium. The ability of the nanoprobes to be internalized by cells could allow magnetic labelling of individual cells. Thus, Gd-SWCNTs show potential as a novel high performance CAs for cellular MRI. This is an ongoing area of research at our laboratory.

References

(1) Merbach AE, Toth, E, Helm L, Editors, The Chemistry of Contrast Agents in Medical Magnetic Resonance Imaging, John Wiley and Sons, Chichester. (2) Swierczewska M, Rusakova I, Sitharaman B. Carbon 2009, 47; 3137-3142.

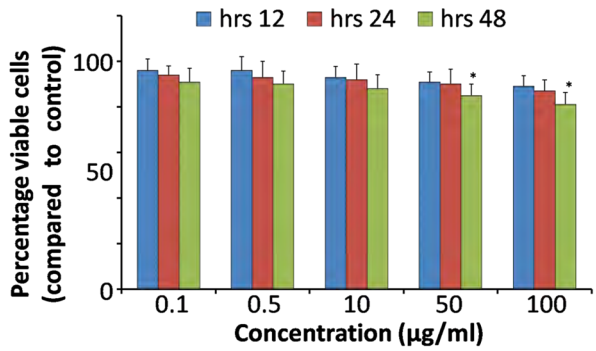

FIGURE 1: Cells viability after treatment with various concentrations of Gd-SWCNT for 48 hrs. No significant change in cell viability with 50µg/ml till 24 hrs. *P<0.05 w.r.t control.

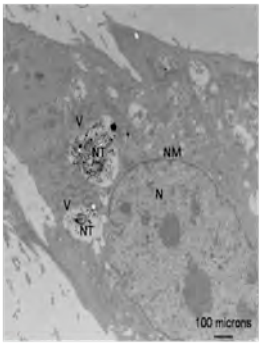

FIGURE 2 Localization of Gd-SWCNT after treatment for 48 hrs in the vacuoles of NIH 3T3 cells. V: vacuole, N: nucleus, NM: nuclear membrane, NT : Nanotubes

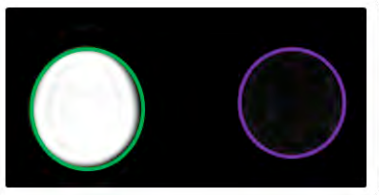

FIGURE 3: T1-weighted MR image of Gd-SWCNTs prepared in 4% gelatin (green) and only 4% gelatin (purple). MR signal is enhanced by the addition of 0.22 mM of Gd-SWCNTs.

Molecular MRI of Angiogenesis in a Mouse Melanoma Model

Giselle A. Suero, Benjamin Bartelle, Cesar Berrios-Otero, Anne. Friedland, Daniel H. Turnbull
Kimmel Center for Biology and Medicine Skirball Institute of Biomolecular Medicine
Biomedical Imaging Program and Department of Radiology, NYU School of Medicine, NY

Introduction: Angiogenesis, the formation of new blood vessels from preexisting mature vasculature, is a critical feature of tumor formation, growth and metastasis. While angiogenesis is a complex and dynamic process involving different vascular components, endothelial cell activation represents a major biomarker in neovasculature formation [1, 2]. Molecular imaging provides a powerful tool that allows specific, *in vivo*, non-invasive and longitudinal characterization of the molecular and functional abnormalities underlying the angiogenic process. [3]. In this study we utilized novel transgenic mice that genetically biotinylate the developing vascular endothelial cells, which we selectively targeted with avidinated probes to achieve contrast enhancement of blood vessels actively involved in angiogenesis.

Methods: T2-Biotag transgenic mice were generated to coexpress an engineered bacterial biotin ligase (BirA) and a cluster of BirA substrate sequences (Biotags) under the expression of a minimal Tie2 promoter to effectively biotinylate endothelial cell membranes during angiogenesis [4]. To demonstrate the potential of this system for analysis of tumor angiogenesis, we subcutaneously inoculated 1.10x6 B16-BL6 melanoma cells in the lower flank to produce a tumor model of adult angiogenesis. To assess targeting to biotinylated developing vasculature, we obtained images one hour after tail vein injection of streptavidin conjugated to Alexafluor-680 (StAv-Alex680) for near infrared (NIR) imaging and avidin-DTPA-Gd (Av-DTPA-Gd) for MRI. The NIR data was obtained at 180-μm resolution on a Licor Odyssey NIR imager and MRI experiments were performed on a 7T micro-MRI (Bruker Biospec), using a volume coil transmit / surface coil receive system (Bruker). Pre and post contrast T1-weighted images were obtained with a 3D gradient echo sequence (TE/TR=3.27/20ms, FA=90°, FOV=2.0 cm^3, matrix=100^3, NEX=6 and imaging time ~27mins). 3D analysis were performed in AMIRA (Visage Imaging) including segmentation and 3D surface rendering to examine increase in signal intensity due to effective contrast binding. After MRI, mice were cardio-perfused and tumors extracted for histological analysis.

Results and Discussion: T2-Biotag transgenic mouse melanomas showed *in vivo* binding of avidinated probes using both NIR (Fig. 1) and MRI (Fig. 2). This system provided high specificity and sensitivity in a melanoma tumor model, selectively labeling neovasculature by targeting angiogenic endothelial cells expressing Tie2. Our results demonstrated that the T2-Biotag mice provide a novel targeting system with the potential to help better understand the molecular events in tumor angiogenesis, such as its initiation and progression and how it relates to specific disease stages. In future, this multimodal imaging system should allow early assessment of therapeutic response and to monitor efficacy of different angiogenesis inhibitors in slowing melanoma progression.

References: [1] Carmeliet P et al. Nature (2000). 407:249–57; [2] Kerbel, R, Folkman J. Nat. Rev. Cancer (2002). 2:727-739; [3] Gillies RJ. J Cell Biochem Suppl (2002). 39: 231–238; [4] Minami T et al (2003). Arterioscl Thromb vasc Biol 23(11):2041-7. [5] Bergers et al. Science. (1999). 284: 808- 812.
Acknowledgements: Work supported in part by NIH grant RO1 HL078665.

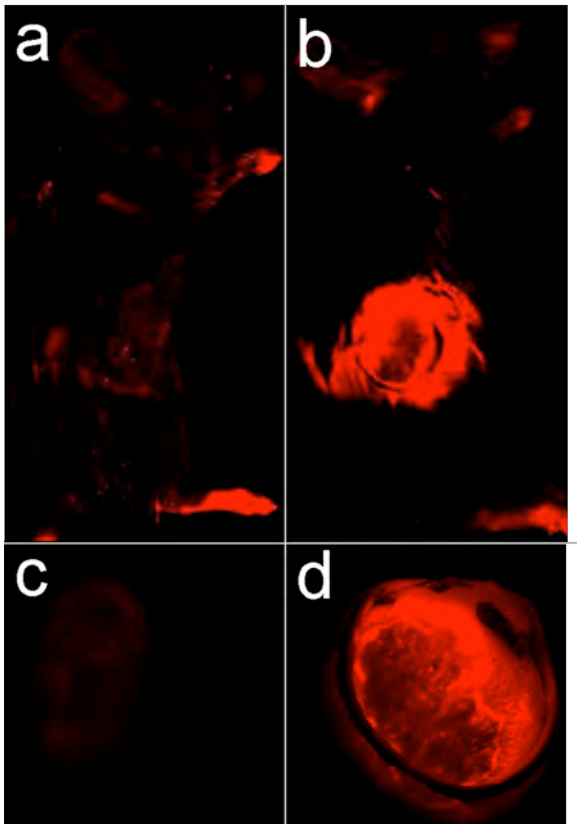

Figure 1. In vivo NIR images (180µm) of WT (a) and T2-Biotag transgenic (b) mice bearing 10 days melanoma tumors, showed a clear difference in binding of Av-Alex 680 in the tumor as well as the surrounding tissue. This difference was confirmed by a high-resolution scan (21µm) of extracted tumors (c, d).

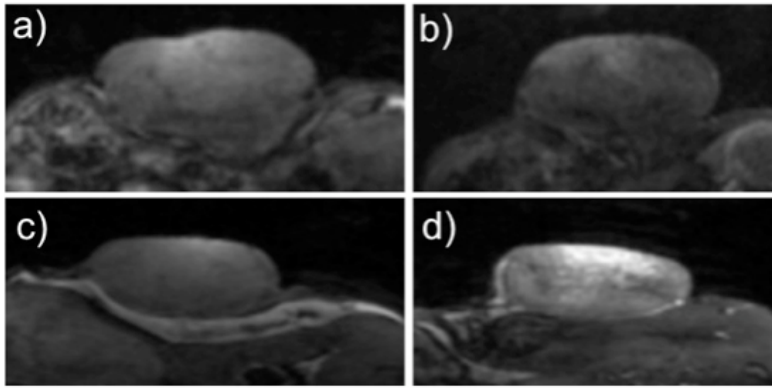

Figure 2. *In vivo* MRI after injection of Avidin-DTPA-Gd shows contrast enhancement in the Biotag transgenic mice. 2d axial sections of 3D GE pre contrast (a,c) and post contrast (b,d) MR images of tumor bearing WT (a,b) and T2-Biotag mice (c,d) that received an intravenous dose of 10mg/ml Av-DTPA-Gd.

Abstracts selected for poster presentation, Cardiovascular Imaging category

Interaction of Gd-rHDL and FeO-rHDL with atherosclerotic plaque components

J. Ayoung[1, 2], C. Blachford[3], Y. Vengrenyuk[3], D.P. Cormode[5], S. Russel[3], K.J. Williams[4], Z.A. Fayad[5], E.A. Fisher[3]
[1]Sarnoff Cardiovascular Research Foundation, Great Falls, VA 22066, [2]Weill Cornell Medical College, New York, NY 10021,[3]New York University School of Medicine, New York, NY 10021, [4]Temple University School of Medicine, Philadelphia PA 19140, [5]Mount Sinai School of Medicine, New York, NY 10029

Atherosclerosis is a major health problem, leading to significant morbidity and mortality. Current methods to evaluate lesions employ invasive techniques and significant amounts of contrast agents. To address this, previous work focused on the development of novel noninvasive imaging agents. This work led to the design of two recombinant high density lipoprotein (rHDL)-like nanoparticles to be used as specific MRI imaging agents of atherosclerotic plaques, Gd-rHDL and FeO-rHDL[1-3]. Both nanoparticles accumulate in atherosclerotic plaques *in vivo*, enhance the MR signal intensity and are taken up by the macrophage cell line J774A.1[1, 3].

This work aims to investigate the mechanism of interaction between the imaging agents and plaque components. We hypothesized the imaging efficacy of the MRI nanoparticles was linked to the nature of interactions between the particles and extracellular matrix components (ECM) of plaques and uptake of the rHDL species by plaque macrophages.

To test our hypothesis we established two *in vitro* systems: 1) a study of the components of the ECM that interact with HDL carrying either Gadolinium (Gd-rHDL) or Iron oxide (FeO-rHDL) and 2) an investigation of the macrophage cell surface proteins that interact with rHDL imaging agents, which may be responsible for cellular uptake.

We assessed the binding of fluorescence-labeled Gadolinium nanoparticles (Gd-rHDL-NBD) for whole ECM derived from bovine aortic endothelial cells (BAEC) or mouse smooth muscle cells (mSMC). After coating wells with cell derived ECM we compared the binding of Gd-rHDL-NBD to that of uncoated wells. Our results indicate the binding to ECM coated wells exceeded uncoated wells. Additionally, Gd-rHDL-NBD showed a higher binding affinity for mSMC-derived ECM compared to BAEC-derived ECM.

To determine whether the imaging element (Gd or FeO), apolipoprotein A-1 (apoA-1) or NBD is selectively transferred to macrophages versus holo-particle uptake, we established *in vitro* assays using mouse peritoneal macrophages. We isolated macrophages from wild type mice (WT), mice deficient in HDL-interacting cell surface proteins scavenger receptor B-1 (SR-B1 -/-) and ATP binding cassette transporter G-1 (ABCG-1 -/-). To assess HDL and particle uptake we incubated cells with rHDL, Gd-rHDL-NBD and FeO-rHDL-NBD. Cells treated with rHDL had apoA-1 localized primarily on the plasma membrane. In SR-B1 -/- and ABCG-1 -/- cells incubated with Gd-rHDL-NBD, the fluor NBD was diffuse throughout the cytoplasm and excluded from the nuclei, while apoA-1 was localized primarily on the plasma membrane. Transmission Electron Microscopic of WT cells incubated with FeO-rHDL-NBD demonstrated FeO localized within vesicles throughout the cell.

These results lend support to our hypothesis that the imaging efficacy of the nanoparticle may be related to its interaction with ECM components. Also in macrophages NBD is selectively transferred to WT, ABCG-1 -/- and SR-B1 -/- macrophages while apoA-1 interacts with a component of the plasma membrane. Furthermore, disruption of SR-B1 and ABCG-1 does not affect uptake of NBD or the interaction of apoA1 with the plasma membrane of macrophages. Future experiments will define what component of ECM is responsible for the binding of rHDL and whether other plasma membrane proteins are required for apoA-I interaction and NBD uptake.

(Research supported by NIH grant HL R01HL078667, Sarnoff Cardiovascular Research Foundation)

References

1. JC Frias, Williams KJ, Fisher EA. Recombinant HDL- like nanoparticle: A specific contrast agent for MRI of atherosclerotic plaques. *J. Am Chem. Soc.* 2004; 126:16316 – 1631.
2. JC Frias, Williams KJ, Fayad ZA, Fisher EA. Properties of a versatile nanoparticle platform contrast agent to image and characterize atherosclerotic plaques by magnetic resonance imaging. *Nano Letters* 2006; 6(10): 2220-2224.
3. DP Cormode, et al. Nanocrystal core high-density lipoproteins: a multimodality contrast agent platform. *Nano Letters*. 2008;8(11) 3715-3723.
4. DP Cormode, Briley-Saebo KC, Mulder WJM, Gilberto J, Aguinaldo S, Barazza A, Ma Y, Fisher EA, Fayad ZA. An ApoA-1 mimetic peptide high density lipoprotein based MRI contrast agent for atherosclerotic plaque composition detection. *Small* 2008; 4(9):1437-1444.
5. KJ Williams, Tabas I. The response to retention hypothesis of early atherogenesis. *Arteriosclerosis, Thrombosis and Vascular Biology*. 1995; 15(5): 551-561.
6. KJ Williams, Tabas I. The response to retention hypothesis of atherogenesis reinforced. *Current Opinion in Lipidology* 1998; 9(5): 471-474.
7. KJ Williams, Tabas I. Lipoprotein retention – and clues to atheroma regression. *Arteriosclerosis, Thrombosis and Vascular Biology*. 2005; 25:1536-1540.
8. DP Cormode, et al. Nanocrystal core high-density lipoproteins: a multimodality contrast agent platform. *Nano Letters*. 2008;8(11) 3715-3723.
9. DP Cormode et al. Comparison of Synthetic High Density Lipoprotein (HDL) contrast agents for MR imaging of atherosclerosis. *Bioconjugate Chemistry*. 2009; 20:937 – 943.
10. I Tabas, Li Y, Brocia RW, Xu SW, Swenson TL, Williams KJ. Lipoprotein lipase and sphingomyelinase synergistically enhance the association of atherogenic lipoproteins with smooth muscle cells and extracellular matrix. *Journal of Biological Chemistry*. 1993; 268(27): 20419-20432.

Title18F-FDG PET/CT for imaging of vessel wall inflammation - Impact of pre-scan glucose levels and FDG circulation time on FDG uptake in the vessel wall

Jan Bucerius[1,2]; Venkatesh Mani[1,2,3]; Claudia Calcagno[1,2]; Colin Moncrieff[1,2]; James H. F. Rudd[7], Josef Machac[4]; Valentin Fuster[3,6]; Michael E. Farkouh[5]; Zahi A. Fayad[1,2,3]

1. Translational and Molecular Imaging Institute, 2. Department of Radiology, 3. Department of Cardiology, Zena and Michael A. Weiner Cardiovascular Institute and Marie-Josée and Henry R. Kravis Cardiovascular Health Center, 4. Division of Nuclear Medicine, Department of Radiology, 5. Cardiovascular Imaging Clinical Trials Unit; Mount Sinai School of Medicine, New York, New York 6. The Centro Nacional de Investigaciones Cardiovasculares (CNIC), Madrid, Spain 7. Division of Cardiovascular Medicine, Cambridge University, United Kingdom

Introduction

18F-fluorodeoxyglucose (18F-FDG) positron emission tomography (PET) is currently being used for imaging of vessel wall inflammation in several clinical trials of novel anti-atherosclerosis therapies as a surrogate marker of treatment efficacy. However, the optimal time between FDG injection and PET imaging of vessel wall (FDG circulation time) is not conclusively established and limited data is available regarding the impact of patients pre-scan glucose levels on the degree of 18F-FDG uptake in arterial vessel walls.

Methods

n=74 (glucose) and n=56 (FDG circulation time) patients, respectively, with either established cardiovascular disease or risk factors for it underwent 18F-FDG imaging to quantify vessel wall inflammation in the ascending aorta and common carotid arteries. FDG uptake (SUV) as well as target-to-background-ratios (TBR) and TBR of the 'most diseased segment' (MDS) of each of the three vessels were measured. A cut-off of FDG uptake values > 2.0 was set to differentiate between inflamed- and non-inflamed vessels. Correlations between circulation time, FDG uptake values, and FDG blood pool activity in the FDG circulation time subgroup as well as multivariate logistic regression analyses, corrected for several patient- and PET related variables in both patient populations were performed to detect an impact of continuous and classified pre-scan fasting blood glucose levels as well as of the FDG circulation time on vessel wall 18F-FDG uptake.

Results

Continuous and elevated classified (≥7.0 mmol/l) pre-scan glucose levels were significantly associated with decreased 18F-FDG uptake values in the aortic and the carotid vessel wall, respectively (Odds ratio; OR: 0.94; p=0.009 and OR: 0.094; p=0028). Contrarily, normal pre-scan glucose levels (<6.1 mmol/l) were significantly associated with a higher incidence of aortic TBR values > 2.0 (OR: 8.0; p=0.022). In the FDG circulation time subgroup,

significantly positive correlations were found between FDG uptake values and circulation times for both the aorta and the carotids. Significantly negative correlations were observed between circulation times and FDG blood pool activity within the superior vena cava (SVC) and the jugular veins (JV). Negative correlations were also observed between FDG blood pool activity and FDG uptake values in the aorta. No correlation was observed between FDG blood pool activity and FDG uptake values in the carotids. Significantly positive correlations between SVC and JV FDG SUV and between SUV uptake in the aorta and the carotids were also observed. Circulation times showed a significantly independent impact on FDG uptake values in the aorta (TBR >2.0: OR: 1.195, p =0.018; MDS >2.0: OR: 1.117, p=0.003) and the carotids (MDS >2.0: OR: 1.059, p =0.005) as revealed by multivariate regression analyses.

Conclusion

Both, pre-scan glucose levels and FDG circulation time significantly impact the 18F-FDG uptake within the aortic and carotid wall and may bias the results of image interpretation in patients undergoing 18F-FDG PET/CT for evaluation of vessel wall inflammation. Appropriate pre-scan glucose levels and FDG circulation times have to be identified by future studies with larger study populations.

Inflammation in human carotid atherosclerosis: a preliminary comparison between dynamic contrast enhanced (DCE) MRI and 18F-FDG position emission tomography (PET)

Claudia Calcagno[1,2], MD, James Rudd[1,2], MD, PhD, Jan Bucerius[1,2], MD, Venkatesh Mani[1,2,3], PhD, Sharath Subramanian[4,5], MD, Sara Fontanez[4,6], BA, David Rosenbaum [2,3], MD, Stephane Silvera[2,3], MD, John Postley[8], MD, Ahmed Tawakol, MD [4,5,6,7], Joseph Machac[2], MD, Valentin Fuster[1,2,3], MD, PhD, Zahi A. Fayad[1,2,3], PhD, FAHA, FACC

[1]Translational and Molecular Imaging Institute, Imaging Science Laboratories, Mount Sinai School of Medicine; [2]Department of Radiology, Mount Sinai School of Medicine; [3]The Zena and Michael A. Wiener Cardiovascular Institute and Marie-Josée and Henry R. Kravis Cardiovascular Health Center, Mount Sinai Hospital; [4]Cardiac MR-PET-CT program, Massachusetts General Hospital; [5]Department of Imaging, Massachusetts General Hospital; [6]Divsion of Nuclear Cardiology, Massachusetts General Hospital; [7]Division of Cardiology, Massachusetts General Hospital; [8]College of Physicians and Surgeons, Columbia University

Introduction: Several studies in the past few years have highlighted the pivotal role of inflammation in the pathogenesis of atherosclerotic plaque[1]. Two non-invasive imaging techniques correlate positively with histological markers of plaque inflammation in both animal models and patients with atherosclerosis: 18F-FDG PET/CT [2,3] and DCE-MRI [4]. However, little is known about the relationship between them and their mutual role in the diagnosis of vulnerable plaques. In this study we investigated the relationship between DCE-MRI and 18-FDG PET/CT parameters in patients with carotid atherosclerosis.

Methods: Thirteen patients with documented vascular disease were recruited. Carotid MR imaging was performed on 1.5T Siemens clinical scanners. T1, T2 and PD weighted axial slices around the carotid bifurcation were acquired using turbo spin echo (TSE) black blood pulse sequences. DCE-MRI was performed on one axial slice using double inversion recovery TSE black blood sequence, after injection of 0.2 mmol/Kg of Gd-DTPA. The change of MR signal intensity in a region-of-interest (ROI) including the entire atherosclerotic plaque was evaluated with a custom-made Matlab (The MathWorks, Inc., Natick, MA,) program. After intra-series registration and de-noising, the area under the signal intensity versus time curve (AUC) was calculated by numerical integration of the time series. To ensure for signal calibration, plaque AUC measures were divided by the corresponding ipsi-lateral sternocleidomastoid muscle AUC. Carotid 18F-FDG PET/CT was performed after injection of 370 MBq of 18F-FDG (120 minutes circulation time). For co-registration between the DCE-MRI and PET/CT datasets, multi-slice PDW MRI was fused with multi-slice CT using a Mirada workstation. The PET and CT images were co-registered using a Leonardo-TrueD workstation. Mean and maximum standardized uptake value (SUV) were measured in carotid arteries by drawing an ROI around the artery. Background SUV was measured in the internal jugular vein. Maximum and mean target to background ratio (TBR) was calculated by dividing the artery SUV by the vein SUV. PET variables were correlated with AUC using Pearson's correlation after appropriate tests for normality of data. A value of $p<0.05$ was considered significant.

Results and Discussion: We found no correlation between maximum and average TBR calculated by PET/CT and AUC calculated by DCE-MRI ($p>0.05$). This finding presents evidence of a possible dissociation between 18F-FDG uptake evaluated by PET/CT and Gd-DTPA uptake evaluated by DCE-MRI in carotid atherosclerotic plaques. However, our study is limited by the fact that only one slice was imaged for DCE-MRI and one source of errors could be mis-registration between the MRI and PET/CT datasets.

Conclusion: In this study we show a lack of correlation between 18F-FDG uptake by PET/CT and AUC by DCE-MRI in carotid arteries of thirteen human subjects. Both techniques are known to positively correlate to histological markers of plaque inflammation. Based on our finding, we speculate that the results of this study may indicate a more complex relationship between Gd-DTPA uptake and plaque composition than previously expected, and we envision a scenario where DCE-MRI parameters may express not only plaque neovascularisation, but also indirectly measure plaque macrophages density and/or lipid content.

References: 1. Moreno PR et al, Circulation 2006; 2. Rudd JH et al, Circulation 2002; 3. Tawakol A et al, Circulation 2006; 4. Calcagno C et al, Arterioscl Thromb Vasc Biol2008

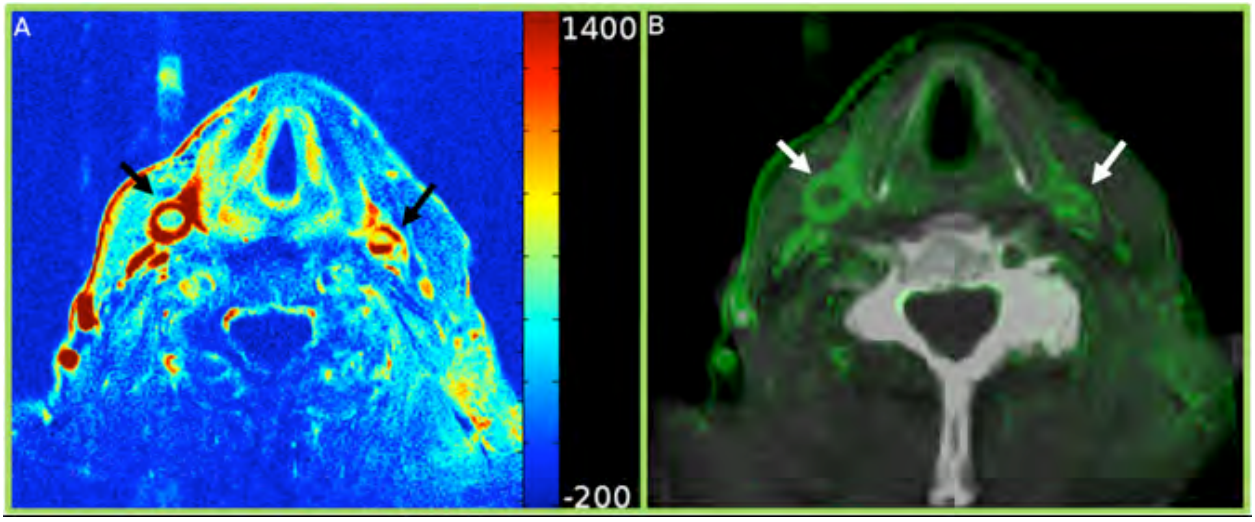

Figure 1. Area under the curve (AUC) map of a representative subject. Panel A, AUC map of the slice chosen for DCE-MRI acquisition. Black arrows indicate right common carotid and left common carotid. Panel B, Overlay of CT slice matching with slice chosen for DCE-MRI (gray color scale) and AUC map (green color scale). White arrows indicate right and left common carotid.

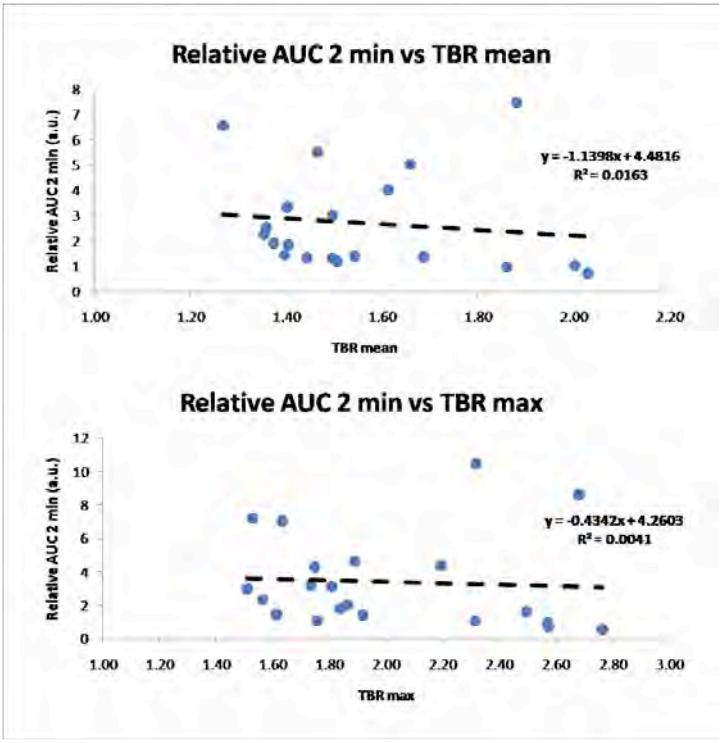

Figure 2. Top panel, correlation between mean TBR and AUC 2 mins; lower panel, correlation between maximum TBR and AUC 2 mins

Intravascular anti-inflammatory efficacy evaluation of pioglitazone in an atherosclerotic rabbit model with multimodality imaging

Stephen D Dickson[1], Esad Vucic[1,2], Claudia Calcagno[1], James RF Rudd[1], James Lin[1], Jessica Mounessa[1], Michelle Roytman[1], Stéphane Potteaux[1], Sotirios Tsimikas[3], Zahi A Fayad[1,2]
[1]Radiology, Mount Sinai School of Medicine; NY, NY
[2]Medicine, Mount Sinai School of Medicine; NY, NY
[3]Vascular Medicine Program, University of California San Diego; La Jolla, CA
Inquires send to Stephen.Dickson@mssm.edu

Introduction: Inflammation is a major contributor to atherosclerotic plaque instability and rupture.[1] Pioglitazone, a PPAR-γ agonist, has been shown to delay atherosclerosis progression in mouse models and increase cardiovascular disease survival rates in high-risk human populations.[2] Pioglitazone displays positive effects through its anti-inflammatory properties, promotion of reversal cholesterol transport, and lipoprotein profile influence.[2] In this study we used a multimodal imaging approach including F18 fluorodeoxyglucose (FDG) PET/CT and dynamic contrast enhanced (DCE) MRI to monitor inflammatory changes of plaque in an atherosclerotic rabbit model[3] during and after pioglitazone treatment. Imaging results were validated with histological analysis of matched aortic sections in order to accurately evaluate therapeutic efficacy.

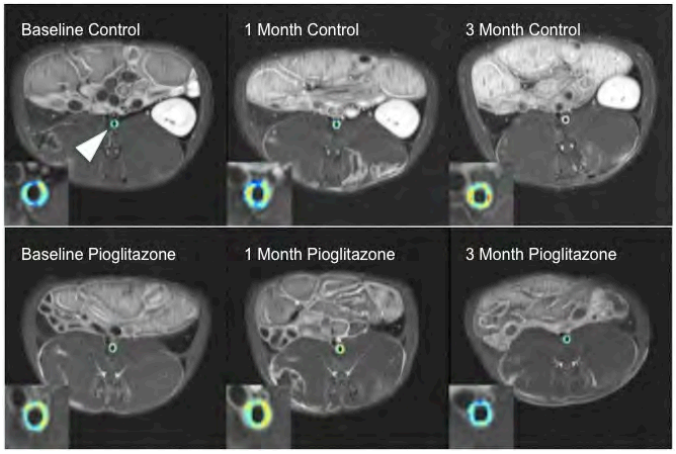

***Figure 1**: DCE-MRI of study groups across three months shows signal decrease in pioglitazone group and not in control group (low AUC high AUC)*

Methods: Atherosclerosis was induced in 13 New Zealand White (NZW) rabbits with 0.3% high cholesterol diet and abdominal aortic double balloon injury. Rabbits underwent baseline DCE-MRI, multicontrast (T1, T2, and PD) MRI, and FDG PET/CT 4-6 weeks following second balloon injury (plaque age = 4 months). Animals were then divided into a control (n=7) and treatment group (n=6). Both groups maintained a 0.15% high cholesterol diet. In addition, the treatment group received 10 mg/kg pioglitazone admixed to diet. DCE-MRI, multicontrast MRI, and FDG PET/CT were again performed after one and three months (*Figure 1, 2)*. DCE-MRI images were analyzed by calculating the area under the signal intensity versus time curve (AUC) of the contrast agent uptake in atherosclerotic plaque. PET/CT images were analyzed by calculating the standard uptake value (SUV) of F18 FDG in aortic sections directly inferior to the left renal bifurcation (0-5 cm *in-vivo*) three hours after injection. Both groups were sacrificed after three months and immuno-histochemistry was performed on a 5 cm length of abdominal aorta using macrophage specific RAM11, ApoB specific MB47 antibodies, and oxLDL specific E06 antibodies.

Results: Three months after pio treatment, DCE-MRI showed a significant reduction in AUC values compared to baseline (p =0.045, Figure 3a) while controls exhibited no difference (p=0.83, *Figure 3a*). FDG PET/CT showed similar SUVs between control and treated animals at baseline (p=0.97, *Figure 3b*) and lower SUVs between groups at one month (p=0.010, *Figure 3b*) and three months (p=0.0025, *Figure 3b*). Immuno-histochemistry showed a significant decrease in macrophage density (p=0.048), a significant decrease in oxLDL density (p=0.044), and decreased LDL plaque density in the treated group as compared to controls (p=0.075). No significant change in vessel wall area was detected with multicontrast MRI from baseline to three months in the control or treatment groups.

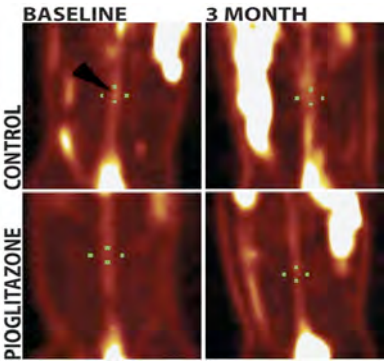

***Figure 2:** FDG PET/CT of study groups, arrow shows region of high SUV*

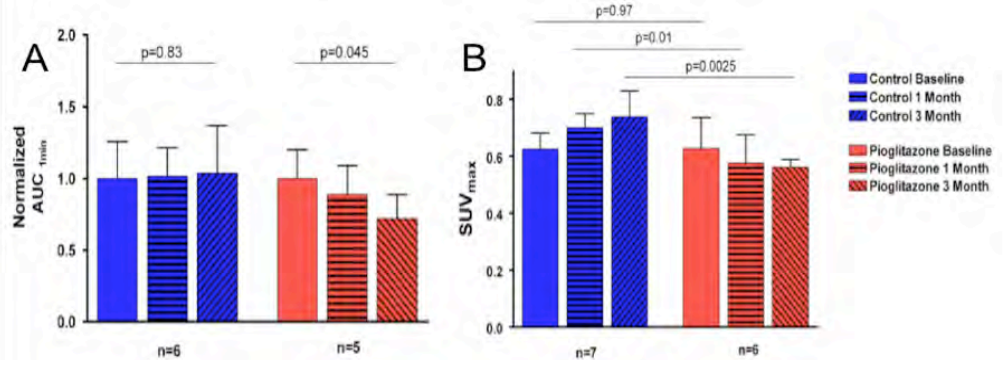

***Figure 3:** A) MRI AUC values after 1 min of contrast enhancement across 3 months. B) FDG uptake values in rabbit abdominal aorta across 3 months*

Conclusion: In this study we showed the ability of DCE-MRI to detect a decrease in vessel wall inflammation after three months of pioglitazone treatment. Positive changes were also observed with FDG PET/CT. These results were validated with macrophage-targeted immuno-histochemistry, indicating therapeutic efficacy of pioglitazone after three months of treatment in a balloon-injured atherosclerotic rabbit model. This multimodality imaging approach could represent a non-invasive technique for future (pre)clinical cardiovascular drug efficacy evaluation.

References: [1] Rocha VZ, Libby P. Nat Rev Cardiol. 2009. [2] Nakaya *et al*. Am J Pathol. 2009. [3] Calcagno *et al*. Art Thromb Vasc Biol. 2008.

Carotid Artery Wall Lipid Quantification by means of 1H-Magnetic Resonance Spectroscopy: Correlation with Carotid Wall Area and Normalized Wall Index.

Raphael Duivenvoorden, MD, Erik S.G. Stroes, MD PhD, John J.P. Kastelein, MD PhD, Aart J. Nederveen, PhD.

Introduction Lipid accumulation in the artery wall is a hallmark of atherosclerosis. Quantification of artery wall lipid content could be of great value to assess cardiovascular disease risk and evaluate drug efficacy. We developed a carotid 1H magnetic resonance spectroscopy (MRS) protocol and assessed the relation between the lipid to water ratio and the arterial wall thickness at the location of the carotid artery.

Methods 3.0 Tesla MRI and MRS scans were performed in the common carotid arteries of 42 subjects (aged 44 ± 13) using a 5 cm single-element coil. 2D CSI data were collected using a point resolved spectroscopy sequence (PRESS) with the following parameters: TR/TE = 1100/30 ms, 5 mm slice thickness, FOV 8 cm, matrix size 20x20, acquisition time 13 min, 1 acquisition. Saturation bands were placed around the artery. Spectra with and without water suppression were obtained. Four voxels positioned at the centre of the artery (total area 100 mm^2) were selected for further analysis and were processed using the 3DiCSI package. Average spectra were processed and peak fitted using jMRUI 2.2. The water peak was assigned to 4.65ppm. Methyl and methylene resonances of fatty acid chains were fitted in their characteristic spectral region (0.8ppm–1.4ppm). A lipid:water ratio was calculated to permit semiquantitative comparison. 3.0 Tesla MRI axial T1-weighted TSE image stacks were acquired at late diastole. Sequence parameters: slice thickness 3mm, non-interpolated pixel size 0.25 x 0.25mm, TE 11ms and TR according to heart rate, active fat suppression (SPAIR) and a double inversion black blood prepulse. Mean wall area (MWA), outer wall area (OWA), normalized wall index (NWI), lumen area (LA) and perivascular area (PVA) that was included in the MRS voxel were determined. Serum tryglicerides (TG) and serum total cholesterol (TC) was assessed in all subjects.

Results and Discussion MWA was 16.4 (5.7) mm^2, NWI 0.33 (0.18), PVA 51.4 (10.3) mm^2, LA 32.3 (5.5) mm^2 and lipid:water ratio 0.34 (SD 0.18). The Pearson's correlation coefficient for lipid:water ratio and MWA was 0.34 ($p=0.02$) and 0.37 ($p=0.02$) for NWI. PVA and LA did not correlate with the lipid:water ratio (-0.25 $p=0.10$ and 0.15 $p=0.31$). In a multivariate analysis including lipid:water ratio, serum TG, serum TC and MWA, the lipid:water ratio was associated with MWA ($p=0.05$) independent of serum TG and TC. For the same analysis with NWI this was borderline significant ($p=0.052$). For PVA and LA this was not significant ($p=0.13$ and $p=0.37$).

Conclusion The lipid:water ratio quantified by MRS of a voxel that includes the carotid artery wall correlated with the carotid artery wall dimensions, independent of serum lipid levels, while it did not correlate with the lumen area and perivascular area. Further research is needed to resolve whether MRS is a useful tool to assess the efficacy of lipid altering pharmacotherapy in the treatment of advanced atherosclerotic lesions.

FIGURE 1

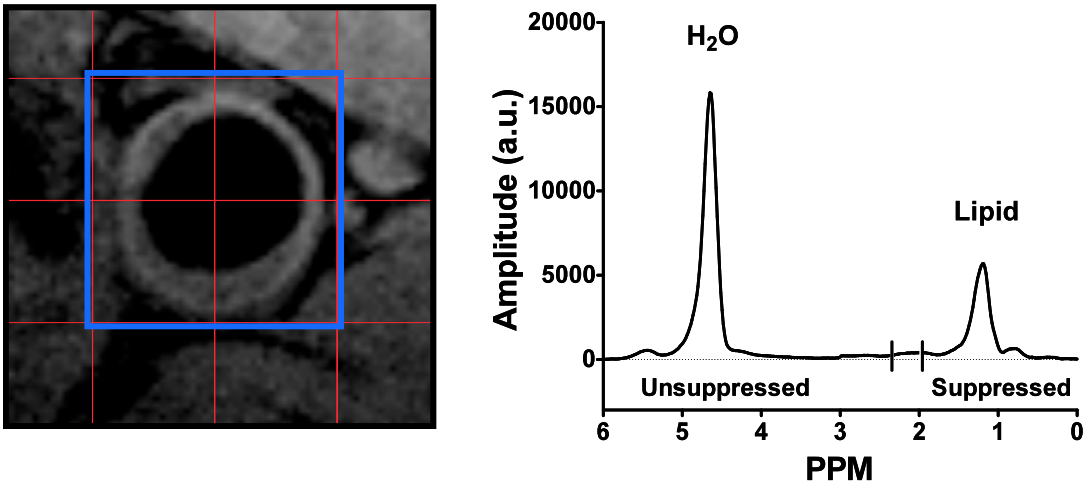

Figure 1. T1-weighted image and 1H-MR spectrum of a volunteer. Four MRS voxels centered over the carotid artery are averaged (blue box). The averaged 10 x 10 x 5 mm MRS voxel includes signal from blood in the lumen, the arterial wall and perivascular tissue. The MRS spectrum is shown on the right.

FIGURE 2

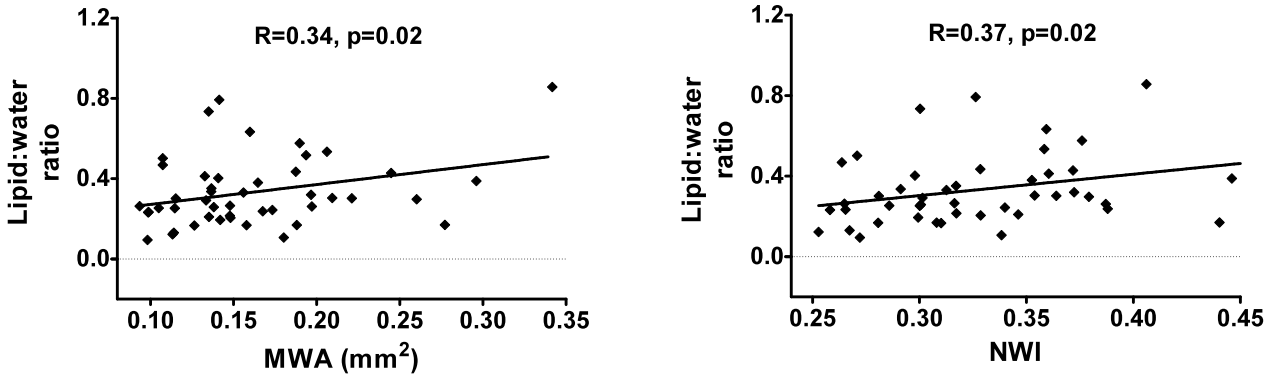

Figure 2. Correlation between the lipid:water ratio and mean wall area (MWA, left) and normalized wall index (NWI, right).

Carriers of Lecithin: Cholesterol Acyltransferase Gene Mutations have Accelerated Atherosclerosis and Outward Remodeling.

Raphael Duivenvoorden, MD, Adriaan G. Holleboom, MD, Bas van den Bogaard, MD, Aart J. Nederveen, PhD, Barbara A. Hutten, PhD, G. Kees Hovingh, MD PhD, Jan A. Kuivenhoven, PhD, John J.P. Kastelein, MD PhD, Eric de Groot, MD PhD, Erik S.G. Stroes, MD PhD.

Introduction Lecithin-cholesterol acyl transferase (LCAT) is a key enzyme in high density lipoprotein cholesterol (HDL-c) metabolism, and (partial) LCAT deficiency results in hypoalphalipoproteinemia. The exact role of LCAT in atherogenesis is subject of debate. Aim of our current study was to address whether carriers of LCAT gene mutations are characterized by increased atherosclerotic burden, ascertained by MRI and ultrasound.

Methods Carotid 3.0 Tesla MRI and B-mode ultrasound measurements were performed in 45 carriers of LCAT gene mutations (43.1±13.2 years) and 45 controls (43.2±12.9 years), matched for age. MRI parameters: Axial T1-weighted end diastolic TSE images acquired with a 5 cm single-element microcoil, slice thickness 3mm, imaging matrix size 240, FOV 60x60mm, non-interpolated pixel size 0.25 x 0.25mm, reconstruction matrix 240, TE 11ms and a heart rate triggered TR, active fat suppression (SPAIR) and a double inversion black blood prepulse. B-mode ultrasound IMT measurements were performed using a Sequoia 512 scanner equipped with an 8L5 transducers (Acuson-Siemens).

Results and Discussion Carriers presented with 38% decreased HDL-c levels ($p<0.001$) and 16% increased trygliceride levels ($p=0.05$). Of the MRI parameters, normalized wall index was 6% (0.34±0.07 vs 0.32±0.05, $p=0.05$), mean wall thickness 19% (0.77±0.32mm vs 0.65±0.14mm, $p=0.03$) and outer wall area 13% (51.9±13.1mm^2 vs 46.0±8.3mm^2, $p=0.01$) larger in carriers than in controls. These differences remained significant after correction for age, gender, body mass index, hypertension, low-density lipoprotein cholesterol, smoking status, family history for cardiovascular disease and accounting for clustering of genetic and/or environmental factors in families. Similar analyses for ultrasound IMT revealed no differences between groups, indicating that our MRI protocol has higher sensitivity to assess vessel wall changes.

Conclusion Carriers of LCAT gene mutations, characterized by profoundly decreased HDL-c levels, exhibit thickened carotid arteries as well as increased outward remodelling on MRI. This suggests they are at increased risk for developing cardiovascular disease. The present findings also imply that raising LCAT activity may be an attractive target in cardiovascular prevention strategies.

Table 1

	Carriers (n=45)	Controls (n=45)	P^1	Adj. P^2
3.0 Tesla MRI				
NWI	0.34 (0.07)	0.32 (0.05)	0.05	0.008
MWA (mm^2)	18.4 (8.8)	14.7 (4.3)	0.01	0.004
MWT (mm)	0.77 (0.32)	0.65 (0.14)	0.03	0.01
OWA (mm^2)	51.9 (13.1)	46.0 (8.3)	0.01	0.02
LA (mm^2)	33.5 (6.7)	31.3 (5.0)	0.08	0.33
B-Mode ultrasound				
MEAN CCIMT (mm)	0.74 (0.33)	0.66 (0.16)	0.19	0.18
MAX CCIMT (mm)	0.89 (0.50)	0.79 (0.19)	0.22	0.22
MEAN cIMT (mm)	0.79 (0.39)	0.71 (0.23)	0.26	0.39
MEAN cIMT (mm)	0.96 (0.52)	0.87 (0.31)	0.31	0.49

Table 1. Differences between carriers and controls in MRI and US parameters. P^1 unadjusted model, P^2 adjusted model.

Figure 1

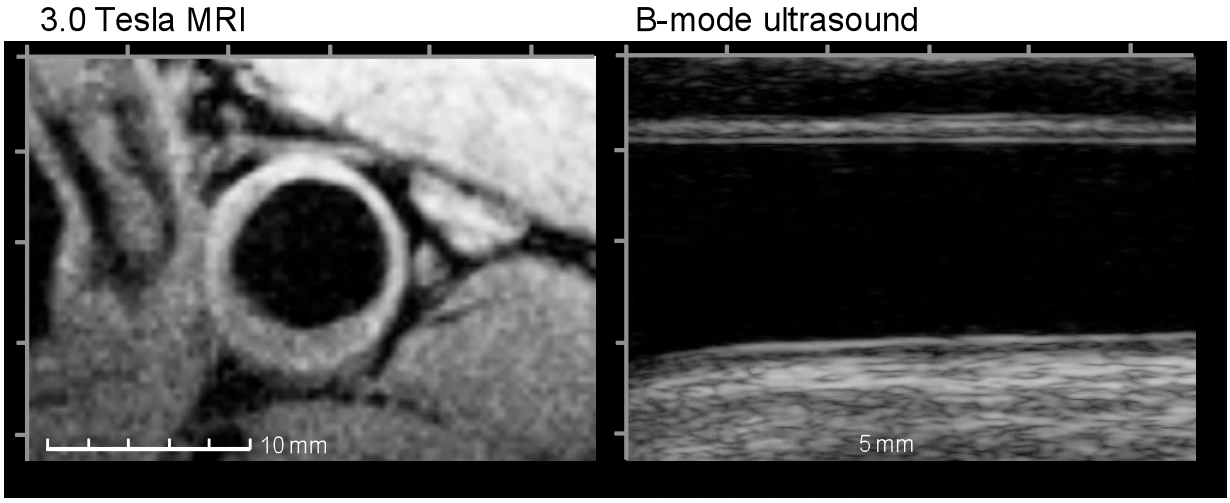

Figure 1. Carotid MRI (left) and carotid ultrasound (right).

Molecular Imaging of Angiogenesis During Wound Healing

Anne E. Friedland, Benjamin B. Bartelle, Cesar A. Berrios-Otero and Daniel H. Turnbull
Kimmel Center for Biology and Medicine at the Skirball Institute of Biomolecular Medicine, New York University School of Medicine, New York, NY

Introduction: The growth of new blood vessels from pre-existing vasculature via angiogenesis is critical for wound healing and organ development. Chronic wounds such as diabetic foot ulcers and ischemic ulcers are the result of impaired or insufficient angiogenesis [1]. Normally, angiogenesis is initiated immediately upon wounding by a number of molecular signals, including hemostatic factors, inflammation, cytokine growth factors and cell-matrix interactions, and continues until the terminal stages of healing [2]. Preclinical mouse models are crucial for understanding the process of angiogenesis. We have developed T2-Biotag transgenic mice, in which biotinylated protein (Biotag) is expressed in vascular endothelial cells by a minimal Tie-2 promoter. These mice can be imaged using avidinated contrast agents with a number of different modalities including near infrared (NIR), ultrasound and MRI.

Methods: As an initial experiment to test the targeting efficiency in vivo, intracardiac injections of an Avidin-FITC (Av-FITC) probe were performed on E11.5 transgenic and wild type embryos, using ultrasound guidance. The fluorescent probe was allowed to circulate for one hour. Subsequently, the embryos were extracted from the uterus, flushed with PBS-heparin solution, and fixed in 4% PFA for histological analysis.
For *in vivo* wound healing studies, transgenic mice and wild-type control mice were ear-punched to induce angiogenesis in the surrounding tissue. They were injected through the tail vein 0-3 days post ear punch with 150-mL of a NIR dye, Streptavidin-Alexa680 (StAv-680). One hour post-injection, the mice were anesthetized and imaged on the Licor scanner at 84mm resolution. Mice were similarly imaged 0-3 days post trauma.

Results and Discussion: Differential binding of the targeted Av-FITC was observed in T2-Biotag transgenic embryos compared to the wild type embryos. Expression of the transgene was significantly higher in the smaller blood vessels and the microvasculature that was undergoing active angiogenesis, compared to the larger, more mature blood vessels within the transgenic embryos (Fig. 1). During wound healing, the T2-Biotag transgenic mice showed significantly more enhancement than the controls in the tissue surrounding the ear punch, with visible enhancement of large blood vessels (Fig. 2). In time-course experiments, enhancement around the ear-punch was the highest at day 0, and decreased slightly over the following three days. However, there was still noticeable contrast in the tissue surrounding the ear-punch day three after injection, suggesting that the site was still undergoing angiogenesis.

Conclusion: From our model, it appears that angiogenesis is initiated within an hour of wounding and continues over the next three days, with the expression of Tie-2 decreasing over the course of the three days. The T2-Biotag system provides a powerful multimodal tool for dynamic studies angiogenesis in embryos and during wound healing. Ongoing studies will focus on other aspects of the wound-healing model, specifically in the brain.

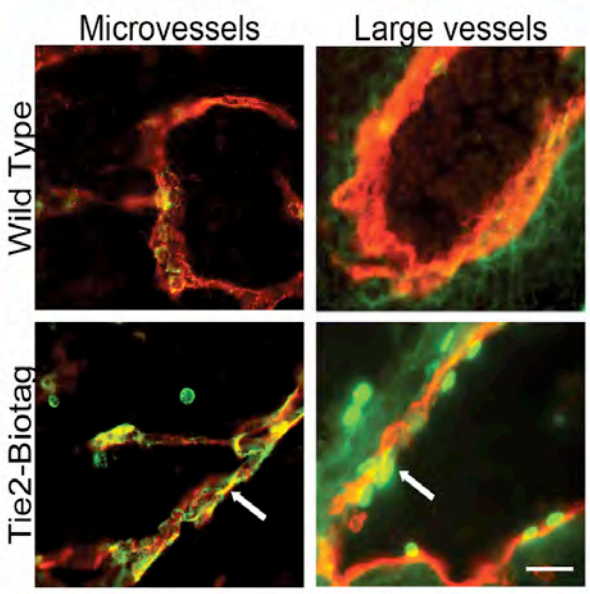

Figure 1. Embryonic vasculature stained with PECAM1 (red) and Av-FITC (green). The Wild Type embryos showed very little Av-FITC binding around either the microvessels or the large vessels, whereas the T2-Biotag mice showed strong Av-FITC binding around both, with particularly high binding around the microvessels.

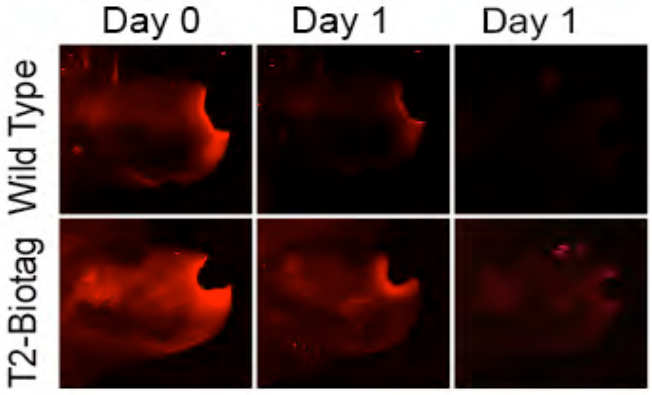

Figure 2. NIR scans of Wild Type and T2-Biotag ears. Wild Type mice showed minor localization of StAv-680 (red), possibly due to inflammation or hemmhoraging around the wound. T2-Biotag animals showed bright labeling in the ear vasculature and a wide corona surrounding the wound.

References:

[1] Li W *et al* Contemporary Surgery (2003). 5: 5-9;
[2] Tonneson M et al J Invest Dermato Symp Proc (2000). 5: 40-46.

Comparison of an 8-channel array coil and a 4-channel array coil in carotid plaque imaging at 3T

Merav W. Galper, [1] Venkatesh Mani, [1] Daniel D. Samber, [1] Raphael Duivenvoorden, [1] and Zahi A. Fayad[1]
1- Mount Sinai School of Medicine, New York, NY

Introduction – High-resolution magnetic resonance imaging (MRI) has emerged as an effective, noninvasive modality to evaluate plaque morphology and composition, which may help predict vulnerability to rupture. Phased-array surface coils have specifically been designed to image atherosclerosis near the carotid bifurcation, but few studies have investigated the effect of element number in achieving good signal-to-noise ratio (SNR), contrast-to-noise ratio (CNR) and overall image quality.
Methods – An 8-channel Philips coil was compared with a Machnet 4-channel coil in *in vivo* bilateral carotid images of eight healthy volunteers using T2W magnetic resonance images. All subjects were scanned using the same protocol, and each subject was imaged using both coils in the same session. Lumen and outer wall boundaries of the carotids were outlined by a trained reader. Quantitative SNR of the lumen, outer wall, and sternocleidomastoid muscle were calculated, as was CNR, using a paired t-test statistical analysis. Qualitative assessment of image quality, flow suppression, artifacts, and vessel wall delineation was also performed.
Results and Discussion – Greater SNR was achieved with the 8-channel coil than with the 4-channel coil for all subjects in both right and left carotids in the vessel wall and lumen and in SCM bilaterally (p values< 0.01 uniformly) (**Figure1**). CNR was also greater with the 8-channel coil than with the 4-channel coil for all anatomical regions of interest (p value <0.05) (**Figure 2**).
Conclusion – Our initial results demonstrate potential benefits of using 8- over 4-channel carotid coil, as increasing the number of elements can increase SNR and CNR.

Figure 1A **Figure 1B** **Figure 1C**

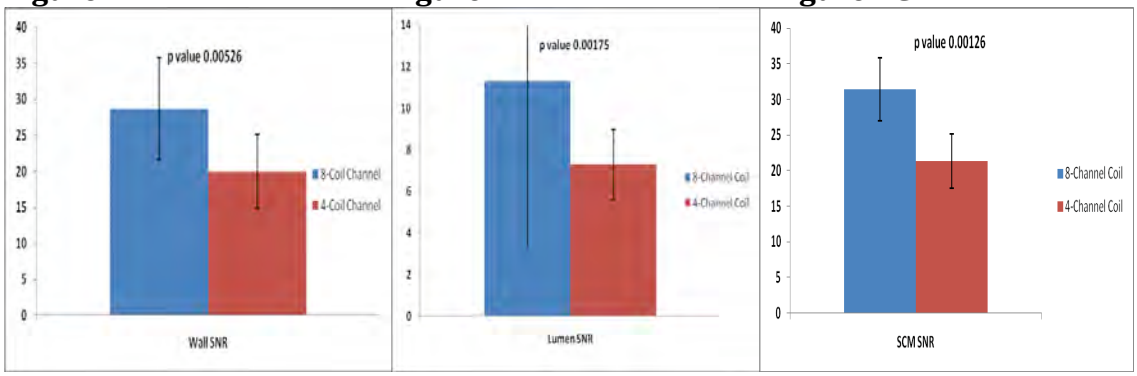

Figure 1. Comparison of SNR values for 8-channel versus 4-channel MRI coil imaging of **A)** carotid artery vessel wall, **B)**carotid artery vessel lumen, and **C)** sternocleidomastoid muscle (SCM).

Figure 2

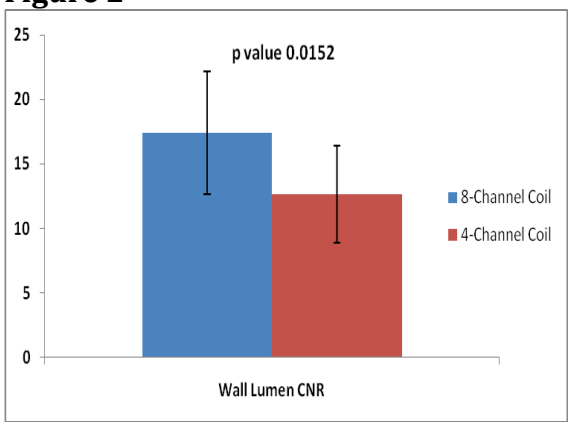

Figure 2. Comparison of CNR values for 8-channel versus 4-channel coil imaging of carotid artery.

Automated Identification of Carotid Wall Boundaries Using a Lesion Space Transformation

Charles. W. Hahm[1], Daniel D. Samber[2], Venkatesh Mani[2], and Zahi A. Fayad[2]
[1]Ischem Corporation, La Jolla, CA., [2]Translational and Molecular Imaging Institute, Mount Sinai School of Medicine, NY., NY. USA

Introduction

The accepted method of assessing the state of atherosclerosis requires the manual identification of vessel wall boundaries by human experts. However, the level of effort required outstrips human capability as study size increases, yet automation of this task remains an elusive goal. We propose a novel algorithm based on the transformation of an image of a vessel into 'lesion space' to achieve automation.

Automated methods of vessel wall tracing often rely on underlying assumptions of tissue morphology. The transformation into lesion space involves the spatial re-mapping of the image to a contour that follows the lumen boundary. This is described as a series of steps, the first of which is an 'unrolling' of the image data (figure 1) followed by a re-alignment of the distances from the lumen. This transformation is based upon an analysis of the tissue structure and facilitates morphologically guided estimates of tissue boundary that are robust in the presence of noise. The algorithm then selects the regions containing the highest contrast to noise ratio and forms a hypothesis of the vessel wall boundary based upon the strongest evidence. Hypotheses of wall boundaries in low contrast to noise areas are then formed by interpolating evidence in high contrast regions. The aim of this approach is to form an estimate that employs both strong evidence as well as reasonable biases implied by the lesion space model in regions where signal quality is poor.

Methods

A total of 300 subjects at medium to high risk for atherosclerosis were imaged on a 1.5 Tesla clinical scanner using a 2D REX turbo spin echo sequence. 12 to 24 transverse proton-density-weighted (PDW) images of the common carotid arteries were obtained per patient. The lumen and outer wall contours of the carotid were manually delineated by experienced researchers for each patient on images of acceptable quality. Data from the same patients were subsequently input into our vessel boundary detection algorithm for analysis.

Results and Discussion

Comparison of traces generated by automated means against those produced manually was very favorable. Correlation between the two methods was excellent in the critical variables of lumen contour area, outer wall area, and vessel wall area. In addition, Bland-Altman analysis performed for these same variables indicated no systematic bias between the automated and manual methods (figure 2).

Conclusion

The algorithm produced results that were found to be consistent with an expert tracer on a large data set of 300 subjects. We hypothesize that the remapping can be extended yet another step in order to transform the lesion into what we term 'canonical lesion space'. In this step, the data rows depicted in lesion space are shifted to align maximal wall width. The result is that that the lesion can be compared directly to a model of progressing lesion development. We theorize that this mapping would be a source of informative features in the automated classification of lesion type.

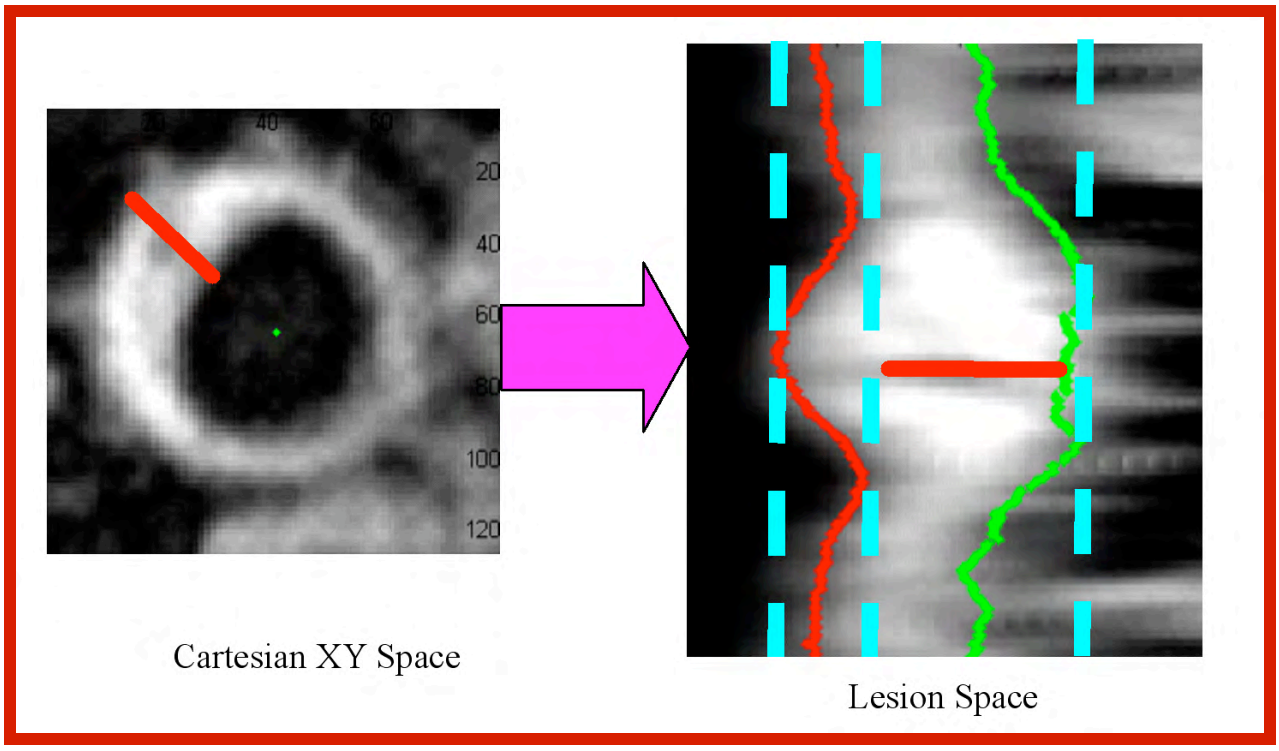

Fig.1: The left panel depicts the input image and reference points prior to transformation into lesion space. The right panel shows the second step of the transformation, prior to column realignment.

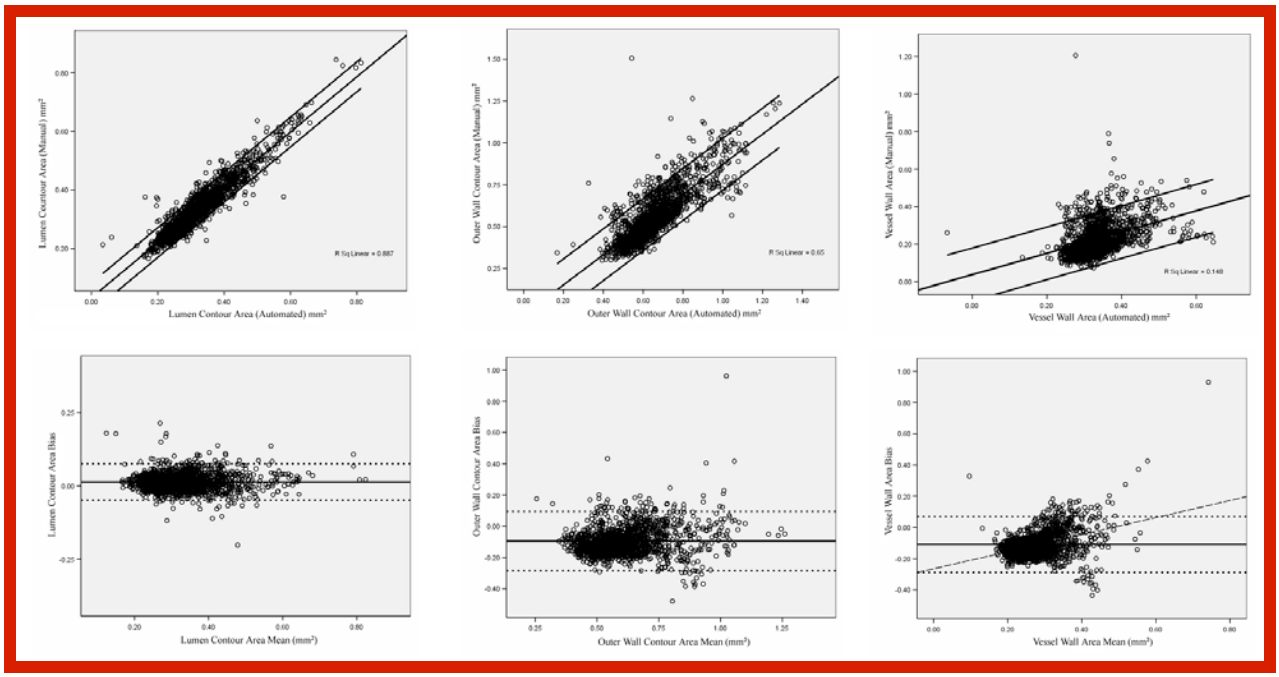

Fig.2: Correlation and Bland-Altman plots of lumen area, outer wall area, and vessel wall area for manual and automated methods.

Manganese based Micelles for the Detection of Vulnerable Atheroscelrotic Lesions

Tuyen Hoang, Peter X Shaw, Sung Kee Ryu, Simone Green, Stephen Dickson, Venkatesh Mani, Zahi A. Fayad, Sotirios Tsimikas, Karen C. Briley-Saebo

Mount Sinai School of Medicine, Molecular Imaging Institute, Department of Radiology and Gene and Cell Medicine

Introduction: Oxidized low-density lipoproteins (OxLDL) are critical to atherogenesis and have been linked to plaque progression and de-stabilization. Recent studies have shown that high levels of OxLDL epitopes, primarily malondialdehyde (MDA)-lysine, are predominant in unstable human lesions. Previously, gadolinium (Gd) based micelles have been used as a platform for the highly sensitive in-vivo detection of MDA-lysine epitopes using Magnetic Resonance Imaging (MRI). However, bio-retention and biotransformation of Gd may limit clinical translatability. Manganese (Mn(II)) is an endogenous paramagnetic metal ion that is safe when administered in the chelated form. Studies indicate that intracellular uptake of Mn(II) results in 10-fold increases in efficacy due to interaction with metalloproteins and/or cell membranes. We therefore hypothesize that is possible to formulate biocompatible contrast agent that is able to detect in vivo oxLDL using MRI. Here, we compared the efficacy and safety of oxLDL targeted Mn(II) and Gd micelles.

Methods: 0xLDL targeted Mn(II) and Gd micelles were synthesized using a thin-film hydration technique and conjugated to the murine monoclonal antibodies for MDA-lysine (MDA2) or human antibody single-chain fragment IK17 targeted to MDA-like fragments. The micelles were characterized by size, zeta potential, Mn or Gd content, binding efficacy, vascular stability, and in vitro uptake by J447A.1 murine macrophages. MR efficacy was evaluated in ApoE-/- mice using T1-weighted black blood imaging sequences (9.4T). Mice were administered either 0.05 or 0.075 mmol/Kg Mn(II) or Gd micelles, respectively via tail vein injection. Confocal imaging was used to verify macrophage uptake.

Results: Due to limitations associated with the hydration spheres, Mn(II) micelles (10±2 nm) exhibited significantly smaller hydrated sizes relative to equivalent Gd micelles (15±2 nm). Additionally, the Mn(II) micelles (-4 mV) exhibited higher zeta potentials relative to equivalent Gd micelles (-6 mV). However, the variation in size and charge did not alter the ability of the oxLDL targeted micelles to bind MDA-LDL, as confirmed via ELISA assays. Transmetallation of Mn(II)micelles was less than half that of Gd micelles at concentrations of zinc and copper above 5 umol/L (**Figure 1a**). Flow cytometry of cells showed significant apoptosis of cells incubated with IK17 labeled Gd micelles relative to equivalent untargeted formulations. 1K17 labeled Mn micelles (**Figure 1b**). Mn and untargeted micelles had similar apoptotic rates. In vivo MR imaging indicated that optimal MR signal enhancement was observed at 48 to 72 hours for Mn(II) micelles with no residual enhancement observed at one week post injection (**Figure 2**). OxLDL targeted Gd micelles exhibited maximum enhancement at 96 hours to 1 week post injection with residual signal observed for more than 8 weeks post injection. At max enhancement, the MR efficacy of Mn(II) micelles did not differ significantly from Gd micelles. Confocal microscopy verified cell uptake of Mn(II) and Gd micelles within intraplaque foam cells 48 hours post injection. All rhodamine was out of the arterial wall within 1 week post injection.

Conclusion: This study demonstrates the feasibility of developing clinically translatable Mn(II) based molecular imaging probes to detect oxidative-epitopes in the arterial wall. An ongoing study seeks to correlate MR signal enhancement with MDA-lysine levels.

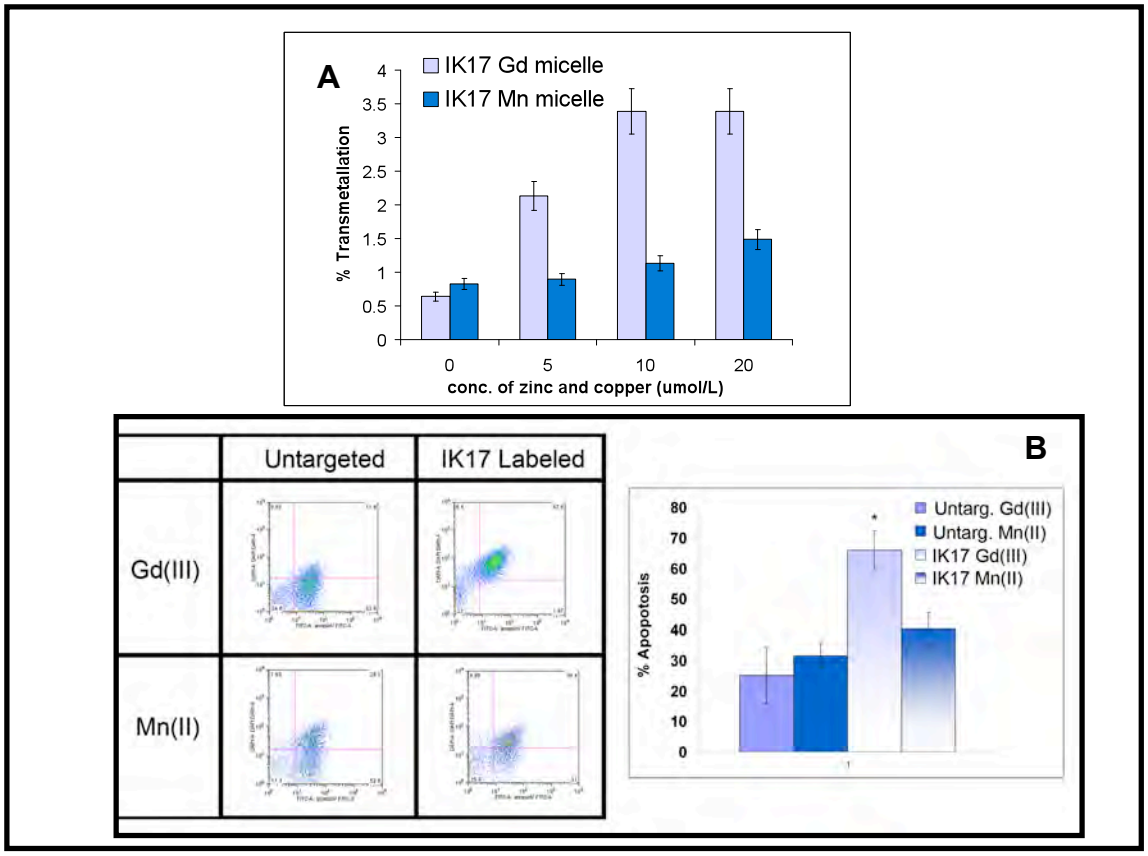

Figure 1: a) Transmetallation after titration of IK17 labeled micelles in known quantities of zinc and copper. b) Flow cytometry of J774A cells after incubation with IK17 targeted and untargeted Mn and Gd micelles.

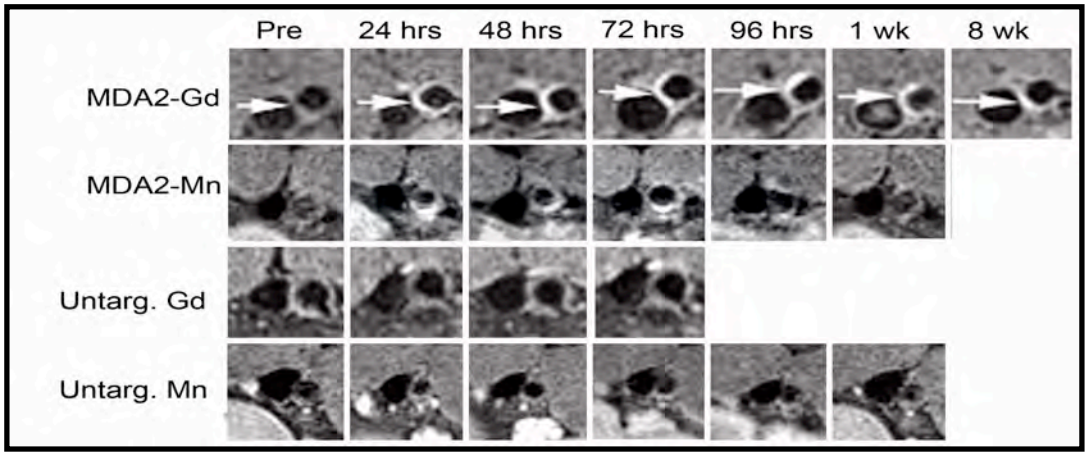

Figure 2: Representative MR images in APOE-/- mice following administration of oxLDL targeted and untargeted Mn(II) and Gd micelles at 9.4T.

(Title)**Multimodality Imaging of Chronic Ischemia**

(Authors) Kiyotake Ishikawa, MD, Dennis Ladage, MD, PhD, Kleopatra Rapti, PhD, Leticia Fernandez-Friera, MD, Ana Maria Garcia-Lopez, MD, Javier Sanz, MD, Roger J. Hajjar, MD, Yoshiaki Kawase, MD, Mario J. Garcia, MD,

(Affiliations) Cardiovascular Research Center, Mount Sinai School of Medicine, New York

(Abstract text, 500 words)

Introduction

Although ischemic cardiomyopathy is commonly caused by chronic obstructive coronary disease, the mechanism of that is still under investigation.

Methods

We present magnetic resonance (MR) and histology findings in a chronic ischemia model in pre-clinical study.

Results and Discussion

Strain analysis of ischemic area revealed significant decrease of radial strain, but sustained circumferential strain. MR image showed myocardial edema exclusively in endocardium layer without delayed hyper enhancement, which implies process of developing hibernated myocardium by repetitive ischemia. From macroscopic view, no myocardial infarction was found, however, mild inflammation was seen only in endocardium with microscopic analysis, whereas no histological change was seen in epicardium. Tunel staining also showed mild ongoing apoptosis in anterior wall, with more apoptosis to the endocardium.

Conclusion

This case illustrates the features of multimodality imaging in chronic obstructive coronary disease and gives us great insight in understanding the mechanism of ischemic cardiomyopathy.

(Maximum of 2 figures, include legends as text)

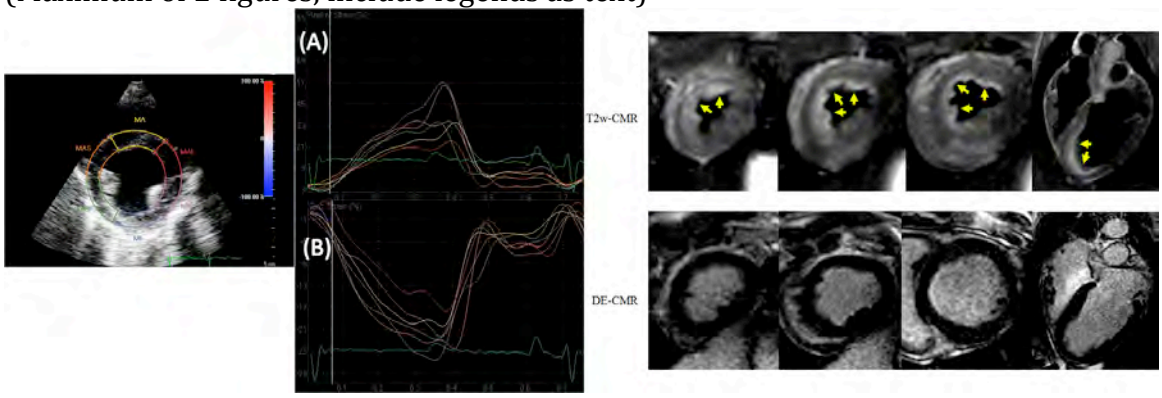

FIGURE 2

Figure 1. Text legend Clinical imaging
Left: Strain analysis of six equally divided segments at the level of papillary muscles. Yellow and red lines are defined as anterior wall. Both radial strain (A) and circumferential strain (B) showed relatively decreased, yet preserved strain rate compared with other regions (CS -19% vs -26%, RS 30% vs 46%; respectively).
Right: Corresponding short axis and long axis images obtained by CMR. T2w-CMR images showed increased signal intensity in the anterior wall (arrows), indicating myocardial edema from ischemia mainly in subendocardium (upper row). However, no specific change was found in delayed enhancement images (lower row).

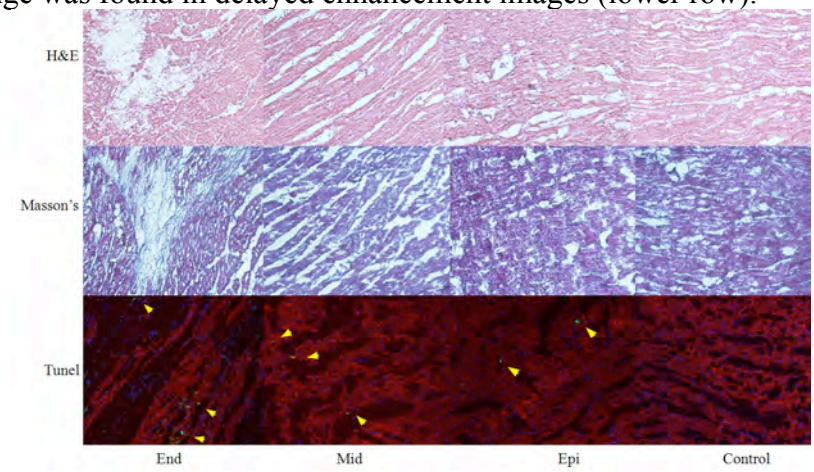

FIGURE 2

Figure 2. Text legend Microscopic image
General histopathology as assessed by H&E (upper) reveals cardiac lesion. Further characterization by Masson's trichrome (middle) staining shows interstitial fibrosis (arrows), which is more severe towards the subendocardium. Bottom: TUNEL staining of myocardial tissue sections for the detection of apoptosis. TUNEL positive nuclei are stained with FITC (green; arrow heads). Cardiomyocytes were identified by α actinin immunostaining (red). Nuclei were stained with DAPI (blue). Percentages of TUNEL positive nuclei were 0.40%, 0.26%, 0.12%, 0.03%; endo, mid, epi, control endo, respectively.

Whole-Body PET/MR: from Benchmark to Nowadays. A Powerful Tool for Cardiovascular Imaging. Preliminary Results

David Izquierdo-García and Zahi A. Fayad
Translational and Molecular Imaging Institute, Mount Sinai Hospital, NY.

Introduction: There are many motivations for combining PET and MR scanners together. The most straight forward are the excellent soft tissue contrast, the elimination of the extra radiation from the CT (used to provide both anatomical and attenuation-correction information) and the multifunctional imaging ability (thanks to a wide spectrum of MR sequences and techniques) that complements the functional molecular information from the PET.

In the case of cardiovascular diseases, multimodality imaging provides a better understanding of the processes taking place in the vascular beds. In particular, PET/MR offers the possibility of accurately combine functional and excellent anatomical information of the targeted damaged area.

History: The idea of combining PET and MRI started even before the introduction of the first clinical PET/CT in 1998. The first design of combined PET and MRI scanner was published by Marsden et al. in 1997 [1]. This system allowed simultaneous PET and MR acquisition by separating the PET scintillation detectors (inside the MR magnet) from the photomultiplier tubes (PMTs, sitting outside the magnetic field) in order to avoid electromagnetic interference between PET and MRI signals. Since then, evolution of technology has provided broader availability to faster and better scintillators (such as LSO or LySO) and new technology detectors based on avalanche photodiodes (APDs) that are insensitive to the magnetic field. However, available up-to-date prototypes provide only reduced field of view due to the technological and economical challenges of large scale models (Pichler et al. [2] and Carpenter et al. [3]).

First combined Whole-Body PET/MR scanner. The first combined Whole-Body PET/MR system developed by Philips in conjunction with the Translational and Molecular Imaging Institute (TMII) has recently being installed at Mount Sinai Hospital. This system provides sequential MRI and PET acquisition by combining standalone PET and MR scanners face to face, together with an innovative rotating bed that accurately positions the patient inside each scanner (see Fig. 1).

First Studies: Our group is currently performing a clinical and a preclinical study to test the performance of this combined Whole-Body PET/MR scanner. The preliminary images show promising and valuable results. Fig. 2 shows comparative images of the same patient on a standard clinical PET/CT scanner (a) and on our combined PET/MR scanner (b). As observed from the figure, the quality of the PET/MR images allow a better visualization and quantification of the vascular beds (mainly aorta and carotids). Fig. 3 presents an example of the visualization of the aorta with both PET and MR images (arrows) in a rabbit model of atherosclerosis (high cholesterol diet following a double balloon injury).

Discussion: Multimodality imaging enhances the power of the separated modalities by automatical combination of functional and anatomical information. The use of PET/MR scanners instead of PET/CT scanners would not only reduce the extra radiation dose to the patient but also would offer higher soft tissue contrast, allowing better visualization and understanding of the underlying disease. In particular, combined Whole-Body PET/MR scanners like the one presented here, would be a very valuable tool for cardiovascular disease imaging, enhancing the detectability and the diagnostic of the damaged vascular beds.

References

1.- Y. Shao , S.R. Cherry, K. Farahani, K. Meadors, S. Siegel, R.W. Silverman and P.K. Marsden. Phys. Med. Biol. 42 (1997) 1965 70.
2.- H.F. Wehrl, M.S. Judenhofer, S. Wiehr and B.J. Pichler, Eur J Nucl Med Mol Imaging (2009) 36 (Suppl 1):S56 S68.
3.- R.C. Hawkes, T.D. Fryer, S. Siegel, R.E. Ansorge and T.A. Carpenter, TCRT, Volume 9, Number 1, February 2010.

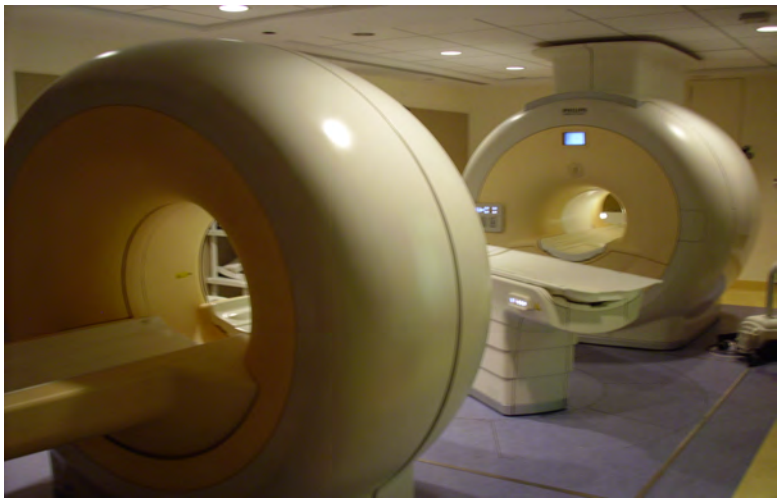

Fig. 1: *Image of the combined Whole-Body PET/MR at TMII in Mount Sinai Hospital*

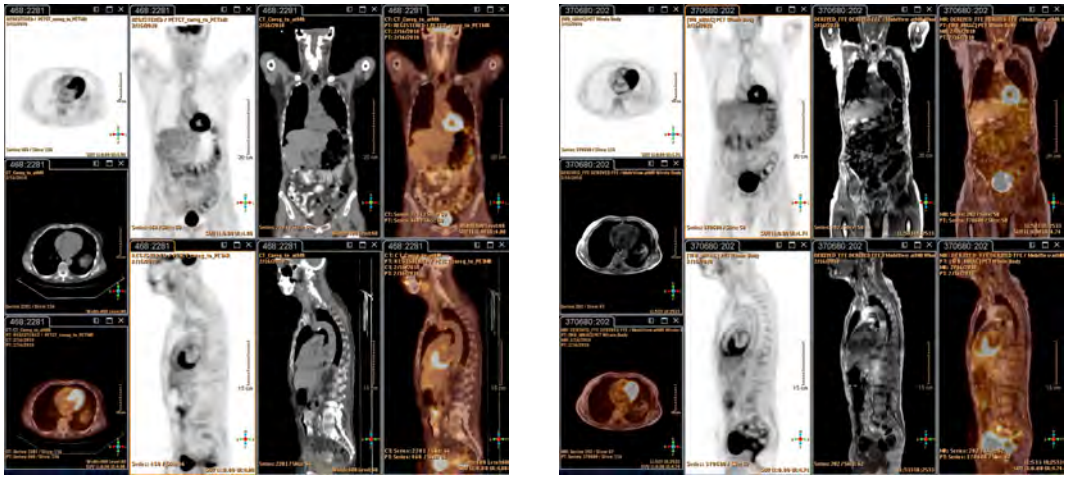

a) b)

Fig. 2: Comparative of image quality within the same patient for a standard clinical PET/CT scanner (a), and our combined Whole-Body PET/MR scanner (b).

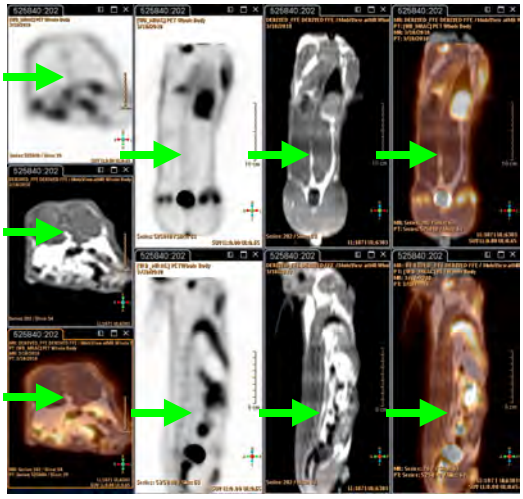

Fig. 3: Evaluation of atherosclerosis on an animal model (White New Zealand rabbit).

In Vivo Characterization of a New Abdominal Aortic Aneurysm Mouse Model with Conventional and Molecular MRI

Ahmed Klink[1], Joeri Heynens[2], Beatriz Herranz[1,3], Erik Sanders[2], Gustav Strijkers[2], Maarten Merkx[4], Klaas Nicolay[2], Ziad Mallat[5], Willem Mulder[1], Zahi Fayad[1]

[1]Translational and molecular Imaging Institute, Mount Sinai School of Medicine, New York, United States, [2]Biomedical NMR, Department of Biomedical Engineering, Endhoven University of Technology, Netherlands, [3]Vascular Imaging and Atherothrombosis, CNIC, Madrid, Spain, [4]Department of Biomedical Engineering, Eindhoven Unviersity of Technology, Eindhoven, Netherlands, [5]Paris Cardiovascular Research Center, INSERM, U689, Paris, France

Introduction: Abdominal aortic aneurysm (AAA) represents a life threatening condition. Recently, an improved model of AAA has been introduced where a combination of angiotensin-II infusion (1 µg/kg/min) and TGF-β neutralization results in a high incidence of fatal AAA rupture in C57BL/6 mice [Wang Y, J Clin Invest. 2009]. The degradation of the extracellular matrix (ECM) has been demonstrated to play a central role in AAA progression. Collagen is an essential component of the ECM and therefore, imaging of collagen may represent a unique opportunity to identify vulnerable AAA. In the current study, we evaluated AAA temporal progression in the aforementioned model using conventional high resolution MRI, while the turnover of collagen was evaluated with nanoparticle-enhanced MR molecular imaging.

Methods: First, AAA progression was monitored in 3 mice using Time of flight (TOF), PD-, T1-, and T2-weighted MRI over a time course of 15 days.

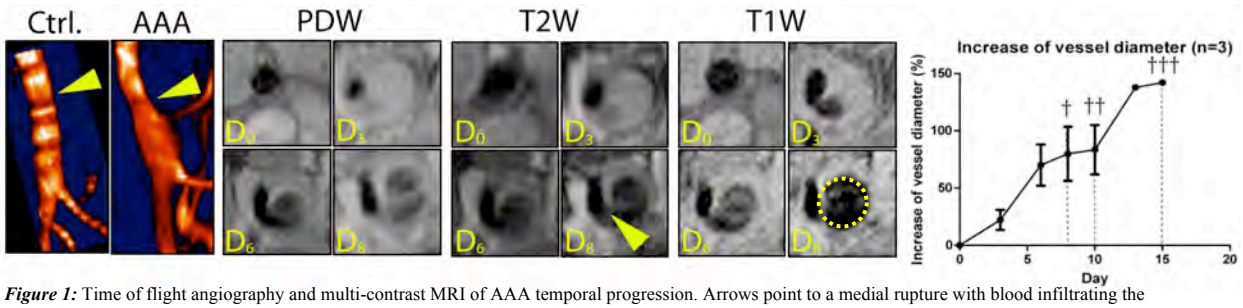

Figure 1: Time of flight angiography and multi-contrast MRI of AAA temporal progression. Arrows point to a medial rupture with blood infiltrating the adventitial tissue. The increase in diameter of the aorta over a 15 days period is reported on the graph.

Paramagnetic micelles (Figure 2A) were prepared as previously described [Mulder WJ, Magn Reson Med. 2007] and CNA35 or the non-binding mutant-CNA35 were conjugated via a sulfhydryl-maleimide coupling method. The specificity of the CNA35 micelles for collagen was evaluated *in vitro*. CNA35 micelles (50 µmol Gd/Kg) were then injected in the tail vein of wild type mice (n=6) that had developed AAA and controls with no AAA (n=3). These animals were MR imaged pre and 32 hours post injection with a T1 weighted spin echo sequence. The CNA35 mutant micelles were applied to AAA mice (n=6) with the same imaging protocol. Aortas were excised for histology (Masson's trichrome), immunohistochemistry, and immunofluorescence with confocal microscopy.

Results: The *in vitro* binding experiment revealed a strong affinity of the CNA35-micelles for collagen, while minimal binding occurred in case of mutant-CNA35.

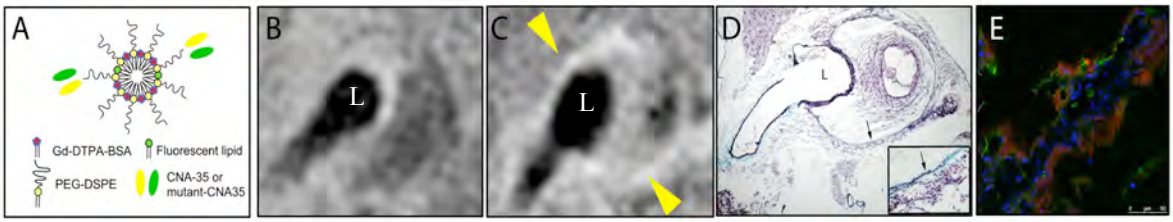

Figure 2: A- Fluorescent and paramagnetic micelles; B- Pre scan of an AAA."L" indicates the lumen; C- Corresponding slice 32hours after injection of CNA35 micelles. Arrows indicates areas of signal enhancement; D- Trichrome Masson's staining displaying presence of collagen in blue (arrow); E- Confocal microscopy representing an overlay of collagen-I marked by immunofluorescence (green), CNA35 micelles (red) and DAPI (blue).

Conventional MRI allowed us to monitor AAA progression at the anatomical level (Figure 1). Multi-contrast sequences revealed a rupture of the medial layer of the aorta with blood consequently infiltrating the adventitial tissue (arrows), and the formation of a false channel (indicated by dotted circle). Further analyses showed a dramatic increase in the diameter of the aorta reaching a 50% growth at day 5. To evaluate the biological processes involved in AAA progression, paramagnetic and fluorescent micelles targeted towards collagen (Figure 2A) were applied. T1-weighted images measured before (Figure 2B) and 32 hours after (Figure 2C) injection of CNA35 micelles images revealed a bright region appearing at the periphery of the aneurysm. Histological examinations of the corresponding slices (Figure 2D) confirmed the presence of AAA and stained positively for a thin layer of collagen in regions of MR signal enhancement. Fluorescent confocal microscopy permitted the precise colocalization of the CNA35 micelles (red) with collagen-I marked by immunofluorescence (green) (Figure 2E). Importantly, animals with early stages or no AAA did not display any significant augmentation in MR signal after injection of CNA35 micelles. Finally, CNA35 mutant micelles did not cause a significant signal enhancement in the MR images post injection.

Conclusion: This study describes the *in vivo* characterization of a novel mouse model of AAA with both conventional and molecular MR imaging. While multi-contrast MRI enabled the clear identification of the anatomical progression of AAA, MR molecular imaging of collagen offered an opportunity to image the turnover of collagen, which is believed to be key in AAA progression and rupture.

DCE-MRI for the evaluation of atherosclerosis in patients with exposure to particulate matter

V. Mani[1], S. T. Sawit[2], C. Calcagno[1], C. Maceda[2], C. Moncrieff[1], Z. A. Fayad[1], J. Moline[3], and M. McLaughlin[2]
[1]Radiology, Mount Sinai School of Medicine, New York, NY, United States, [2]Cardiology, Mount Sinai School of Medicine, New York, NY, United States,
[3]Community & Preventive Medicine, Mount Sinai School of Medicine, New York, NY, United States

Background: Air Pollution, particularly exposure to particulate matter (PM) has been associated with significant adverse health effects leading to increased morbidity and mortality. Cumulative epidemiological and experimental data have shown that exposure to air pollutants leads to increased cardiovascular ischemic events and increased atherosclerosis. As a result of their greater propensity to induce systemic oxidative and proinflammatory effects, exposure to smaller particles is believed to be more pathogenic. An estimated 40,000 men and women worked at "Ground Zero" and Staten Island Landfill (wreckage depository site) after 11 September, 2001 and were exposed to thousands of tons of fine PM, cement dust, glass fibers, asbestos, lead, PCBs, and other pollutants. Among this group include law enforcement personnel in whom we attempt to evaluate the effect of this PM exposure on atherosclerosis using dynamic contrast enhanced (DCE) MRI and reactive hyperemia peripheral arterial tonometry (PAT).

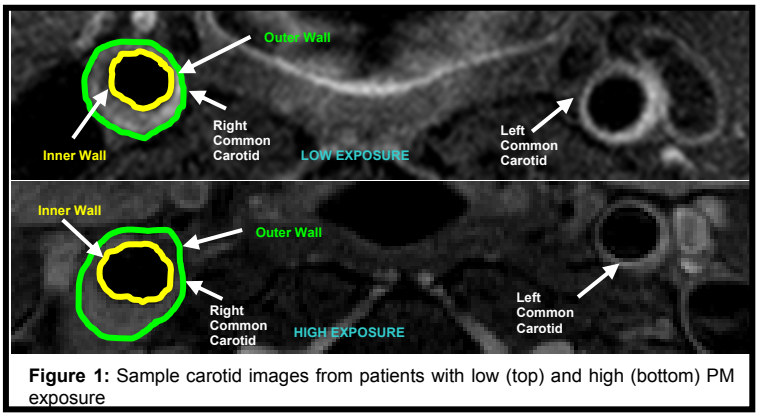

Figure 1: Sample carotid images from patients with low (top) and high (bottom) PM exposure

Hypothesis: We hypothesize that DCE-MRI and PAT can be used to evaluate differences in atherosclerosis in law enforcement personnel subjected to high and low PM exposure.

Table 1: DCE-MRI and PAT for the low and high PM exposures

	Exposure	N	Mean	Std. Deviation	p-value
AUC1 Right Carotid	LOW	5	20.9060	10.04009	0.212
	HIGH	12	14.3283	9.26524	
AUC2 Right Carotid	LOW	5	57.5040	25.97819	0.167
	HIGH	12	41.8792	17.68759	
AUC7 Right carotid	LOW	5	350.9520	93.23058	**0.008**
	HIGH	12	216.9142	78.46576	
AUC1 Left Carotid	LOW	5	28.1140	11.80217	0.080
	HIGH	12	18.8617	8.15998	
AUC2 Left Carotid	LOW	5	74.4480	38.30808	0.183
	HIGH	12	53.7733	22.85591	
AUC7 Left Carotid	LOW	5	368.4820	107.80063	**0.046**
	HIGH	12	255.0775	93.94292	
PAT	LOW	8	1.9675	.40063	0.058
	HIGH	14	1.6850	.25990	

Methods: 22 subjects (20 male) with either high (n=14) or low (n=8) exposure to PM underwent PAT followed by an MRI scan on a 3T Philips whole body scanner. 4 slices just below the right carotid bifurcation were first obtained using 2D black blood T1, T2 and PD weighted Fast Spin Echo images from all subjects. Imaging parameters were as follows: pixel size: 0.5 x 0.5 mm^2; slice thickness = 3mm; gap = 0.3mm; SPIR fat saturation; FOV = 16 x 16cm; TR = 2000ms(T2W, PDW)/1000ms (T1W); TE = 8.3ms(T1W, PDW)/50ms (T2W); Echo Train Length = 15 and NEX = 4. Subsequently, T1W black blood DCE images following injection of 0.1mMol/kg of Gd-DTPA as contrast agent were also obtained using similar parameters as T1W imaging except for NEX = 1 and number of acquisition = 25 with a temporal resolution of 32 seconds. Morphometric analysis was performed on T2-W FSE images yielding wall area, lumen area and wall thickness measurements for all patients. Area under the signal intensity vs. time curve for 1 minute, 2 minutes and 7 minutes (AUC1, AUC2 and AUC7) were obtained from the DCE images using a custom software program in MATLAB by manually tracing both the lumen and outer vessel walls of left and right common carotid arteries. Sample black blood T2W images and AUC7 maps obtained from low and high PM exposure patients are shown in **Figures 1 and 2**. MRI measures were correlated with PAT using Pearson's correlation. The differences in DCE-MRI parameters and PAT between the high and low exposure groups were compared using independent samples t-test. A p-value <0.05 was considered statistically significant.

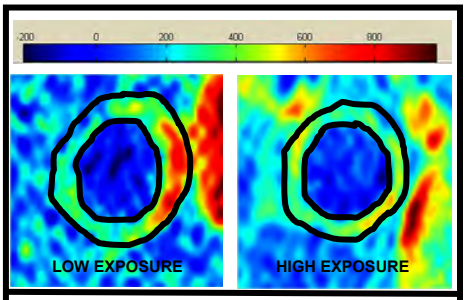

Figure 2: Sample DCE MRI AUC (7 minutes) images from a low and high PM exposure patients

Results: There was a significant correlation between DCE-MRI AUC measures and vascular reactivity (surrogate for endothelial function) measured by PAT (higher values of PAT indicate better endothelial function, **Figure 3**). There were NO significant differences between the low and high exposure groups in terms of patient characteristics (total cholesterol, LDL, HDL, blood pressure, BMI, fasting blood sugar, testosterone and waist to hip ratio) and vessel wall morphometrics (lumen area, total vessel area, vessel wall area and wall thickness for both carotids). However, the high exposure group had significantly lower AUC7 for both left and right carotids. DCE-MRI AUC measures and PAT values for the low and high PM exposure groups are shown in Table 1.

Conclusions: DCE-MRI AUC measures correlate with PAT and may be used to evaluate differences in atherosclerosis due to different levels of PM exposure.

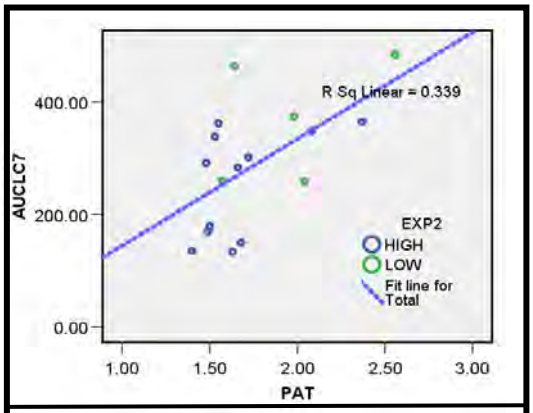

Figure 3: Correlation between DCE-MRI AUC 7 minutes and PAT; p < 0.05

Improving robustness of the assessment of brachial artery endothelial function by flow mediated dilation using 3T MRI

C. Moncrieff[1], V. Mani[1], C. Calcagno[1], M. V. Sevillano[1], R. Fayad[1], D. D. Samber[1], J. S. Aguinaldo[1], S. Ramachandran[1], and Z. A. Fayad[1]
1Radiology, Mount Sinai School of Medicine, New York, NY, United States

Background: Endothelial dysfunction is one of the manifestations of vascular diseases such as atherosclerosis. Studies have shown that the vessel wall endothelium is critical for vascular homeostasis and a dysfunctional endothelium in peripheral vasculature is an independent predictor of future cardiovascular events in individuals at risk for cardiovascular disease. Flow mediated dilatation (FMD) of the brachial artery assessed using either ultrasound or MRI has been used to evaluate endothelial function in human subjects. Previous studies have also shown that MRI measures of FMD have higher inter-study reproducibility and are less operator dependent while still correlating well with ultrasound measures, thereby making MRI the preferred method for evaluating FMD. FMD by MRI is evaluated by bright blood techniques such as Fast Low Angle Shot (FLASH) or balanced–steady state free precession (b-SSFP) cine sequences. FLASH sequences are not ideal as the contrast obtained is dependent on flow velocity. b-SSFP sequences on the other hand produce image contrast that is relatively flow independent but require excellent field homogeneity. It is difficult to obtain good field homogeneity especially at the sides of the patient's body for obtaining b-SSFP images without frequency artifacts especially while using surface coils at 3T.

Purpose: The purpose of this study was to examine the coil/patient set up for acquisition of b-SSFP cine images of the brachial artery to evaluate FMD at 3T.

Figure 1: Set up for 3D brachial b-SSFP imaging using 8-channel knee coil. Patient is in head first prone position with arm extended above the head.

Methods: 7 healthy volunteers (4 female), aged 26-43 were scanned with a bright blood cine b-SSFP sequence on a 3T Philips scanner. b-SSFP sequence was used to reduce the effects of flow on signal contrast obtained. For obtaining better magnetic field homogeneity, the 8 channel knee volume coil, placed as close to the magnet iso-center as possible was used for signal acquisition. To position the brachial artery in the center of the knee coil, the subjects were placed in a head first prone position with the target arm extended above their head as shown in Figure 1. Imaging parameters were as follows: FOV = 12cm x 12 cm; pixel size= 0.5 x 0.5mm in-plane; slice thickness=3mm; TR/TE=5/2.5ms;NEX=1; peripheral gating; 30 phases per cardiac cycle; volume shim; no fat suppression. Images were obtained before and 5 minutes after a cuff on forearm was inflated to supra-systolic pressure. Images were graded on a scale of 1-5 (1=best) with regard to overall image quality, vessel lumen delineation and artifacts. The subjects were also asked to score the comfort level during the scan procedure on a scale of 1-5 (1=most comfortable).The set up is shown in Figure 1. Total scan time was approximately 6 minutes per subject.

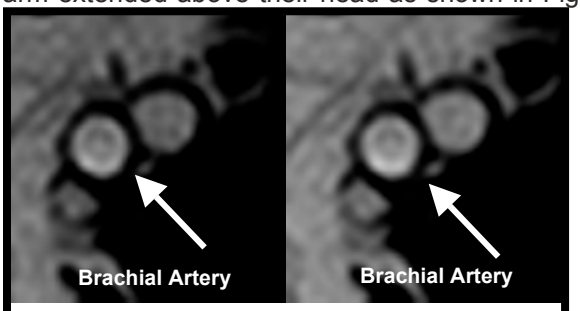

Figure 2: Sample 3T b-SSFP images from a cine using the setup described in Figure1. Vessel lumen is clearly delineated with no artifacts.

Results: Sample images using the setup described are shown in Figure 2. Sample images using a traditional setup of a surface coil on a patient lying head first supine in the magnet bore are shown for comparison in Figure 3. Overall image quality for the setup in Figure 1 was 1.4±0.5 for overall image quality, 1.2± 0.3 for vessel lumen delineation and 1.4 ± 0.3 for artifacts. The patient comfort was 2.2 ± 1.3.

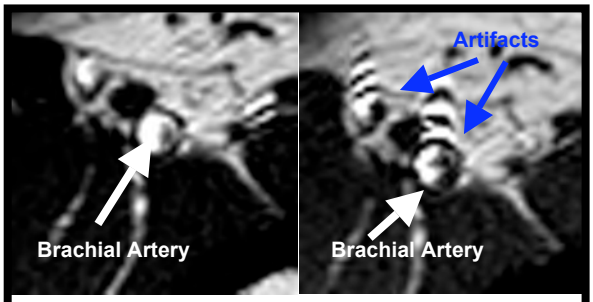

Figure 3: Sample 3T b-SSFP images from a cine using conventional setup with surface coil and patient in head first supine position. Significant artifacts can be seen.

Conclusions: b-SSFP cine images can be obtained with excellent image quality and adequate patient comfort at 3T using the setup described above for measurement of FMD.

IVIM Diffusion MRI for the Diagnosis of Liver Cirrhosis

Jignesh Patel, Eric Sigmund, Henry Rusinek, Marcel Oei, Bachir Taouli

Department of Radiology, New York University Langone Medical Center and Mount Sinai Medical Center

Introduction

- IVIM (IntraVoxel Incoherent Motion) model: both molecular diffusion of water and microcirculation of blood in the capillary network (perfusion) contribute to diffusion signal (1)
- ADC provides pure diffusion and perfusion information (1)
- Liver ADC has been showed to be decreased in moderate/severe fibrosis compared to mild/no fibrosis (2-4)
- Using IVIM model: ADC and D* (perfusion-related diffusion parameter) were shown to be lower in cirrhosis vs. normal liver (5)

Objective

- Quantify liver IVIM parameters and assess their role for discriminating cirrhotic from non-cirrhotic liver

Patients and Methods

- Prospective study, IRB approved
- 31 subjects (M/F 23/8, mean age 51.4 y)
- 13 with normal liver (including 8 volunteers) and 18 with cirrhosis
- 1.5 T (Avanto, Sonata, Symphony, Siemens Medical Solutions)
- Coronal fat suppressed free breathing or PACE SS EPI (TR/TE 2900-4500/76; FOV 350-360 mm; slice thickness/gap 8/0-1.4 mm; 15 slices; 2-3 averages; b=0-50-100-150-200-300-500-700-1000 sec/mm²; GRAPPA 2, 112-192x128-192 mm)
- Image analysis:
  - 25 subjects assessed (12 normal, 13 cirrhosis)
  - 6 patients excluded due to poor image quality (motion or SNR < 2 on b1000)
  - SI measured on large ROIs right hepatic lobe for each b-value (3 ROIs averaged)
  - IVIM parameters obtained using bi-exponential diffusion fit (Igor Pro software)
- **IVIM parameters (Fig. 1):**
  - PF (Perfusion Fraction, surrogate of blood volume)
  - D* (pseudo-diffusion coefficient, surrogate of blood flow)
  - D (true diffusion coefficient): using b > 200 sec/mm²
  - ADC: using all b-values (mono-exponential fit)

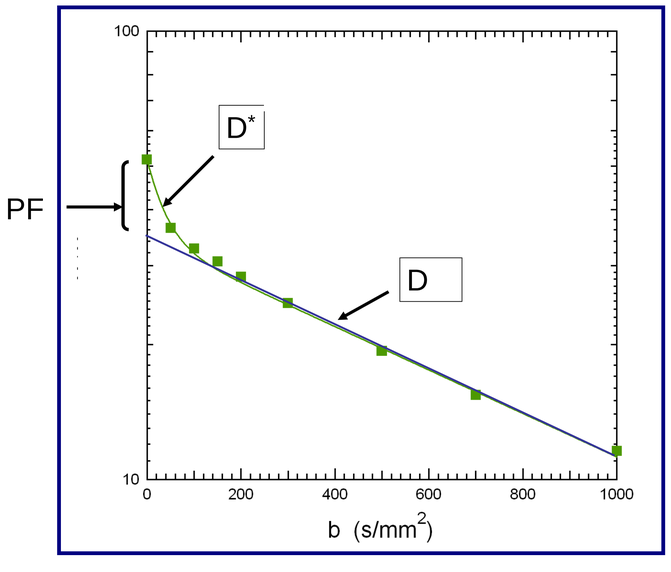

Fig. 1: Liver signal decay follows a biexponential curve

Results

- Significant difference in IVIM parameters between normal and cirrhotic livers, with lower IVIM parameters for cirrhotics **(Table 1)**
- ADC and PF were most significantly different between normal and cirrhotic livers **(Fig. 2, 3)**

	Normal (n=12)	Cirrhotic (n=13)	P
PF(%)	34.2 6.6	25.4 7.5	0.0071
D*	40.0 12.9	27.9 10.5	0.0392
D	1.15 0.19	1.0 0.2	0.0471
ADC	1.76 0.31	1.4 0.2	0.0051

Table 1: IVIM parameters (Mean SD) in normal and cirrhotic patients

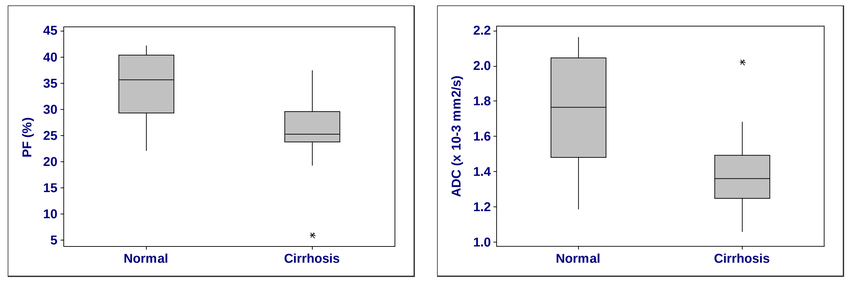

Fig. 2: Box plot distribution of perfusion fraction (PF) and ADC in cirrhosis and normal liver (*: outlier, top and bottom of the boxes: 25-75% percentiles of data, line in the box: median value)

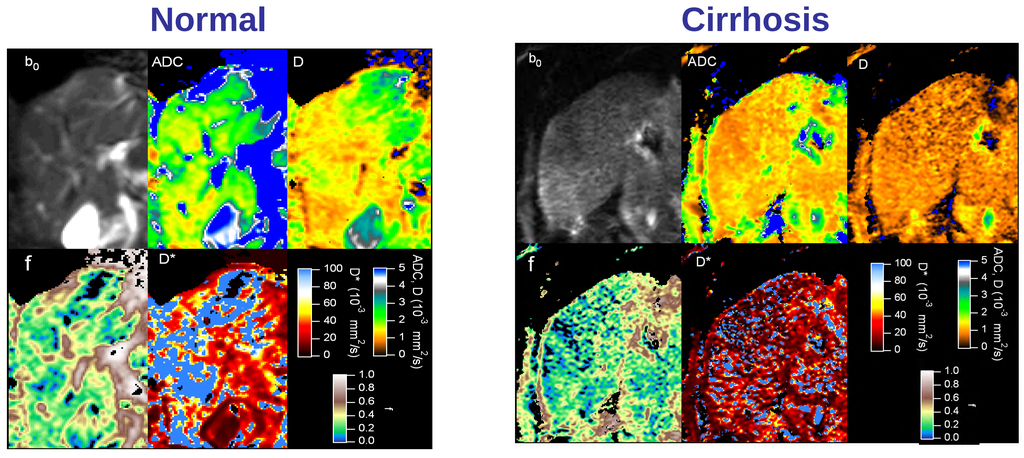

Fig. 3: Coronal voxel based parametric maps of IVIM parameters for a normal and a cirrhotic liver. b=0, ADC, D, PF, and D* images demonstrating qualitative differences between normal and cirrhotic liver.

Discussion and Conclusion

- Our study confirms prior reports that ADC is lower in cirrhosis, however concomitant perfusion confounds ADC at lower b-values (5)
- PF has a potential role as a surrogate marker for liver fibrosis and cirrhosis, which was not shown in the prior study by Luciani et al (5)
- Limitations: did not assess intermediate stages of fibrosis, small sample size
- Future directions: comparison with dynamic contrast enhanced MRI and MR elastography

References

1. *Le Bihan, et al. Radiology 1988 Aug;168(2):497-505*
2. *Lewin et al. Hepatology 2007 Sep;46(3):658-65*
3. *Taouli et al. AJR 2007 Oct;189(4):799-806*
4. *Taouli et al. JMRI 2008 Jul;28(1):89-95*
5. *Luciani et al. Radiology 2008;249(3):891-9*

Filtering and Phase-Correlation Based Registration of Dynamic Contrast-Enhanced Magnetic Resonance Images

Sarayu Ramachandran, Claudia Calcagno and Zahi A. Fayad
Mount Sinai School of Medicine, New York, NY, USA

Introduction: Previously used to characterize tumor vascularity, dynamic contrast-enhanced magnetic resonance (DCE-MR) imaging is now frequently used to identify and study inflammation of atherosclerotic plaque. By examining the tissue uptake of the contrast agent over time using signal intensity curves, it may be possible to draw inferences regarding the composition and neovasculature of the plaque. In order to compute accurate time-signal intensity curves all the images in the dynamic series need to be properly aligned. However due to patient motion and low signal-to-noise ratio (SNR), there can be significant misalignment that can corrupt the analysis. Thus de-noising and image registration procedures need to be implemented prior to analyzing the dynamic image series. This study examines anisotropic diffusion filtering and phase-correlation based registration for aligning DCE-MR data.

Methods: The image processing techniques were tested on a set of DCE-MR images of the right common carotid artery of 20 patients. The images were acquired using a black blood, double-inversion recovery, turbo spin-echo sequence. The images were filtered with three iterations of a non-linear anisotropic diffusion filter[1]. The filtered images were cropped to an 80x80 pixel region surrounding the artery and were aligned using phase-correlation based registration. The phase-correlation method uses the Fourier-shift theorem to detect motion between consecutive images in the time series. A Kalman filter was also included in the registration process to attenuate noise effects. In a second scheme, instead of registering consecutive images, the average of 5 successive images was computed and the gradients of the average image and the current image were registered using the phase-correlation method with Kalman filter. The improvement to the alignment of the series was quantified using a correlation coefficient (CC) measure between consecutive images. Mean CC values were computed for the original data set, after filtering with the anisotropic filter, after registration using phase-correlation and the Kalman filter and finally after averaging and registration of the gradients with phase-correlation and Kalman filtering. A one-way ANOVA analysis of the mean CC was used to compare the performance of the various processing methods.

Results and Discussion: Application of the anisotropic filter resulted in smoothing of the homogeneous regions of the image while still maintaining the edges. Registration of the filtered and cropped image using phase-correlation with the Kalman filter is shown in Fig. 1. The ANOVA analysis showed that phase-correlation registration with Kalman filtering produced significant improvement in the mean CC compared to the un-filtered, un-registered data ($p < 0.001$). There was no statistically significant difference between phase-correlation registration of the images and registration of the gradients of the average images ($p > 0.05$).

Conclusion: In this study we examined a filtering scheme and registration method for processing DCE-MR images. The anisotropic diffusion filter smoothed the images while still preserving the edges. Registration with phase-correlation and the Kalman filter improved the alignment of the dynamic series. The use of gradients of average images for registration did not produce any significant improvement in the registration except in a few patient studies with low original CC values. Filtering and registration of DCE-MR images were accomplished using simple image processing techniques.

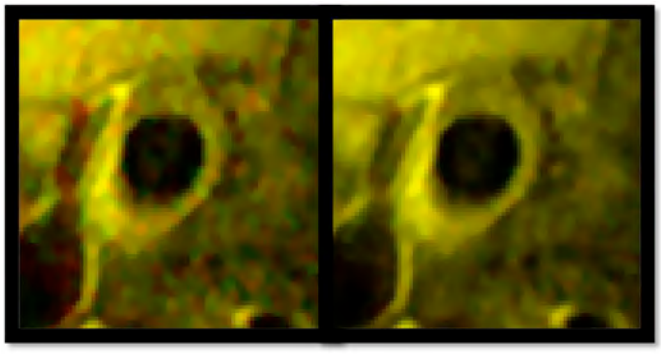

Figure 1. Cropped section from two consecutive frames overlaid (a) prior to registration and (b) after registration with phase-correlation and Kalman filtering showing the improved alignment of the images.

References: 1. P. Perona and J. Malik, IEEE Pattern Anal. Machine Intell., 12(7):629-639, July 1990

In Vitro Labeling Of Porcine Mesenchymal Stem Cells With Positive MR Contrast agent Ferex

Author Block: Tejas R. Shah, MD, Daniel K. Han, BA, Elisa Yaniz-Galende, PhD, Karen Saeboe, PhD, Christine Chung BS, Michael L. Marin, MD, FACS
Peter L. Faries, MD, FACS

Mount Sinai Medical Center, New York, NY.

Introduction: Mesenchymal stem cell (MSC) transplantation is a promising strategy for the treatment of vascular disorders. However, in vivo tracking of MSCs is elusive despite technological advances in imaging. The aim of this study was to perform in vitro evaluation of Ferex, a novel superparamagnetic iron oxide, to track by MRI as a labeling agent for porcine MSCs.

Materials & Methods: Porcine MSCs were isolated by Ficoll-Paque separation of bone marrow aspirates. MSCs were incubated for 24 hours with two concentrations of Ferex (25ug/ml and 50ug/ml) and two cationic transfecting agents (protamine sulfate and Poly-L-Lysine). The MSCs were analyzed for cellular toxicity, functional capacity, phenotypic change, and cellular iron incorporation.

Results & Discussion: Following 24hr incubation, viability was 88.6% with Ferex-protamine complexes vs. 83.8% with Ferex-PLL complexes. Overall signal uptake was greatest with Ferex-PLL complexes at 1.24 ± 0.1 pg Fe/cell with 100% labeling efficiency (Table 1). FACS analysis demonstrated positive CD-90 and CD-44 signals with negative CD-45 and CD-117 signals in all conditions indicative of a MSC population, with the least changes in Ferex-PLL labeled cells (% Gated: 6.31). Proliferation was assessed with % confluence 5 days post-incubation and Ferex-PLL labeled cells had the highest % confluence (75%) compared to control (85%).
The major findings of this study are that intracellular endosomal magnetic labeling of porcine mesenchymal stem cells is possible with the most effective modality via Poly-L-Lysine. The simple and straightforward method of creating a complex of PLL with the FDA-approved ferumoxides through electrostatic interactions allows the efficient incorporation of iron oxide nanoparticles into the endosomes for magnetic cell labeling without requiring novel synthesis or covalent binding of proteins or antibodies to the dextran coating. Labeling efficiency was reproducible in approximately 100% of the labeled mesenchymal stem cells with low concentrations of iron oxides.

Conclusions: Porcine MSCs can be effectively labeled with Ferex. Ferex-PLL complexes provide the greatest Fe uptake with acceptable cellular viability. MSCs labeled by Ferex-PLL complexes maintain their phenotypic and proliferative properties. The implications of this finding can be translated to clinical trials by having a safe and effective labeling technique to facilitate the ability to perform cellular MR imaging to monitor the migration of cells in vivo following their transplantation or intravenous administration.

Table 1

Table 1: Fe^{+} Content		
Sample	**Total [Fe] mM**	**pg Fe /cell**
Control	**<DL**	**<DL**
50 ug / PLL	**0.167**	**1.24 ± 0.1**
50 ug / Protamine	**0.018**	**0.128 ± 0.03**
50 ug / Protamine	**0.017**	**0.127 ± 0.04**
50 ug / plain	**0.042**	**0.316 ± 0.01**
50 ug / plain	**0.019**	**0.140 ± 0.07**
25 ug / PLL	**0.092**	**0.686 ± 0.1**
25 ug / PLL	**0.085**	**0.635 ± 0.03**
25 ug / Protamine	**0.054**	**0.406 ± 0.05**
25 ug / Protamine	**< DL**	**< DL (0.037)**
25 ug / plain	**<DL**	**<DL (0.027)**
25 ug / plain	**<DL**	**<DL (0.022)**

New application of optical agent to image angiogenesis in hind limb ischemia

Yared Tekabe, Alexander Klose, Joane Luma, Alfredo Morales, Lynne Johnson
Columbia University, New York, N.Y.

Introduction Peripheral artery disease (PAD) is a prevalent clinical problem that contributes to significant morbidity. A natural process to restore nutrient perfusion to hypoxic limbs occurs through HIF1α induced production of VEGF that stimulates angiogenesis. In this study we investigated whether optical imaging can be used as a non-invasive tool to identify and follow molecular mechanisms involved in the angiogenesis process. We used fluorophore labeled RGD (IntegriSense 750 nm, VisEn Medical) that targets avb3 integrin expression occurring during capillary sprouting.

Methods: Under isoflurane anesthesia the inguinal ligament and the upper half of the left femoral artery was exposed in seven mice. The vascular bundle was ligated below the inguinal ligament proximally and just above the bifurcation into the superficial and deep femoral arteries distally. All arterial and venous branches connected to the isolated segment of femoral vessels were tied off. The vein and the artery are cut between proximal and distal ligatures and the skin incision was closed. The right leg served as control. Between 3 and 7 days later under isoflurane a catheter was inserted in a jugular vein and 2nmol IntegriSense was injected. Three hours later mice were underwent optical imaging in the PhotonImager (BiospaceLab, France). The excitation wavelength was set at 660 nm and fluorescence light was collected with a cut-off pass filter above 700 nm. Autofluorescence was removed at an excitation wavelength of 580 nm. After completion of imaging the mice were sacrificed and the hind limbs prepared for histology (lectin staining for capillary sprouting) and immunohistology for RGD. Regions of interest were drawn around the fluorescence signal in the left (ligated) limb and right (control) limb and ratios R of the photon flux [photons $s^{-1}cm^{-2}sr^{-1}$] in the L/R limbs calculated.

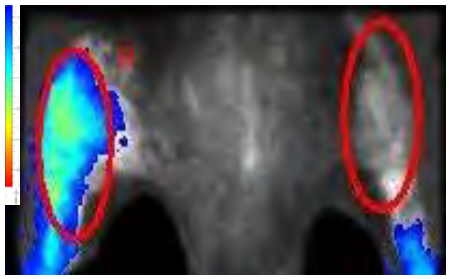

Fig. 1: Image of photon flux [photons $s^{-1}cm^{-2}sr^{-1}$]. Fluorescence image was taken above 700 nm and autofluorescence-corrected. ROI (left: ligated; right: control) is used for calculating R.

Results and Discussion: The fluorescence images showed increased signal in the ligated limb in all mice. The ratio of photon flux in the left limb to right limb averaged R=1.86 (range 1.15 to 3.47). Lectin staining showed capillary sprouting in the ischemic limbs and fluorescent staining showed co-localization of the RGD fluorescence to CD 31 positive (endothelial) cells.

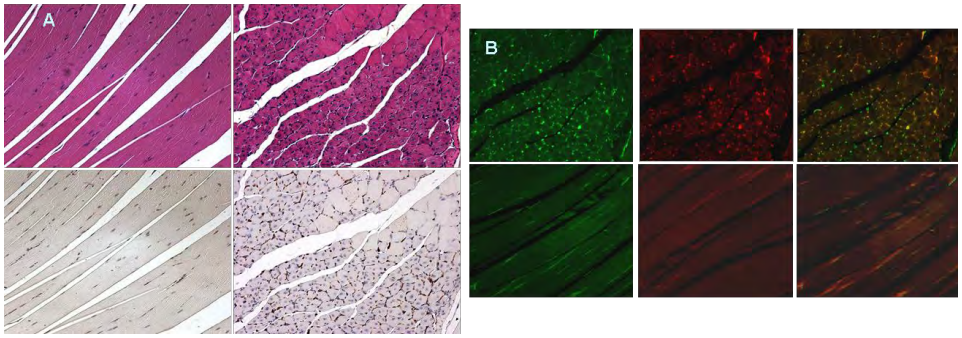

Fig. 2: Panel A shows H&E staining on top and lectin staining on bottom with right (control limb) sections on left showing normal skeletal muscle and left (ischemic) limb on right showing dying muscle cells. Panel B shows ischemic limb on top and control limb sections on bottom. The panels on left are CD31 staining, middle are RGD, and right are fused images.

Conclusion:
Fluorescence imaging can be used to follow angiogenic response to hind limb ischemia and may have applications in development of drugs to improve limb perfusion.

Quantitative Analysis of Aortic and Carotid Atherosclerotic Plaque Inflammation Using $^{18\text{-}F}$ FDG PET/CT Imaging, a Mid Term Follow up Study

Ling de Yang [1], James H.F. Rudd[1], Kelly S. Myers1[1], Ajay Nemade[1], Rima Fayad[1], Josef Machac[2], David Rosenbaum[1], Ash Rafique[2], Michael Farkouh[3], Valentin Fuster[4], and Zahi A. Fayad[1] .
[1]Translational and Molecular Imaging Institute, [2]Division of Nuclear Medicine, Department of Radiology, [3]Cardiovascular Imaging Clinical Trials Unit, [4]The Zena and Michael A. Wiener Cardiovascular Institute and Marie-Jos´ee and Henry R. Kravis Cardiovascular Health Center, Mount Sinai School of Medicine.

Introduction: Atherosclerosis is a global epidemic and likely to become the leading cause of death worldwide by 2010. Vulnerable atherosclerotic plaques susceptible to rupture, causing the most serious complications as acute coronary syndromes and stroke. $^{18\text{-}F}$ FDG-PET can measure metabolic activity as a marker of inflammation, therefore detect vulnerable plaque within great arteries. The short term reproducibility of FDG-PET for atherosclerosis is excellent in aorta, carotid and peripheral arterials. The purpose of this study is to compare FDG uptake between two separate FDG-PET scans, in patients (pts) with known atherosclerosis.

Methods: 18 asymptomatic pts (age 64±7, 63% male, all on statins) with established vascular disease underwent two separate FDG PET/CT studies, one to two years apart (15±5 month), among them, 12 pts had two aorta scans and 16 pts had two carotid (CA)scans. There were no major changes in pt's clinical condition and medication between scans. Aorta PET used 2D mode, 3 beds acquired and 10 min/bed. Carotid used 3D mode for 15 minutes/bed. Aortic measurement was divided into ascending (Asc), arch, descending (Desd), and abdominal (Abdn) segments. FDG uptake was auto quantified as standardized uptake values (SUV) for mean, maximal (Max), and most diseased segment (MDS) for every transaxial image, then, averaged and corrected by venous activity as background to create a target-to-background ratio (TBR) for each vessel segment. Paired t-tests were used, and $p<0.05$ is significant

Results and Discussion: Paired comparisons performed between follow up and baseline for Max and MDS and mean TBR. (1) Increased Max TBR in follow up PET in Asc (from 1.92 to 2.05, $p < 0.05$), Desd (from 1.76 to 1.90, $p < 0.01$), Abdn (from 1.72 to 1.77, $p = 0.1$), left CA (from 1.71 to 1.81, $p < 0.05$) and right CA (from 1.78 to 1.88, $p < 0.05$), comparing with baseline, but no significant changes in arch (p = NS). (2) Increased MDS TBR in follow up PET in Asc (from 2.03 to 2.15, $p = 0.1$), Desd (from 1.98 to 2.16, $p < 0.01$), Abdn (from 1.98 to 2.11, $p < 0.01$), left CA (from 1.84 to 1.97, $p < 0.05$) and right CA (from 1.91 to 2.03, $p = 0.07$), again, no significant changes in arch (p = NS). (3) No significant changes (p = NS) found between the two PET mean TBR for all aorta and carotid territories. (4) By summing all the vessel territories, Max and MDS TBR increased (from 1.79 to 1.88, $p < 0.0001$, and from1.94 to 2.06, $p < 0.0001$, respectively), no significant changes in mean TBR over the follow up period (p =NS).

Conclusion: Quantitative FDG PET/CT is an excellent tool for tracking the disease evolution over time, and monitoring the vascular response to anti-inflammation and lipid-lowering drug therapy. **I**ncreasing FDG uptake in Max and MDS TBR measurement, indicate pathogenesis progression of locally high FDG uptake from atherosclerotic plaque inflammation, despite routine anti-atheroma drug therapy as in this population. This study also shows relative stable mean TBR measurement over time, indicates that mean TBR is useful for monitoring the imaging quality and reliability, and may be used to detect bigger scale of systematic vascular inflammation. More patients and longer term follow up for exploring the nature course of atherosclerotic plaque inflammation is desired.

Figure 1

Comparison of PET FDG uptake in all 80 Vessel Segments at Baseline and Follow up, For MDS, Max and Mean TBR measurement

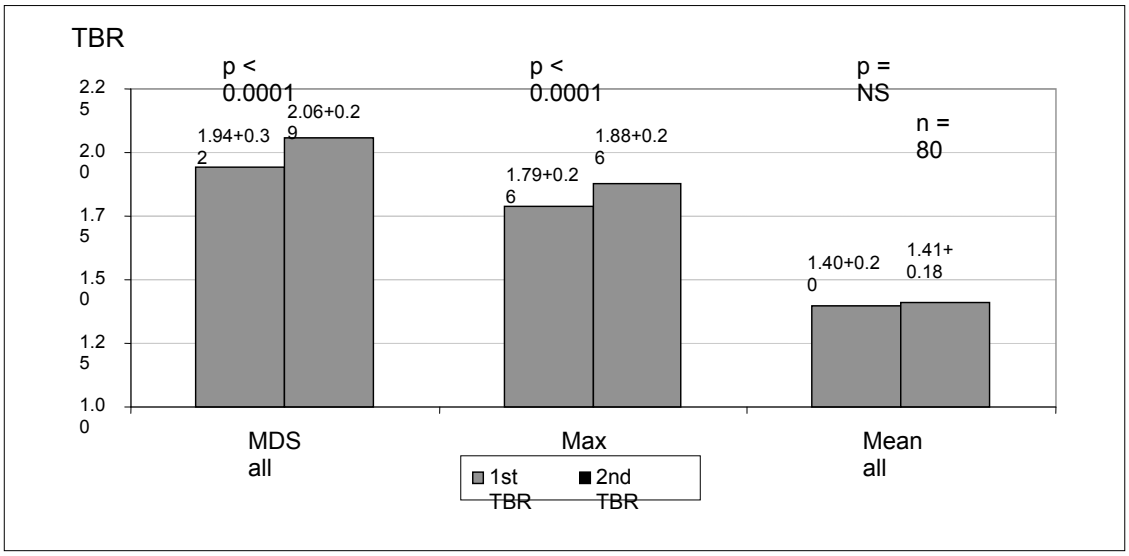

Figure 2

Follow up PET image, aorta summed max TBR increase 0.73 over the whole vessel segment, comparing with baseline

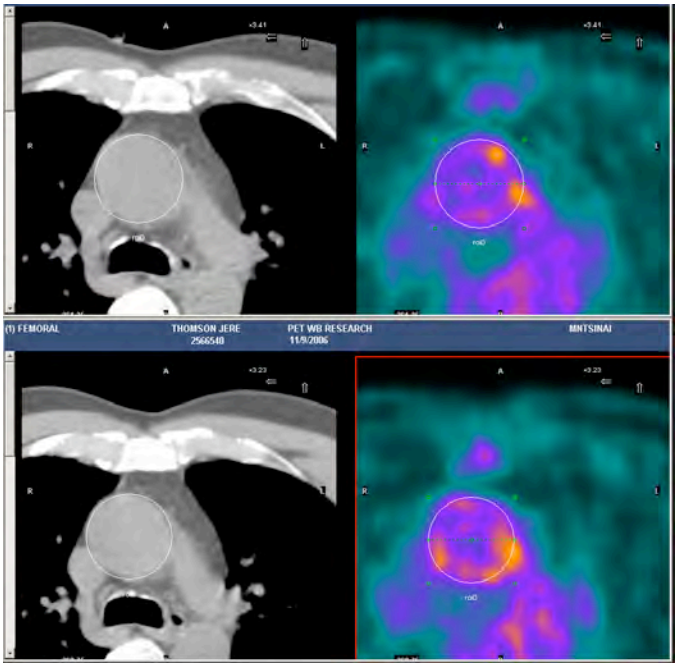

PET/CT Baseline

PET/CT Follow Up 11 Months Later

Abstracts selected for poster presentation, Neuro Imaging category

Dopamine transporter gene variation modulates activation of striatum in youth with ADHD

Anne-Claude Bédard, Ph.D.[1], Kurt P. Schulz, Ph.D. [1], Edwin H. Cook Jr., M.D. [2], Jin Fan, Ph.D,[1,3], Suzanne M. Clerkin, Ph.D. [1], Iliyan Ivanov, M.D. [1], Jeffrey M. Halperin, Ph.D. [1,4], Jeffrey H. Newcorn, M.D.[1]

[1]Department of Psychiatry, Mount Sinai School of Medicine, New York, New York
[2]Department of Psychiatry, University of Chicago at Illinois, Chicago, Illinois
[3]Department of Neuroscience, Mount Sinai School of Medicine, New York, New York
[4]Department of Psychology, Queens College of the City University of New York, Flushing, New York

Introduction Polymorphisms in the 3' UTR variable number tandem repeat (VNTR) of exon 15 of the dopamine transporter gene (DAT1) have been linked to attention-deficit hyperactivity disorder (ADHD); moreover, variability in DAT1 3'UTR genotype may contribute to both heterogeneity of the ADHD phenotype and differences in response to stimulant medications. The impact of this VNTR on neuronal function in individuals with ADHD remains unclear despite evidence that the polymorphisms influence dopamine transporter expression.

Methods We used event-related functional magnetic resonance imaging to examine the impact of DAT1 3'UTR genotype on brain activation during response inhibition in unmedicated children and adolescents with ADHD. Twenty-one youth with ADHD who were homozygous for the 10-repeat (10R) allele of the DAT1 3'UTR and 12 youth who were carriers of the 9-repeat (9R) allele were scanned while they performed a Go/No-Go task. Response inhibition was modeled by contrasting activation during correct No-Go trials versus correct Go trials.

Results and Discussion Participants who were homozygous for the DAT1 3'UTR 10R allele and those who had a single 9R allele did not differ on percent of trials with successful inhibition, which was the primary measure of inhibitory control. Yet, youth with the DAT1 3'UTR 10R/10R genotype had significantly greater inhibitory control-related activation than those with one 9R allele in the left striatum, right dorsal premotor cortex, and bilaterally in the temporoparietal cortical junction (Figure 1).

Conclusion These findings provide preliminary evidence that neural activity related to inhibitory control may differ as a function of DAT1 3'UTR genotype in youth with ADHD. Heterogeneity in the association between DAT1 genotype and brain activation within ADHD raises the possibility that genotype may contribute to the observed inconsistent findings of striatal hypoactivation during Go/No-Go tasks in children and adolescents with ADHD [e.g., 1, 2], and differential response to medication, and in particular, to stimulants [e.g., 3, 4, 5]. Although more research is needed in this area, findings from the present study add to those already published in describing the heterogeneity of DAT neuroanatomy and neurophysiology in ADHD [6], and illustrating the functional consequences of polymorphisms of DAT1 3'UTR.

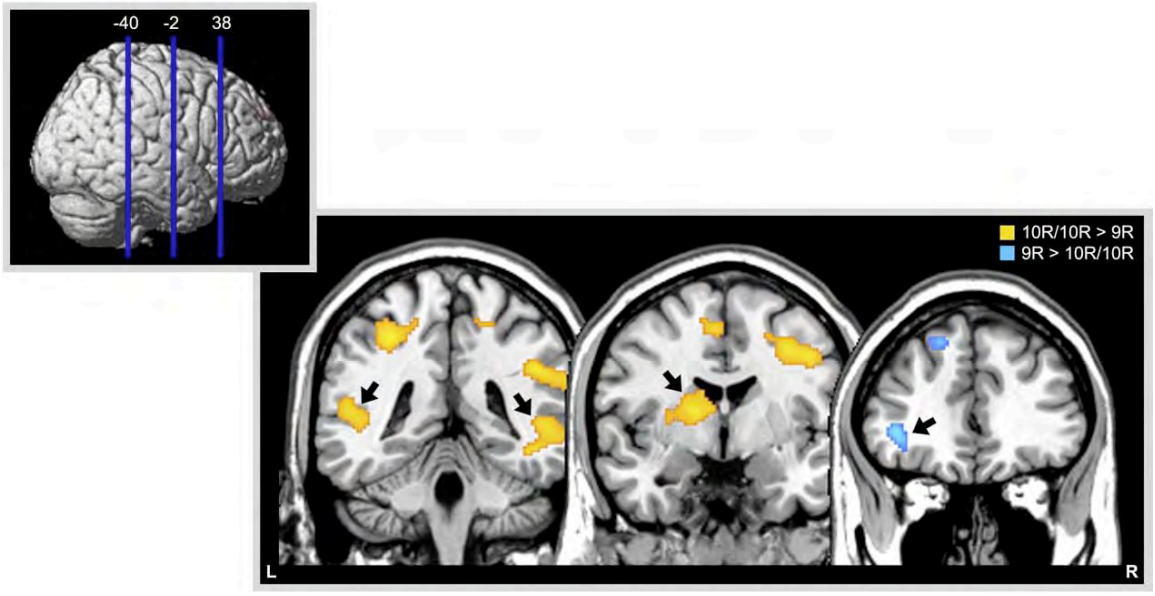

Figure 1. Regions showing significant differences in BOLD responses to successful response inhibition (correct No-Go events minus correct Go events) in youth with attention-deficit hyperactivity disorder (ADHD) who were homozygous for the *DAT1* 3'UTR 10-repeat (10R) allele compared to those who are heterozygous for the 9-repeat (9R) allele. Arrows indicate the temporoparietal cortical junction (left section), striatum (middle section), and inferior frontal gyrus (right section). The activations were significant at $p < 0.05$ corrected with a voxel extent > 100 voxels. The inset depicts the position and Talairach coordinates for the sections.

References

1. Durston, S., et al., *Activation in ventral prefrontal cortex is sensitive to genetic vulnerability for attention-deficit hyperactivity disorder.* Biol Psychiatry, 2006. **60**(10): p. 1062-70.
2. Durston, S., et al., *Differential patterns of striatal activation in young children with and without ADHD.* Biol Psychiatry, 2003. **53**(10): p. 871-8.
3. Winsberg, B.G. and D.E. Comings, *Association of the dopamine transporter gene (DAT1) with poor methylphenidate response.* J Am Acad Child Adolesc Psychiatry, 1999. **38**(12): p. 1474-7.
4. Stein, M.A., et al., *Dopamine transporter genotype and methylphenidate dose response in children with ADHD.* Neuropsychopharmacology, 2005. **30**(7): p. 1374-82.
5. Gruber, R., et al., *Dopamine transporter genotype and stimulant side effect factors in youth diagnosed with attention-deficit/hyperactivity disorder.* J Child Adolesc Psychopharmacol, 2009. **19**(3): p. 233-9.
6. Volkow, N.D., et al., *Depressed dopamine activity in caudate and preliminary evidence of limbic involvement in adults with attention-deficit/hyperactivity disorder.* Arch Gen Psychiatry, 2007. **64**(8): p. 932-40.

In Vivo Evidence of Axonal Transport Perturbation in a Mouse Model of Tauopathy : A Track-Tracing MEMRI study

A. Bertrand[1&2], U. Khan[2], D. M. Hoang[2], D. Novikov[2], P. Krishnamurthy[1], B. W. Little[2], H. B. Rajamohamedsait[1], S. Pun, E. M. Sigurdsson[1] and Y. Zaim Wadghiri[2]
[1] Dep. of Physiology and Neuroscience, and [2] Dep. of Radiology, NYU Medical Center.

Introduction: Functional alterations of axonal transport have been suggested to occur in the early stages of Alzheimer's disease [1,2]. We hypothesized that Tract-Tracing-Manganese-Enhanced-MRI (TT-MEMRI) should detect early axonal transport impairments in a mouse model of tauopathy.

Methods: Ten JNLP3 (P301L) transgenic mice (Tg) and 4 wild-type mice (WT) were imaged on a 7T magnet at 3 and 6 months of age, using a nasal TT-MEMRI protocol with 9 imaging time points [3]. Four regions of interest (ROI), located along the olfactory system, were defined on MR images: the glomerular layer, the mitral cell layer, the anterior and the posterior part of the piriform cortex. In each ROI, the evolution of signal intensity, indicative of manganese propagation, was fitted to a one-dimensional flow-diffusion model, in order to estimate for each individual mouse in each ROI the following parameters: the peak value, the time to peak and the maximal ascending slope (Fig1A). After the 6 month-old examination, animals were sacrificed, and the presence of tauopathy in the brains was assessed by immunohistochemistry using MC1 and PHF1 antibodies.

Results and Discussion: A significant decrease of peak value was observed in the aged Tg mice compared to both aged-matched WT and young Tg mice, in the 2 proximal ROI (Fig1B, T-test, $p<0.05$-0.01). A significant decrease of maximal slope was observed in the aged Tg mice compared to young Tg mice, in the 2 proximal ROI (Fig1C, T-test, $p<0.05$-0.01). A significant increase of time to peak was observed in the aged Tg mice compared to aged-matched WT in se second ROI (Fig1D, T-test, $p<0.05$). Tauopathy was present in both the olfactory bulb and the piriform cortex of all Tg mice, and absent in the brains of WT (Fig 2).

Conclusion: Our results provide the first *in vivo* evidence of axonal transport impairment in a mouse model of tauopathy, assessed non-invasively by TT-MEMRI. Among the parameters we studied, the peak value appears to be the most sensitive biomarker of tauopathy, likely reflecting the initial uptake of Mn by neurons via their calcium channels. In contrast, the time to peak and maximal slope were less sensitive but should be more reflective of the axonal transport of Mn along the microtubule system.

References [1] Stoking GB, Lillo C, Falzone TL, et al. Axonopathy and transport deficits early in the pathogenesis of Alzheimer's disease. *Science 2005;307:1282-8*. [2] LaPointe NE, Morfini G, Pigino G, et al. The amino terminus of tau inhibits kinesin-dependent axonal transport. *J Neurosci Res 2009;87:440-51.* [3] Cross DJ, Flexman JA, Anzai Y, et al. Age-related decrease in axonal transport measured by MR imaging in vivo. Neuroimage 2008;39:915-26.

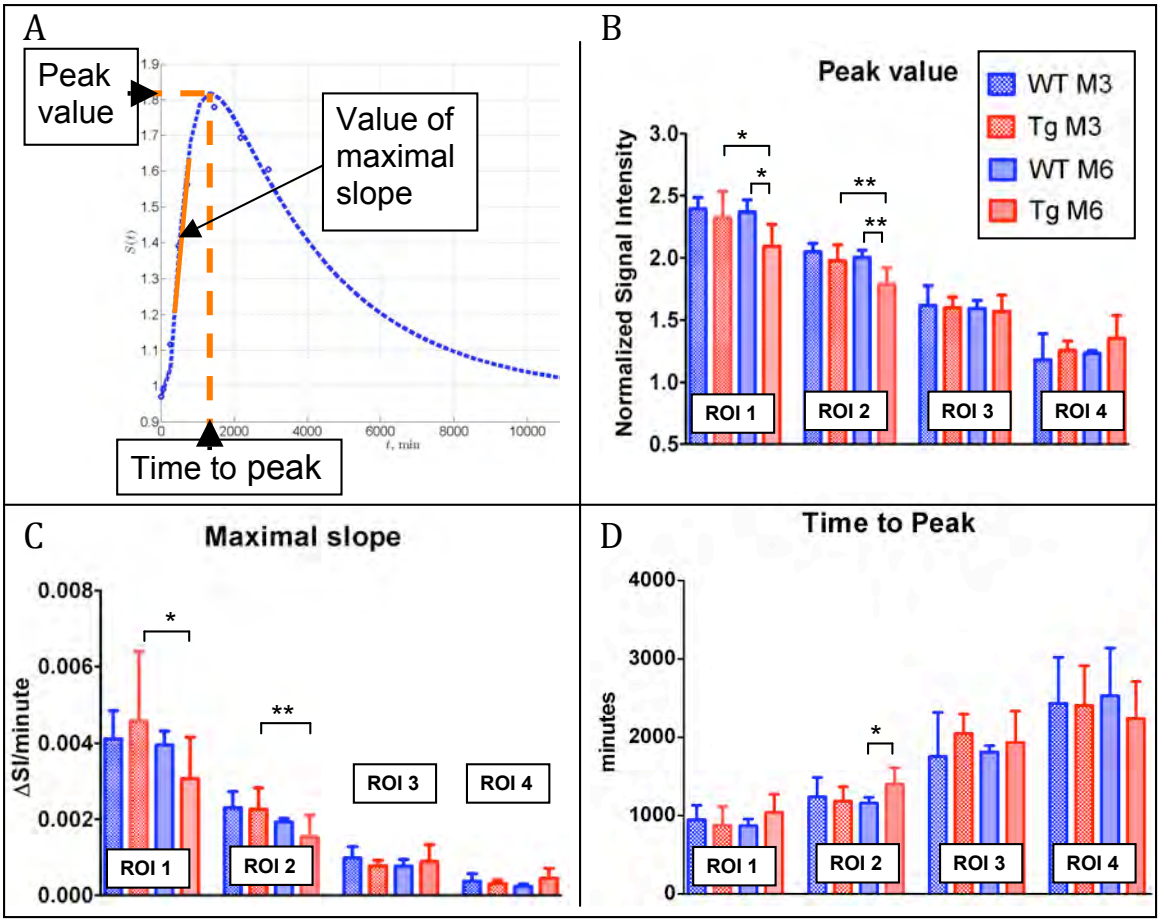

Fig 1: Estimation of peak value, maximal slope and time to peak in the different mouse groups.

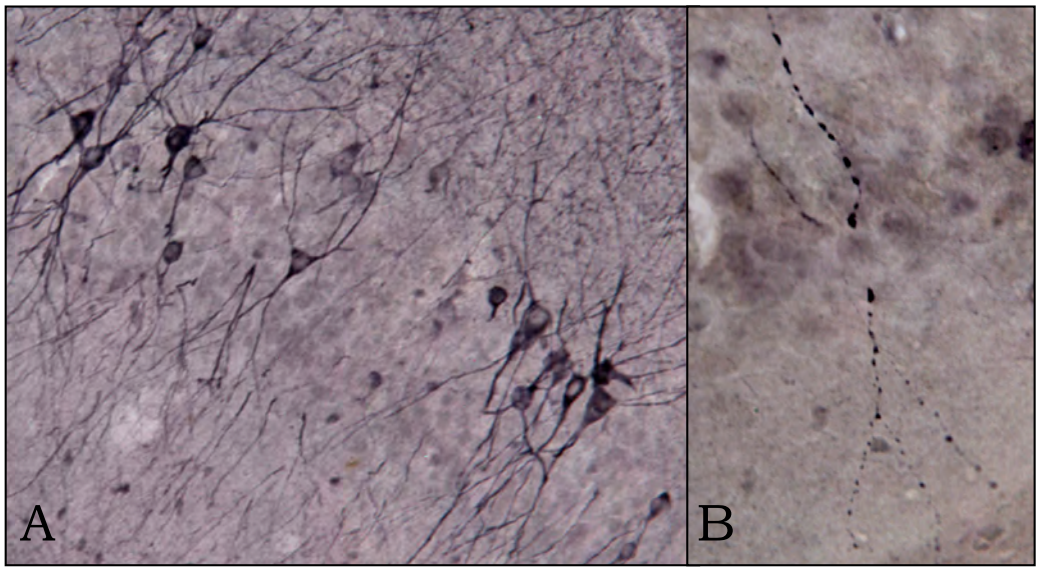

Fig 2: In the piriform cortex of a 6-month-old Tg mouse, neurons show a strong positivity for MC1 antibody, which recognizes a pathological conformation of tau (**2A**: x20 and **2B**: x40 magnification)

Suspicious Findings in Exploratory Whole-Brain Analyses

D. M. Carpenter[1], E. L. Eaves[1], J. Ng[1], P. R. Hof[2] and C. Y. Tang[1,3]
[1]Radiology, [2]Neuroscience, [3]Psychiatry, Mount Sinai School of Medicine, New York, New York,

INTRODUCTION

Voxel based analyses (VBA), also known as Statistical Parametric Mapping (SPM), are commonly used for exploratory analysis of functional or structural neuroimaging data. The popular technique is relatively easy to use and can survey the entire brain but the method yields inconsistent results (Kanaan 2005). It is difficult to challenge the validity of published works and review submissions because the nature of the immense datasets that underlie VBA results prohibits its presentation in journals. In this abstract we use a simple data set to explore sources of type I errors in areas that often yield positive results and present findings that can serve as a guide for critiquing these SPM presentations.

MATERIALS AND METHODS

Subjects. Two healthy volunteers were recruited and gave informed consent with no history of mental illness. Subjects underwent several imaging sessions over 7 consecutive business days (n=7 for each subject).

Image Acquisition. All imaging sessions were performed on a 3T Allegra MRI scanner (Siemens, Ehrlangen, Germany). Image normalization was performed using SPM2 with common protocols. Voxel-by-voxel t tests were created to search for significant differences between the subject's FA measures (n = 7 for each subject).

RESULTS

An exploratory VBA t test between the scans of two subjects was performed to investigate how minor misalignment issues can influence the results (Figure 1). The goal of the exploratory analysis is to detect white matter FA differences but a closer visual inspection reveals type I errors. Inspection of areas of high contrast suggested that image misalignments underlie some of the detected differences (see corpus callosum and external capsule of enlarged section of Figure 1). Outlines of the significant clusters were overlaid on the mean of the normalized images from subject A and C (Figure 1 middle and right columns, respectively). The image inspection revealed that the positive findings in these regions were clearly due to image misalignments. This observation remained with a wide range of smoothing kernel sizes. Not all clusters were investigated in this manner but a qualitative inspection is convincing that high contrast regions are susceptible to error using this method.

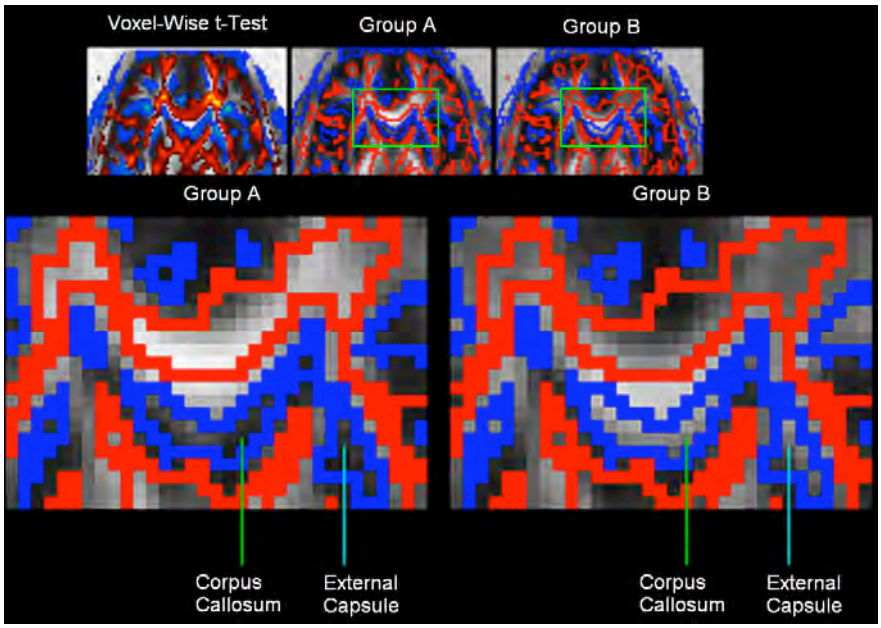

Figure 1. The columns of images (left to right) show t values ($p < 0.01$), and outlines of positive and negative clusters on subject A and subject C. The green boxed areas are enlarged on the right to show misalignments of the corpus callosum and external capsule.

DISCUSSION

In this study we investigated the potential for erroneous conclusions to be drawn from VBA images. The most striking findings were the type I errors in regions that are commonly reported in DTI studies (Kanaan 2005). Several regions were clearly due to image misalignments that resulted in comparisons between white matter and non-white matter regions that, due to tissue differences in FA, yielded positive findings.

This study's findings by no means render all VBA results errors but offer a guide to identify suspicious results. Particular scrutiny should be given to high contrast areas, such as ventricle white matter borders. Special attention should be given to these areas in studies with known anatomical differences between groups, such as ventricular variations in schizophrenia (Keefe 1998). The results presented here should educate authors, readers and reviewers in order to scrutinize findings in the VBA-DTI literature. DTI-tractography is a sensitive, specific and sophisticated alternative for white matter investigations (see TMII Symposium abstracts Goodman et al, and Mitsis et al).

Essential Role for NFkB in Stress-Induced Synaptic Plasticity and Behavior

Daniel J. Christoffel[1], Samuel A. Golden[1], H. Francisca Ahn[1], Cindy Reyes, Scott J. Russo[1]

[1]Friedman Brain Institute, Mount Sinai School of Medicine, New York, NY USA

Introduction

Mood and anxiety disorders are devastating afflictions that affect a large portion of the population. The neural mechanisms underlying mood and anxiety disorders are largely unknown, however, a detailed understanding of the neural substrates and molecular underpinnings of these diseases will provide more effective treatments. Chronic social defeat stress in rodents produces a long-lasting behavioral syndrome that can be used to model certain aspects of depression-like behavior in rodents. The purpose of the current study is to investigate neural correlates that may be responsible for the long-term behavioral phenotype observed after social defeat. Previous work investigating the effects of stress has focused largely on the limbic circuitry between the amygdala and hippocampus, relatively little is know about the role of the nucleus accumbens (NAc).

Methods

Analyses of dendritic spine size, shape, and density were performed using confocal imaging of Lucifer-Yellow filled cells and semi-automated analysis of selected dendritic segments with NeuronStudio. Ultrastructural analysis of PSD length was performed on serial strips on a transmission electron microscope, and measurements were performed in Photoshop. For viral manipulation of behavior, intracranial surgeries were performed to deliver virus to the NAc.

Results and Discussion

We first determined whether social stress causes any structural changes in NAc synapses. Spine analysis revealed an increase in the total spine density ($p=0.05$) in medially located medium spiny neuron (MSNs) in NAc shell. We found that susceptibility was associated with an increase in immature stubby spines ($p=0.005$). We also found a strong correlation between stubby spine density and social interaction (SI) score ($p=0.01$, $r^2=0.65$) suggesting that this structural alteration could be mediating the behavioral phenotype. To further examine the role of synaptic changes associated with social defeat stress we performed an ultra-structural analysis of post-synaptic density (PSD) length. Social defeat induced a shift towards smaller PSDs($p= 0.02$), consistent with our spine analysis and we also observed a similar positive correlation between PSD length and SI score ($p= 0.002$, $r^2=0.58$).

Conclusion

These changes in neuronal morphology may be the result of the activation of nuclear factor kappa B (NFκB) signaling pathways. While little is known about the role of this transcription factor in structural plasticity, we have observed significant increases in NFκB in NAc after social defeat stress. Furthermore, using a herpes simplex viral vector to express mutant Inhibitor of kappa Kinase to either activate or inhibit NFkB signaling (IKKca & IKKdn, respectively) we find that activation of this pathway is both necessary and sufficient to induce the susceptibility phenotype. Future studies to examine whether these manipulations also block stress-induced changes in neuronal morphology are currently underway.

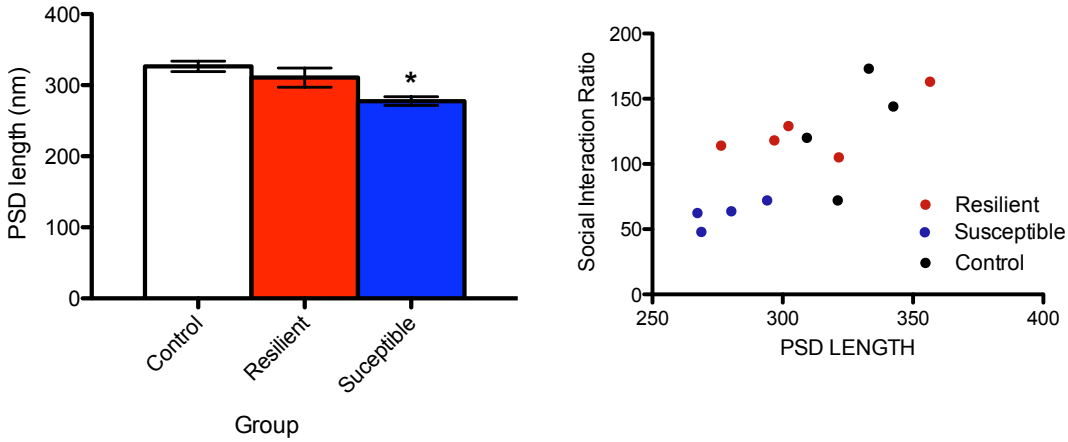

Figure 1. The average PSD length is significantly reduced in susceptible animals and the length of the PSD correlates with the Social Interaction Ratio.

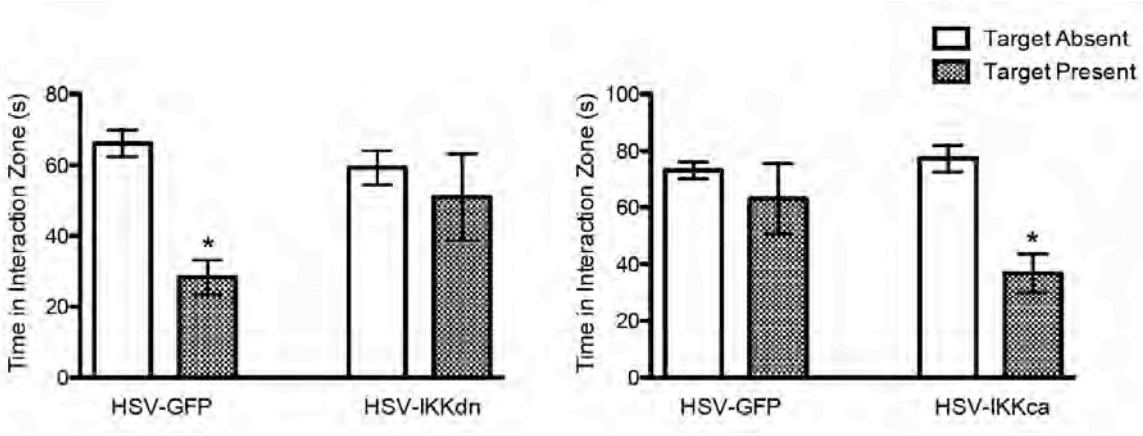

Figure 2. NFκB is necessary and sufficient for the social avoidant phenotype.

Guanfacine Potentiates Dorsolateral Prefrontal Cortex Activation Evoked by Warning Cues

SM Clerkin[1]; KP Schulz[1]; JM Halperin[1, 2]; JH Newcorn[1]; I Ivanov[1]; CY Tang[1]; J Fan[1]
Mount Sinai School of Medicine[1]; Queens College, City University of New York[2]

Introduction

The phasic increase in the readiness to detect and respond to an impending stimulus following the presentation of a warning cue, known as alerting, is thought to be mediated by the locus coeruleus norepinephrine system[1]. Prior research has focused on the role of presynaptic α_{2a} autoreceptor inhibition of locus coeruleus (LC) firing and resultant down-regulation of NA release in alerting[2]. However, α_{2a} adrenoceptors also act as heteroceptors to regulate neuronal excitability in select terminal regions, including dorsolateral prefrontal cortex (DLPFC). Guanfacine, is a selective α_{2a}-adrenoceptor agonist, and has been shown to increase delay-related firing in PFC[3]. Therefore, to test the role of α_{2a} adrenoceptors in alerting among healthy young adults, we combined the use of functional magnetic resonance imaging (fMRI) with a double-blind, placebo controlled guanfacine challenge. Behavioral and neural responding during a simple cued-reaction time task was measured.

Method

Sixteen healthy young adult volunteers participated in two fMRI scans, during which they performed a simple cued reaction time task. Participants were randomly assigned to guanfacine/placebo during the first scan session, and administration of the medication was double-blinded. Neural activity related to visual stimulation, cues, and targets was modeled with an implicit baseline that was modeled during 30-seconds of fixation at the beginning and end of each run. Statistical significance for the imaging results was set at $p < .01$, uncorrected; $k = 100$.

Results and Discussion

There was a strong alerting effect for both treatment conditions, with decreased RT to cued targets versus uncued targets. However, there was no main effect of Treatment, nor was there a significant Treatment X Cue interaction for RT. Fairly similar patterns of cue-related BOLD signal changes were observed with guanfacine and placebo in regions of the alerting network, including (DLPFC), cingulate and frontal motor areas, temporoparietal junction (TPJ), thalamus, and striatum. However, comparison of treatment effects on cue-related BOLD signal changes revealed that guanfacine produced marked increases in the cue-evoked activation in a region of the cerebellum and DLPFC that correspond to the well-described actions of postsynaptic α_{2a} adrenoceptor stimulation.

Conclusion

Guanfacine produced increased cue-evoked activation of the anterior cerebellum and DLPFC, and the current procedures provide an opportunity to test postsynaptic α_{2a} adrenoceptor function in the prefrontal cortex in the pathophysiology of several psychiatric disorders.

FIGURE 1

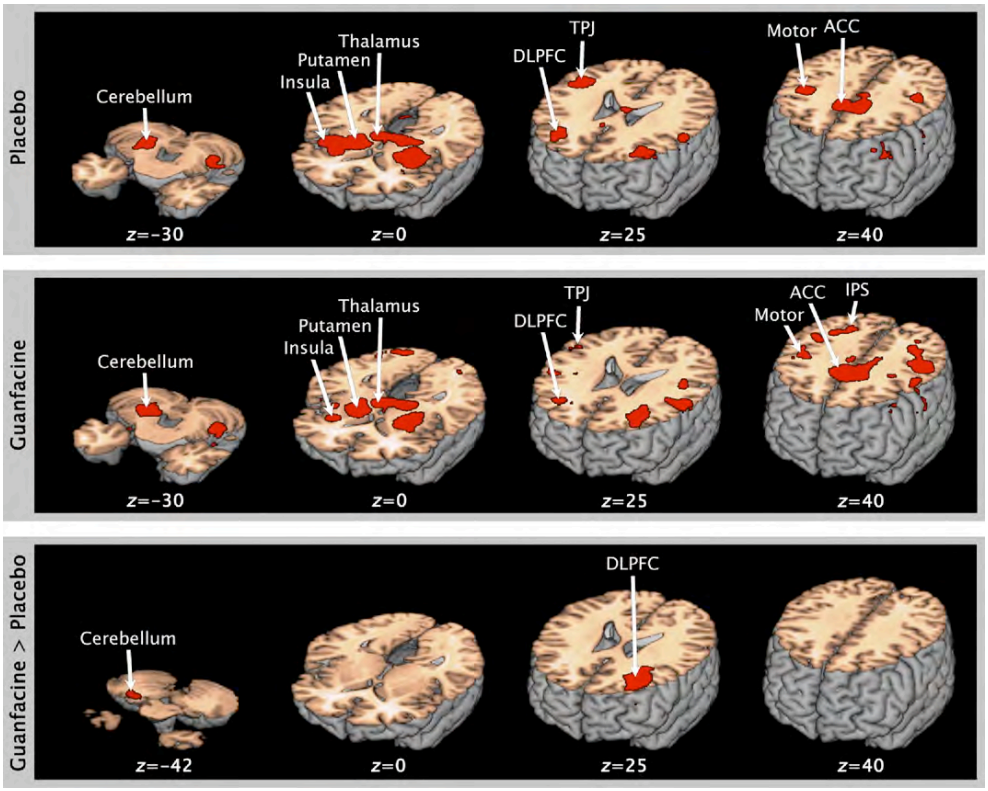

Figure 1. Cue-evoked BOLD signal increases with placebo (top row) and 1 mg oral guanfacine (middle row). Cue-evoked BOLD signal responses were significantly greater for guanfacine than placebo in left DLPFC and right inferior cerebellum (bottom row). ACC, anterior cingulate cortex; IPS, intraparietal sulcus; TPJ, temporoparietal junction.

References

These data were published in:

Clerkin, S.M., Schulz, K.P., Halperin, J.D., Newcorn , J.H., Ivanov, I., Tang, C.Y., Fan J. (2009). Guanfacine potentiates the activation of prefrontal cortex evoked by warning signals. *Biological Psychiatry*, 66, 207-312.

1. Posner, M. I. & Petersen, S. E. (1990). The attention system of the human brain. *Annual Review of Neuroscience, 13,* 25 – 42.
2. Coull, J. T., Nobre, A. C., Frith, C. D. (2001). The noradrenergic α2 agonist clonidine modulates behavioural and neuroanatomical correlates of human attentional orienting and alerting. *Cerebral Cortex,* 11, 73-84.
3. Arnsten, A., Cai, J. X., Goldman-Rakic, P. S. (1988). The alpha-2 adrenergic agonist guanfacine improves working memory in aged monkeys without sedative or hypotensive side effects. *Journal of Neuroscience, 8,* 4287 – 4298.

Increased brain lactate uptake and metabolism during hypoglycemia after ketogenic diet-induced brain adaptations in rat.

H.M. De Feyter[1], K. L. Behar[1], L. Drewes[2], R.A. de Graaf[1], D.L. Rothman[1]

[1]Diagnostic Radiology, Yale University, New Haven, CT, USA; [2]Biochemistry & Molecular Biology, University of Minnesota, Duluth, MN, USA

Introduction

Intensive insulin treatment to control blood glucose levels in individuals with (type I) diabetes places them at increased risk for iatrogenic hypoglycemia. Repetitive hypoglycemic events lead to brain adaptations resulting in failing counterregulatory hormone response and lack of warning symptoms normally associated with decreasing glucose levels (hypoglycemia unawareness) (1). Increased capacity to oxidize alternative monocarboxylic acids (MCA, e.g. lactate and ketone bodies) associated with increased blood-brain barrier MCA transport *via* the MCA transporter 1 (MCT1) has been suggested as such brain adaptations (2). Of the MCAs in blood, lactate is present at the highest concentration during hypoglycemia and therefore an important candidate to replace glucose (2).

To further investigate the role of blood lactate as alternative fuel during hypoglycemia, we studied brain lactate transport and metabolism in rats maintained on a ketogenic diet, which is known to enhance MCT1 expression (3). *In vivo* ^{1}H-[^{13}C] magnetic resonance spectroscopy (MRS) was used in combination with [3-^{13}C]-lactate infusion under hyperinsulinemic-hypoglycemic conditions.

Methods

Long Evans rats were fed normal chow (NC, n=5) or a ketogenic diet (KD, n=5) based on 91% fat and 9% protein (Harlan Teklad, # TD96355) for 15-16 days. All *in vivo* NMR measurements were performed using a 9.4T horizontal bore magnet interfaced to a Varian spectrometer. ^{1}H-[^{13}C] spectra were acquired from a 180 μL voxel (6 × 5 × 6 mm^3) positioned in the middle of the cortex (4). After scout imaging, voxel positioning and shimming, insulin infusion was started (0.02 μL/min/g body weight, 2.5 U/ml solution). Upon establishing steady state plasma glucose levels of ~ 2.3 mM, infusion of [3-^{13}C]-lactate (0.157 μL/min/g body weight, 0.4 mM solution) and *in vivo* MRS acquisition were started and continued for ninety minutes. POCE difference spectra were fitted using an LC model approach with in-house built software. Plasma lactate concentration and ^{13}C enrichment were determined using a POCE sequence at a 500 MHz high resolution spectrometer.

Results and Discussion

Sixteen minutes after the start of the [3-^{13}C]-lactate infusion plasma lactate concentrations and enrichment were 1.7 ± 0.3 mM and 32.5 ± 3.6 % in NC animals; and 1.8 ± 0.4 mM and 39.1 ± 3.9% in KD rats. Figure 1a depicts the ^{13}C signal of glutamate C4 and lactate C3. KD rats showed a robust increase in ^{13}C-labeled lactate and glutamate levels compared to control animals fed normal chow. Figure 1b shows POCE difference spectra averaged over the last 45 min of [3-^{13}C]-lactate infusion acquired from a KD and NC animal.

Conclusion

We conclude that adaptations in response to the ketogenic diet enhance lactate transport and/or metabolism in rats during hypoglycemia. Whether such effects enhance support of neurons and/or astroglia during hypoglycemia or provides neuro-protection remains to be shown. Further studies are underway to disentangle the contributions of transport and oxidation of lactate. Such new insights have relevance both to insulin therapy for diabetes and to conditions treated with ketogenic diets such as epilepsy and brain tumors (5, 6).

Figure 1.

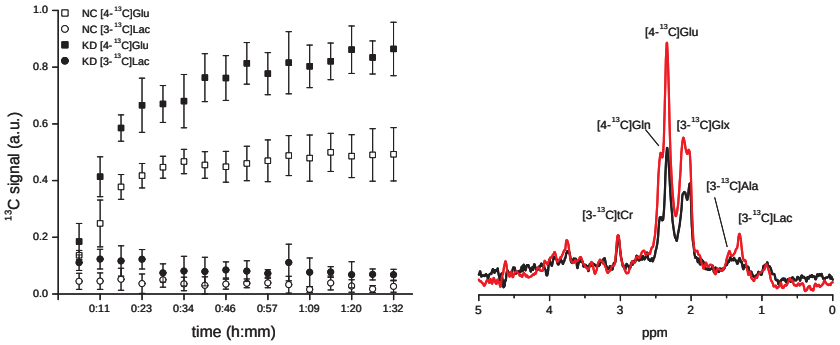

Figure 1 a) ^{13}C signal amplitude of brain glutamate (Glu) and lactate (Lac) of fitted POCE difference spectra during the infusion of [3-^{13}C]-lactate in arbitrary units. **b)** POCE difference spectra averaged over the last 45 min of [3-^{13}C]-lactate infusion of a NC (black) and KD (red) rat.
Peak annotations: tCr: total creatine; Glu: glutamate; Gln: glutamine; Glx: glutamate+glutamine; Ala: alanine; Lac: lactate. Original spectra were scaled at the 3.02 ppm tCr peak before calculation of the difference spectra. Error bars are standard deviation.

References

1. Cryer PE: *N Engl J Med* 350:2272-2279, 2004; 2. Mason GF *et al. Diabetes* 55:929-934, 2006; 3. Leino RL, *et al. Neurochem Int* 38:519-527, 2003; 4. de Graaf RA *et al. NMR in biomedicine* 16:339-357, 2001; 5. Kossoff EH *et al*. J Child Neurol 24:979-88, 2009; 6. Seyfried TN *et al. J. Cancer Res Ther* Sep;5 Suppl 1:S7-15, 2009

Effects of occupational solvent exposure on brain function: an fMRI study

E. L. Eaves[1], D. M. Carpenter[1] , J. Ng[1], Ganeshalingam, N. , G. Lange[3,4], N. L. Fiedler[5], and C. Y. Tang[1,2]

[1]Radiology, Mount Sinai School of Medicine, New York, New York, United States,
[2]Psychiatry, Mount Sinai School of Medicine, New York, New York, United States,
[3]Psychiatry, UMDNJ-New Jersey Medical School, West Orange, New Jersey, United States,
[4]Radiology, UMDNJ-New Jersey Medical School, West Orange, New Jersey, United States,
[5]Environmental and Occupational Medicine, UMDNJ- Robert Wood Johnson Medical School, Piscataway, New Jersey, United States

Introduction

Studies show exposure to solvents has neurobehavioral effects in humans. However, few studies have examined the effects of solvents on regional brain function. In this report we used Blood Oxygen Level Dependent (BOLD) functional Magnetic Resonance Imaging (fMRI) to investigate the functional deficits of subjects with long-term occupational solvent exposure. Subjects underwent fMRI while performing a Sternberg task and N-back working memory task. We used an exploratory voxel-wise and a region of interest (ROI) analysis to test the hypothesis that the occupationally exposed subjects show hypo-activation in regions associated with working memory when compared to a carefully matched control group.

Methods

Imaging. All imaging was performed on a 1.5T Allegra MRI scanner (Siemens, Ehrlangen, Germany). Functional MRI BOLD images were acquired with a gradient echo-planar using the following protocol: 32 axial slices, 3mm skip 1mm, TR=2.5s, TE=30 ms, flip angle=90°, FOV=21 cm, matrix size=64x64. fMRI data was analyzed using SPM2 (Wellcome Department of Cognitive Neurology, London). Images were motion corrected, smoothed ($6mm^3$) and coregistered to a matching T2 weighted image and then normalized to the standard MNI template. A version of the Sternberg memory task was used in a block designed fMRI. Activation was quantified as the difference between the maintenance phase of the Sternberg task and the inter-trial rest period of the block design. Imaging data were analyzed for patient specific N-back related activation by contrasting the fixation and task performance periods in a block design.

Subjects. A total of 39 controls (carpenters, painters and glazers) and 46 solvent exposed subjects (painters) with > 10 years of exposure to organic solvent mixtures but who were otherwise healthy, were recruited from a larger study evaluating the cognitive and sensory effects of chronic solvent exposure. Data from 30 controls and 29 exposed subjects were analyzed for the Sternberg task, and data from 29 controls and 34 exposed subjects were analyzed for the N-back task.

Results and Discussion

Voxel-wise t-tests were used to explore differences in activation related to the fMRI tasks. As hypothesized, subjects that were exposed to organic solvents showed decreased activation in the dorsolateral prefrontal cortex (DLPFC) and also some regions of the cingualate gyrus. Specifically, the exposed subjects showed decreased activation during the Sternberg task in the left DLPFC, and dorsal regions of the cingulate gyrus and supplementary motor areas of the frontal cortex (Figure 1). Figure 1 shows the group activation map in red of all subjects that performed the Sternberg task overlayed on a brain in the standard MNI space. Positive and negative t-values that met statistical criteria ($p < 0.01$; cluster size > 16) were overlayed in green and blue, respectively; thus, areas of green indicate lower activation in exposed patients while blue indicates higher activation. The activation map and color scheme in Figure 2 is the same as Figure 1 and shows the results from the N-back working memory task. During this task, decreased activation of the exposed subjects was seen bilaterally in the DLPFC and a region of the anterior cingulate. The voxel-wise comparisons between the BOLD activations of exposed and non-exposed subjects did not reveal any significant increased activity in the exposed sample (no blue) so we are not able to conclude the use of a compensatory diffuse regions of activation in solvent exposed subjects. We further investigated the

effects of solvent exposure by extracting BOLD activations from regions of interest (ROIs) and testing for dose-effect relationships. Spherical volumes of 3mm radii were extracted from the most activated region of each cluster by each task. The amount of activation from each region was entered into Statistica for further analysis. Partial correlation coefficients were computed for solvent exposure and regional activation while controlling for the confounding factors of verbal IQ, lead exposure, lifetime alcohol, marijuana and cocaine use. The Sternberg activations did not reveal significant correlations between solvent exposure and activation when the potential confounds were included in the analysis. The N-back activations, however, showed negative correlations between activation and solvent exposure. The finding is consistent with t-test results that showed a decrease in activation related to solvent exposure

Conclusion

As hypothesized, the results suggest that prolonged occupational solvent exposure is related to a decreased activation in regions associated with working memory. The two pronged approach, the Sternberg and N-back tasks, revealed similar deficits. The consistency as well as the results of the ROI analysis bolsters confidence in the results of the exploratory analysis. Additionally, the lack of clusters with increased activation support a hypothesis that solvent exposure is related to hypo-activation of brain structures involved in working memory.

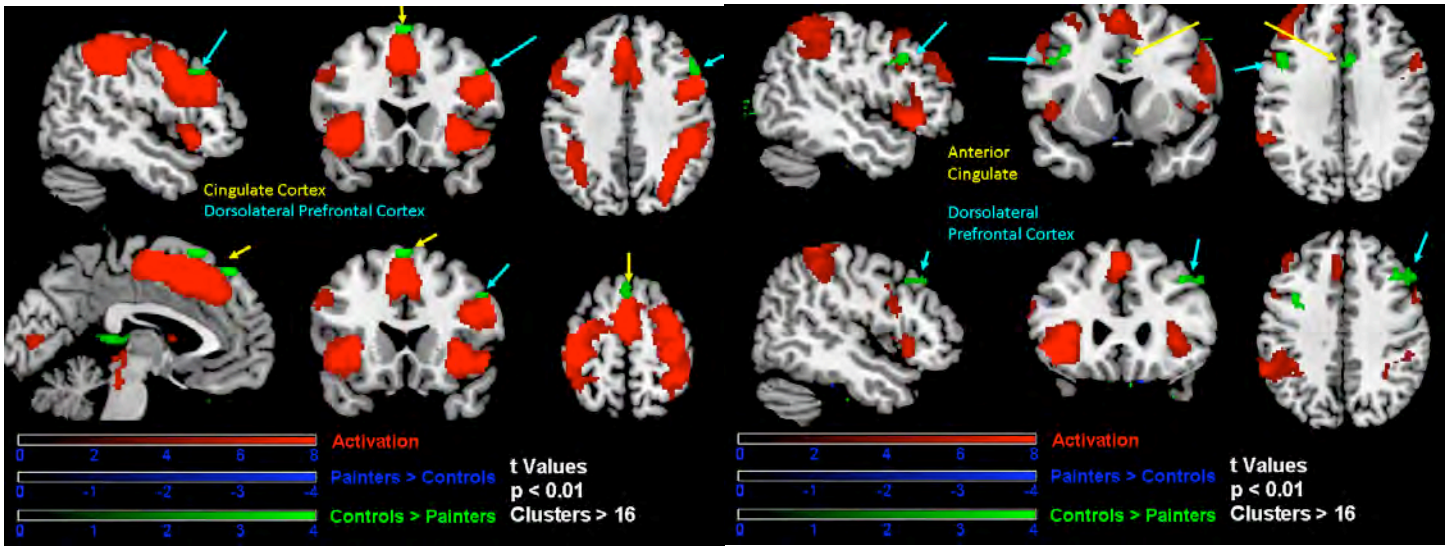

Figure 1. t-test results for the Sternberg (left) and N-back (right) tasks. There were 30 control and 36 exposed subjects analyzed for the Sternberg task. Twenty-nine control and 33 exposed subjects were analyzed for the N-back task.

Funded by NIOSH # R01 OH008198

Structural Neural Correlates of Symptom Dimensions in Pediatric Obsessive-Compulsive Disorder

Andrew R. Gilbert[1, 2], Jorge R.C. Almeida[2], David Mataix-Cols[3], Mary L. Phillips[2]

[1]Department of Psychiatry, Mount Sinai School of Medicine, New York, NY, [2]Department of Psychiatry, University of Pittsburgh School of Medicine, Pittsburgh, PA, [3]Psychological Medicine and Psychology, Institute of Psychiatry, London, United Kingdom.

Introduction

Obsessive-Compulsive Disorder (OCD) is a clinically heterogenous disorder and recent factor analytic studies have identified at least four temporally stable symptom dimensions. We recently conducted a functional neuroimaging study of pediatric OCD patients and found reduced activity in neural regions underlying emotional and cognitive processing in response to symptom provocation. A preliminary structural analysis revealed smaller gray matter volumes (GM) in several neural regions of significant abnormal activity. The structural neural correlates of symptom dimensions early in the course of illness, however, remain to be fully elucidated.

Methods

GM was measured in 18 pediatric OCD patients (OC) and 18 matched healthy controls (HC) using voxel based morphometry (VBM), controlling for age and total brain GM. Regression analyses were carried out between whole brain GM and age of onset, OCD, anxiety, and depression severity scores, and individual symptom dimension severity scores.

Results and Discussion

We found significant GM differences between OC and HC in the right occipital lobe (OC>HC; $p<0.001$, uncorrected) and left dorsolateral prefrontal cortex [DLPFC] (OC<HC; $p<0.05$, corrected). There was a significant negative correlation between right orbitofrontal cortex (OFC) GM and contamination severity ($p<0.05$, corrected). Significant negative correlations were found between bilateral cerebellum GM and symmetry severity ($p<0.001$, uncorrected). Significant positive correlations were found between left parietal and bilateral cingulate GM and symmetry severity ($p<0.001$, uncorrected). Earlier onset of OC symptoms was significantly associated with more GM in right OFC, parietal lobe and parahippocampal gyrus and less GM in bilateral cingulate and left cerebellum.

Conclusion

Our findings suggest distinguishable structural neural correlates of OC symptom dimensions early in the course of illness as well as developmental effects upon these neural systems. While contamination symptom severity was associated with GM in emotion processing regions, symmetry severity was associated with GM in attentional and motor processing regions. Furthermore, earlier onset of OCD was associated with differential GM patterns in these regions.

FIGURE 1

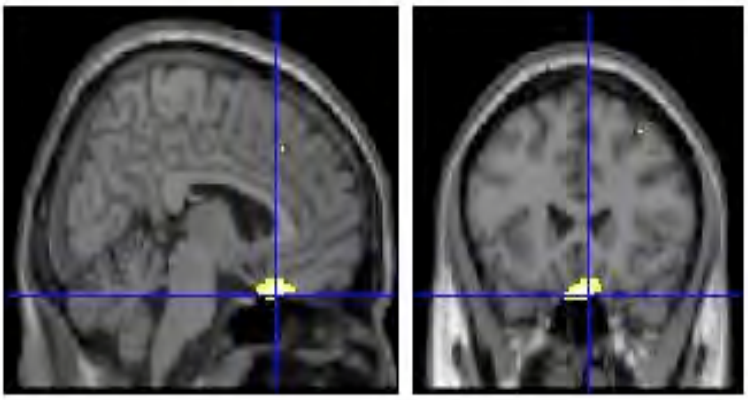

Figure 1. Significant negative correlation between right orbitofrontal cortex (4 24 -24) gray matter volume and contamination/washing symptom severity ($p<0.05$, corrected).

FIGURE 2

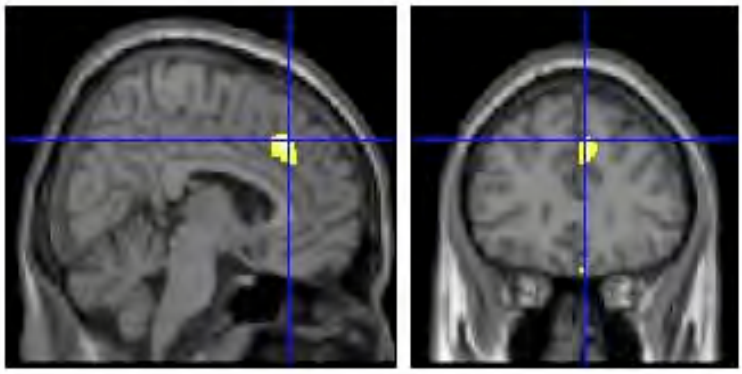

Figure 2. Significant positive correlation between right cingulate gyrus (6 30 40) gray matter volume and symmetry/ordering symptom severity ($p<0.001$, uncorrected).

References

1. Gilbert AR, Akkal D, Almeida JRC, et al. Neural correlates of symptom dimensions in pediatric obsessive-compulsive disorder: a functional magnetic resonance imaging study. *J Am Acad Child Adolesc Psychiatry.* 2009; 48(9): 936-44.
2. Mataix-Cols D, Wooderson S, Lawrence N, et al. Distinct Neural Correlates of Washing, Checking, and Hoarding Symptom Dimensions in Obsessive-Compulsive Disorder. *Arch Gen Psychiatry.* 2004; 61:564-576.
3. Rauch SL, Dougherty, D.D., Shin, L.M. Neural correlates of factor-analyzed OCD symptom dimensions: A PET study. *CNS Spectrums*. 1998;3(7):37-43.
4. Bloch MH, Landeros-Weisenberger A, Rosario MC, et al. Meta-Analysis of the Symptom Structure of Obsessive-Compulsive Disorder. *Am J Psychiatry*. 2008; 165: 1532-1542.
5. Van den Heuvel OA, Remijnse PL, Mataix-Cols D, et al. The major symptom dimensions of obsessive-compulsive disorder are mediated by partially distinct neural systems. Brain. 2009; 132: 853-868.

Diffusion Tensor Imaging and Tractography in Adolescent-Onset Borderline Personality Disorder

Marianne Goodman, M.D., David Carpenter, Ph.D., Jennifer Avedon, B.S., Antonia S. New, M.D.

Introduction: Borderline Personality Disorder (BPD) is a disabling disorder characterized by poor affect regulation and poor impulse control. It is relatively common, affecting 2-5.9% of the population (Coid et al. 2006; Grant et al. 2008), and has serious clinical consequences, including suicide rates at 50 times the general population (Skodol et al. 2002). We focused on adolescent-onset BPD because the symptoms of BPD often emerge during adolescence, and because adolescence is a critical period of brain development during which, for example, there is the most rapid change in gray matter volume of a variety of cortical regions (Giedd et al. 2008). While a number of studies have explored abnormalities in functional brain imaging in adult BPD, and two studies have pointed to DTI abnormalities in BPD, no study has previously examined DTI with tractography in adolescent-onset BPD.

Methods: We conducted structural brain imaging with DTI and tractography on 14 adolescent inpatients with BPD and 13 age- and sex-matched controls. Subjects with BPD met DSM-IV (SCID-II) and Diagnostic Interview for BPD-revised (DIB-R) criteria for BPD, while controls had no current axis I or II diagnosis as assessed by the SCID-P and SCID-II. All BPD adolescents met criteria for major depressive disorder, as is characteristic of inpatients with BPD.

DTI was acquired on a 3T Siemens Allegra and processed in the Image Analysis Core of Mount Sinai. In-house software and FSL (http://www.fmrib.ox.ac.uk/fsl/) was used for pre-processing and DTI-tractography. A study-specific-template was created using the FSL-TBSS package and used to outline DTI-tractography (for method see Carpenter 2008). Fractional anisotropy (FA) was calculated from the DTI-tractography of the following tracts: genu and splenium of the corpus callosum, inferior bilateral longitudinal fasciculus, and bilateral cingulum bundle (Figure 1).

Figure 1: DTI-Tractography of an adolescent.

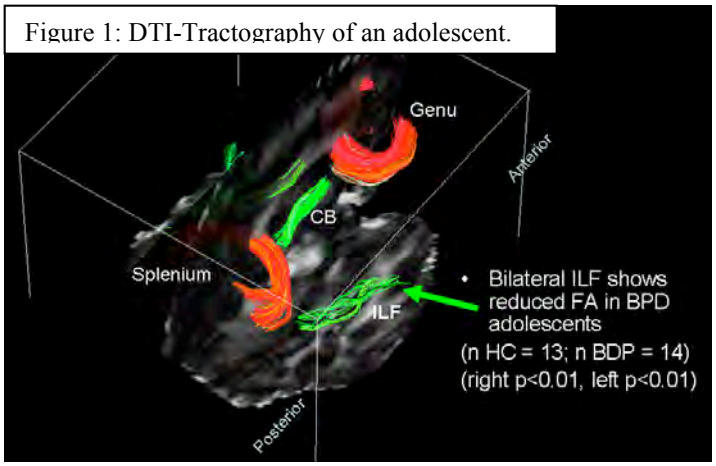

Results: A tract specific decrease in FA was found in the ILF of BPD patients (left ILF $t=3.13$ $p<0.005$; right ILF $t = 2.92$ $p<0.008$; $p>0.1$ for other tracts). In addition to the bilateral decrease in FA in the ILF in BPD adolescents compared to controls, we also found significant inverse correlations between clinical measures of aggression and mood instability with FA in the ILF (Buss Perry Aggression Questionnaire: $r=-.39$, $p=<.05$, right ILF, $r=-.60$, $p<.002$; Affective Lability Scale: $r=-.46$, $p=<.02$). Correlations of FA in the ILF were not significant for measures of depression.

Conclusion:

While the function of the ILF is poorly understood, individuals with brain lesions specifically in this area show poor ability to name objects (Mandonnet et al, 2007) difficulty in recognition of facial affect (Philippi et al, 2009). This is very interesting because a profound deficit in the ability to name and describe feelings has been found in BPD. Moreover, we have shown high levels of alexithymia in adult BPD (New et al, in review). Our finding of low FA in the ILF, supporting the notion of disruption in white matter efficient signal conduction, in the brain area related to object naming and emotion recognition provides a very interesting possible neural substrate for this difficulty in naming and describing affect in BPD.

Functional Dissociation of the Frontoinsular and Anterior Cingulate Cortices in Empathy for Pain

Xiaosi Gu[1,2], Xun Liu[1], Kevin G. Guise[1,2], Thomas P. Naidich[3], Patrick R. Hof [4], and Jin Fan[1,4]

[1]Department of Psychiatry, [2]Graduate School of Biological Sciences, [3]Department of Radiology, and [4]Department of Neuroscience,
Mount Sinai School of Medicine, New York, New York 10029

Introduction

Empathy refers to the ability to understand and echo other people's sensory and emotional states (Gu et al., 2010). The frontoinsular cortex (FI) and the anterior cingulate cortex (ACC) are known to be involved in empathy for others' pain (Singer et al., 2004; Jackson et al., 2005; Gu and Han, 2007). The FI has been historically considered as a limbic sensory region, and is responsible for polymodal sensory integration (Critchley, 2004; Critchley et al., 2004; Craig, 2009), while the ACC is known as a limbic motor cortex that participates in voluntary control of multiple domains of behaviors (Bush et al., 2000). Although it is widely accepted that both FI and ACC are co-activated in processing empathy for others' pain, and much of the research has focused on the commonality of FI and ACC, it remains unclear why such structurally distinct regions appear functionally inseparable and what distinct roles they each play in cognitive processes such as empathy for pain. The current study aimed to investigate the specific roles of FI and ACC involved in empathy for others' pain.

Methods

We used functional MRI to explore the functional dissociation between FI and ACC involved in empathy for pain using a modified empathy for pain task (Singer et al., 2004; Jackson et al., 2005; Gu and Han, 2007). Participants viewed color photographs depicting human body parts (hands or feet) in painful or non-painful situations and performed either pain judgment (painful/non-painful) or laterality judgment (left/right) of the body parts. Event-related analyses of the fMRI data from the two tasks were conducted using statistical parametric mapping (SPM).

Results and Discussion

Behavioral data (reaction time and accuracy) confirmed that all four experimental conditions had equivalent cognitive load. Neuroimaging data indicated that activation of FI, rather than ACC, showed significant increase for painful compared to non-painful images, regardless of the task requirement. First, FI robustly responded to the sight of others' pain bilaterally, regardless of whether the observer was explicitly asked to evaluate pain. Second, ACC activation did not differentiate between painful and non-painful stimuli, or between pain judgment and laterality judgment; that is, increase in activation due to empathy for pain was significantly greater in FI than in ACC. These findings suggest a clear functional dissociation between FI and ACC in which FI is more domain-specific than ACC in processing of empathy for pain.

Conclusion

We showed for the first time that when cognitive load is carefully matched between painful and non-painful conditions, the FI, but not the ACC, specifically responds to empathy for pain, suggesting a more direct and essential role of FI than ACC in processing empathy for pain. This finding challenges the current consensus that the ACC is indispensable in empathetic responses, and singles out the importance of the FI in empathetic processes (Gu et al., 2010).

FIGURE 1

Figure 1 Sample stimuli of the experimental stimuli set of 216 digital color photographs showing another person's left or right body hand/foot in painful or non-painful situations. Each stimulus was displayed for 2,500 ms followed by a fixation of 1,500 ms. Subjects were asked to choose between "non-painful" and "painful" for the Task Pain (TP), and "left" and "right" for the Task Laterality (TL) through button press.

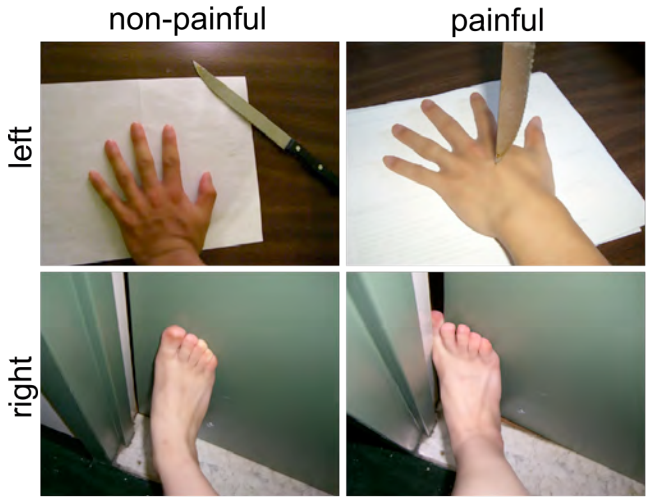

FIGURE 2

Figure 2. ROI analysis of the parameter estimates of ACC and FI for four experimental conditions (TP-non-painful, TP-painful, TL-non-painful, TL-painful). (A) Localization of ACC and FI ROIs derived from activations common to all four experimental conditions. (B) ACC showed comparable activation levels to all four conditions; FI showed significant increased activation for painful compared to non-painful stimuli independent of the task. This ROI-by-stimulus interaction was significant (see Results for details). (C) Responses in left FI and right FI separately. Error bars represent 95% confidence intervals. ACC: anterior cingulate cortex; FI: frontoinsular cortex.

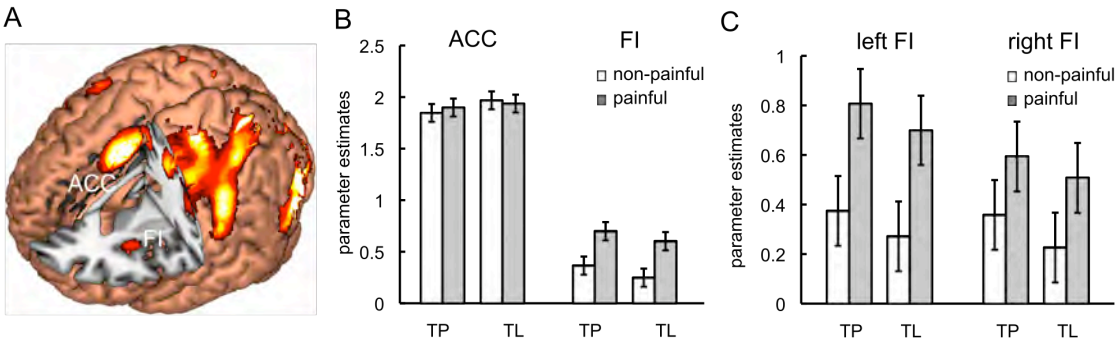

References

Bush G, Luu P, Posner MI (2000) Cognitive and emotional influences in anterior cingulate cortex. Trends Cogn Sci 4:215-222.

Craig AD (2009) How do you feel--now? The anterior insula and human awareness. Nat Rev Neurosci 10:59-70.

Critchley HD (2004) The human cortex responds to an interoceptive challenge. Proc Natl Acad Sci U S A 101:6333-6334.

Critchley HD, Wiens S, Rotshtein P, Ohman A, Dolan RJ (2004) Neural systems supporting interoceptive awareness. Nat Neurosci 7:189-195.

Gu X, Han S (2007) Attention and reality constraints on the neural processes of empathy for pain. Neuroimage 36:256-267.

Gu X, Liu X, Guise KG, Naidich TP, Hof PR, Fan J (2010) Functional dissociation of the frontoinsular and anterior cingulate cortices in empathy for pain. J Neurosci 30:3739-3744.

Jackson PL, Meltzoff AN, Decety J (2005) How do we perceive the pain of others? A window into the neural processes involved in empathy. Neuroimage 24:771-779.

Singer T, Seymour B, O'Doherty J, Kaube H, Dolan RJ, Frith CD (2004) Empathy for pain involves the affective but not sensory components of pain. Science 303:1157-1162.

The Alerting Network in Attention-Deficit/Hyperactivity Disorder

J. M. Halperin[1,2]; S. M. Clerkin[1]; O. G. Berwid[1,2]; J. Fan[1]; C.Y. Tang[1]; S. Harty[2], J. Trampush[2]; K. P. Schulz[1]

Mount Sinai School of Medicine[1]; Queens College, City University of New York[2]

Introduction

We utilized functional magnetic resonance imaging (fMRI) to test a neurodevelopmental model of ADHD (Halperin & Schulz, 2006), which posits that deficits in subcortical alerting/arousal mechanisms contribute to the development of ADHD and remain present in adulthood.

Method

A longitudinal sample of 16 probands who were first diagnosed with ADHD in childhood and 15 never-ADHD controls were clinically evaluated and scanned using fMRI. A cued reaction time (RT) task was used to probe the alerting system. This simple RT task evokes activation within subcortical and cortical regions of the brain known to receive innervation from the LC noradrenergic system, and produces a behavioral alerting effect, with faster RT to cued targets than non-cued targets (Clerkin et al, 2009). Brain activity related to alerting was modeled by subtracting neural responses to correct non-cue events from neural responses to correct Cue events. This contrast isolated cue-related activity by subtracting out the processing of similar visual stimuli. Significance was set at $p < .01$, uncorrected; $k = 100$.

Results and Discussion

Adults with ADHD and controls activated similar brain regions during alerting, however, controls demonstrated greater activation in the supplementary motor area (SMA), while probands demonstrated significantly greater activation in the inferior frontal gyrus (IFG) and the cerebellum. The SMA is involved in motor planning. The IFG provides stimulus-driven control of the LC-NA system and might be involved in the decision process that results in the motor response to the target. The cerebellum also receives dense LC-NA innervation, and might be involved in motor preparation to a greater extent among those with ADHD compared to controls. There was a main effect of Cue on RT ($F = 250$, $p < .00001$), but no group differences in RT were found, thus neural responses were not due to differences in behavior.

Conclusion

The differences observed in SMA, IFG, and cerebellum suggests subtle discrepancies in the alerting system among those with and without a childhood diagnosis of ADHD, providing preliminary support for the tested neurodevelopmental model of ADHD.

FIGURE 1

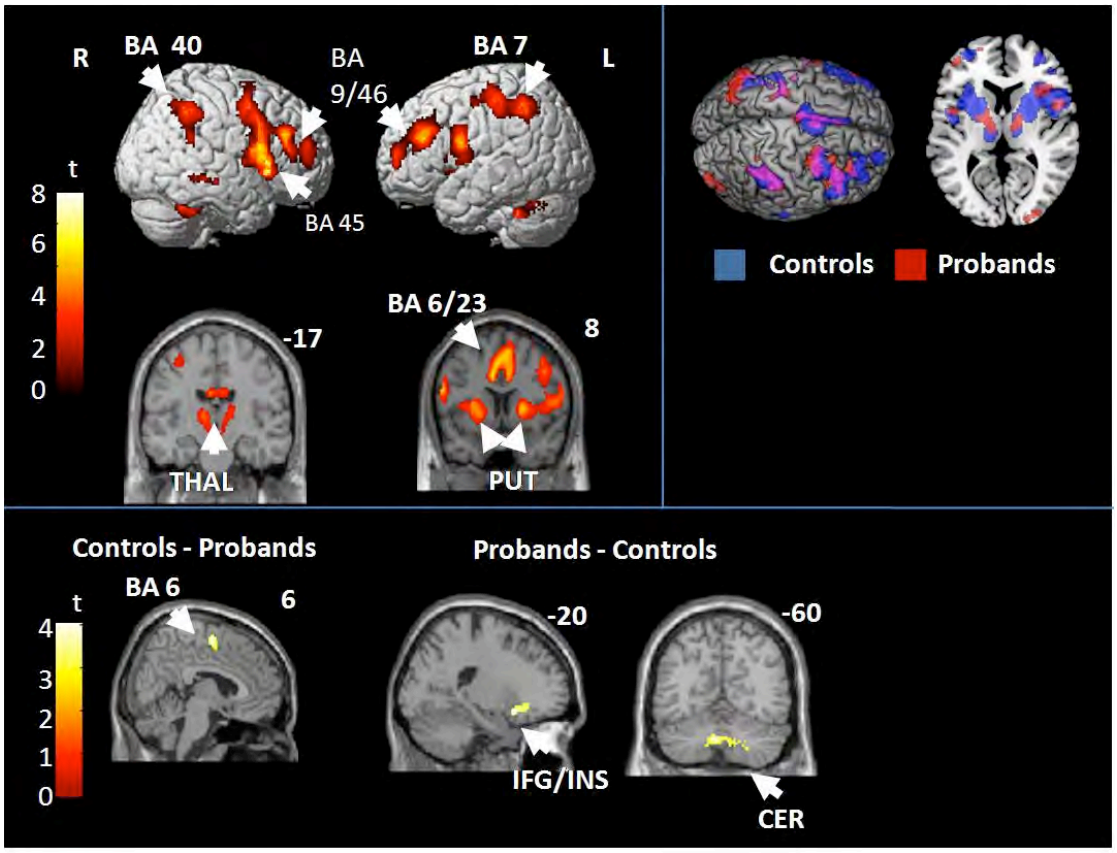

Figure 1. Neural activation in response to cues (Cue – Noncue constrast). **Top Left:** Activation in controls. **Top Right:** Controls and probands activated similar cortical and subcortical regions. **Bottom:** Group differences in the cue response. All $p < .01$, uncorrected; $k = 100$.

References

Clerkin, S.M., Schulz, K.P., Halperin, J.D., Newcorn , J.H., Ivanov, I., Tang, C.Y., Fan J. (2009). Guanfacine potentiates the activation of prefrontal cortex evoked by warning signals. *Biological Psychiatry*, 66, 207-312.

Halperin, J. M. and Schulz, K. P. (2006). Revisiting the role of the prefrontal cortex in the pathophysiology of attention-deficit/hyperactivity disorder (ADHD). *Psychological Bulletin*, 132, 560-581.

Mri of histological tissue: effect of passive gadolinium-staining

Dung Minh Hoang, M.Sc.[1,2], Allal Boutajangout, Ph.D.[1], Anne Bertrand, M.D.[1], Susan Pun, B.Sc.[1], Latifa Fakri-Bouchet, Ph.D.[2], Einar Sigurdsson, Ph.D.[1], Thomas Wisniewski, M.D.[1], Youssef Zaim Wadghiri, PhD[1].

[1]NYU School of Medicine, New York, NY, USA, [2]Universite Claude Bernard Lyon-1, Villeurbanne, France.

Introduction

Amyloid β burden (Aβ) in transgenic (Tg) mouse models have been visualized by MRI either through endogenous detection, using Aβ-specific contrast agents, or using non specific-contrast agent (the so-called "passive staining" technique). Precise correlation between MRI and histology has been an ongoing challenge to validate these studies. An elegant approach directly imaging tissue sections using a histological MRI probe was proposed to enable correlation from the same exact sections. Using a similar MRI probe designed in-house, we studied the effect of passive staining with Magnevist© (Gd) on Tg mouse plaque detection.

Methods

Sections from APP (Tg2576) and APP/PS1 Tg mice (N=5) and age-matched C57BL/6 controls (N=7) were floated in either HEPES buffer or HEPES doped with Gd (0.5mM to 5mM). Each sample was then sandwiched between two glass cover slips, inserted into the histological probe interfaced to a 7-Tesla magnet and imaged with a T2* sequence with a 2-hour and 8-hour duration. Samples were then stained with Congo Red. MR and histological images were analyzed using the ImageJ software to calculate signal-to noise ratios (SNR) and also to match dark spots and Congo-red positive deposits.

Results and Discussion

Using 5 mM Gd passive staining allowed for a global 2x increase of the SNR (Fig 1A-D) where the 2-hr scan reached the SNR level obtained in 8-hr without Gd (Fig 1B-C). This was accompanied by ~2.8x increase in gray and white mater contrast confirming the unequal redistribution of Gd throughout the brain as previously reported in whole brain studies. After Gd passive staining, numerous cortical dark spots were visible and matched Congo red positive deposits; these dark spots were not visible or were faintly visible without Gd (Fig 1E-G).

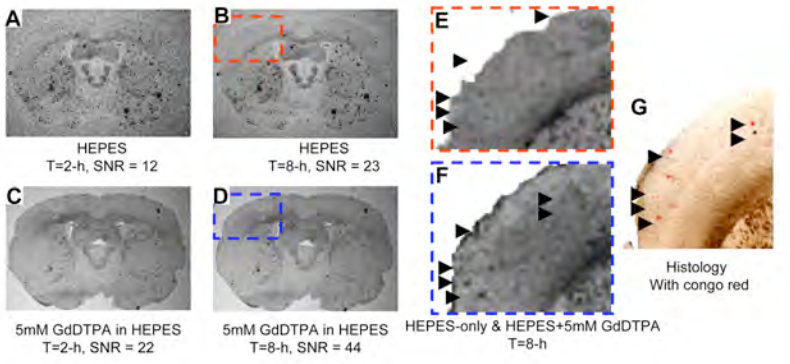

Conclusion

This histo-MRI study demonstrated that Gd passive staining doubles MRI sensitivity, and increased contrast between Aβ plaques and surrounding tissue, thus confirming previous ex vivo and in vivo whole brain studies. The gain in sensitivity and contrast achieved will enable to investigate smaller structures.

Vestibular Phenotypes in *Gbx2* Mutant Mice Revealed by Contrast Enhanced MRI

Edward J. Houston[1], Kamila U. Szulc[1,2], Roy V. Sillitoe[3], Alexandra L. Joyner[3], Daniel H. Turnbull[1,2]

[1]Kimmel Center for Biology and Medicine at the Skirball Institute of Biomolecular Medicine, and [2]Department of Radiology, New York University School of Medicine and [3]Developmental Biology Program, Sloan Kettering Institute, New York NY

Introduction: The cerebellum (Cb) is most widely known for its essential role in motor coordination and vestibular function [1]. *Gbx2* conditional knockout (CKO) mutant mice have defects in the Cb in the form of deletion of the central region, the vermis, which is most commonly affected in human cerebellar hypoplasias [2]. Additionally, these mice display abnormalities in the anatomy of flocculus-paraflocculus (FL-PFL) complex, a part of the vestibulo-cerebellum (VC) that receives projections from the vestibular organs (VO), and is critical for maintaining balance and spatial orientation. In this study, we characterize abnormal development of the FL-PFL complex during early postnatal stages in *Gbx2*-CKO mutant mice and demonstrate that abnormalities in this region are accompanied by previously unreported abnormalities in vestibulo-cochlear organ (VCO).

Methods: *Developmental MEMRI Studies*: Mn^{2+} was delivered to neonates through milk after maternal intraperitoneal (IP) injection of $MnCl_2$ in isotonic saline (40mg/kg). The neonatal mice were imaged 24h later from postnatal day P3 to P11. 3D T1-weighted gradient echo (GRE) datasets with 100-µm isotropic resolution covering the whole brain were acquired during each imaging session. *Contrast enhanced micro-MRI*: Mice were perfused transcardially with a 10mM solution of Magnevist. The brains were left in the skulls and kept in 1mM solution of contrast agent in paraformaldehyde (PFA) until imaging 24-72h after perfusion. 3D T1-weighted GRE images were acquired with 50-µm isotropic resolution. All MRI data were collected on a 7T Bruker micro-MRI system. Volumetric analysis and 3D renderings were performed using AMIRA. Deformation based morphometric (DBM) analysis were performed to calculate local brain volume changes, as described previously [3, 4, 5].

Results and Discussion: The whole brain DBM analysis revealed abnormalities in *Gbx2*-CKO mice in the cerebellar vermis, hemispheres, FL-PFL complex and cerebellar nuclei, as well as alterations of adjacent midbrain structures [Fig. 1]. These results were in excellent agreement with the previous semi-automated volumetric analyses, which revealed a smaller FL-PFL in *Gbx2*-CKO mice at all developmental stages that were analyzed [Fig. 2]. Additionally, high resolution micro-MRI data revealed structural abnormalities in VCO that develops in close proximity to the FL-PFL region and sends projections to it [Fig. 3].

Conclusion: Different types of contrast-enhanced MRI allowed us to perform a comprehensive characterization of vestibular defects, which pointed to novel findings in *Gbx2*-CKO mutant mice in VC and VCO. Our study also indicates the potential complex interplay between brain and sensory organs during development.

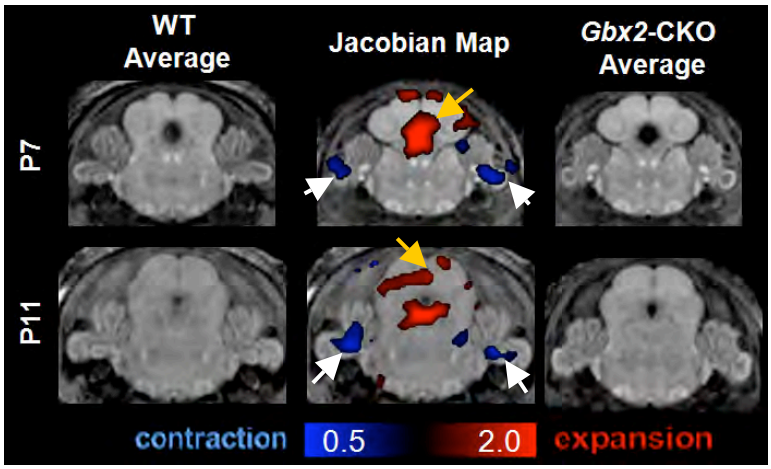

Figure 1. DBM analysis revealed differences in volume and shape in several regions of the *Gbx2*-CKO mouse brain, including a reduction in the FL-PFL complex (white arrows), and an expansion of dorsal midbrain structures and the 4th ventricle (yellow arrows).

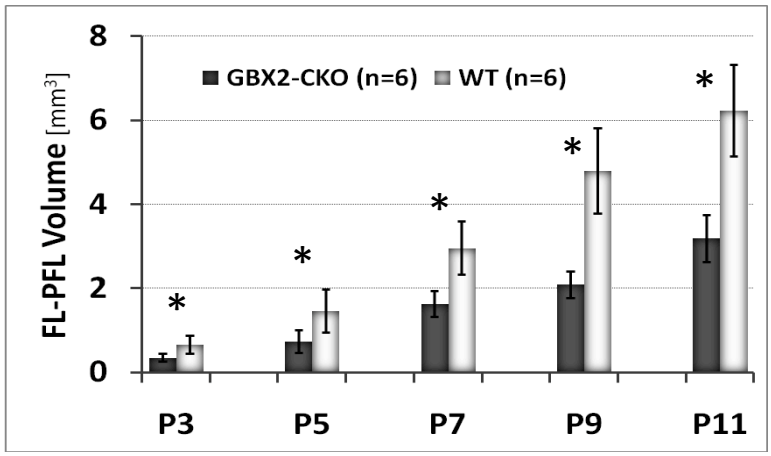

Figure 2. Results of volumetric analysis show a significantly reduced volume of the FL-PFL complex in *Gbx2*-CKO mice at all developmental stages. These results are in agreement with reduction of volume in this region identified using DBM.

Figure 3. 3D reconstruction of vestibulo-cochlear organ based on micro-MRI images in (a) wt and in (b) *Gbx-2*-CKO mice. Regions of the cochlea and semicircular canals can be seen in detail in the context of the Cb. Comparison of 3D reconstructions of VCO of (c) WT and (d) *Gbx2*-CKO mice. An arrow indicates a partial deletion of the *Gbx2*-CKO cochlear region.

References: [1] Sillitoe RV, Joyner AL (2007). *Ann Rev Cell Dev Bio* 23: 549-77; [2] Li JY et al. (2002). *Neuron* 36: 31-43; [3] Kovacevic N et al. (2005). *Cereb Cortex* 15: 639-45; [4] Nieman BJ et al. (2007). *Human Brain Mapp* 28: 567-75; [5] Lerch JP et al. (2008). *Neuroimage* 39: 32-9.

Brain Activation in Preadolescents with Low vs. High risk for Subsequent Substance Abuse

Iliyan Ivanov, M.D. [1] Xun Liu, Ph.D. [1] Suzanne M. Clerkin, Ph.D. [1] Kurt P. Schulz, Ph.D. [1]
Jin Fan, Ph.D. [1] Jeffrey M. Halperin, Ph.D. [1, 2] Jeffrey H. Newcorn, M.D. [1]
Mount Sinai School of Medicine[1]; Queens College, City University of New York[2]

Introduction

Childhood attention deficit/hyperactivity disorder (ADHD) has been associated with increased risk for the development of later substance use disorders (SUD). We evaluated neural correlates of SUD vulnerability in drug naïve youth with ADHD using functional magnetic resonance imaging (fMRI). We examined the degree to which parental history of addiction is associated with differences in blood oxygen level dependent (BOLD) signal activation in the brain reward and executive control neurocircuits. We hypothesized differential brain activation in the nucleus accumbens (NAcc), dorsal anterior cingulate cortex (dACC) and orbito-frontal cortex (OFC) in drug naïve children with ADHD at high (i.e. ADHD + family history of SUD) vs. low (i.e. ADHD alone) risk for SUD.

Method

Twenty drug-naïve children with ADHD ages 8-13, were scanned while performing the Anticipation, Conflict, and Reward (ACR) task, an event-related adaptation of the Monetary Incentive Delays (MID) task, which adds a measure of conflict resolution to existing reward anticipation and outcome conditions. High (N=10, M=9, F=1) and low (N=10, M=8, F=2) risk groups were established based on the presence of parental history of substance abuse. The effects of anticipation, conflict, and reward were tested by applying appropriate linear contrasts. A separate regressor for parental history of addiction was added. Results are reported at an uncorrected threshold $p<.01$ and a cluster threshold $\kappa \geq 100$ voxels . In addition, we recruited a control group of age matched children without ADHD/parental history of SUD who are being analyzed.

Results and Discussion

Reward cue/outcome trials activated anterior cingulate gyrus (ACG), ventral striatum (VS) and insula in all subjects. The HR group specifically exhibited increased BOLD signal activation in the orbito-frontal cortex (OFC) bilaterally and the right posterior cingulate gyrus during money-win outcomes (Fig 1) and the right insula and the right ACG during money-loss outcomes (Fig 2) when compared to the LR group. Conversely, the LR group exhibited increased BOLD signal activation in the ACG during the conflict resolution trials in comparison to the HR group.

Conclusion

These results suggest that family history of substance abuse may be associated with i) altered sensitivity of the mesolimbic reward system to positive/negative reward outcomes and ii) decreased activation of the executive control system during conflict resolution tasks in youth with ADHD.

Figure 1. HR group exhibited increased BOLD signal in bilateral OFC and posterior cingulate gyrus during money-win trials of the ACR task when compared to LR participants.

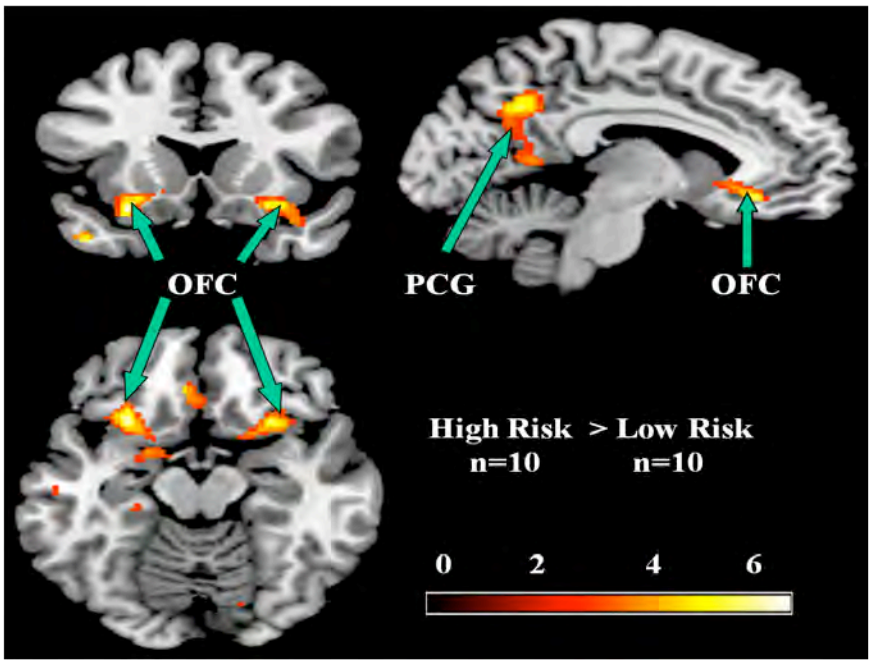

Figure 2. HR group exhibited increased BOLD signal in the right insula and the right anterior cingulated gyrus during money-loss trials of the ACR task when compared to LR participants.

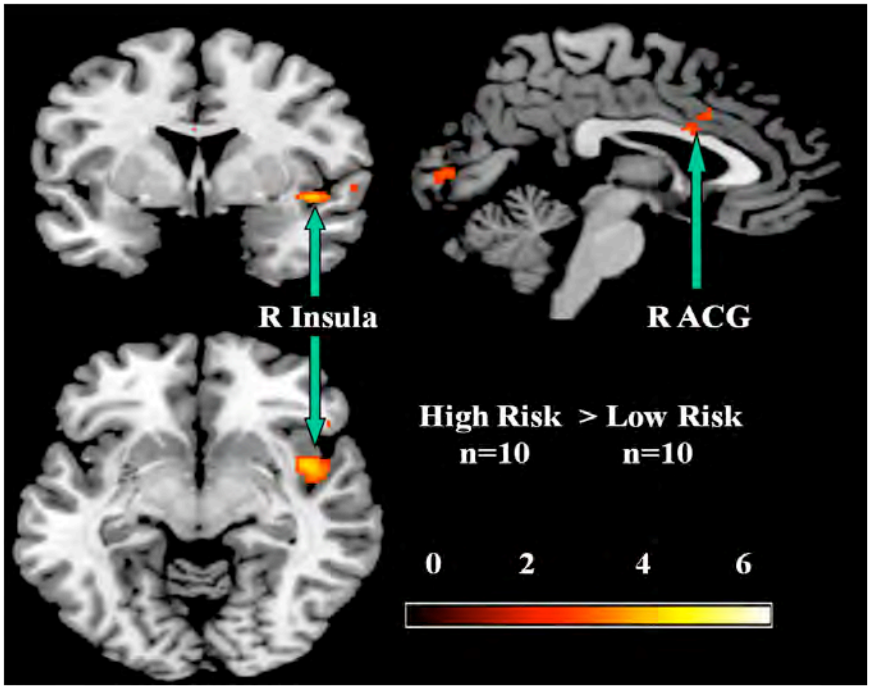

References

1. Knutson, B., A. Westdorp, E. Kaiser, and D. Hommer, FMRI visualization of brain activity during a monetary incentive delay task. Neuroimage, 2000. 12(1): p. 20-7.

2. Galvan, A., T.A. Hare, C.E. Parra, J. Penn, H. Voss, G. Glover, and B.J. Casey, Earlier development of the accumbens relative to orbitofrontal cortex might underlie risk-taking behavior in adolescents. J Neurosci, 2006. 26(25): p. 6885-92.

3. Gatzke-Kopp LM, Beauchaine TP, Shannon KE, Chipman J, Fleming AP, Crowell SE, Liang O, Johnson LC, Aylward E. Neurological correlates of reward responding in adolescents with and without externalizing behavior disorders. J Abnorm Psychol. 2009 Feb;118(1):203-13.

Enhanced Mn Transport in a Mouse Model of AD expressing Amyloid β Pathology: A Track Tracing MEMRI Study

U. Khan[1], A. Bertrand[1,2], D. M. Hoang[1], D. Novikov[1], B. W. Little[1], S. Pun[1], E. M. Sigurdsson[2,3], Y. Z. Wadghiri[1]

Departments of [1]Radiology, [2]Physiology & Neuroscience and [3]Psychiatry

Introduction

Amyloid β (Aβ) plays an essential role in the Alzheimer's disease (AD) pathophysiology. There is *in vitro* evidence that Aβ oligomers can impair fast axonal transport [1]. Manganese-Enhanced MRI (MEMRI) studies in a transgenic model (Tg2576) of AD over expressing human APP mutation confirmed the deleterious effect of Aβ on axonal transport measured by a decrease in the rate of signal change [2]. We utilized Tg6799 5xFAD mice which demonstrate accelerated Aβ pathology [3]. In our experiment we plotted normalized signal intensities of Mn and characterized transport function spread over a period of 7 days. Interestingly our preliminary results suggest a general trend of increased neuronal conduction including an increase in rate of change in signal intensity. Our overall goal aims at better characterizing axonal transport impairment *in vivo* using a panel of different biomarkers over a long timeframe window [4].

Methods

Six 6-month-old Tg6799 5xFAD [3] and five 6-month-old WT mice were imaged using a tract-tracing MEMRI (TT-MEMRI) protocol with 9 imaging time points (1 pre and 8 post-nasal injection of MnCl2, see [4]) spread over 7 days. Four regions of interest (ROI) were defined on MR images, corresponding to 4 consecutive areas of the olfactory system (Fig1). In each ROI we applied a one-dimensional flow-diffusion model to estimate the peak value (Pv) of the relative manganese concentration and the corresponding time to reach Pv (Pt). Presence of Aβ pathology was assessed in the brains by immuno-histochemistry using 6E10 and 4G8 antibodies.

Results and Discussion

A trend of increased Pv And decreased Pt is observed in Tg relative to control littermate WT-5xFAD (Fig 1) in the glomerular layer. Similarly, the rate of change in signal intensity (ΔSi/t) was also increased in the upslope in Tg compared to the same WT-5xFAD control (Fig 2). Expression of Aβ deposits was confirmed both in the olfactory bulb and the piriform cortex. We anticipated that the accelerated Aβ pathology in the Tg-5xFAD mouse model would lead to an early neuronal impairment translating into a decrease Pv, increase Pt and a decrease in ΔSi/t in this Aβ mouse model. However these results suggest increased uptake and faster propagation of Mn in Tg-5XFAD. Increased Pv signifies superior neuronal recruitment and greater Mn transported whereas decreased Pt implies faster speed of propagation as confirmed by the trend of increase in ΔSi/t.

Conclusion

Our preliminary results, although not significant, depicts an evident difference in trend between the two groups that can be seen in the plots. If confirmed, our results would demonstrate the first evidence of enhanced neuronal conduction *in vivo* in Aβ pathology AD mice. The lack of significance can be attributed to the variability in pathology known in this model. Hence, instead of categorizing by age-group, we are currently assessing the amyloid burden in each subject. This will allow us to establish a precise correlation of the Aβ burden with the various biomarkers of neuronal transport inferred from our study.

References

[1] Pigino G, Morfini G, Atagi Y, et al. Disruption of fast axonal transport is a pathogenic mechanism for intraneuronal amyloid b*. PNAS USA. 2009;106:5907-1.* **[2]** Smith KD *, Kallhoff V, Zheng H, Pautler RG.* In vivo axonal transport rates decrease in a mouse model of Alzheimer's disease. *Neuroimage 2007;35:1401-8.* **[3]** Oakley H, Vassar R, et al. Intraneuronal _-Amyloid Aggregates, Neurodegeneration, and Neuron Loss in Transgenic Mice with Five Familial Alzheimer's Disease Mutations: Potential Factors in Amyloid Plaque Formation. *The Journal of Neuroscience 2006; 26(40):10129 –40.* **[4]** Cross DJ, Flexman JA, Anzai Y, et al. Age-related decrease in axonal transport measured by MR imaging in vivo. *Neuroimage 2008;39:915-26.*

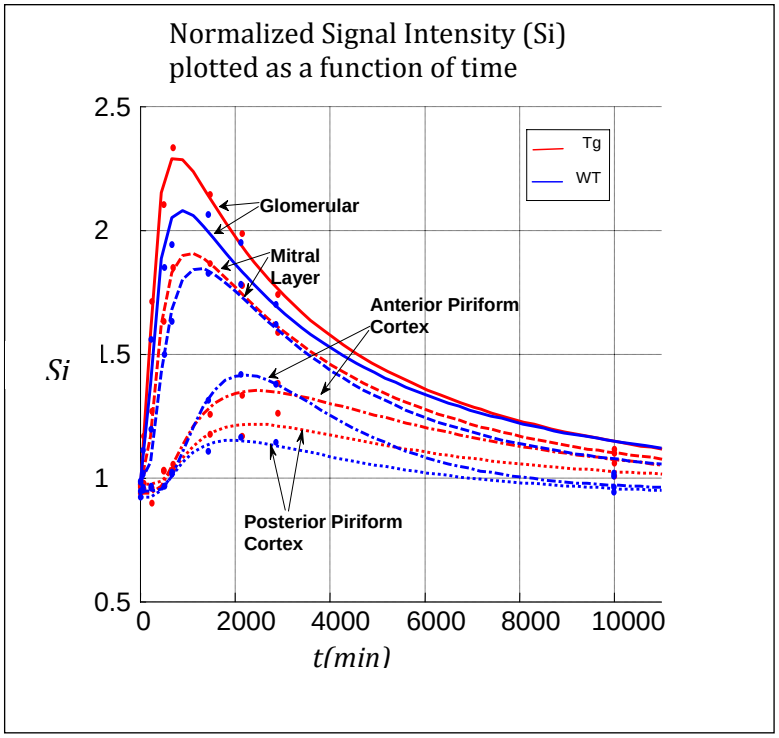

Figure 1. A differentiating trend of increased peak signal intensity and decreased time to peak is prominent in the proximal ROI (glomerular layer).

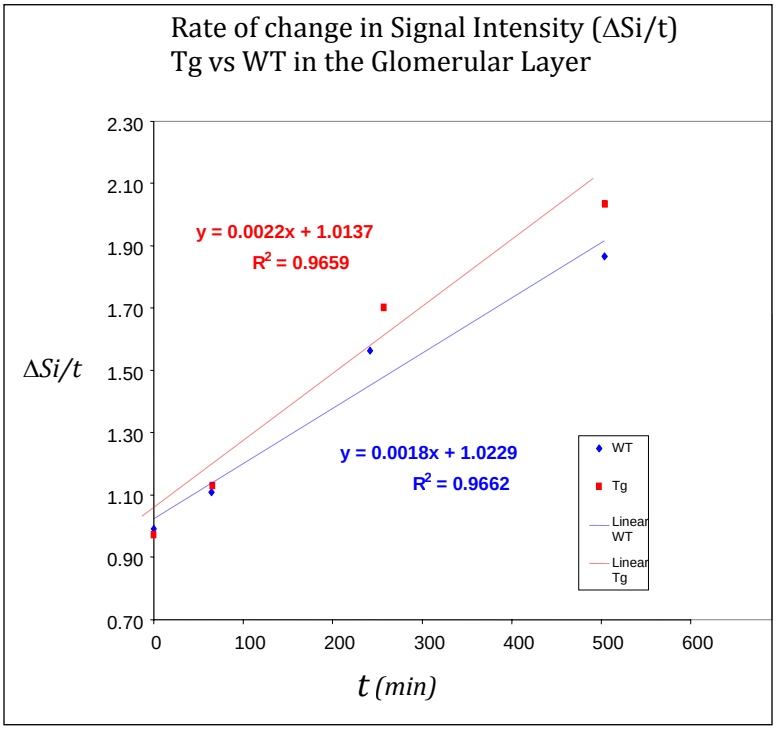

Figure 2. TG-5xFAD compared to WT-5xFAD show a distinct increase of ΔSi/t in the Glomerular Layer.

[^{11}C]raclopride Displacement by Leptin Depends on Individual Susceptibility to Weight Gain

Michael Michaelides[1,2], Ronald Kim[2], Mala Ananth[2], Gene-Jack Wang[2], Nora D. Volkow[3], & Panayotis K. Thanos[1-3]

[1]Department of Psychology, Stony Brook University; [2]Behavioral Neuropharmacology and Neuroimaging Lab, Brookhaven National Laboratory; [3]Laboratory for Neuroimaging, NIAAA

Introduction: Mesolimbic dopamine (DA) is involved in non-homeostatic feeding, in particular the motivational and rewarding properties of food [1]. We previously documented low DA D2 receptor (D2R) binding availability in the striatum of obese individuals [2] and obese rats [3]. These studies have suggested that low concentrations of striatal D2R or impaired DA-D2R signaling may underlie motivational and reward-related behavioral deficits that can lead to overeating and obesity. Leptin, a peripheral messenger that conveys the status of long-term energy (fat) stores to the brain may be involved in such deficits but interactions between leptin and striatal D2R have not yet been investigated. The aim of this study was to examine the role for leptin in modulating striatal DA-D2R interactions *in-vivo*. **Methods:** We measured striatal D2R binding potential (BP) in response to intraperitoneal (IP) administration of saline or leptin (20, 40, 80 μg/kg) in Sprague-Dawley rats using [^{11}C]raclopride and small animal positron emission tomography (μPET). A test-retest procedure was used to scan each rat at baseline and then two hours later following a saline or leptin challenge. **Results and Discussion:** Saline-treated rats showed a ~45% and ~120% increase in BP in the dorsal and ventral striatum respectively (Figure 1). 20 and 40 μg/kg leptin significantly decreased BP by ~30% in the dorsal striatum but did not affect BP in the ventral striatum. 80 μg/kg leptin produced variable results in both the dorsal and ventral striatum with some rats showing increases and others decreases in BP. Linear regression analysis was carried out in an attempt to explain this variability (Figure 2). Leptin decreased BP in rats that showed the least amount of weight gain at 1 and 2 months after scanning but increased BP in rats that showed the greatest weight gain at these same time points. [^{11}C]raclopride is highly displaceable by DA [4] and therefore short-term decreases/increases in BP are thought to reflect increases/decreases in D2R stimulation by DA (via DA-raclopride competition for D2R binding sites). Our results suggest that low peripheral leptin concentrations can lead to increases in striatal DA-D2R binding while higher doses produce variable effects on DA-D2R binding and that these effects depend on susceptibility to weight gain. **Conclusion:** Since deficits in leptin signaling are common in obesity, these results suggest that striatal DA-D2R binding deficits observed in obesity may be driven in part by differences in leptin signaling. Moreover, these results suggest that disturbances in leptin signaling may play a role in other disorders that involve deficits in DA-D2R signaling such as drug addiction, schizophrenia and depression.

FIGURE 1

Figure 1. [^{11}C]raclopride displacement in the dorsal and ventral striatum as assessed using the % change in [^{11}C]raclopride BP between the two scans.

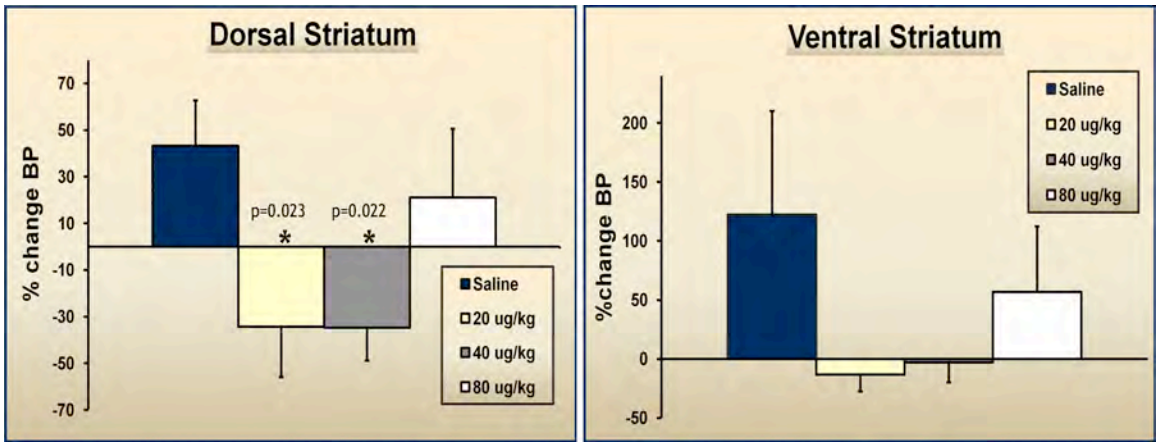

FIGURE 2

Figure 2. [^{11}C]raclopride displacement in the striatum as assessed using the % change in [^{11}C]raclopride BP between the saline and 80 µg/kg leptin scanning sessions correlated with propensity to weight gain as measured using the % change in body weight at 1 and 2 months post scan.

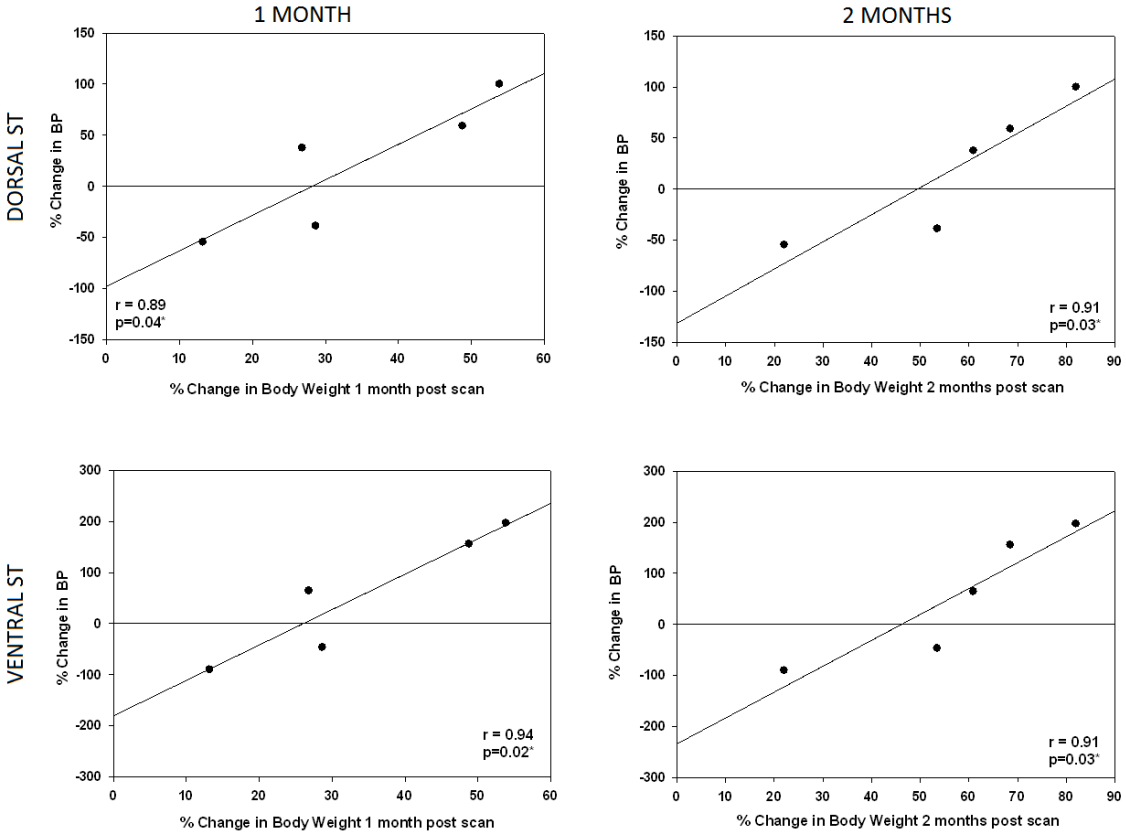

References

1. Berridge, K.C. and T.E. Robinson, *What is the role of dopamine in reward: hedonic impact, reward learning, or incentive salience?* Brain Res Rev, 1998. **28**(3): p. 309-69.
2. Wang, G., et al., *Brain dopamine and obesity.* Lancet, 2001. **357**(9253): p. 354-7.
3. Thanos, P., et al., *Food restriction markedly increases dopamine D2 receptor (D2R) in a rat model of obesity as assessed with in-vivo muPET imaging ([(11)C] raclopride) and in-vitro ([(3)H] spiperone) autoradiography.* Synapse, 2008. **62**(1): p. 50-61.
4. Morris, E.D. and K.K. Yoder, *Positron emission tomography displacement sensitivity: predicting binding potential change for positron emission tomography tracers based on their kinetic characteristics.* J Cereb Blood Flow Metab, 2007. **27**(3): p. 606-17.

Diffusion tensor imaging in OIF/OEF combat veterans with blast-related mild traumatic brain injury with and without PTSD

Effie M. Mitsis, PhD[1, 2], David Carpenter, PhD[1, 3], Daniel Weiner, BA[2], Rachel Shiovitz, BA[1], Gregory Elder, MD[1, 2], Adrian Cristian, MD[1, 2], Charlene Bang, PhD[1, 2], Cheuk Y. Tang, PhD[1, 3], Erin Hazlett, PhD[1, 2]

[1]Mount Sinai School of Medicine, Department of Psychiatry and the Neuroscience PET Laboratory, New York, NY 10029, [2]James J. Peters Veterans Affairs Medical Center, Bronx, NY 10468, [3]Mount Sinai School of Medicine, Department of Radiology and the Imaging Sciences Laboratory, New York, NY 10029

Introduction: Use of *in vivo* measures to understand the mechanisms of brain damage after acute and repeated exposure to blast overpressure is in its infancy. Questions remain regarding whether blast-related TBI (TBI_B) can be characterized as a unique pathophysiological entity. Diffusion tensor imaging (DTI) is a technique that allows examination of the integrity of white matter tracts and holds promise as a sensitive tool in identifying impairment in mild TBI. Tractography analysis was used to examine DTI fractional anisotropy (FA) and mean diffusivity (MD) in subjects with TBI_B as compared to a group of healthy, civilian controls (HC_C).

Methods: Age- and sex-matched, right-handed subjects were veterans with TBI_B (N=10; mean[SD] age = 28.3[6.13]) and HC_C (N=10; mean[SD] age = 28.5[6.22]; 8M/2F, both groups). Veterans were recruited through the Bronx VAMC and were diagnosed with blast-related mild TBI following evaluation by a multi-disciplinary team of clinicians. All imaging was conducted within MSSMs Department of Radiology. PTSD diagnosis was obtained from each veteran's medical record (N=7). TBI_B subjects were on average 3.5 years post-deployment (Range = 1-5 years) and were exposed to primary blast wave. None had a previous head injury prior to participation in the study. Multivariate analysis of covariance (MANCOVA), using PTSD as a covariate, examined group differences in white matter tracts in the right and left pyramidal tracts, inferior longitudinal fasciculus, and cingulum bundle (CB), and the genu and splenium of the corpus callosum. DTI was processed and analyzed by the Image Analysis Core of Mount Sinai School of Medicine. An optimized DTI-tractography algorithm was applied that maximizes accuracy and reproducibility for white matter investigations.

Results and Discussion: Significant increases were found in FA in the TBI_B subjects, as compared to HC_C in right pyramidal tract ($F_{1,18}$= 4.6, p=.045), right CB ($F_{1,18}$=4.5, p=.048) and left CB ($F_{1,18}$=7.40, p=.015). Analysis of MD resulted in significantly decreased diffusivity in the left ILF ($F_{1,18}$=4.68, p=.045) and right CB ($F_{1,18}$=7.25, p=.015).

Conclusion: Findings demonstrate white matter deficiencies in combat veterans with blast-related mild TBI not accounted for by a diagnosis of PTSD. These findings support the hypothesis that blast-related mild TBI represents a unique neurobiological entity.

Table 1. Tractography analysis of fractional anisotropy in white matter tracts in combat veterans with blast-related mild TBI as compared to normal controls.

Brain Region	Controls Mean(SD)	Blast Mean(SD)	*F	p
Right Pyramidal Tract	542.24(19.8)	576.72(29.5)	4.66	.045
Right Cingulum Bundle	535.61(45.1)	584.91(53.7)	4.55	.048
Left Cingulum Bundle	551.12(30.5)	614.26(63.3)	7.40	.015

***Note:** PTSD as a covariate; ILF=Inferior Longitudinal Fasciculus

Table 2. Tractography analysis of mean diffusivity in white matter tracts in combat veterans with blast-related mild TBI as compared to normal controls.

Brain Region	Controls Mean(SD)	Blast Mean(SD)	*F	p
Left ILF	2367.72(99.1)	2260.33(70.5)	4.68	.045
Right Cingulum Bundle	2236.56(67.2)	2150.11(81.6)	7.25	.015

***Note:** PTSD as a covariate; ILF=Inferior Longitudinal Fasciculus

Figure 1. Tractography analysis of brain regions indicating significant differences between combat veterans with blast-related mild TBI and healthy controls

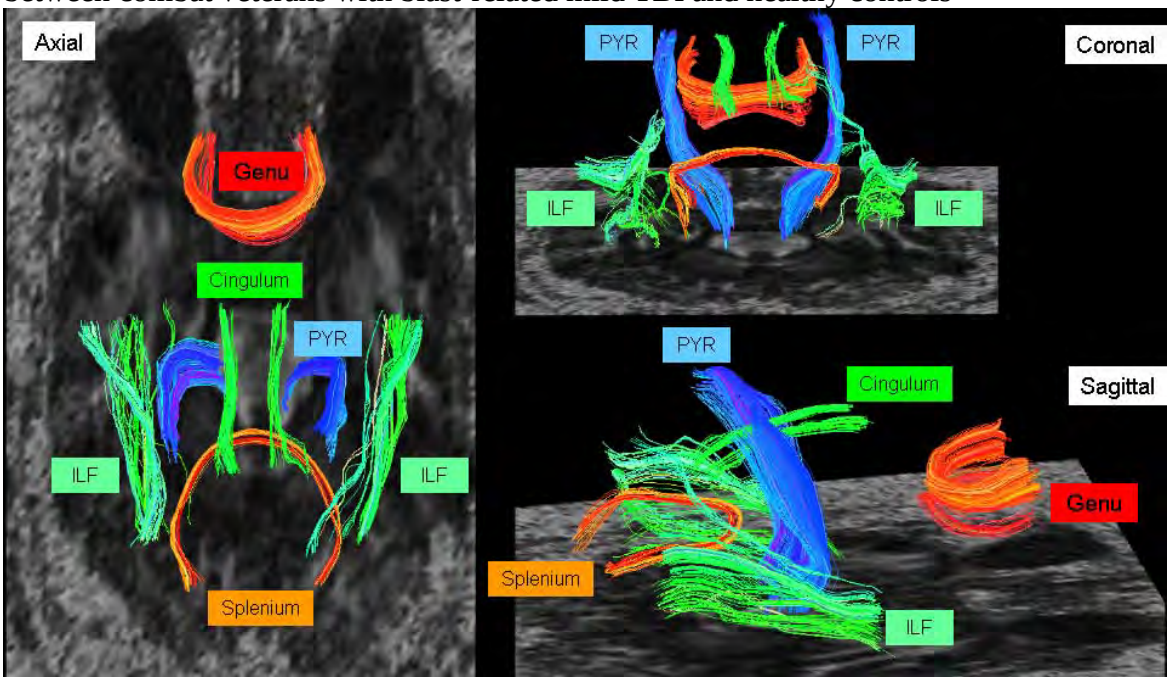

Clinical MR Imaging features of A Murine Model Of Melanoma Brain Metastasis

A. Morsi[1&2], E.B. Voura[2], S. Pun[1], D. M. Hoang[1], A. Baig[1], E. Parker[2], J.G. Golfinos[2] and Y.Z. Wadghiri[1]

Departments of [1]Radiology and [2]Neurosurgery, New York University Medical Center.

troduction: 95% of patients with melanoma brain metastases succumb to their disease within six months of diagnosis. T normal vasculature of these tumors is believed responsible for this poor prognosis by hindering delivery of chemothera d oxygen, crucial for successful radiation therapy. Anti-angiogenic drugs are thought to restore a normal blood supply in t mor (Jain *et al*., 2007). Non-invasively following a reliable murine model of melanoma brain metastasis is crucial to bet derstand the vascular dynamics and to assess the vascular changes induced by anti-angiogenic regimens prior to th aptation to the clinic.

ethods: An intracarotid injection of 10^5 B16-F10 melanoma cells was performed on C57Bl6 mice (Perides *et al.* 200 umorigenesis was followed over 4 weeks with serial MRI scans. The MRI protocol consisted of acquiring (150-µn solution 3D brain datasets of contrast agent-free pre-T2 weighted RARE (30-min) to delineate the endogenous effect ema from the tumor and both pre-T1 weighted (T1-w, 15-min) and pre-T2* weighted datasets (30-min)to map the presen melanin. Subsequent to a femoral injection of Gd Magnevist representing a clinical double dose (120 µl of 50 µM dDTPA per 30 g mouse weight), a post-T1-w sequence (15-min) was acquired to monitor the presence of leakage.

esults: 100% of the tumors identified were ventricular or leptomeningeal and not parenchymal as observed clinically (1a, nfirming reports by Fiddler *et al*. (1999). Even so, MRI studies conducted using this model displayed characteristic clini diological findings (Gaviani *et al.*, 2006): edema on T2RARE (2a), T1 brightening from melanin without contrast (2b) a elanin susceptibility effect on T2* (2c), as well as increased T1 brightening with contrast agent denoting leakage (2d). C MRI technique also provided accurate longitudinal assessment of growth rates and volumetric changes (2e,f,).

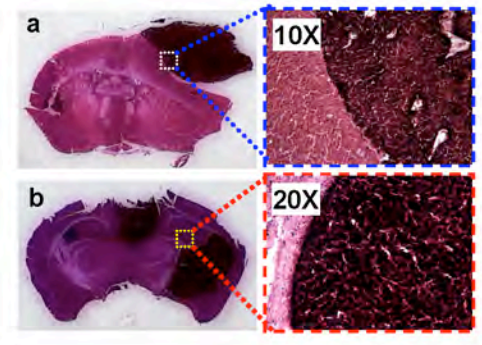

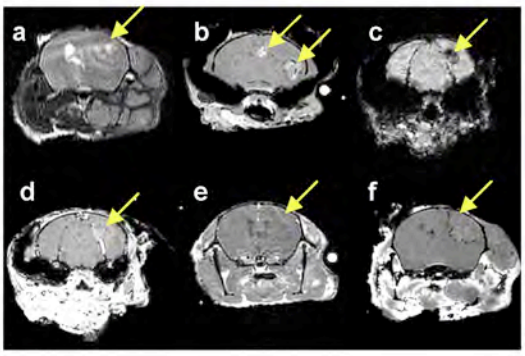

Figure 1: **Histological features of murine melanoma brain metastasis. (a)** Meningeal growth with distinct molecular layer (no evidence of cellular infiltration). **(b)**Intraventricular growth not infiltrating ependymal cell lining.

Figure 2: **Imaging features of melanoma brain metastasis**
(a)*Edema* using T2-RARE; **(b)** Melanin T1-brightening **(c)** Melanin T2* darkening **(d)** Leakage using contrast agent T1-brightening **(e-f)** Longitudinal monitoring of tumor growth.

onclusion: Our µMRI analyses are reminiscent of clinical radiological findings of melanoma brain metastasis and show th MRI is a valuable tool to monitor metastatic brain tumorigenesis. The dynamic tumor morphometry observed using c ngitudinal studies provided an accurate assessment of tumor size during tumorigenesis - an improvement over conventio ngle end point analyses using histology.

eferences:

dler , *et al.*, *The biology of melanoma brain metastasis.* Cancer and Metastasis Reviews 18:387-400(1999);
aviani *et al.*, *Improved Detection of Metastatic Melanoma by T2*-Weighted Imaging*. American Journal Neuroradiolo :605– 08(2006);**Jain , *et al.***,*Angiogenesis in brain tumors*. Nature 8: 610-622(2007); **Perides *et al.***,*The fibrinolytic syste cilitates tumor cell migration across the blood-brain barrier in experimental melanoma brain met astasis*. BMC Cancer 6: 006)

Reduced Ventral Striatal/Ventral Pallidum Serotonin$_{1B}$ Receptor Binding Potential in Major Depressive Disorder

James W. Murrough[1], Shannan Henry[2], Jian Hu[2], Jean-Dominique Gallezot[3] Beata Planeta-Wilson[3] John F. Neumaier[4], Alexander Neumeister[1,2]

[1]Mood and Anxiety Disorders Program, Department of Psychiatry, Mount Sinai School of Medicine, New York, NY
[2]Molecular Imaging Program, Clinical Neurosciences Division, VA National Center for PTSD, VA Connecticut Healthcare System, West Haven, CT
[3]Positron Emission Tomography Center, Department of Diagnostic Radiology, Yale University School of Medicine, New Haven, CT
[4]Department of Psychiatry, University of Washington, Seattle, WA

Introduction: Although abnormal serotonin (5-HT) function is convincingly implicated in the pathophysiology of major depressive disorder (MDD), the precise nature of this dysfunction continues to remain elusive (1,2). Rigorous research focusing on the role of specific 5-HT receptor subtypes and functional consequences of receptor anatomical localization may provide new insight into the mechanisms of MDD. Towards this end, emerging preclinical research suggests an important role for the 5-HT$_{1B}$ receptor subtype in behavioral regulation and depressive phenotypes (3). In particular, 5-HT$_{1B}$ receptor expression is decreased in an animal model of depression and p11, an important intracellular protein involved in 5-HT$_{1B}$ signaling, is decreased in post-mortem brains of depressed patients (4). The 5-HT$_{1B}$ receptor is found primarily as presynaptic terminal auto- and hetero-receptors, with particularly high densities occurring in the striatum and pallidum. 5-HT$_{1B}$ heteroreceptors located within the striatum have been shown specifically to play an essential role in antidepressant action (5). The aim of the current study was to determine 5-HT$_{1B}$ receptor function in the region of the ventral striatum/ventral pallidum (VS/VP) in MDD using positron emission tomography (PET) and the selective 5-HT$_{1B}$ receptor radioligand [^{11}C]P943. Based on preclinical data, we hypothesized that MDD would be characterized by reduced [^{11}C]P943 binding in the region of interest (ROI).

Methods: Ten participants with MDD (30.8±9.5 yrs, 5 male/5 female) in a current major depressive episode and 10 matched healthy control participants (30.7±10.5 yrs, 5 male/5 female) participated in this study. PET scans were acquired for 120 minutes at rest using a single intravenous injection of high-specific activity [^{11}C]P943 (6) on an HRRT PET scanner (207 slices, resolution less than 3 mm full-width at half-maximum in 3D acquisition mode). The VS/VP ROI was taken from the template for SPM2 and applied to the PET data to produce time-activity curves in reference to the cerebellum.

Results and Discussion: Within the VS/VP ROI, [^{11}C]P943 BP_{ND} was significantly reduced in the MDD group compared to the healthy control group (1.37±0.13 and 1.68±0.16, respectively; 18.7% between-group difference; $p<0.001$) (Fig. 1). Consistent with preclinical and postmortem data, our findings suggest abnormally reduced function of

VS/VP 5-HT_{1B} receptors in humans with MDD. This result may be particularly pertinent to the pathophysiology of MDD given the prominent role of this region in neurocircuitry models of depression (7). Abnormal 5-HT_{1B} heteroreceptor function may contribute to dysfunctional reward signaling within the striatum and nucleus acumens via interaction with dopamine, γ-amino-butyric acid or glutamate systems. In support of this hypothesis, the antidepressant effects of a 5-HT_{1B} agonist were found to specifically depend on 5-HT_{1B} heteroreceptor on non-serotoninergic neurons, and an antidepressant effect of a 5-HT_{1B} agonist was found when infused directly into the caudate and putamen, but not when infused into other brain regions (5).

Conclusions: Our findings suggest reduced 5-HT_{1B} receptor signaling in the VS/VP in MDD and contribute to the therapeutic rationale for testing 5-HT_{1B} agonists as a novel class of antidepressants.

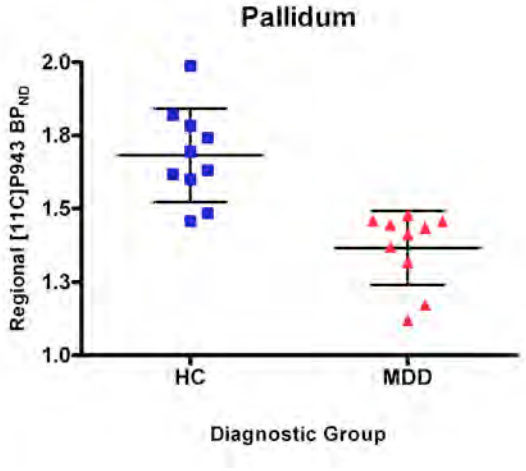

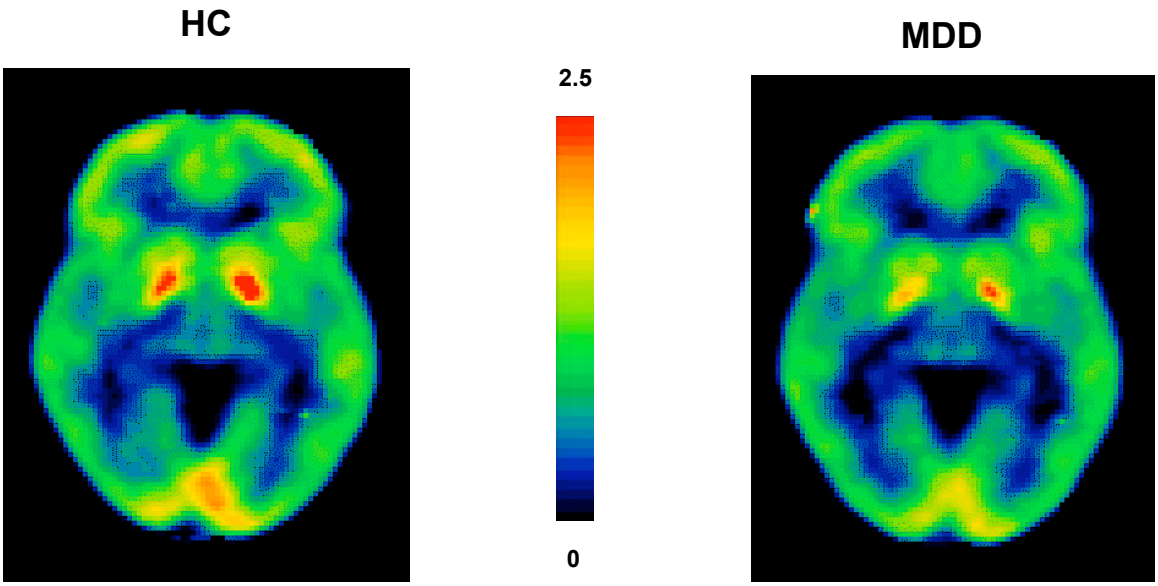

Figure 1. Upper panel: plot showing significant differences in ventral striatum/ventral pallidum (VS/VP) region of interest [^{11}C]P943 binding potential (BP_{ND}) between patients with major depressive disorder (MDD) and healthy control subjects (HC). Lower panel: average [^{11}C]P943 BP_{ND} co-registered positron emission tomography images illustrate reduced VS/VP [^{11}C]P943 BP_{ND} in MDD (right) relative to HC (left).

References

1. Jans LA, Riedel WJ, Markus CR, Blokland A: Serotonergic vulnerability and depression: Assumptions, experimental evidence and implications. Mol Psychiatry 2007; 12:522-543
2. Belmaker RH, Agam G: Major depressive disorder. N Engl J Med 2008; 358:55-68
3. Sari Y: Serotonin1B receptors: From protein to physiological function and behavior. Neurosci Biobehav Rev 2004; 28:565-582
4. Svenningsson P, Chergui K, Rachleff I, Flajolet M, Zhang X, El Yacoubi M, Vaugeois JM, Nomikos GG, Greengard P: Alterations in 5-HT1B receptor function by p11 in depression-like states. Science 2006; 311:77-80
5. Chenu F, David DJ, Leroux-Nicollet I, Le Maitre E, Gardier AM, Bourin M: Serotonin1B heteroreceptor activation induces an antidepressant-like effect in mice with an alteration of the serotonergic system. J Psychiatry Neurosci 2008; 33:541-550
6. Nabulsi N, Huang Y, Weinzimmer D, Ropchan J, Frost JJ, McCarthy T, Carson RE, Ding YS: High-resolution imaging of brain 5-HT 1B receptors in the rhesus monkey using [11C]P943. Nucl Med Biol 2010; 37:205-214
7. Krishnan V, Nestler EJ: The molecular neurobiology of depression. Nature 2008; 455:894-902

Emotional Dysregulation in ALS Patients: an fMRI study of Pre-Frontal and Occipital Neural Dysfunction during Visual Emotional Stimulus Processing

Ritesh Ramdhani MD, Michael E Silverman PhD, Dale Lange MD,
Mark Sivak MD, Ji-Yeoun Yoo MD, Thomas Naidich MD, Martin A Goldstein MD
Departments of Neurology and Neuroradiology
Mount Sinai School of Medicine
New York, NY USA

Introduction

Extensive behavioral[1], neurophysiologic[2], and functional imaging data[3] suggest that ALS can be complicated by neuropsychological dysfunction. While it has long been recognized that a type of fronto-temporal lobar dementia (FTLD) can complicate a minority of both sporadic and familial ALS (so called FTLD-motor neuron disease), a more significant number manifest clinically-significant behavioral dysfunction, especially regarding emotional dysregulation (e.g., pseudobulbar affect)[4]. Prior studies have attributed the majority of non-demented ALS cognitive impairment to executive dysfunction, presumably secondary to ALS-related prefrontal cortex involvement[5]. However, the precise neural substrates of ALS-related neurobehavioral dysregulation have not been well-characterized. Therefore, the objective of this study was to better elucidate the neural mechanisms mediating ALS-related neuropsychological dysfunction.

Methods

11 non-demented ALS patients and 11 healthy comparison subjects, all right-handed, participated after providing informed consent in a protocol approved by the Institutional Review Board of the Mount Sinai School of Medicine. We developed a novel neuropsychological visual *Go/No-Go* activation paradigm, aimed to specifically probe aberrant emotional regulation and consequent executive dyscontrol in ALS subjects compared to age- and gender-matched healthy comparison subjects. The neuropsychological activation task involved serial presentation of emotionally-valenced images in a tilted or non-tilted manner. Discrimination of the tilt/non-tilt attribute formed the basis of index finger *Go/No-Go* response selection: subjects were instructed to button press (or withhold button press) in response to tilted (or non-tilted) stimulus. Image stimuli consisted of positive, neutral and negative selections from the International Affective Picture System (Lang et al 2005). All image presentations were counterbalanced for valance type and level of arousal (high/low), as well as presentation as a *Go* or *No-Go* signal. Task performance was concurrent with gradient EPI-BOLD fMR image acquisition. FSL software was employed for image analysis with an initial threshold of $p<.01$. Present study focused on differential neural responsivity to high vs. low arousal stimuli.

Results and Discussion

fMR image interaction contrast analysis of [Normals vs. Patients] x [HighArousalStimuli vs. LowArousalStim] revealed greater neural activity in a distributed fronto-striatal neural network including anterior cingulate, superior medial frontal, right superior frontal, and bilateral caudate regions. Occipital visual regions also revealed increased activity in normal subjects relative to ALS patients (despite identical visual stimuli), suggesting aberrant pre-potentiation of emotional visual stimulus processing. Thus, non-demented ALS subjects demonstrated relatively reduced fronto-striatal function while processing highly-arousing visual stimuli. This network suggests a prefrontally-based potential neural substrate for top-down emotional regulatory failure in ALS, plausibly contributing to clinical features of ALS-related behavioral dyscontrol, including pseudobulbar affect.

Conclusion

Relative to matched normal control subjects, ALS patients demonstrate reduced recruitment of a distributed fronto-striatal neural network while processing emotionally-charged visual stimuli. They further revealed, relative to normals, aberrant potentiation of visual cortical processing of emotional visual stimuli. These findings offer potential mechanistic insight into disinhibitory

behavior in ALS patients, including pathologic laughing and crying (PLC) dysproportionate to environmental context.

FIGURE 1

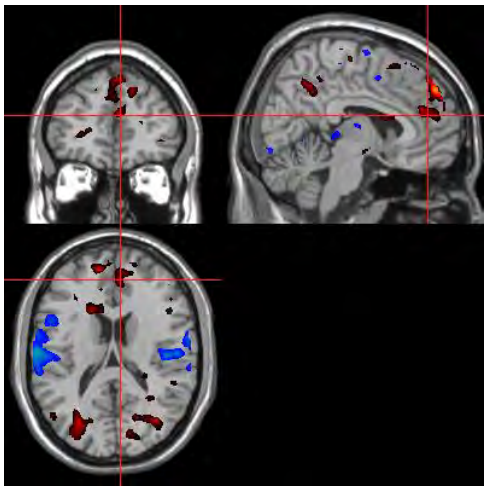

Figure 1: Statistical parametric map of interaction contrast [Normals vs. Patients] x [HighArousalStim vs. LowArousalStim] revealing increased BOLD response in anterior cingulate (as well as frontal and occipital regions) in normal subjects relative to ALS patients.

FIGURE 2

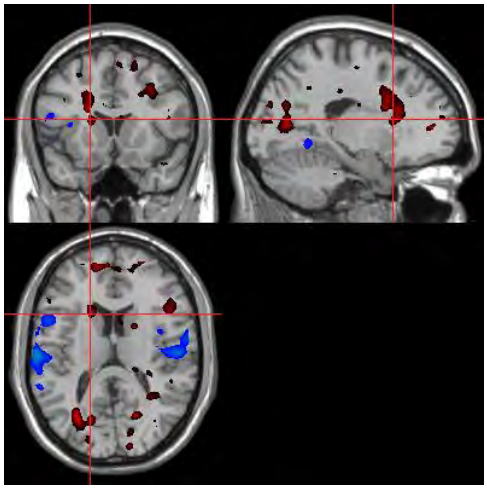

Figure 2: Statistical parametric map of interaction contrast [Normals vs. Patients] x [HighArousalStim vs. LowArousalStim] revealing increased BOLD response in caudate (as well as frontal and occipital regions) in normal subjects relative to ALS patients.

References

1. Murphy JM, Henry RG, Langmore S et al. (2007) Continuum of frontal lobe impairment in ALS. *Arch Neurol* 64:530-34.

2. Hanagasi HA, Gurvit IH, Ermutlu N et al. (2002) Cognitive impairment in ALS: evidence from neuropsychological investigation and event-related potentials. *Cognitive Brain Research* 14:234-44.

3. Abrahams S, Goldstein LH, Simmons A et al (2004) Word retrieval in ALS: a functional magnetic resonance study. *Brain* 127:1507-17.

4. Massman PJ, Sims J, Cooke N et al. (1996) Prevalence and correlates of neuropsychological deficits in ALS. *J Neurol Neurosurg Psychiatry* 61:450-5.

5. Neary D, Snowden JS, Mann DMA (2000) Cognitive change in motor neuron disease / amyotrophic lateral sclerosis. *Journal of the Neurological Sciences* 180:15-20.

Dendritic spines contacting multisynaptic boutons share spatial and morphological similarity

James E. Reilly[1], Hugo H. Hanson[1], Mónica Fernández-Monreal[1], Alfredo Rodriguez[1,2], Erik B. Bloss[1], William G. Janssen[1], Susan L. Wearne[1,2], Patrick R. Hof[1,2], Greg R. Phillips[1]
Fishberg Department of Neuroscience[1] and Computational Neurobiology and Imaging Center[2]
Mount Sinai School of Medicine, One Gustave L. Levy Place, Box 1065, New York, NY 10029

Introduction

Excitatory presynaptic boutons contacting multiple postsynaptic specializations are termed multisynaptic boutons (MSBs). The number of MSB synapses as a percentage of all synapses increases with synaptogenic stimuli. Newly grown spines usually contact MSBs rather than single-synaptic boutons (SSBs). How MSBs might feature in synaptic development has yet to be determined.

Methods

We imaged GFP filled cultured neurons by confocal laser-scanning microscopy (CLSM) then used correlative light and electron microscopy (CLEM) to verify MSB-contacting spine pairs. We evaluated four criteria for MSB spine pairs compared to control pairs: spine head distance, spine orientation, spine head volume, and spine type. All spine parameters except orientation were evaluated automatically in NeuronStudio using 3-dimensional dendritic reconstructions.

Results and Discussion

MSB profiles exist in cultured hippocampal neurons to a degree comparable to that reported for MSB synapses *in vivo*. In our cultured neurons, the number of immunolabeled MSB profiles as a percentage of all synaptic profiles remained relatively constant over time. Compared to control spine pairs, MSB-contacting spine pairs were approximately 30% closer to each other, more frequently angled towards each other, had more similar head volumes, and were more likely to be mushroom spines.

Conclusion

The similarity in spine volume and type for MSB spine pairs is consistent with the notion that synaptic stimulation is a primary influence on spine morphology.

References

Rodriguez A, Ehlenberger DB, Hof PR, Wearne SL. 2006. Rayburst sampling, an algorithm for automated three-dimensional shape analysis from laser scanning microscopy images. Nature Protocols 1(4):2152-2161.

Rodriguez A, Ehlenberger DB, Dickstein DL, Hof PR, Wearne SL. 2008. Automated three dimensional detection and shape classification of dendritic spines from fluorescence microscopy images. PLoS ONE 3(4):e1997.

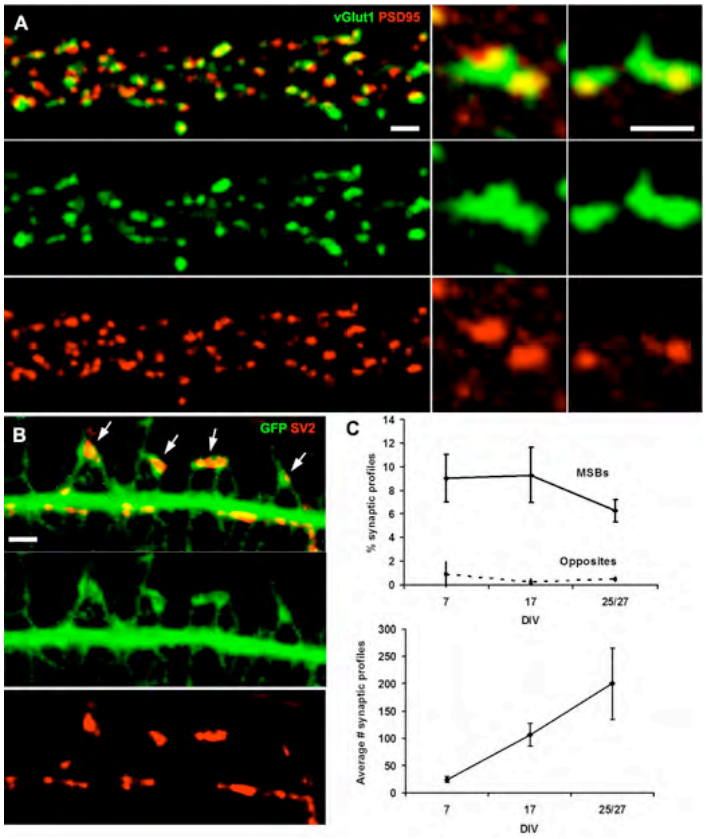

Figure 1. Immunolabeled MSB profiles in cultured neurons. (A) CLSM z-stack projection of a dendritic segment with fluorescently immunolabeled vGlut1 (green) and PSD95 (red). Enlarged examples of MSB and SSB profiles are at right. Scale bars are 2 μm for left panels and 0.5 μm for right panels. (B) CLSM z-stack projection of a dendritic segment from a GFP-transfected neuron (green) with fluorescently immunolabeled SV2 (red). Arrows point to MSB profiles of SV2 puncta in contact with multiple GFP-filled spines. Scale bar is 2 μm. (C, top) Number of immunolabeled vGlut1 and PSD95 MSB profiles per neuron as a percentage of all synaptic profiles per neuron with increasing time in culture. Neurons at 25 and 27 DIV were counted together as a single time point. "Opposite" is the number of opposite MSBs (i.e., PSD95 puncta in contact with multiple vGlut1 puncta) as a percentage of all synaptic profiles. (Bottom) Average number of immunolabeled vGlut1 and PSD95 synaptic profiles per neuron with increasing time in culture. Neurons at 25 and 27 DIV were counted together as a single time point.

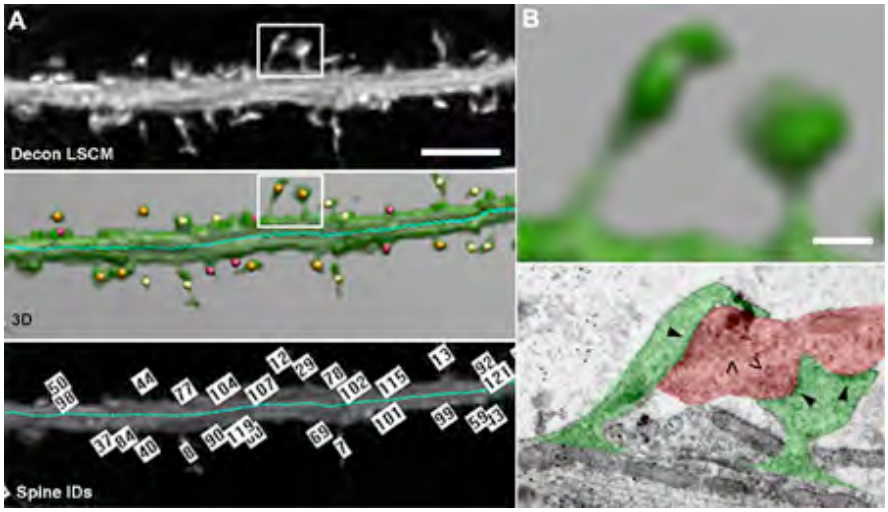

Figure 2. CLSM spine detection and CLEM verification of MSB-contacting spines. (A, top) Deconvolved CLSM z-stack projection of dendritic segment. CLEM-verified MSB-contacting spines are boxed. Scale bar is 2 μm. (Middle) NeuronStudio 3D rendering of the z-stack. The thin blue line runs along the dendrite automatically traced by NeuronStudio. The colored dots indicate spines automatically detected, measured, and classified by type in NeuronStudio. Mushroom spines get orange dots, thin yellow, and stubby red. (Bottom) Same CLSM z-stack projection showing NeuronStudio spine identification numbers. (B, top) NeuronStudio 3D rendering of CLEM-verified MSB-contacting spines boxed in (A, top and middle). Scale bar is 0.5 μm. (Bottom) Single section EM of the MSB-contacting spines. Bouton is shaded red and spines green. Arrowheads point to postsynaptic densities. Carets point to presynaptic vesicles.

Diffusion tensor anisotropy in the cingulate gyrus in schizophrenia

Devorah Segal[1], M. Mehmet Haznedar[2], Erin A. Hazlett[2], Jonathan J. Entis[2], Randall E. Newmark[2], Yuliya Torosjan[2], Jason S. Schneiderman[2], Joseph Friedman[2], King-Wai Chu[2], Cheuk Y. Tang[3], Patrick R. Hof[1]

Departments of [1]Neuroscience, [2]Psychiatry, and [3]Radiology, Mount Sinai School of Medicine, New York, NY 10029.

Introduction

It has been proposed that schizophrenia results partly from altered brain connectivity. The anterior cingulate cortex in particular has been demonstrated to be affected in schizophrenia, with studies reporting reduced volume, altered neuronal arrangement, decreased anisotropy in diffusion tensor images, and hypometabolism.

Methods

We used a 3T Siemens scanner to acquire structural and diffusion tensor imaging in age- and sex-matched groups of 41 adults with chronic schizophrenia, 6 adults with recent-onset schizophrenia, and 38 healthy control subjects. We manually traced the anterior and posterior cingulate gyri on all subjects and then compared the volume and anisotropy across groups for the left and right anterior and posterior cingulate gyri. The anterior cingulate gyrus was divided axially into six equal segments, and the posterior cingulate gyrus into two segments. Volume was calculated for the anterior and posterior gyri, and average anisotropy was then calculated for each individual segment, looking separately at gray and white matter.

Results and Discussion

We found decreased overall relative left and right gray matter volume in the anterior cingulate gyrus in persons with schizophrenia compared with healthy controls. Additionally, in both gray and white matter of the cingulate, we found that recent-onset patients had the highest anisotropy, chronic patients had the lowest, and controls were intermediate.

Conclusion

Our results provide additional evidence for the presence of both white and gray matter abnormalities in the cingulate gyrus, which has been implicated in schizophrenia.

Cingulum bundle white matter in MAG-knockout mice

Devorah Segal[1], David Carpenter[2], Vahram Haroutunian[3], Cheuk Y. Tang[2, 3], Patrick R. Hof[1]

Departments of [1]Neuroscience, [2]Radiology, and [3]Psychiatry, Mount Sinai School of Medicine, New York, NY 10029.

Introduction

White matter dysfunction is has become a focus of schizophrenia research. Myelin associated glycoprotein (MAG), along with other oligodendrocyte-derived genes, has been found to have lower expression levels in schizophrenia, and several measures of white matter integrity have been found to be abnormal in schizophrenia. Abnormalities have specifically been noted in the anterior cingulate gyrus, among other regions.

Methods

In this study, we looked at mice lacking the MAG gene as a potential model of dysmyelination. Using 16 mice (9 knockouts and 7 controls), we used the stereological "Space Balls" method to estimate myelinated fiber length density in the adult mouse cingulum bundle. We also performed diffusion anisotropy imaging in the same animals and an additional MAG-knockout mouse. We measured fractional anisotropy in a region of the cingulum bundle and compared across genotype.

Results and Discussion

We found no differences in cingulum myelinated fiber length density between the two groups, although we did note an age-related decrease regardless of genotype. No differences were noted in FA measurements between the two groups, but an age-related decrease was noted as well.

Conclusion

We failed to find a difference in either myelinated fiber length density or diffusion anisotropy in the cingulum bundle of MAG-knockout mice compared to wildtype controls. These measures are not, therefore, affected by the dysmyelination resulting from a lack of MAG. Our finding of decreases in both these measures with increasing age, however, suggests a correspondence between these two investigational methods.

Neuroimaging Negative Emotion in Postpartum Depression; Identifying A Unique Phenotype of Depression.

Michael E. Silverman[1], Holly Loudon[2], Xun Liu[1], Casey Mauro[1], Martin A. Goldstein[3]

1. Mount Sinai School of Medicine, Department of Psychiatry
2. Mount Sinai School of Medicine, Department of Obstetrics, Gynecology and Reproductive Science
3. Mount Sinai School of Medicine, Department of Neurology

Introduction:

Postpartum depression (PPD) is a potentially catastrophic condition that follows pregnancy, affecting both the mother and the newborn. With a reported prevalence between 13-22%[1,2] PPD is the most common complication of childbearing. Behaviorally similar in presentation to major depression (MDD)[3], specific differences in the clinical presentation of PPD have been identified.[4,5] As a result, its classification as a specifier of MDD continues to be questioned.[6,7]

Over the past decade neuroimaging research has revealed much about the functional organization of the brain in depression. Among the brain structures consistently showing abnormalities of function in depressed patients is the amygdala, a cortical structure recognized as a critical processing area in both normal and pathological emotional responses. [8] While the heterogeneity between and within samples has made interpretation of overall findings difficult,[9] the overwhelming majority of findings associated with the amygdala in depressed subjects involve increased baseline cerebral blood flow and metabolism in comparison with healthy controls during the resting period.[10,11,12]

We hypothesized that women with PPD would demonstrate increased activity in the amygdala in response to negative linguistic stimuli with threat content compared to asymptomatic postpartum control subjects. Such a finding would be consistent with the majority of fMRI reports of MDD.

Methods

17 postpartum women were presented with emotionally valenced word probes, within an integrated gradient echo planar imaging - blood oxygen level dependent (EPI-BOLD) fMRI protocol 6-8 weeks postpartum. Correlational analyses were conducted to determine the association between amygdala activity to the presentation of negative stimuli and PPD symptomatology.

Results and Discussion

BOLD response for threat words in the right amygdala was moderately correlated (negative) with severity of PPD symptoms, (x,y,z: 19,6,–15; r=-.536, two-tailed $p_{corr} \leq .027$) in that subjects reporting fewer PPD symptoms demonstrated greater responsivity to linguistic stimuli with negatively-valenced threat content compared to those with greater symptomotology (Figure 1). While a weak relationship

between BOLD response and threat related stimuli was revealed in analyses of the left amygdala, this difference was not statistically significant (r=-.403, two-tailed p_{corr}=n.s.).

In order to further confirm the specificity of amygdala responsivity to threat stimuli associated with PPD symptoms, ROI analyses of *threat vs neutral stimuli* and *negative vs neutral stimuli* in relation to EPDS scores were conducted. Correlation coefficients of the pairwise comparisons between the differential BOLD signal for the *threat vs. neutral* and *negative vs. neutral* contrasts with PPD symptoms revealed significant differences in the *threat vs neutral* contrast (r=-.474, p<.027; Figure 2), but not the *negative vs neutral* contrast (r=-.043, n.s.).

Conclusion

Contemporary diagnostic nosology considers PPD to be a specifier of a MDD. The primary novelty of this study relies on the attempt to identify changes in amygdalar activity specifically associated with PPD. The key finding was that unmedicated postpartum women expressing significant depressive symptoms failed to activate right amygdala regions in response to threat-related linguistic stimuli relative to healthy postpartum comparison subjects – **a pattern distinct from cerebral responsivity generally associated with MDD** – which may point to PPD being a unique phenotype of depression.

FIGURE 1

Figure 1. Scatter plot of the Edinburgh Postnatal Depression Scale (EPDS) total score over mean BOLD response at the maxima of the right amygdale (x, y, z; 19, 6, −15) in the threat condition showing a substantial relationship (r=-.536, $p_{corr} \leq .027$ two-tailed) between the lack of postpartum depressive symptoms and increased amygdala activation.

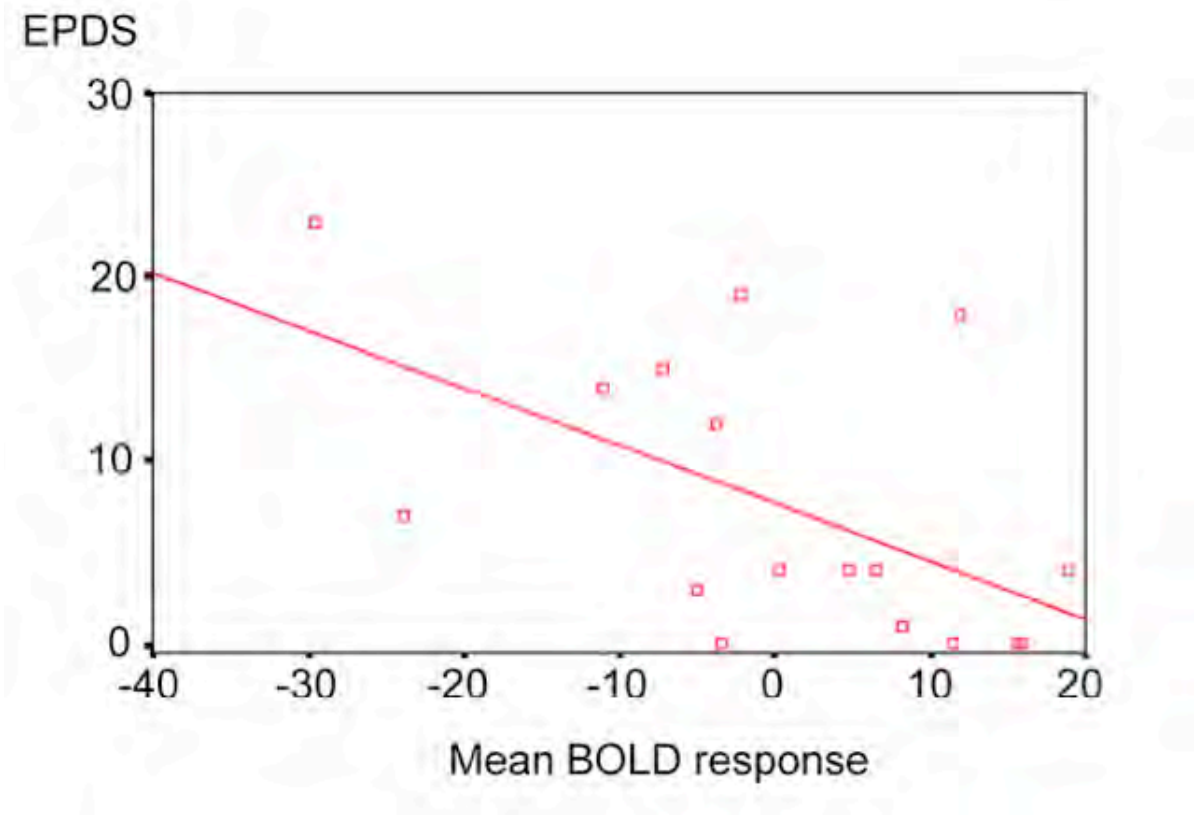

FIGURE 2

Figure 2: Statistical map for the contrast of threat v neutral stimuli demonstrating differences in BOLD response in the right amygdala associated with PPD symptomology as measured by the overall EPDS score (P<.05, uncorrected for visualization).

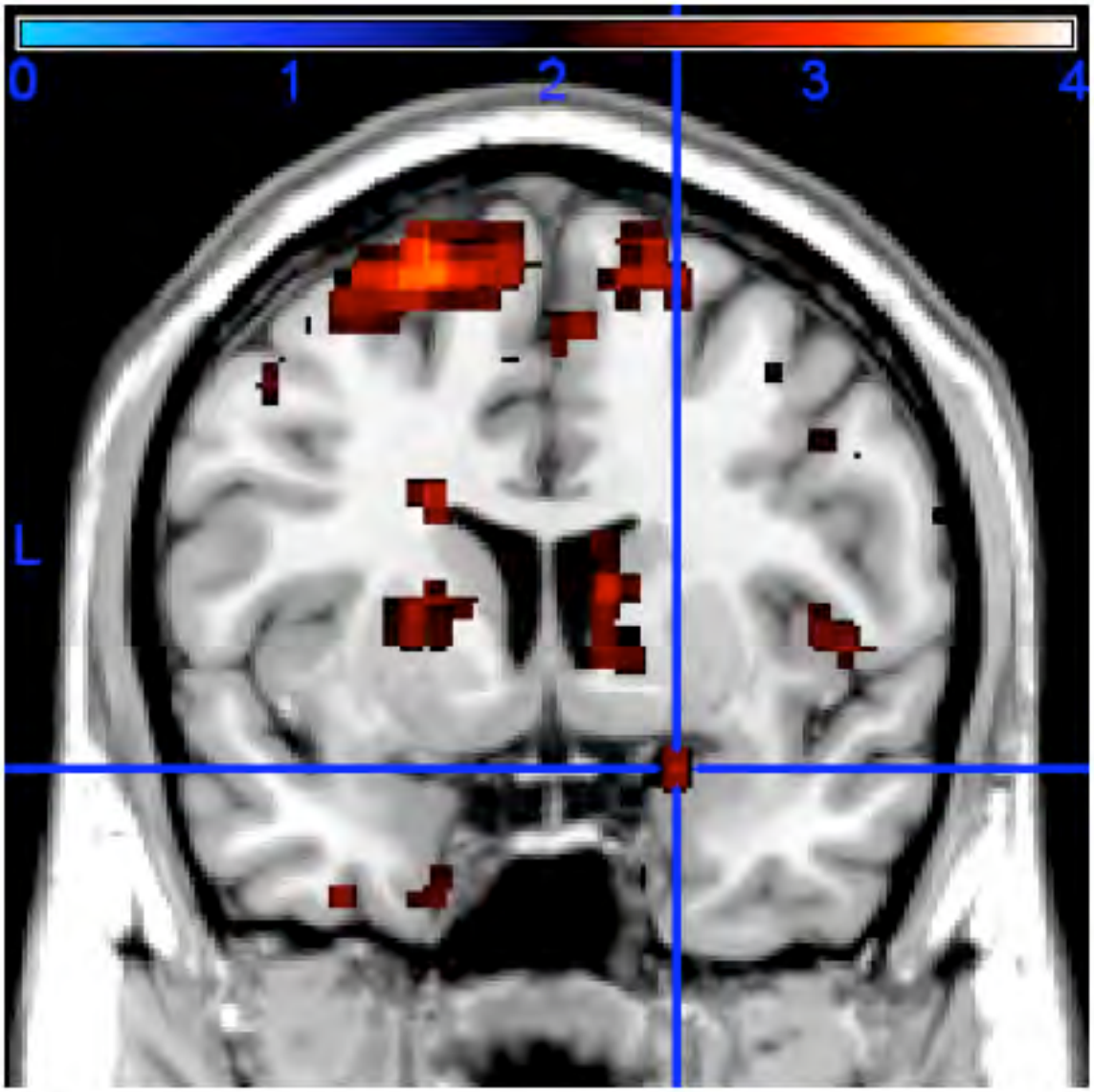

References

1. Centers for Disease Control and Prevention. Prevalence of Self-Reported Postpartum Depressive Symptoms - 17 States, 2004-2005. *Morbidity & Mortality Weekly Report (MMWR)* 2008;57:361-366.

2. Wisner K, Parry BL, Piontek CM. Postpartum Depression. *N Engl J Med* 2003;347:194-199.

3. Bernstein IH, Rush AJ, Yonkers K, Carmody TJ, Woo A, McConnell K, et al. Symptom Features Of Postpartum Depression: Are They Distinct? *Depress Anxiety* 2008; 25:20–26.

4. Lonstein JS. Regulation of anxiety during the postpartum period. *Frontiers in Neuroendocrinology* 2007;28:115–141.

5. Cooper C, Jones L, Dunn E, Forty L, Haque S, Oyebode F, et al. Clinical presentation of postnatal and non-postnatal depressive episodes. *Psychological Medicine* 2007;37:1273–1280.

6. Jolley SN, Betrus P. Comparing postpartum depression and major depressive disorder: issues in assessment. *Issues Ment Health Nurs* 2007;28:765-80.

7. Silverman ME, Loudon H, Safier M, Protopopescu X, Leiter G, Goldstein M. Neural dysfunction in postpartum depression: An fMRI pilot study. *CNS Spectrums* 2007;12:853-862.

8. Phillips ML, Drevets WC, Rauch SL, Lane R. Neurobiology of emotion perception II: implications for major psychiatric disorders. *Biol Psychiatry* 2003;54:515–528.

9. Drevets W. Neuroimaging and neuropathological studies of depression: implications for the cognitive-emotional features of mood disorders. *Curr Opin Neurobiology* 2001;11:240-249

10. Drevets W. A functional anatomical study of unipolar depression. *J Neurosci* 1992;12:3628-3641

11. Drevets WC, Bogers W, Raichle ME. Functional anatomical correlates of antidepressant drug treatment assessed using PET measures of regional glucose metabolism. *Eur Neuropsychopharm* 2002;12:527-544.

12. Siegle GJ, Konecky RO, Thase ME, Carter CS. Relationships between amygdala volume and activity during emotional information processing tasks in depressed and never depressed individuals: An fMRI investigation. *Ann. N.Y. Acad. Sci*. 2003;985:481-484.

Resting state connectivity of the laryngeal motor cortex in humans

Kristina Simonyan[1] and Barry Horwitz[2]

[1]Departments of Neurology and Otolaryngology, Mount Sinai School of Medicine, [2]National Institute on Deafness and Other Communication Disorders, National Institutes of Health

Introduction

The larynx region of the motor cortex in humans is indispensible for the control of voluntary voice production. Patients with bilateral lesions in this region are unable to speak and sing (Jürgens, 2002). Despite its high importance in voluntary voice production, the literature on the central organization of the laryngeal motor cortex in humans is sparse (Brown et al., 2008, Loucks et al., 2007, Olthoff et al., 2008, Simonyan et al., 2007). We recently identified the structural and functional motor cortical networks underlying voluntary voice and breathing production in healthy humans (Simonyan et al., 2009). Functional connectivity of the laryngeal motor cortex during both tasks largely reflected its structural connectivity; however, a prominent difference between these networks was the pronounced left-hemispheric laterality during voice production compared to bilaterally distributed networks during breathing. The aim of this study was to identify whether the resting state connectivity of the laryngeal motor cortex would comprise brain regions involved in the functional and structural networks of voluntary voice and breathing production.

Methods

Twelve healthy right-handed monolingual English-speaking subjects (mean 54.6 years old) participated in the study. Subjects rested in the scanner with their eyes closed. Whole-brain images were acquired on a 3T GE Signa scanner (TR = 2 s, TE = 30 ms, FOV = 240mm, slice thickness 4mm, 33 sagittal slices). Data pre-processing in AFNI included corrections for motion, physiological noise and slice timing, low-pass filtering and normalization to Talairach-Tournoux space. Resting state correlation maps were generated by extracting time courses from the bilateral seed regions in the ventral primary motor cortex (area 4p), which were identified in our previous study as the local activation maxima for voluntary voice and controlled breathing production. Correlation coefficients were calculated between seed time courses and each brain voxel, averaged across subjects and thresholded at corrected $p \leq 0.05$. ROI analyses examined hemispheric lateralization of the resting state networks during each task ($p \leq 0.0125$).

Results and Discussion

Resting state networks of the laryngeal motor cortex associated with the activation maxima for both voluntary voice and controlled breathing production exhibited significant bilateral correlations with the laryngeal/orofacial and trunkal regions of the primary motor and sensory cortex, premotor cortex, including SMA, inferior frontal gyrus, insula, parietal operculum, superior/medial temporal, angular and supramarginal gyri, cingulate cortex, precuneus, occipital cortex, putamen, caudate nucleus, thalamus, and cerebellum *(Fig. 1)*. Resting networks associated with both tasks showed right-hemispheric lateralization (all $p < 0.0005$), but did not differ significantly between the tasks.

Conclusion

Strong correlations of the laryngeal motor cortex during the resting state were established with the same brain regions involved in the structural and functional networks of this region during both voluntary voice and controlled breathing production. When combined with our previous results (Simonyan et al., 2009), our findings suggest that only the functional laryngeal motor cortical networks associated with highly learned laryngeal behavior (e.g., voluntary voice production) have distinct organization from the structural and resting networks of this region in healthy humans.

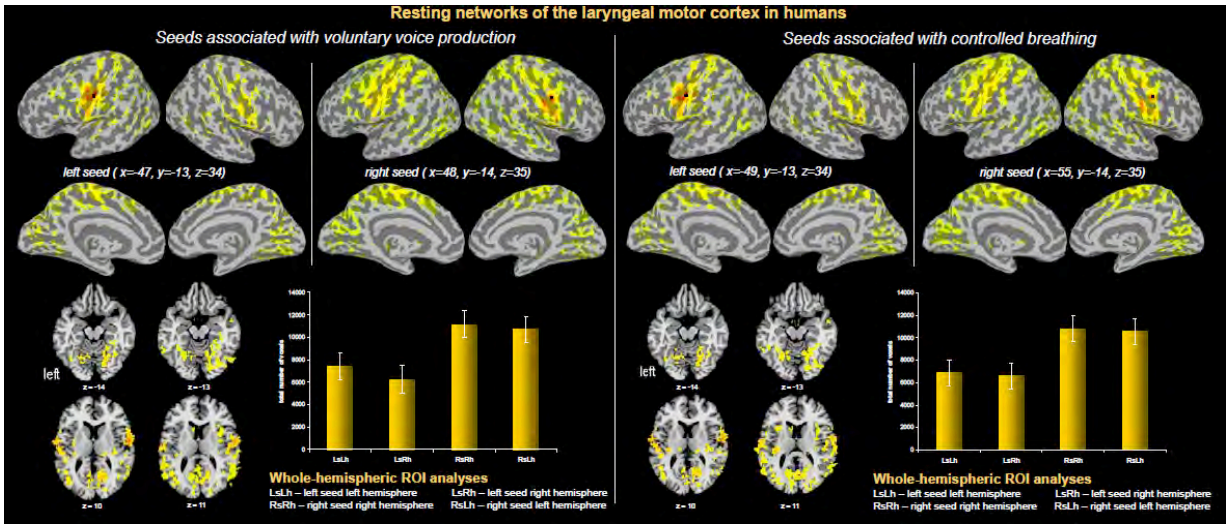

References

Brown, S et al. (2007), A Larynx Area in the Human Motor Cortex, *Cerebral Cortex*, vol. 18, pp. 837-845.

Jurgens, U (2002), Neural pathways underlying vocal control, *Neuroscience & Behavioral Reviews*, vol. 26, pp. 235-258.

Loucks, TM et al. (2007), Human brain activation during phonation and exhalation: common volitional control for two upper airway functions, *NeuroImage*, vol. 36, pp. 131-143.

Olthoff, A et al. (2008), Cortical sensorimotor control in vocalization: a functional magnetic resonance imaging study, *Laryngoscope*, vol. 118, pp. 2091-2096.

Simonyan, K et al. (2007), Functional neuroanatomy of human voluntary cough and sniff production, *NeuroImage*, vol. 37, pp. 401-409.

Simonyan, K et al. (2009), Functional but not structural networks of the human laryngeal motor cortex show left hemispheric lateralization during syllable but not breathing production, *Journal of Neuroscience,* 29(47):14912-14923.

Studies of Cerebellum Development and Function in Mice using Mn-Enhanced MRI

Kamila U. Szulc[1,2], Edward J. Houston[1], Feng Pan[1], Wenbiao Gan[1], Alexandra L. Joyner[3], Daniel H. Turnbull[1,2]

[1]Kimmel Center for Biology and Medicine at the Skirball Institute of Biomolecular Medicine, and [2]Department of Radiology, New York University School of Medicine and [3]Developmental Biology Program, Sloan Kettering Institute, New York NY

Introduction: Manganese (Mn)-enhanced MRI (MEMRI) has been used for *in vivo* structural and functional brain studies in rodents [1, 2, 3]. In the present study, we applied MEMRI to analyze normal cerebellum (Cb) development *in vivo* in FVB/N mice. We also explored the potential of MEMRI to detect and analyze neural activity in the Cb during rotarod stimulation. The ultimate goal of this project is to generate an atlas of normal Cb development in mice, including patterns of neuronal activity in the mouse Cb during defined motor tasks. This database will provide an important resource for future phenotype analyses of mutant mice with defects in Cb development.

Methods: *Studies of Cb Development:* Mn^{2+} was delivered to neonates through milk after maternal intraperitoneal (IP) injection of $MnCl_2$ in isotonic saline (40mg/kg). Neonatal mice were imaged 24h after the injection every other day from postnatal day P1 to P11 and from P2 to P10. *Studies of Cb Function:* P21 ±1 day mice were injected IP with $MnCl_2$ (40mg/kg). The mice in the experimental group were run on a rotarod for 3h immediately prior to the MRI. For both structural and functional studies 3D T1-weighted MRI data with 100-μm isotropic resolution were acquired for each animal on a 7T Bruker-micro-imaging system using a mouse head coil. All mice were anesthetized during the scan with isoflurane (1.0-1.5% in air). 3D visualization and quantitative analysis were performed using a combination of commercial (Amira) and open-access deformation-based morphometry (DBM) analysis software [4, 5, 6].

Results and Discussion: MEMRI data provided sufficient contrast and resolution to visualize changes in Cb morphology that take place within the first week and a half of early postnatal development in mice (Fig. 1). These datasets enabled qualitative and quantitative analysis of neonatal Cb patterning. Functional studies revealed statistically significant ($p<0.05$) enhancement in regions receiving projections from the vestibular system such as flocculus-paraflocculus complex and lobule IX, anterior portion of lobules IV/V and VIa to which spino-cerebellar tract projects, carrying information from the limbs (Fig. 2). In addition to the Cb, MEMRI enhancement was also detected in the left somatosensory cortex and bilaterally in the amygdala, the region of the brain associated with fear processing.

Conclusion: In summary, the above work demonstrates feasibility of *in vivo* longitudinal MEMRI studies of Cb development in individual mice showing that it is possible to obtain anatomical data to analyze the rate of growth, volume and shape changes of the Cb, its subregions and regions connected to it through projections. Additionally, functional MEMRI studies of brain networks involved in motor task suggest that MEMRI has potential to become a useful tool for anatomical phenotyping both Cb structure and function in normal and mutant mice.

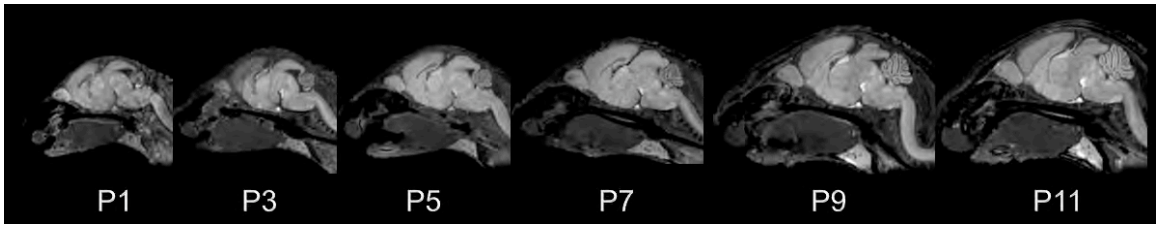

Figure 1. A representative dataset from an individual animal imaged every other day from P1 to P11. Images show mid-sagittal sections through the brain and cerebellum (Kamila – please mark the Cb on one panel, probably P11 is best).. During this critical period of postnatal development, the brain grows significantly and the Cb, in addition to changes in size, undergoes dramatic morphological transformation to achieve its full foliation pattern, including the subdivision of the Cb into lobules and sublobules.

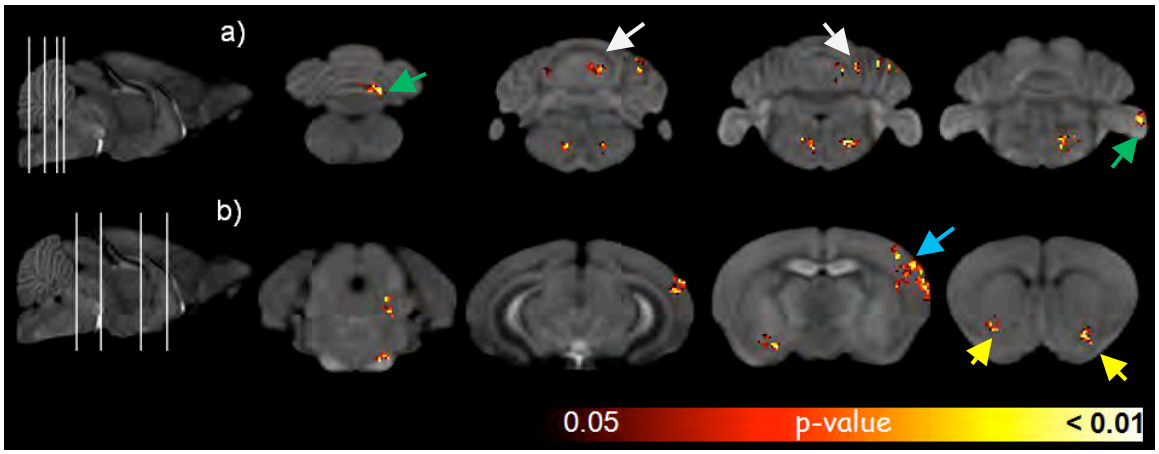

Figure 2. Activity maps, representing regions of significant Mn enhancement in mice performing rotarod training, compared to mice with no defined motor stimulation (n=5 in each group; $p<0.05$). The maps show regions on increased activity in the Cb and brainstem (a) and midbrain and forebrain areas (b). The arrows indicate areas of activity in the parts of the Cb receiving projections from spino-cerebellar tract (white arrows) and regions known to be involved in balance control (green arrows). Increased signal intensity can be also observed in left somatosensory cortex (blue arrow) and bilaterally in fear processing region of the brain, the amygdala (yellow arrows).

References: [1] Silva AC et al. (2004). NMR Biomed 17: 532-43; [2] Yu X et al. (2005). Nat Neuroscience 8: 961-8; [3] Koretsky AP, Silva AC (2004). NMR Biomed 17: 527-31; [4] Kovacevic N et al. (2005). *Cereb Cortex* 15: 639-45; [5] Nieman BJ et al. (2007). *Human Brain Mapp* 28: 567-75; [6] Lerch JP et al. (2008). Neuroimage 39: 32-9.

Comparison of neuronal morphology in pyramidal neurons of the CA1, dentate gyrus, and prefrontal cortex of APP knockout and APLP2 knockout mice

Jessica Walsh[1], Sheue-Houy Tyan[2], Brea Midthune[2], Ann Yu-Jung Shih[2], Simone Eggert[2], Patrick R. Hof[1], Edward Koo[2], and Dara L. Dickstein[1]
[1]Mount Sinai School of Medicine New York, NY, USA
[2]University of San Diego, La Jolla, CA, USA

Introduction

The amyloid precursor protein (APP) plays a pivotal role in the pathogenesis of Alzheimer's disease (AD). The processing of APP involves proteolytic cleavage by β- and γ-secretases to produce amyloid β protein (Aβ), the major protein component of the senile plaques in AD. The possible functions of APP include mediation of neurite outgrowth, cell adhesion, and regulation of synaptic plasticity and transmission. Many of these functions extend to the two homologues of APP, APLP1 and APLP2. Our recent studies suggest that mice lacking the APP gene show significant morphological alterations in dendrites of neurons located in brain regions associated with AD pathology, specifically CA1 and dentate gyrus (DG) in the hippocampus, and prefrontal cortex (PFC).

Methods

We compared the possible changes in neuronal morphology, in aged APP-/- mice to aged APLP2-/- mice. Mice were perfused and intracellular injections of Lucifer Yellow were made in neurons in the CA1, DG, and PFC regions. Neurons were traced using Neurolucida software (MBF Bioscience) and Sholl analysis was performed to quantify dendritic length and complexity.

Results and Discussion

CA1 neurons show shorter apical length and decreased number of intersections in aged APP-/- mice compared to APLP2-/- ($p < 0.05$), along with significant differences in Sholl analysis of basal dendritic length and number of intersections ($p < 0.05$). DG granule cells showed no appreciable difference in mean dendritic length and number of intersections. PFC pyramidal neurons showed significant differences in shorter apical length and number of intersections, along with apparent differences in Sholl analysis of basal dendritic length and number of intersections. These results are consistent with the in vitro findings.

Conclusion

These findings suggest that APP plays a key role in the formation and complexity of dendrites. Knocking out APLP2 does not produce any noteworthy changes in dendritic length or complexity, suggesting that it is not necessary for neurite outgrowth. However, APP-/- mice do show marked decreases in dendritic morphology. Furthermore, the deficits seen in the APP-/- mice suggest that APLP2 and APLP1 cannot compensate for the loss. Further studies will focus on the alternations in spine density and spine types in these animals.

References

1. Dawson, G.R., Seabrook, G.R., Zheng, H., Smith, D.W., Graham, S., O'Dowd, G., Bowery, B.J., Boyce, S., Trumbauer, M.E., Chen, H.Y. et al. (1999) Neuroscience 90, 1–13

2. Heber, S., Herms, J., Gajic, V., Hainfellner, J., Aguzzi, A., Rulicke, T., von Kretzschmar, H., von Koch, C., Sisodia, S., Tremml, P. et al. (2000) J. Neurosci. **20**, 7951–7963

3. Scholl DA (1953) Dendritic organization in the neurons of the visual and motorcortices of the cat. J Anat **87**,387-406

4. von Koch CS, Zheng H, Chen H, Trumbauer M, Thinakaran G, van der Ploeg LH, Price DL, Sisodia SS (1997) Generation of APLP2 KO mice and early postnatal lethality in APLP2/APP double KO mice. Neurobiol Aging 18:661-669

5. Walsh, D., Klyubin, I., Fadeeva, J., Cullen, W., Anwyl, R., Wolfe, M., Rowan, M. and Selkoe, D. (2002) Nature (London), 416, 53–539

6. Zheng, H., Jiang, M., Trumbauer, M.E., Sirinathsinghji, D.J.S., Hopkins, R., Smith, D.W., Heavesn, R.P., Dawson, G.R., Boyce, S., Conner, M.W. et al. (1995) Cell **81**, 525–531

Abstracts selected for poster presentation, Nanomedicine category

The TMII Departmental Cell Tracking Core Facility: Program Overview

Karen C. Briley-Saebo

Mount Sinai School of Medicine, Department of Radiology and Gene and Cell Medicine

Introduction: The recent advances in immunotherapeutics and cell based vaccines have highlighted the need to develop diagnostic imaging methods that enable in vivo detection and monitoring of therapeutic cells. In order for these novel therapeutics to transition into a clinical setting, validated pre-clinical models tare required that provide information related to optimal injection routes, optimal cell sub-type/activation and optimal labeling conditions for induction of the desired therapeutic or adaptive immune response. As a result the main goal of the TMII cell tracking core is to develop and provide novel technology to allow for non-invasive in vivo detection of therapeutic cells. The specific aims of the program are summarized as follows:

- Development and validation of pre-clinical models.
- Development and optimization of cell labeling techniques.
- In vivo and ex vivo imaging of animals and cells.
- Acquisition of preliminary data for new grant applications, support funded studies and generation of data for IND submissions.

Methods: Since focus is placed on clinical translatability, cell labels that are FDA approved for other indications are preferred. To date studies using iron oxide particles such as Feridex and Ferex have been performed for the in vivo tracking of a variety of cells by magnetic resonance imaging (MRI). Additionally, MR cell tracking using paramagnetic materials such as Gadoflourine M have also been performed.

We have clearly shown that the cell origin, activation state and phenotype may greatly influence the ability of the cells to sequester iron oxide based labels. Focus is therefore placed on the optimization of cell loading as well as characterization of the cells post labeling. As a result, the core has developed and validated a variety of methods to quantify and characterize intercellular uptake of a variety of cell labels. Additionally the core has developed methods to evaluate the affect of labeling on cell viability, function and phenotype.

TMII currently has one dedicated system for MR imaging of mice (9.4T). In addition, we have optimized MR imaging of mice, rabbit and pig at clinically relevant fields (3T). Although TMII will obtain a micro-PET scanner in 2012, we are currently able to perform PET/MR imaging in rabbits and pigs using a state-of-the-art clinical whole body sequential PET/MR scanner. Preliminary pre-clinical PET studies using copper (Cu^{64}) labeled materials have indicated that PET labels with long half-lives such as copper or zirconium may allow for sensitive longitudinal tracking of duel PET/MR labeled cells in vivo.

Prior to in vivo imaging, all diagnostic imaging protocols are validated using in vitro cell phantoms. The sensitive of the method is determined based upon the number of cells that can be visualized or detected within a given voxel. The sensitivity data is used to plan the longitudinal in vivo imaging studies as well as to determine the effect of cell division or metabolism on the signal observed. Other phantoms may also be utilized prior to in vivo imaging to allow for optimization the imaging sequences used.

The core provides raw data sets and images (dicom) as well as full post processing and evaluation of pre-clinical data. Although the core has only been active for less than 1 year, pre-clinical data has all ready been used in the submission of three NIH grants and 1 DOD grant. Since the goal of the program is to provide data for IND submission, all studies are preformed in the spirit of GLP/GCP.

Results: **Fig.1** shows a composite of some of the on-going pre-clinical studies. Reported studies are given in references 1-3.

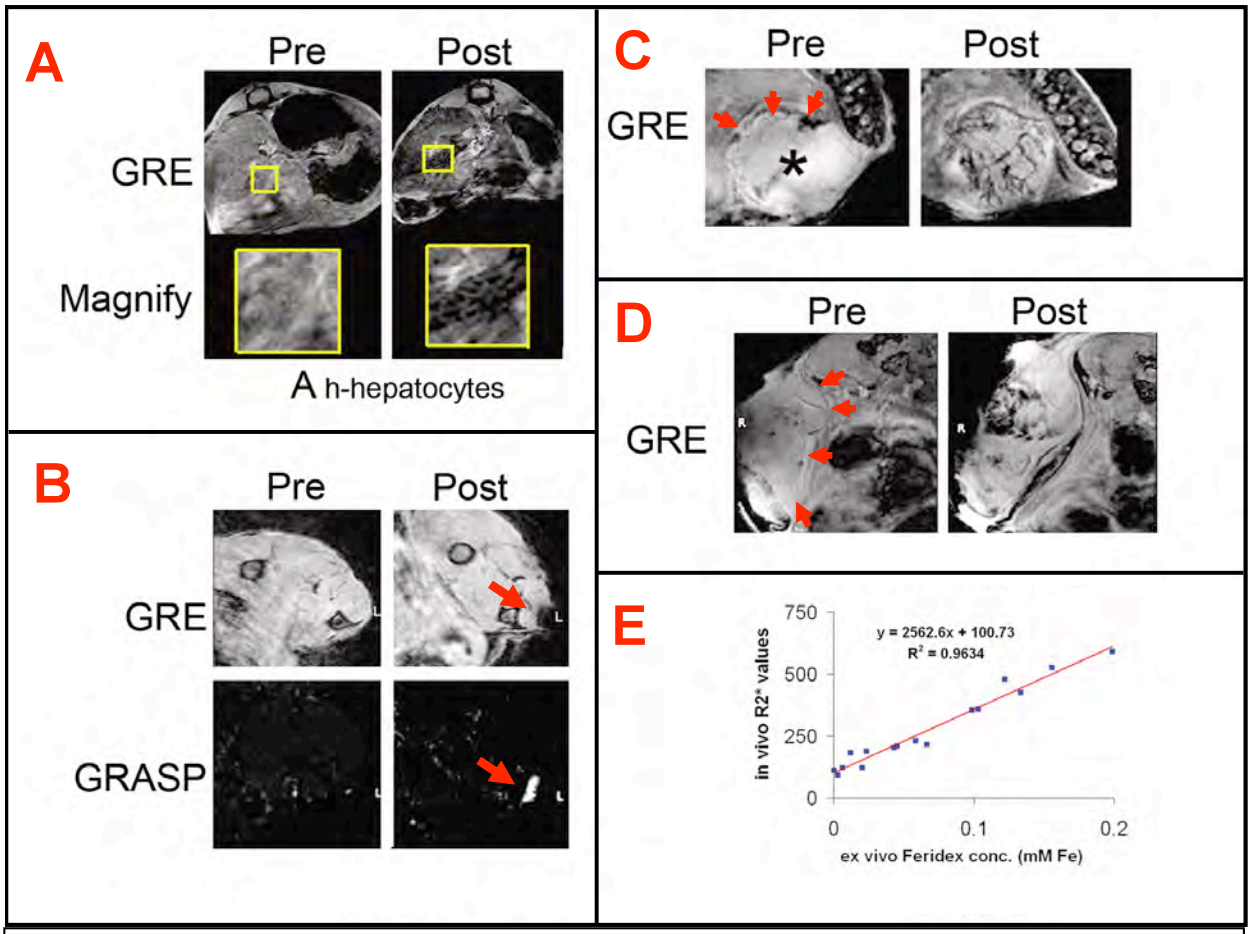

Fig.1: A) MR images of Feridex labeled human monocytes prior to and 24 hours after injection into the portal vein of immunedeficient mice. The yellow box shows area of magnification. MR signal loss indicative of iron laden cells shown as compartmentalized islets. B) MR images of Feridex labeled human dendritic cells prior to and 24 hours after foot pad injection. Red arrow indicates draining lymph node. MR signal loss and MR signal gain observed on GRE and novel GRASP sequences, respectively. C) Feridex labeled myeloid derived suppressor cells prior to and 48 hours after i.v. injection in tumor bearing mice. Red arrows indicate the border of the tumor within the liver. D) MR image of Feridex labeled antigen primed human monocytes prior to and 48 hours after i.v. injection in tumor bearing mice. Red arrows show tumor border relative to the mouse flank. E) Correlation between in vivo MR signal obtained (as R2*) and the ex vivo iron content determined in the spleen of mice 24 hours after i.v. injection of Feridex labeled human dendritic cells.

Conclusions: TMII cell tracking core allows provides validated pre-clinical models to allow for the in vivo detection and monitoring of therapeutic cells.

References:

1) FASEB J. 2009 Nov 25. [Epub ahead of print]
2) JACC Cardiovasc Imaging. 2009;2(9):1114-22.
3) Magn Reson Med. 2008;60(1):73-81.

Collagen-targeted HDL Nanoparticles for Molecular Imaging of Plaque Regression

Wei Chen[1], Willem JW Mulder[1], David P Cormode[1], Zahi A Fayad[1], Edward A Fisher[2]

1. Translational and Molecular Imaging Institute, Mount Sinai School of Medicine
2. Departments of Medicine (Cardiology), New York University Medical Center

Introduction: High density lipoprotein (HDL) is an endogenous nanoparticle. We previously developed HDL-like probe to assess the progression of atherosclerotic plaques using magnetic resonance (MR) molecular imaging. In the present study, we modify this HDL nanoparticle platform to follow the regression of atherosclerotic plaques non-invasively using MR imaging by specifically targeting collagen via a rerouting strategy.

Methods: We reconstituted discoidal HDL (rHDL) and included amphiphilic gadolinium chelates for MR imaging in the lipid corona. To reroute rHDL nanoparticles to collagen, collagen-specific peptides were conjugated to these particles (rHDL-EP3533). The binding of rHDL-EP3533 to collagen was examined in vitro on rat collagen I coated plates using optical techniques. The efficacy of rHDL-EP3533 in tracking the regression of plaques was evaluated in vivo in a Reversal mouse model using MR imaging. Non-specific EP3612 peptides modified rHDL (rHDL-EP3612) was used as control.

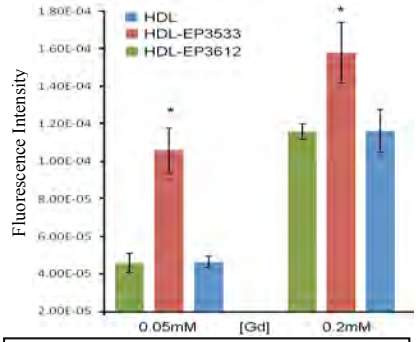

Figure 1. In vitro binding of nanoparticles to rat collagen I.

Results and Discussion: rHDL-EP3533 had significantly higher binding to rat collagen type I in comparison with rHDL and non-specific rHDL-EP3612 (Figure 1). The collagen content in the atherosclerotic plaques of Reversa mice increased while macrophage content decreased at 28 days after induction of plaque regression. We found rHDL and rHDL-EP3612 showed enhanced signal in MR images at Day 0 (Figure 2) due to high macrophage content, while no enhancement for rHDL-EP3533 due to low collagen content. However, at Day 28, only rHDL-EP3533 showed significant enhancement for the plaque (Figure 1) due to high collagen content.

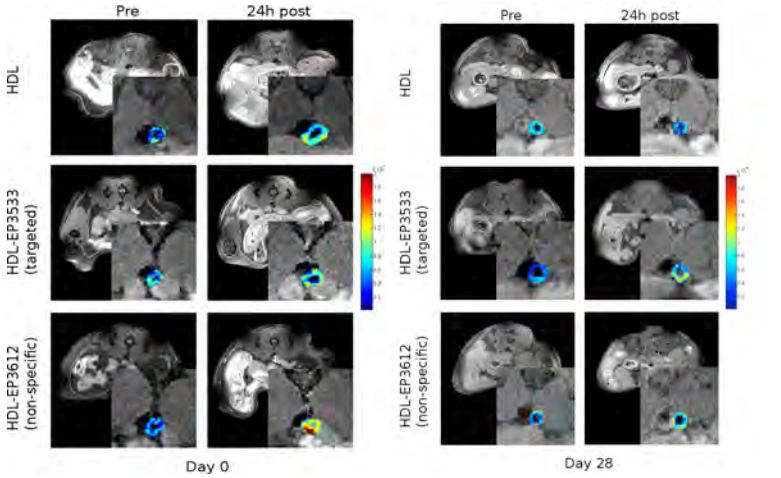

Figure 2. In vivo MR imaging of abdominal aortas during plaque regression.

Conclusion: This study demonstrated the ability of modified rHDL nanoparticles to target collagen in vitro and in vivo, which allows non-invasive visualization of plaque regression by MR imaging.

Iron oxide nanoparticles with a fluorescent and tunable coating to allow multimodal imaging of gene delivery to different cell populations in the liver

David P. Cormode,[1] Gitte O. Knudsen,[1] Amanda Delshad,[1] Nicole Parker,[1] Peter A. Jarzyna,[1] Claudia Calcagno,[1] Torjus Skajaa,[1,2] Karen C. Briley-Saebo,[1] Ronald E. Gordon,[3] Zahi A. Fayad,[1] Savio L. C. Woo,[1] Willem J. M. Mulder[1]
1 – Mount Sinai School of Medicine, 2- Aarhus University, 3 – Mount Sinai Hospital,

Introduction - There are many liver diseases where the delivery of DNA to the hepatocytes could provide therapy. However, most delivery systems are sequestered in the Kupffer cells before ever reaching the hepatocytes. In the current study, we developed a versatile nanoparticle platform (A) and investigated its suitability for multimodal imaging of gene delivery to the hepatocytes.

Methods - Iron oxide nanocrystals were coated with the DNA binding polymer PMAL and varying quantities of polyethylene glycol (PEG) functionalized lipids. The resulting nanoparticles (NPs) were characterized with respect to diameter, stability in serum, toxicity, DNA loading capacity and zeta potential. In vitro transfection experiments were carried out and studied using confocal microscopy. Preliminary in vivo experiments were carried out in mice where the livers were visualized with MRI in vivo and with TEM ex vivo.

Results and Discussion - The mean diameters of the NPs were 19, 19 and 25nm for respectively 0%, 5% and 10% PEG functionalized lipids in the coating. After 24h of incubation in 10% FBS the size of the 0% PEG-lipid particle doubled while the size of the 10% PEG did not significantly change. In vitro assays showed the changes in viability caused by these particles to be insignificant. NP uptake by cells and subsequent gene expression was investigated by confocal microscopy imaging. MRI of injected mice showed that our particles accumulated in the liver (B), while TEM imaging revealed that increasing inclusion of PEG in the coating allowed the nanoparticles to access the hepatocytes (C).

Conclusion - We have developed a flexible, polymer-coated iron oxide nanoparticle platform that can be employed for delivery of DNA to hepatocytes with low toxicity and can be visualized with MRI, TEM and optical techniques.

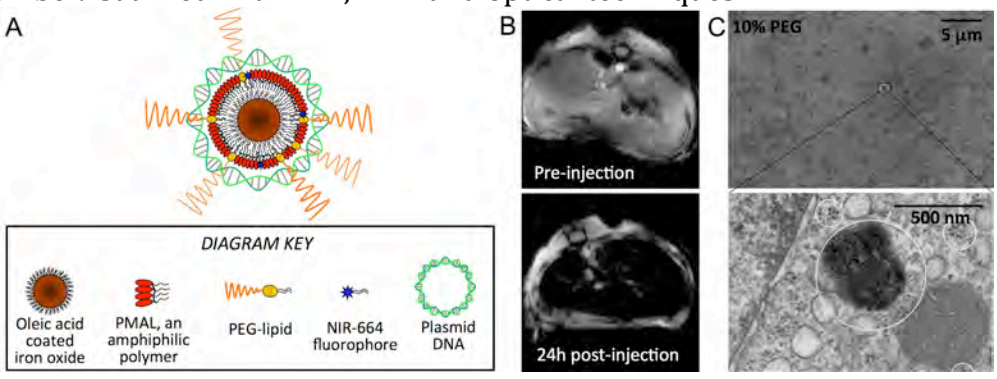

Figure 1. A) schematic of the nanoparticle structure. B) MRI images of a mouse at the liver level. C) TEM images of liver hepatocytes of a mouse injected with 10% PEG nanoparticles.

The effect of imaging parameters and physical environment on the relative contrast produced by gold nanoparticle and iodine contrast agents in computed tomography imaging

Merav W. Galper, [1] David P. Cormode, [1] May T. Saung, [1] Zahi A. Fayad[1]
1- Mount Sinai School of Medicine, New York, NY

Introduction - There have been many recent studies where nanoparticles whose payload is gold, bismuth, or other elements have been proposed as contrast agents for computed tomography (CT). The advantages of such nanoparticle contrast agents over clinically iodinated small molecules are longer circulation times, targeted imaging, and, ostensibly, greater CT contrast. In the current study, we investigated the effect of a variety of CT scanning parameters and physical settings on the comparative contrast of gold nanoparticle (AuNP) and iodine contrast agents.
Methods – Samples of AuNP were synthesized and diluted to eight different concentrations ranging from 1M to 10 mM. Iodine contrast agent (Isovue) was diluted to similar concentrations. The solutions were imaged using a 256-slice Philips Brilliance iCT scanner under different settings, including X-Ray tube voltage, X-ray tube current, reconstruction kernel, and scanning protocol. Samples were also scanned in air, three different volumes of water, and under a block of calcium phosphate to simulate the presence of bone.
Results and Discussion – For example, at a current of 100mA, higher energies levels resulted in lower attenuation of iodine, whereas gold maintained similar attenuation across energy ranges. Scanning with a beam rich in high-energy X-rays may therefore result in improved contrast between gold and tissue. Reconstruction kernel can have an effect on the attenuation of images.
Conclusion – This study sheds light on the relative performance of gold nanoparticles compared with iodine contrast, delineates the factors that are important for generating greatest contrast when using gold nanoparticles, and establishes recommended sample imaging conditions for evaluating novel CT contrast agents.

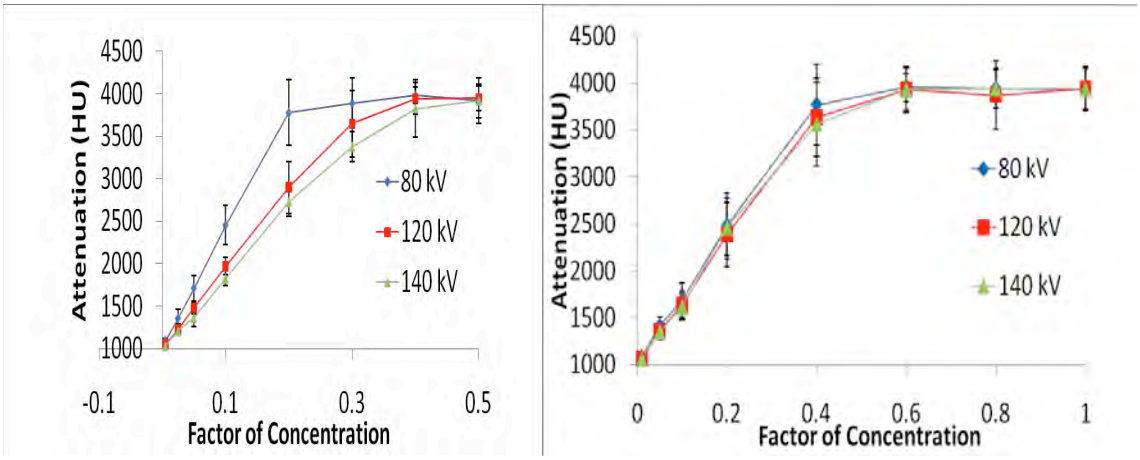

Figure 1. A) Energy dependent attenuation of iodine at different energies. B) Energy independent attenuation of gold at difference energies.

A MULTIFUNCTIONAL NANOPARTICLE PLATFORM FOR DELIVERY OF DIAGNOSTIC AND THERAPEUTIC AGENTS TO TUMORS

Anita Gianella, Peter A. Jarzyna, David P. Cormode, Zahi A. Fayad, Willem J.M. Mulder
Translational and Molecular Imaging Institute, Department of Radiology, Mount Sinai School of Medicine

Background and aim: Multifunctional nanoparticles are useful for combined therapy and non-invasive imaging of pathologies. The aim of the current study is to develop a multifunctional probe that carries glucocorticoids as well as diagnostic materials. The potential of this platform for targeting, imaging and treating cancer was evaluated in a mouse tumor model.

Methods and Results: The nanoparticles used consist of an oil-in-water emulsion, 50-60 nm in diameter. The soybean oil was loaded with oleic acid coated iron oxide nanocrystals, for MR imaging as well as prednisolone acetate valerate for therapeutic purpose. The nanoemulsions were stabilized by PEGylated and ordinary phospholipids and additionally labeled with the near infrared dye Cy7 for enable fluorescent imaging (NIRF) detection. Tumors were established in six-week-old male Swiss mice by subcutaneous injection of $2x10^6$ human colon carcinoma LS174T cells. The tumor targeting capability of the nanoemulsions were studied 8-10 days after the cell injections. Mice were imaged pre-injection with T_2-weighted MRI scans and an NIRF instrument. Subsequently they received an intravenous injection of nanoemulsion equivalent to 60 mg iron/kg, 45 μg Cy7/mouse and 10 mg/kg prednisolone acetate valerate. After nanoemulsion administration the animals were frequently imaged with NIRF until 6 hours, and after 24hours (Fig. 1A). MRI was performed after 6 and 24 hours, just before sacrifice (Fig. 1B). At the tumor level, an increase in fluorescence and T_2-weighted signal loss, occurred in NIRF and MR images, respectively, confirming the nanoparticle accumulation. The accumulation of our nanoparticle platform in the tumor interstitial space occurs via the enhanced permeability and retention effect, which is a typical phenomena observed in tissue with a leaky vasculature, such as tumors. Moreover, to test the therapeutic potential of nanoemulsions carrying the glucocorticoid drug, five mice received a first injection of nanoparticles (equivalent to 10 mg/kg of prednisolone acetate valerate) as soon the tumors were palpable (day 6) and a second injection after three days (day 9); five saline injected mice served as controls. Tumor size was measured daily until sacrifice. Preliminary data revealed a distinct inhibition of tumor growth in mice injected with nanoemulsion loaded with glucocorticoid compared to the saline group (Fig.1C).

Conclusion: The preliminary data show this nanoparticle platform can be used as a drug delivery and imaging probe. Further experiments using peptide-targeted nanoemulsions will be performed to enhance therapeutic action.

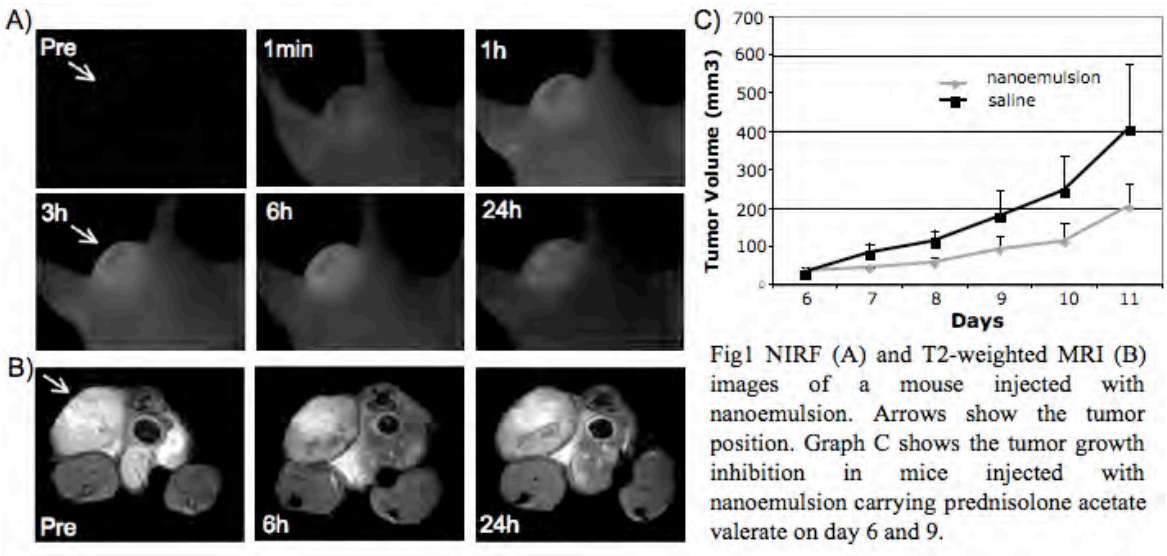

Fig1 NIRF (A) and T2-weighted MRI (B) images of a mouse injected with nanoemulsion. Arrows show the tumor position. Graph C shows the tumor growth inhibition in mice injected with nanoemulsion carrying prednisolone acetate valerate on day 6 and 9.

Gold and Silver Nanoparticles Functionalized With High Gadolinium Payload As *In Vivo* T1-Brightening Contrast Agents

Lindsay K Hill[1], Talha S Siddiqui[2], Dung Minh Hoang[1], Susan Pun[1], Marc A Walters[2] and Youssef Z Wadghiri[1]

[1]Department of Radiology, NYU School of Medicine, New York, NY, USA

[2]Department of Chemistry, New York University, New York, NY, USA

Introduction:

The aims of designing MRI multimodal agents have been to narrow the agent's biodistribution and amplify enhancement. Nanotechnology is key in the fabrication of such agents that carry a multiplicity of interior or surface-bound contrast agents [1-2]. Silver and Gold metal nanoparticles offer attractive platforms for imaging with their ability to bind a cocktail of surface-linked molecules. Previously described silver nanoparticles have been prone to aggregation due to large binding tethers and oxidation. The use of a short thiol linker was anticipated to reduce such aggregation, and the use of gold to eliminate oxidation. Utilizing these nanoparticles, our group [3] and others [4-8] have demonstrated that this approach can provide effective T1-contrast for visualization of tissue and vasculature. In the research described here we have designed new multimodal Gd-nanoparticles and have tested the effect of colligated polyethyleneglycol (PEG) chains on particle distribution, clearance, and contrast. The relaxivity and solubility of the nanoparticles, as well as clinically-used Magnevist, were tested *in vitro* and their biodistribution was assessed by *in vivo* full-body MRI.

Methods:

Synthesis: These nanoparticles were prepared as described by Kim et al. [9] and were derivatized using a chemically modified DTPA with a thiolate-terminated tether at the β-carbon of DTPA's central carboxylate group. The bi-functional ligand is anchored via the thiol and binds Gd with five carboxylates and three secondary amine groups.

MRI: *In vitro* and *in vivo* testing of the nanoparticles was performed on a 7-T Bruker micro-MRI system, interfaced to a 200-mm horizontal bore magnet (Magnex Scientific, Yarnton, UK) with 750-mT/m and actively shielded. To assess contrast over 2hours, a modified 3DGE sequence acquiring a self-gating signal was used retrospectively for artifact-free image reconstruction. The *in vivo* protocol in Wild Type mice consisted of a pre-injection scan and ten post-scans to monitor biodistribution and clearance through the kidneys and bladder of GdDTPA (Magnevist, 3μmol/30g mouse weight) or pegylated and non-pegylated GdDTPA-SH-Ag or GdDTPA-SH-Au (not shown) (1μmol equivalent Gd/30g). The sequence parameters were FOV=76.8x25.6x25.6mm^3, Matrix=384x128x128, Resolution=(200μm)^3, TR/TE=15/4ms, Averages=3, Acquisition Time=12-mn. The Flip Angle (18º) was chosen to provide the greatest T1-enhancement contrast [8]. During the MR image acquisition, mice were anesthetized with Isoflurane.

Results and Discussion:

The surface derivations using a short thiol tether demonstrated increased solubility in aqueous media compared to previously described constructs [3]. PEG further increased particle solubility and longevity throughout the 2hour study. *In vitro* studies demonstrated an improvement of the relaxivity. Additionally, *in vivo* studies showed an increased plasma half-life of the pegylated particles compared to non-pegylated versions and to Magnevist. In contrast to Magnevist-injected mice, the enhancement observed with the nanoparticles was notably more pronounced throughout the study with three times less Gd [Fig. 1].

Conclusion: In summary, we have designed and prepared new multivalent paramagnetic Gd-nanoparticles as efficient T1-enhancing MRI probes. The pegylated derivations in particular demonstrate great potential as Blood Pool agents due to their size and Gd-payload. These pegylated and non-pegylated Gold and Silver nanoparticles thus prove to be stable T1- brightening agents to visualize tissue and vasculature *in vivo*.

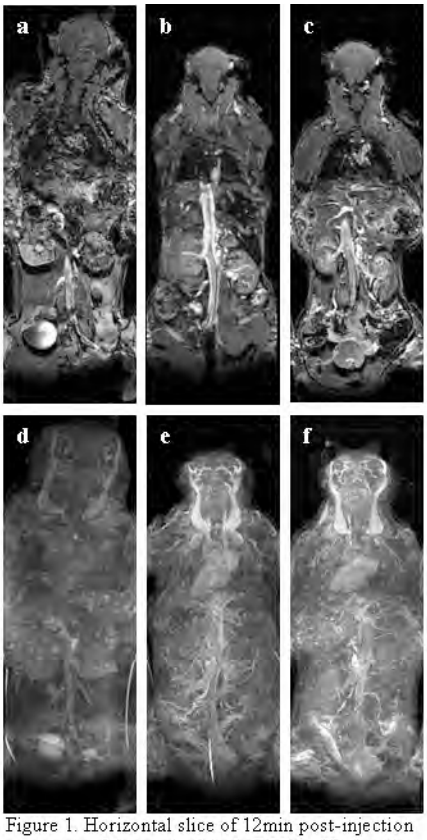

Figure 1. Horizontal slice of 12min post-injection scans using Magnevist (a), GdDTPA-SH-Ag (b), and GdDTPA-SH-AgPEG (c). (d-f) Maximum Intensity Projections of a-c.

Acknowledgments: This research was supported in part by the American Health Assistance Foundation grant A2008-155 (YZW), Alzheimer Association grant IIRG-08-91618 (YZW), Tilker Medical Research Foundation (Y.Z.W. and M.A.W.) and by the NYU Applied Research Support Fund (Y.Z.W. and M.A.W.).

References:

[1] Meade, TJ *et al.*, Neurobiol., 2003, 13, p597. **[2]** Sosnovik *et al.*, Curr. Opin. Biotechnol., 2007, 18, p4. **[3]** Siddiqui, TS *et al.*, J. of Colloid & Interf. Sci., 2009, 337,,p88. **[4]** Debouttière, PJ *et al.*, Adv. Funct. Mater., 2006, 16(18), p2330. **[5]** Alric, C *et al.*, J. Am. Chem. Soc. 2008, 130(18), p5908. **[6]** Park JA *et al.*, Bioorg. Med. Chem. Lett. 2008, 18(23) p6135. **[7]** Marradi M *et al.*, Chem. Cummun., 2009, p3922. **[8]** Bridot, J-L*et al*, J. Am. Chem. Soc., 2007, 129, p5076. **[9]** Joo TH *et al.*, Chem. Phys. Lett. 1984, 112(1), p65. **[10]**) Nieman B *et al.*, 2009 61(5), p1148.

Multi-Spectral Optical Molecular Tomography Of Nanoparticles

Alexander D. Klose[1], Bradley J. Beattie[2], Yared Tekabe[3], Lynne Johnson[3]

[1] Department of Radiology, Columbia University, New York, NY 10032; [2] Memorial Sloan-Kettering Cancer Center, New York, NY 10068; [3] Department of Medicine, Columbia University, New York, NY 10032; Contact: ak2083@columbia.edu

Most work in clinical and pre-clinical optical imaging has been limited to direct or planar imaging of light that escapes through the tissue surface. Unlike high-energy photons, used in Positron Emission Tomography (PET) or in Single Photon Counting Emission Tomography (SPECT), light in the visible and near-infrared (e.g., 1-2 eV: 500 nm – 800 nm) is strongly scattered and partially absorbed in biological tissue. Therefore, planar surface images of optical reporter probes in small animals (Fig. 1) contain little information about the actual depth and strength of the source of light emission (fluorescent dye, reporter gene, nanoparticles).

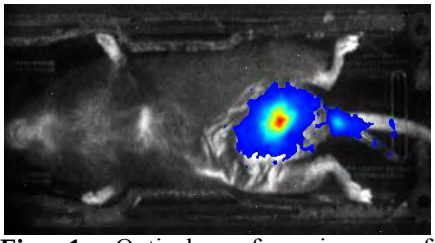

Fig. 1: Optical surface image of fluorescent quantum dots (QDs) in a rectal catheter inside a small animal.

Optical Molecular Tomography (OMT), on the other hand, reconstructs the three-dimensional (3D) spatial distribution and concentration of light-emitting reporter probes in tissue by using multi-spectral planar images. Fig. 2 shows a schematic of two different multi-spectral OMT methods. On the left in Fig. 2, the tissue surface is illuminated with light at different wavelengths between 580 nm and 660 nm and fluorescent nanoparticles, such as quantum dots (QDs), are stimulated for fluorescence light emission. QDs have a broad absorption spectrum, which coincides with the large varying extinction spectrum of hemoglobin in tissue. In fact, the optical properties of QDs and hemoglobin are exploited for 3D image reconstruction [1]. Moreover, the QDs can be conjugated to antibodies or peptides for targeting specific cell surface receptors (VEGF, integrin) and, hence, serve as a beacon. Next, the fluorescence light is measured by a camera on the tissue surface. Using different excitation wavelengths, a computer algorithm based on a light propagation model [1], calculates the 3D location of the QDs in vivo. An alternative multispectral OMT method is shown on the right in Fig. 2. Self-illuminating QDs or bioluminescent reporter systems emit light between 600 nm and 680 nm, which is measured by a camera at different emission wavelengths. No external excitation light source is required. Again, due to the spectral properties of hemoglobin in tissue, 3D tomographic images can be reconstructed. Fig. 3 shows the reconstructed location of an optical probe that has been inserted into a small animal with a rectal catheter. A co-registered CT scan confirms the accurate location of the reconstructed optical source.

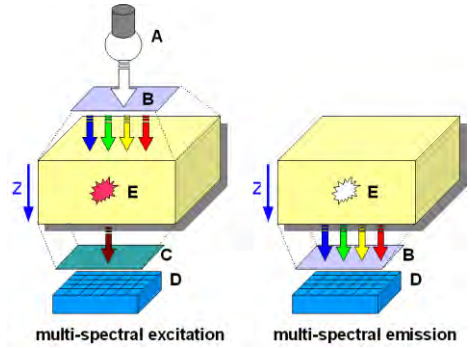

Fig. 2: Schematic of OMT methods with either multi-spectral excitation (left) or emission (right). (A) white light source, (B) wavelength-tunable emission filter, (C) bandpass filter, (D) optical camera, (E) light emitting probe (e.g., QDs) inside tissue.

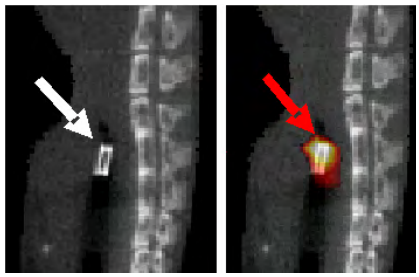

Fig. 3: Tomographic reconstruction of a light source (hot scale) on top of co-registered CT (gray scale). Probe has been placed in rectum of a mouse.

Acknowledgements: This work was supported in part by Columbia University's CTSA grant UL1 RR024156 from NCRR/NIH, and by grants NCI-4R33CA118666 and 5U54CA126513-029001 from the National Institutes of Health (NIH).

[1] Klose, A.D., *Hyperspectral excitation-resolved fluorescence tomography of quantum dots*, Optics Letters 34(16), 2477-2479 (2009).

An In-Vitro Assay to Test the Binding Affinity of a Peptide Targeted to CCR7: A Potential Targeting Moiety for Nanoparticle Functionalization.

Stewart Russell, Department of Medicine, New York University Medical Center
Sergio Trombetta, Department of Pathology, New York University Medical Center
Raymond Tu, Department of Chemical Engineering, The City College of New York
Zahi A. Fayad, Mount Sinai School of Medicine
Edward A. Fisher, Department of Medicine, New York University Medical Center

Summary: *CCR7 is a chemokine receptor expressed by immune cells that has been shown to be upregulated in regressing atherosclerotic lesions relative to advancing lesions in vivo. An image enhancement agent targeted to this receptor could be used to differentiate between progressing and regressing plaque. CCL-19 is a native ligand to this receptor, and binding affinity has been shown to be associated with conservation of the 7 amino acids of the N-terminus. We have synthesized a peptide consisting of these 7 residues, and developed an in vitro competition binding assay to determine the affinity of the peptide fragment to CCR. Confocal fluorescence scanning microscopy shows that the binding of CCL-19 is inhibited by the targeting peptide. This assay will be extended to nanoparticles functionalized with the targeting peptide, and can easily be adapted to other targeting moieties and nanoparticle platforms.*

Introduction: Chemokine receptor 7 (CCR7) has been shown to be necessary for the reduction of macrophages in a plaque undergoing regression [1], making it the primary known target for differentiation of disease state. In addition, chemokine ligand 19 (CCL-19), is a chemo attractant for immune cells, and a high-affinity binding ligand for CCR7. A promising approach by [2, 3] has shown the high affinity binding of CCL-19, is due to the 7 residues of the N-terminus.

Methods: HEK-293 cells are transfected with a GFP-labeled CCR7. Unlabeled targeting peptide is applied at 6 concentrations between 2×10^{-15} to 2×10^{-9} M and incubated for 15 minutes. The native ligand, CCL-19, labeled with Alexa-532 fluorescent dye, is added at 2×10^{-13} M to the live monolayer and allowed to bind for 15 minutes. Binding affinity is determined by relative fluorescence by confocal microscopy or plate reader.

Results and Discussion: We show that CCL-19 binds to our in vitro cell construct and that the targeting peptide will compete for binding of CCR7.

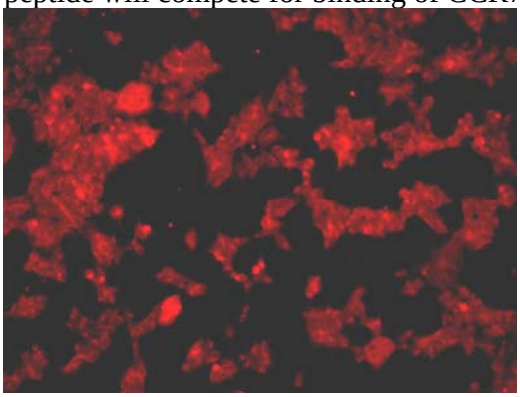

Figure 1) Red-labeled CCL-19

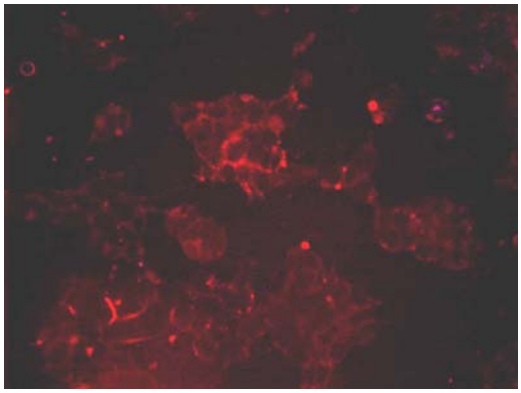

Figure 2) CCL-19 with 2 ug/mL targeting peptide

Conclusions: We have shown that the 7 amino acid peptide corresponding to the N-terminus of CCL19 can be used as a targeting moiety for specific binding to CCR7. This assay will be extended to nanoparticles functionalized with the targeting peptide, and can easily be adapted to other targeting moieties and nanoparticle platforms.

1. Trogan, E., et al., *Gene expression changes in foam cells and the role of chemokine receptor CCR7 during atherosclerosis regression in ApoE-deficient mice.* Proc Natl Acad Sci U S A, 2006. **103**(10): p. 3781-6.
2. Ott, T.R., et al., *Determinants of high-affinity binding and receptor activation in the N-terminus of CCL-19 (MIP-3 beta).* Biochemistry, 2004. **43**(12): p. 3670-8.
3. Ott, T.R., et al., *The N-terminal domain of CCL21 reconstitutes high affinity binding, G protein activation, and chemotactic activity, to the C-terminal domain of CCL19.* Biochem Biophys Res Commun, 2006. **348**(3): p. 1089-93.

Developing Gold Nanoparticles as a Targeted Contrast Agent for CT Imaging of Angiogenesis

May Tun Saung[1], David Cormode[1], Jun Tang[1], Peter Jarzyna[1], Willem Mulder[1], Zahi Fayad[1]
1. Mount Sinai School of Medicine, New York, NY

Introduction – Nanoparticles with gold payload have been proposed as contrast agents for targeted molecular imaging of phagocytotic cells using computed tomography (CT). In the current study, we have developed a nanoparticle contrast agent for CT that has a higher payload of gold than our previously reported agents, and may enable non-phagocytotic cells such as angiogenic endothelial cells to be imaged.

Methods – Different methods were used in an attempt to produce nanoparticles with increased gold payload. Method 1: The iron-oxide core oil-in-water emulsions synthesis reported by PA Jarzyna et al (Biomaterials, 2009) was modified for synthesis of gold-core emulsions of similar dimensions. Modifications included using different oils, lipids, gold nanoparticles (AuNP) caps (oleic acid & oleylamine vs. dodecanethiol) and changing the AuNP to oil-lipid ratio. Method 2: Gold nanoparticles were synthesized without oil with DSPC, DSPE-PEG 2000 and Mal-PEG lipids. The AuNP to lipid ratio was varied to optimize the formation of gold micelles. Gold particles with the highest payload were functionalized with 1) RGD peptides to target to endothelial cells' αvβ3 integrin receptors, 2) RAD peptides for control, and 3) fluorescent molecules Cy5.5 and Rhodamine for fluorescence-based imaging techniques. *In vitro* experiments using HUVEC (human umbilical vein endothelial) cells were carried out with RGD-functionalized gold particles targeted to αvβ3 integrin receptors, and with negative controls of RAD-functionalized gold particles and HUVEC cells without gold particles. The results of these experiments were evaluated with confocal microscopy, and CT.

Results and Discussion – The gold cores were not efficiently incorporated into the oil emulsions for any of the modifications of the oil-emulsion synthesis process, resulting in low concentrations of gold. Synthesizing gold nanoparticles without oil resulted in a high payload of gold per particle. Curiously, both low and high ratios of lipid to gold cores resulted in lower amounts of nanoparticles with high payload. This finding suggested an optimal lipid content for AuNP micelle formation. The results of preliminary experiments on the uptake of these nanoparticles by HUVEC cells will be presented. Refer to the figures in the text.

Conclusion – This study shows that gold contrast agents with a high payload can be synthesized when using an optimal AuNP to lipid ratio. Targeted gold nanoparticles with high payload may allow non-phagocytotic cells such as angiogenic endothelial cells to take up only a few nanoparticles before resulting in a significant increase in CT contrast . Gold particles targeted to endothelial cells' αvβ3 integrin receptors could enable CT imaging of angiogenesis that is present in various disease processes such as cardiovascular disease and cancer.

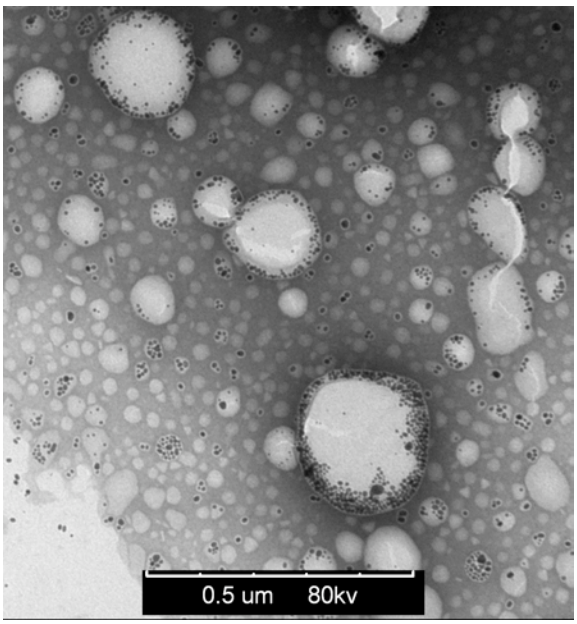

Figure 1 - Gold emulsions formed with oil

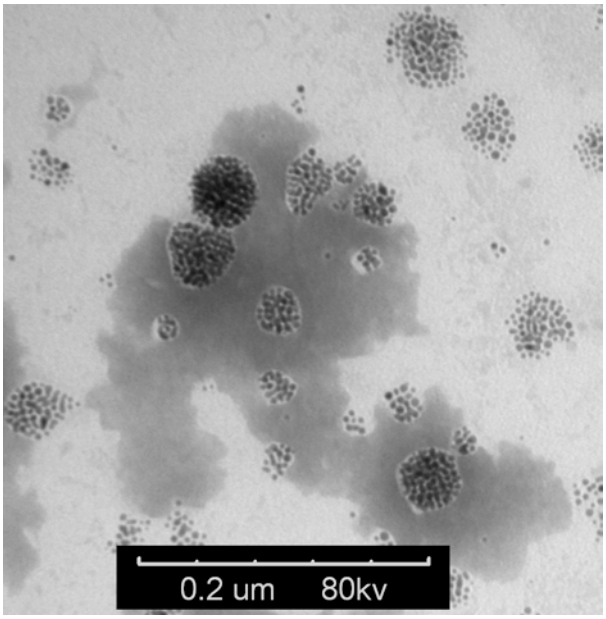

Figure 2 - Gold micelles formed without oil

Synthetic high-density lipoprotein as a platform for exploiting the pleiotropic effect of simvastatin

Jun Tang, David P. Cormode, Willem J.M. Mulder, Zahi A. Fayad
Radiology, Mount Sinai School of Medicine, New York, NY
Corresponding: Jun.Tang@mssm.edu

Background: Simvastatin is widely used for reducing cardiovascular and cerebrovascular events. By inhibiting HMG-CoA, simvastatin can not only inhibit cholesterol synthesis but also synthesis of many other molecules that play key roles in essential cell functions. Therefore, simvastatin's pleiotropic effects—non cholesterol-lowering effects—have been great interest for years. Studies showed that simvastatin could have anti-inflammatory and cholesterol-lowering independent effect upon atherosclerosis development [1] as well as anti-tumor growth effect in several solid tumors, such as breast cancer [2]. However, the bioavailability of hydrophobic simvastatin in atherosclerotic plaque or solid tumors is very low if given orally. In this study, we developed synthetic high-density lipoprotein based nano-particles, which aim at solving poor bioavailability of simvastatin and enhance its pleiotropic effect.

Methods: sHDL particles were synthesized by the following method: DMPC and MHPC were mixed at given weight ratio and then dissolved in chloroform and methanol mixture. Differing quantities of simvastatin were added to this solution. sHDL particles were formed by hydration, sonication, and addition of ApoAI. Nanoarticles were characterized in terms of component composition, size, and morphology. To evaluate the therapeutic efficacy of sHDL formulations, they were applied to two breast cancer tumor cell lines (MCF-7 and MDA-MB-231) and one monocyte/macrophage cell line (J774A.1). Cells were treated with sHDL containing simvastatin, control sHDL, or free simvastain dissolved in DMSO. 48 hours after treatment, cell viability of different groups was evaluated by determining intracellular ATP concentration.

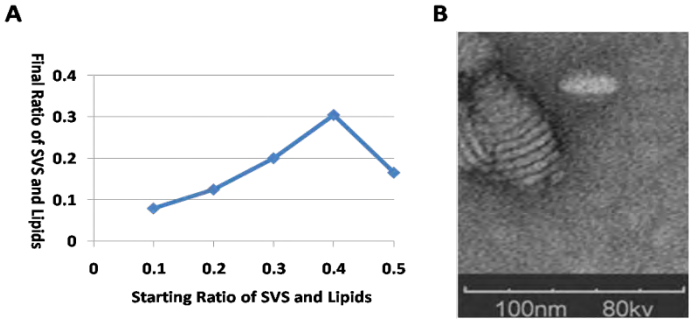

Figure 1. Ratio of simvastatin to phospholipid in final particles and representative TEM morphology. A) Syntheses started with different amount of simvastatin (SVS) compared to 10 mg phospholipid, and the highest ratio of simvastatin to phospholipid in final product was achieved when began with 4 mg simvastatin. B) Representative TEM image of sHDL with final ratio 0.3 of simvastatin and phospholipids was shown.

Results: In final sHDL particles, the highest ratio of simvastatin to phospholipid was 0.3 (Fig 1A). They have disc-like morphology, with diameter around 25 nm (Fig 1B). *In vitro* cell viability assays showed that 48 hours treatment of sHDL-simvastatin at concentration 20 μM decreased cell viability of J774A.1 and MDA-MB-231, which retained 18% and 55% cell viability respectively (Fig 2, first two panels). However, MCF-7 didn't respond to even 20 μM simvastatin sHDL treatment (Fig 2, last panel).

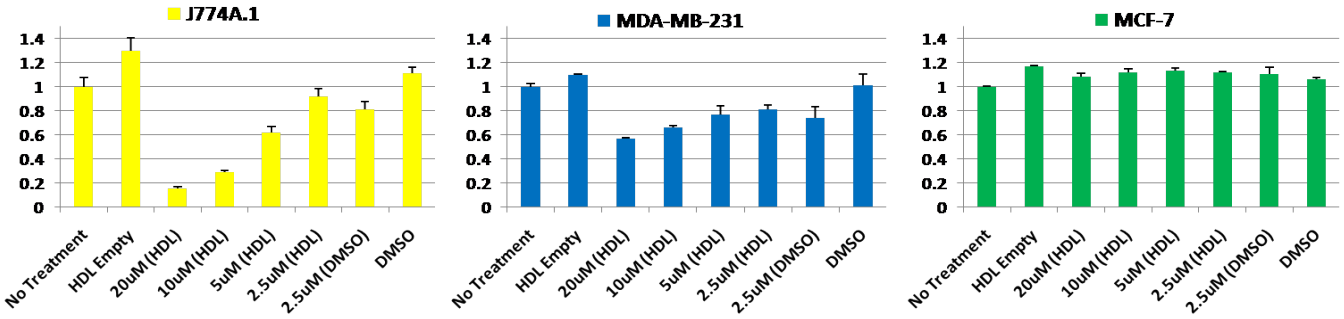

Figure 2. *In vitro* cell viability of different cell lines after 48 hours treatment of simvastatin sHDL. A) Monocyte/macrophage derived murine cell line J774A.1 was incubated with sHDL at various concentrations, simvastatin dissolved in DMSO, and controls. The same experiments were done in MDA-MB-231 and MCF-7.

Conclusion and perspectives: Our data showed a promising sHDL platform for delivering simvastatin to cells *in vitro*. The high payload of sHDL nanoparticles indicated they could carry decent percentage of simvastatin, but still retain sHDL properties. *In vitro* experiments showed that one monocytes/macrophages cell line and one breast cancer cell line are susceptible to sHDL-simvastatin particles. In the future, we will test the *in vivo* efficacy of the sHDL particles in an atherosclerosis mouse model and a breast cancer mouse model.

References: 1. M. Abe, M. Matsuda, H. Kobayashi, *ATVB* **28** 871-877. 2. S. Kotamraju, C.L. Willams, B. Kalyanaraman, *Cancer Res* **67** 7386-7394

Abstracts selected for poster presentation, Cancer Imaging category

Kurtosis Model Analysis of Diffusion-Weighted MRI in Prostate

Louisa Bokacheva[1], Yousef Mazaheri[1,2], Hedvig Hricak[2], Jason Koutcher[1]
Departments of [1]Medical Physics and [2]Radiology
Memorial Sloan-Kettering Cancer Center, New York, NY 10021

Introduction

Diffusion-weighted (DW) MRI signal decays exponentially with increasing diffusion weighting given by the b-value (1). In some tissues including prostate, this dependence is non-monoexponential (2). The purpose of this study was to analyze the DW data in prostate with kurtosis model (3): $S(b) = S_0\exp(-bD+(1/6)K D^2 b^2)$, where D is the distributed diffusion coefficient and K is the apparent kurtosis.

Methods

One patient (52 y.o.) with biopsy-proven prostate cancer provided informed consent and was imaged at 3T (Signa; GE) using DW spin-echo EPI sequence (TR/TE = 3500/124 ms, 128x128, slice/gap 4/4 mm, field of view 160x160 mm^2) at 12 b-values from 0 to 1650 s/mm^2. Maps of D and K were created using nonlinear least-squares (NLS) fitting and maximum likelihood estimation (MLE). ROIs were drawn in peripheral zone (PZ), transition zone (TZ) and a region suspicious for cancer (SC). The noise variance σ^2 was measured in the center of endorectal coil.

Results and Discussion

Signal-to-noise ratio (SNR) varied from 62σ in PZ to 19σ in TZ. Signal versus b-value in all ROIs was non-monoexponential. NLS and MLE provided similar D and K values in PZ and SC ($D_{SC}<D_{PZ}$; $K_{SC}>K_{PZ}$), but in TZ, NLS provided 10% lower D and 30% higher K than MLE (Fig.1). The discrepancy between NLS and MLE results in TZ can be attributed to the bias caused by non-Gaussian noise in magnitude DW data.
At low SNR, MLE underestimates and NLS overestimates kurtosis and both methods have low precision.

Conclusion

The DW signal in prostate can be described by the kurtosis model; however, the calculated parameters are strongly affected by the presence of noise.

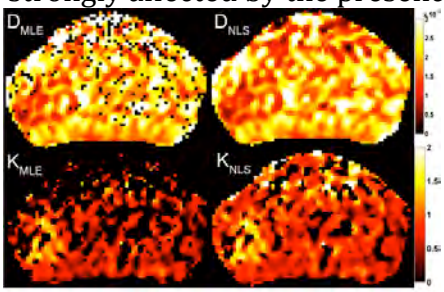

Figure 1. Maps of D and K obtained using MLE and NLS. Maps of D (top) are in units of mm^2/s and kurtosis maps (bottom) are dimensionless.

References

(1) Padhani et al. Neoplasia 2009;11:102-125.
(2) Mulkern et al. MRI 2006;24:563-568.
(3) Jensen et al. MRM 2005;53:1432-1440.

The use of MRI in defining the kinetics of MDSC migration in a murine model of colon cancer

Samuel Eisenstein[1,2], Karen Saeboe[3], Celia Divino[1], Shu-Hsia Chen[2]
[1]Dept. of Surgery, [2]Dept. of Gene and Cell Medicine, [3]Dept. of Radiology, Mount Sinai Medical Center, New York, NY 10029

Introduction: Myeloid derived suppressor cells (MDSCs) are a heterogeneous group of immature immune cells which have been shown to migrate to tumor sites and suppress host anti-tumor immune responses. While MDSCs are synonymous with cancer progression, it may be possible to hijack some of the properties which enable them to target tumor sites and employ them in delivery of tumor-specific therapies, creating a biological Trojan Horse. A better understanding of the kinetics of this migration are first necessary in order to optimize therapeutic options.
Methods: MDSCs were isolated from tumor-bearing BALB/c mice via percoll fractionation followed by ly6C antibody selection. Cells were labeled via PKH26 membrane dye as well as via coculture for four hours in complete RPMI medium with feridex, and adoptively transferred to BALB/c mice with 1x1cm MCA26 liver tumors. Mice underwent MRIs prior to transfer, and then daily, and were sacrificed at various time points for organ harvesting and FACS staining. MDSCs as well as the ly6C$^-$ fraction were also infected with VSV-GFP virus for 4 hours on ice and transferred to mice with 5x5mm liver tumors and compared for survival to mice receiving i.v. injections of VSV, PBS, and uninfected MDSCs. Immune staining was performed using and antibody versus the VSV-G protein.
Results and Discussion: Herein we show that in an adoptive transfer model of metastatic colon cancer, MDSCs preferentially migrate to tumor sites. We first achieve this through FACS analysis where we show the level of PKH26 labeled MDSCs increases in the tumor site up to day 3 after transfer followed by clearance of transferred cells through the spleen. We are then able to use this data to confirm findings we have made through the use of novel MRI technology. First we show effective feridex labeling of *ex vivo* derived MDSCs which leads to dose-dependant signal loss in MRI phantoms. Next, by scanning the mice receiving feridex-loaded MDSCs daily, we are able to show a similar peak of MDSCs in the tumor at day 3, and more impressively, we are able to show that within the tumor these cells specifically migrate to perivascular locations as well as to the periphery of the tumor. Finally we show significantly improved survival in tumor bearing mice treated with MDSCs armed with vesicular stomatitis virus (VSV) when compared to other types of VSV-loaded cells, as well as when compared to a similar dose of i.v. injected VSV.
Conclusion: By employing novel MRI technology, we are able to show the kinetics of MDSC migration in a metastatic tumor model, which we can confirm through immunostaining. This is the first time that this migration has been shown in a longitudinal model. Employing these properties, we are able to significantly prolong survival in a murine model. The improvement of therapeutic efficiency we show using VSV may also be applied to a variety of other tumor-specific therapies in the future. There is much potential in this method for translation to the treatment of human cancers.

Assessing the Tumor Microenvironment in Head and Neck Squamous Cell Carcinoma: Pretreatment Multimodality Imaging with ^{1}H-Magnetic Resonance Spectroscopy, Dynamic Contrast-Enhanced MRI and ^{18}F-FDG PET

Jacobus F.A. Jansen[1,2]; Heiko Schöder[2]; Nancy Y. Lee[3]; Hilda. E. Stambuk[2]; Ya Wang[1]; Matthew G. Fury[4]; Snehal G. Patel[5]; David. G. Pfister[4]; Jatin P. Shah[5]; Jason A. Koutcher[1,2,4]; and Amita Shukla-Dave[1,2]

Departments of [1]Medical Physics, [2]Radiology, [3]Radiation Oncology, [4]Medical Oncology, and [5]Surgery, Memorial Sloan-Kettering Cancer Center, New York, NY.

Introduction

Multimodality imaging (MMI) allows the study of tumor microenvironment characteristics [1]. The goal of the present study was to correlate data from proton magnetic resonance spectroscopy (^{1}H-MRS), dynamic contrast-enhanced MRI (DCE-MRI) and ^{18}F-fluorodeoxyglucose (^{18}F-FDG) positron emission tomography (PET) in nodal metastases of patients with head and neck squamous cell carcinoma (HNSCC) for assessment of tumor metabolism and perfusion in vivo. Additionally, pretreatment MMI data was evaluated for its efficacy in predicting short-term response to treatment.

Methods

Metastatic neck nodes were imaged with ^{1}H-MRS, DCE-MRI and ^{18}F-FDG PET [Figure 1] in 29 newly diagnosed HNSCC patients before treatment. Short-term radiological response was evaluated at 3-4 months [2]. The correlations between ^{1}H-MRS (choline concentration, Cho/W [3]]), DCE-MRI (volume transfer constant, K^{trans}; volume fraction of the extravascular extracellular space, v_e; and redistribution rate constant, k_{ep} [4]) and ^{18}F-FDG PET (standard uptake value, SUV) were calculated using non-parametric Spearman rank correlation. Additionally, a one-way ANOVA was applied to assess the potential effect of necrosis. To predict the short-term response in 24 patients, logistic regression analysis was performed.

Results and Discussion

A significant positive correlation was found between Cho/W and TLG ($\rho = 0.661$, $p = 0.007$), suggesting that increased cellular proliferation requires increased glucose metabolism. Cho/W correlated negatively with heterogeneity measures std(v_e) ($\rho = -0.532$, $p = 0.004$) and std(k_{ep}) ($\rho = -0.516$, $p = 0.006$). Necrosis also had a significant effect on these measures (ANOVA, $p < 0.01$), suggesting that an increased cellular proliferation rate is related to lower heterogeneity (i.e., necrosis). SUV values correlated strongly with MRI tumor volume ($\rho = 0.691$, $p = 0.003$). A significant, positive correlation was found between v_e and SUV ($\rho = 0.517$, $p = 0.028$). As it has been suggested that v_e is a measure of cellularity [5], ^{18}F-FDG uptake in HNSCC might reflect tumor aggressiveness, which is closely related to proliferative activity and cellularity [6]. Logistic regression indicated that std(K^{trans}) and mean(k_{ep}) were significant predictors of short-term response ($p < 0.09$). Patients with incomplete clinical response had higher std(K^{trans}) and lower mean(k_{ep}) values than did patients

with complete response. The short-term responses of 21 (87.5%) of the 24 patients included could be predicted correctly using the above two variables, and the area under the ROC curve was 0.76 [95% CI 0.56 0.97] [Figure 2].

Conclusion

Pretreatment multimodality imaging with ^{1}H-MRS, DCE-MRI and ^{18}F-FDG PET in HNSCC patients shows clear potential for facilitating patient-specific treatment. Furthermore, DCE-MRI provides predictive markers for short-term response to treatment which need to be validated in a larger patient population study.

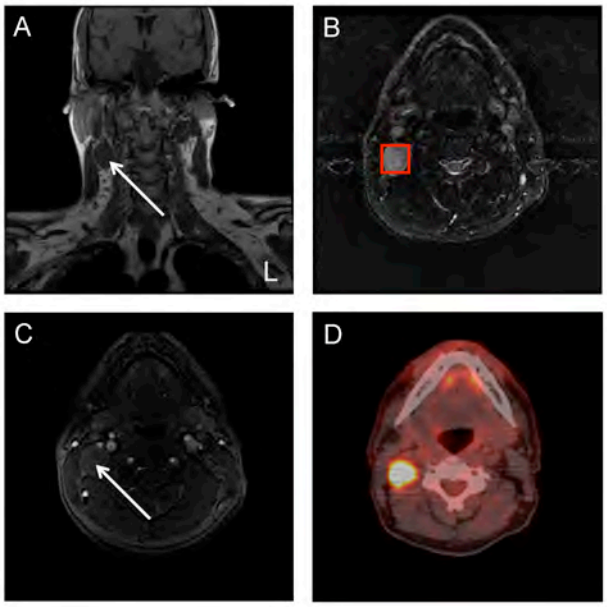

Figure 1. Multiplanar MRI and ^{18}F-FDG PET/CT images illustrating the right neck lymph node of a HNSCC patient (male, 37 years old, primary nasopharyngeal cancer). (A) Coronal T1-weighted, (B) axial short tau inversion recovery with ^{1}H-MRS voxel overlaid, and (C) axial T1-weighted postcontrast MR images showing the anatomy of the neck. The node is indicated with a white arrow in (A) and (C). The voxel of interest for ^{1}H-MRS is indicated in red in (B). In (D) the corresponding ^{18}F-FDG intensity map is shown overlaid on a CT image, indicating ^{18}F-FDG uptake in the node.

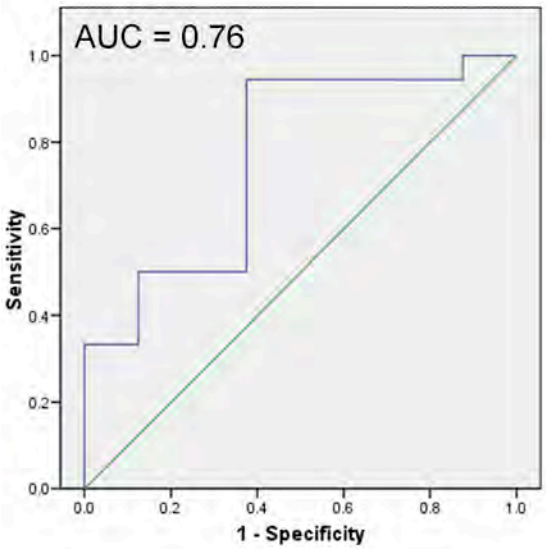

Figure 2. ROC curve constructed using the predicted probabilities of the logistic regression model for the prospectively obtained imaging parameters (significant predictors: std(K^{trans}) and mean(k_{ep})). AUC: area under the curve.

References

[1] Plathow, J Nucl Med. 2008 49:43S; [2] Yao, Int J Radiat Oncol Biol Phys. 2005 63:991; [3] Provencher, MRM. 1993 30:672; [4] Tofts, JMRI. 1999 10:223; [5] Li, PNAS 2008 105:17937; [6] Kitagawa, Eur J Nucl Med Mol Imaging. 2003 30:63.

Acknowledgement: This research was supported by NIH RO1-CA 115895

RGD-conjugated nanoemulsions for tumor imaging and phenotyping

Peter A. Jarzyna[1], Wei Chen[1], Zahi A. Fayad[1] and Willem J.M. Mulder[1]
[1]Translational and Molecular Imaging Institute (TMII), Mount Sinai School of Medicine

Introduction: For tailored oncological treatment and therapy, it would be highly desirable to know the microvessel density (MVD) and hence angiogenic activity of a tumor. This is currently not achievable by natural tissue contrast with in vivo magnetic resonance (MR) or optical imaging. A nanocarrier platform based on oil-in-water nanoemulsions with an average droplet size that is tunable in the range of 30 - 100 nm has been developed before and described in our lab as a useful contrast agent for tumor imaging with MR and optical methods via passive targeting. The aim of the current study is to show its value for active targeting in the context of phenotyping of different tumors with distinct MVD by using the RGD moiety. The latter is known to bind to the αvβ3 integrin, which is overexpressed during angiogenesis in the endothelial cells of the vasculature of tumors. Two subcutaneous tumor models with different human cancer cell lines (EW7: low MVD; LS174T: high MVD) in swiss nude mice were used to acquire characteristic accumulation kinetics.

Methods: The nanoemulsion is manufactured with the lipid film-hydration method. After sonication, the concentrated formulation is split into half and conjugated with RGD solution in an overnight reaction (maleimide-thiol coupling). For the near infrared (NIR) imaging a Cy7 dye linked to a lipid is used. The formulations used for the MRI contain oleic acid capped iron oxide nanocrystals in the soybean oil core of the droplets.

Results: The NIR tumor uptake kinetics revealed statistically significant differences for the accumulation of the targeted contrast agent for the time points of 1 h, 2 h, 4 h, and 6 h between the two different tumor models (Fig. 1). Confocal microscope images provided proof for the binding of the nanoparticles to the endothelial cells (Fig 2A,B). The MRI data collected so far shows a different pattern of signal loss between the tumors of the targeted (LS174T vs. EW7) groups. In the targeted LS174T group the signal loss is detected predominantly in or close to the periphery where angiogenesis is occurring, while in the control group the distribution seems more evenly spread throughout the entire tumor (Fig. 2C).

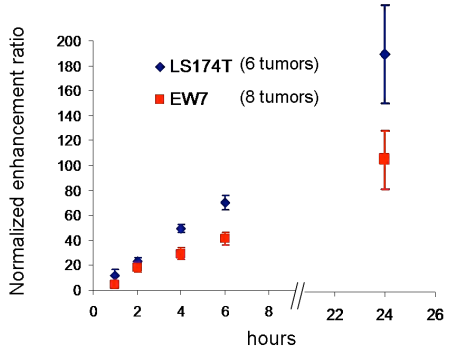

Figure 1: NIR in vivo kinetics (mean±SE).

Conclusion: This data so far shows the nanoparticle platform to be a useful contrast agent for the in vivo phenotyping of tumors with distinct differences in MVD and angiogenesis.

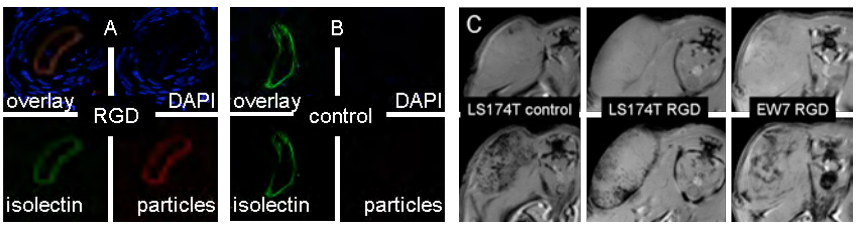

Figure 2: Confocal images of the endothelial cells (LS174T tumors): A) targeted B) control. MRI (T_2*) results: C) left: LS174T (control particles), middle: LS174T (RGD), EW7 (RGD). Upper panel: pre, lower

Title: *Ex vivo* High Resolution Imaging with a miniaturized endoscopic microscope to discriminate benign and malignant upper aerodigestive mucosa

Lauren Levy[1], Claris Smith[1], Vivek Gurudutt[1], M.D, Marita Teng[1], M.D, Michael Rivera[2], MD,Sharmila Anadasabapathy[3], M.D, Eric Genden[1], M.D, Ann Gillenwater[4], M.D, Rebecca Richards-Kortum[5], M.D, Andrew Sikora[1], M.D/PhD

Departments of [1]Otolaryngology – Head and Neck Surgery, [2]Pathology, [3]Gastroenterology, Mount Sinai Medical Center

[4]Department of Head and Neck Surgery, UT MD Anderson Cancer Center, Houston, TX

[5]Department of Bioengineering, Rice University, Houston, TX

Introduction: High resolution optical imaging is a relatively new modality which allows for the acquisition of real time images of epithelial tissue, thus providing the capability to spatially resolve structural changes in the epithelium , as well as physiological changes in the tissue with the use of contrast agents that indicate neoplastic progression. Optical imaging provides a mechanism to discriminate between normal and cancerous mucosa in the upper aerodigestive tract at the time of tumor resection allowing for more precise tumor ablation while minimizing the amount of healthy tissue removed. This study evaluates the feasibility of using a high- resolution microendoscope(HRME) to discriminate between normal and cancerous mucosa in the upper aerodigestive tract, as there is a critical need to define intraoperative margins during tumor resection.

Methods: Following resection for biopsy-proven squamous cell carcinoma of the upper aerodigestive tract sites of both grossly "normal" and suspicious mucosa were imaged with the fiber optic endoscope after surface staining of nuclei with proflavin. Imaged areas were marked with India ink to allow correlation with conventional histologic analysis, performed following HRME

Results and Discussion: We observed that areas of histopathologically confirmed carcinoma had increased density of nuclei, and greater disorganization, when compared to the confirmed normal mucosa. In some cases, lesion margins could be visualized by moving the probe across the transition zone from normal to cancerous mucosa. In some heavily keratinized specimens, autofluorescence artifact limited the ability to view cell nuclei.

Conclusion: Optical imaging provides non-invasive visualization of the epithelium in real time. Previous studies report optical imaging of noeplastic change in both the oral cavity and esophagus. This study demonstrates that the use of high resolution optical imaging of the human aerodigestive tract can complement existing techniques by identifying areas of abnormal mucosa suitable for biopsy, or assisting in intraoperative margin determination. Limitations include keratinization artifact and the potential for submucosal tumor spread below the imaging depth. Despite these limitations, high resolution imaging offers numerous advantages. Perhaps most compelling is the fact that these systems can be both low-cost and portable. Thus, they have the potential to

be used *ex vivo* or *in vivo* (through a conventional endoscope or handheld unit), to enhance surveillance and to precisely define lesion margins at the time of resection. Additionally, these instruments can be combined with a robotic surgical device to further reduce the morbidity and mortality following tumor ablative surgery. By both assisting with early identification of malignant lesions and more precisely defining tumor margins, high resolution optical imaging offers a chance of not only avoiding unnecessary surgery but also improving patient survival. The continued refinement of this optical imaging technology may provide benefits in the management and treatment of patients with HNSCCA.

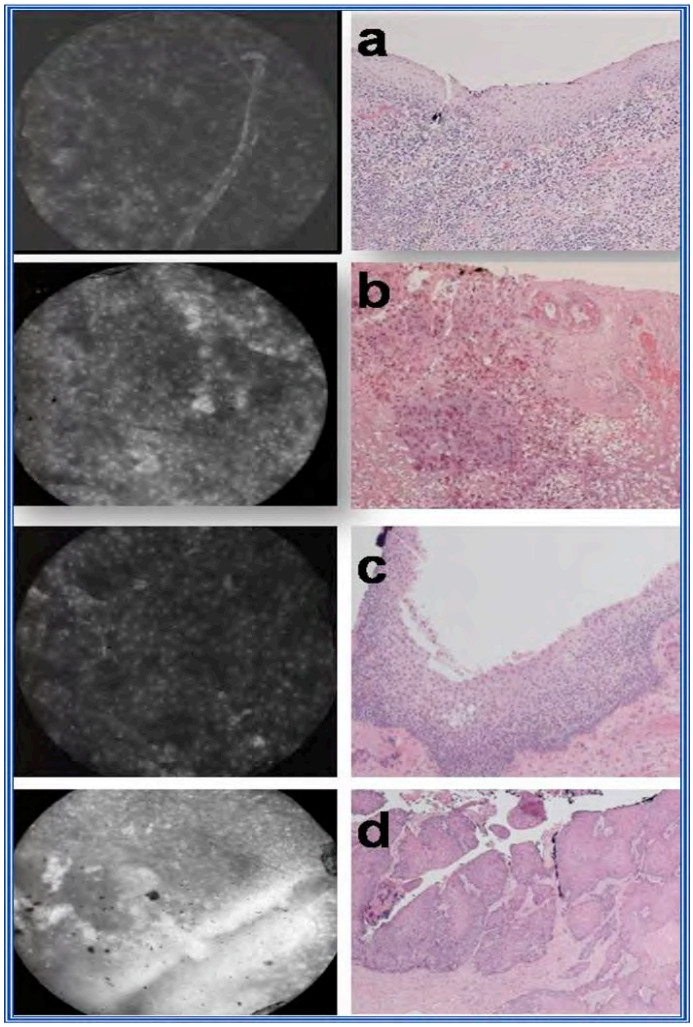

Figure 1. Images obtained using the HRME (Left) with corresponding histopathological images (Right). **a**.benign squamous epithelium of the tongue, **b.**squamous cell carcinoma of the tongue, **c**.benign laryngeal squamous epithelium, **d**. laryngeal squamous cell carcinoma. The images of malignant mucosa have nuclear density, and disorganized pattern of nuclei.

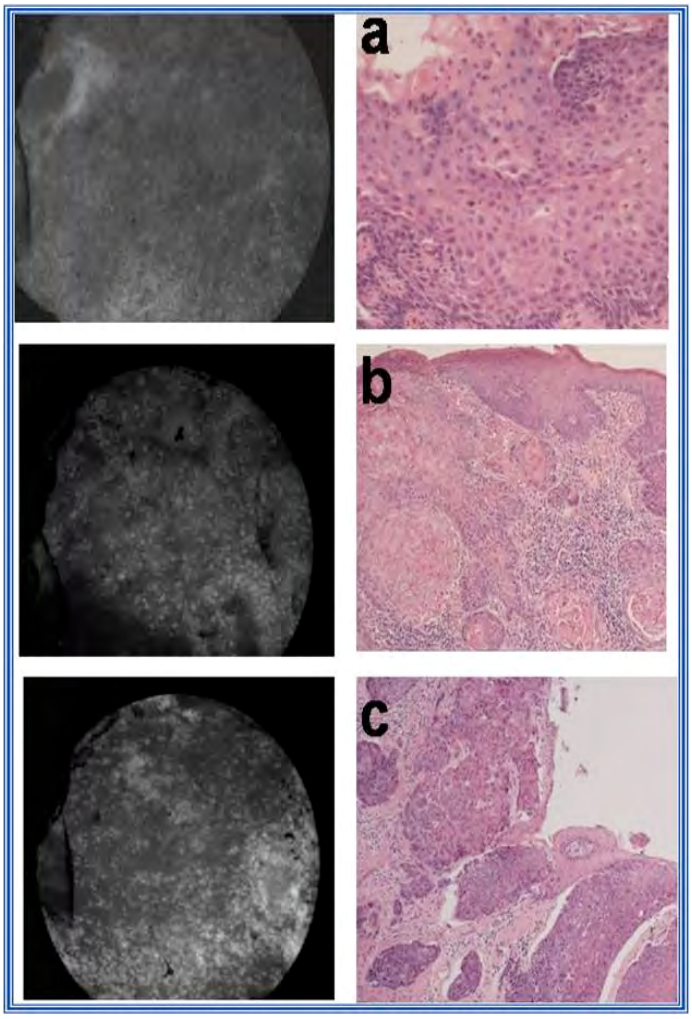

Figure 2. Squamous cell carcinoma located in a. hypopharynx, b.floor of mouth, and c.larynx.

References

Gillenwater AM, Jacob R, Richards-Kotrum R. Flourescence spectroscopy: a technique with potential to improve the early detection of aerodigestive tract neoplasia. Head and Neck (1998) 20(6): 226-62.

Muldoon TJ, Pierce MC, Nida DL, Williams MD, Gillenwater AM, and Richards-Kotrum R. Subcellular-resolution molecular imaging with living tissue by fiber microendoscopy. Opt Express (2007) 15: 16413-23

Ramanujam N, Mitchel MF, Mahadevan A, et al. In vivo diagnosis of cervical intraepithelial neoplasia using 337 nm excited laser-induced florescence. Proc Natl Acad Sci USA (1994) 91; 10193-97.

Shaun D, Sung CK, Genden EM. Transoral robotic surgery using an image guidance system. The laryngoscope (2008) 118(11): 2003-05.

Schwarz RA, Gao W, Daye D, et al. Autoflorescence and diffuse reflectance spectroscopy of oral epithelial tissue using a depth sensitive fiber active probe. Applied Optics (2008) 47(6); 825-34.

Pavola I, Weber CR, Schwarz RA, et al. Flourescence Spectroscopy of oral tissue: Monte Carlo modeling with site-specific tissue properties. J. Biomed Opt (2009) 14(1): 041009.

Amalgamating nanomaterials, radionuclides, and antibodies to image tumor vasculature

Michael R. McDevitt, Alessandro Ruggiero, Jason P. Holland, Carlos H. Villa, Shanna R. Sprinkle, Jason S. Lewis, David A. Scheinberg
Departments of Medicine, Radiology, Molecular Pharmacology and Chemistry, Memorial Sloan-Kettering Cancer Center, 1275 York Avenue, New York, NY 10065.

Introduction Advances in cancer diagnosis and treatment require improvements in the agents used to image disease. Key modifications that enable these agents to specifically target disease, increase signal-to-noise, rapidly clear from the blood, and incorporate multiple imaging modalities would be valuable developments. Nanomaterials are being investigated as delivery platforms for diagnostic and therapeutic cargoes to target disease. Pharmacokinetic (PK) studies of tumor-targeting carbon nanotubes (CNT) have demonstrated rapid blood compartment clearance, high specific activity (S.A.), multi-modal imaging capability and tumor-specific accumulation in vivo. We performed imaging with prototype ^{89}Zr-CNT-IgG constructs in a murine model vs. appropriate controls. **Methods** The ^{89}Zr-labeled CNT construct was synthesized with the E4G10 antibody (anti-monomeric VE-cadherin (VE-cadh$_m$) to target the tumor vascular network. Dynamic imaging of LS174t tumor bearing mice using positron emission tomography (PET) was performed. Controls included a non-specific antibody construct and blocking the VE-cadh$_m$ epitope with excess unlabeled E4G10. **Results and Discussion** The CNT constructs rapidly cleared the blood (<1 h) and the E4G10-appended construct specifically targeted tumor vasculature. The construct S.A. and clearance were significantly improved relative to antibody-alone constructs. **Conclusion** The PET images indicated that the specific construct accumulated in the tumor and rapidly cleared the blood compartment. Because of the CNT-component of the construct, i) the S.A. was amplified to provide better signal-to-noise without detrimentally impacting immunoreactivity and ii) PK was altered to provide an advantage for rapid imaging.

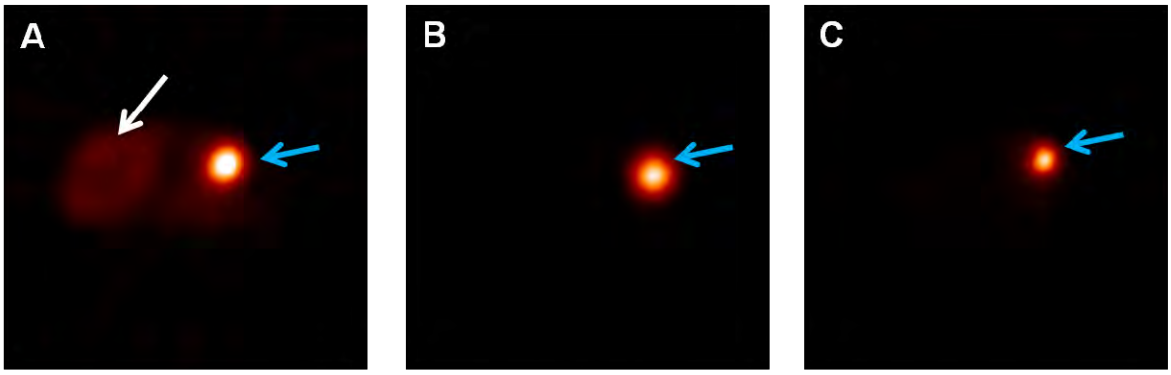

Figure 1. Representative transverse PET images at 4h post iv-administration of A) ^{89}Zr-CNT-E4G10; B) ^{89}Zr-CNT-anti-KLH (non-targeting isotype control IgG2a); and C) ^{89}Zr-CNT-E4G10 + excess unlabeled E4G10 (cold blocking control). Each mouse received a single dose of CNT construct containing approx. 0.12 mCi of ^{89}Zr and 0.006 mg of CNT in 0.2 mL that was administered iv via the retro-orbital sinus. n.b., The white arrow in panel A shows tumor uptake (absent in panels B and C). A portion of the kidney (blue arrow) was also contained in these slices for reference. The tumor volumes (measured with calipers) were 936, 380, and 1048 mm^3 in the mice in panels A, B, and C respectively.

Support: 5R21CA128406, R01CA55349, P01CA33049, the Experimental Therapeutics Center, the Brain Tumor Center, the Office of Science (BER), U. S. Department of Energy (Award DE-SC0002456) and Imclone for the E4G10 antibody.

Translational and Molecular Imaging Institute

Mission of the Translational and Molecular Imaging Institute

Zahi A. Fayad, Ph.D.
Director, TMII

Juan Gilberto Aguinaldo, M.D., C.C.R.P.
Manager, TMII

The mission of *The Translational and Molecular Imaging Institute (TMII)* is to research, develop, and apply a new generation of imaging methodologies in order to advance preclinical and translational research activities. This will result in new methods for drug delivery, as well as in the establishment of new classes of contrast agents which may improve disease detection, disease characterization, clinical diagnosis, treatment and monitoring of therapeutic responses.

The institute aims to promote an array of next-generation, world-class biomedical imaging resources to be used by clinical and translational researchers of the various institutes at Mount Sinai as well as by our collaborators. TMII provides advanced, highly efficient and cost-effective imaging services, and offers expertise for the development and validation of new procedures, encouraging interdisciplinary collaborations that merge the gap between preclinical and clinical research.

One of the key missions of the institute is to educate researchers, postdoctoral fellows, students and technicians about biomedical imaging advances through targeted seminars, research fellowships, publications, established training programs and symposiums such as the one held today.

TMII is organized in three different Programs and a Core: The Cardiovascular Imaging Program is headed by Zahi A. Fayad, Ph.D.; the Neuroimaging Program by Cheuk Y. Tang, Ph.D., the Nanomedicine Program by Willem J.M. Mulder, Ph.D.; and the Cell Tracking Core is directed by Karen Briley-Saebo, Ph.D.

TMII is at the forefront of advancing the science of imaging and translational research, and facilitates the transformation of clinical medicine.

Translational and Molecular Imaging Institute
TMII
MSSM
Mount Sinai School of Medicine

Cardiovascular Imaging Program

The Cardiovascular Imaging Program is focused on developing and using noninvasive imaging methods that allow the early detection, prevention, and treatment of cardiovascular disease. Despite considerable therapeutic advances over the past 50 years, cardiovascular disease is the leading cause of death worldwide. This is mainly a result of the increasing prevalence of atherosclerosis, owing to the ageing population, the improved survival of patients with atherosclerotic cardiovascular disease and, above all, the widespread under-recognition and undertreatment of individuals with risk factors for atherosclerosis. Atherosclerosis is characterized by the thickening of the arterial wall to form an atherosclerotic plaque, a process in which cholesterol deposition, inflammation, extracellular-matrix formation and thrombosis have important roles (see Sanz and Fayad Nature 2008; 45:953-957). Symptoms occur late in the course of disease and are usually caused by the narrowing of the lumen of the artery, which can happen gradually (as a result of progressive plaque growth) or suddenly (as a result of plaque rupture and, subsequently, thrombosis). The resultant decrease in blood supply can affect almost any organ, although coronary heart disease and stroke are the most common consequences.

Traditionally, diagnosis of atherosclerosis was possible only at advanced stages of disease, either by directly revealing the narrowing of the arterial lumen (stenosis) or by evaluating the effect of arterial stenosis on organ perfusion. We are developing and using, new imaging approaches that allow the assessment not only of the morphology of blood vessels but also of the composition of the vessel walls, enabling atherosclerosis-associated abnormalities in the arteries (including the coronary arteries) to be observed, down to the cellular and molecular level in some cases. Some of these approaches are now in clinical use or are being tested in clinical trials, whereas others are better suited to basic (preclinical) and translational research.

Zahi A. Fayad, Ph.D.

Director Translational and Molecular Imaging Institute
Professor of Radiology
Professor of Medicine (Cardiology)

Neuro Imaging Program

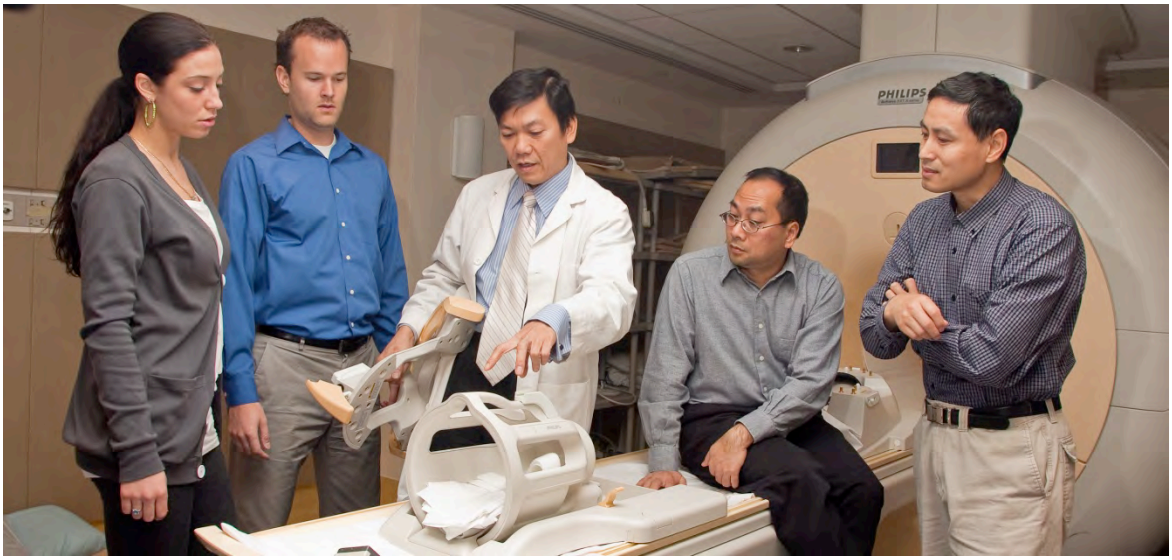

The mission of the Neuro Imaging Program is to research, develop and apply new technologies to non-invasively diagnose brain diseases and to further our general understanding of normal as well as abnormal brain anatomy and function. The multidimensional Neuro Imaging Program involves studies ranging from human and non-human primates to various mouse models of human diseases. The program reflects a close collaboration between the departments of Radiology, Psychiatry, Neurology and Neuroscience.

Technological advances in imaging technologies have opened up new avenues for basic, translational and preclinical studies of brain and behavior. Our laboratories has access to the state of the art imaging modalities including 9.4T and 7.0T micro-MRI animal scanners, in-vivo animal biophotonic imaging, human 3T head and whole body 3T MRI, PET/CT as well as the latest PET/MR scanners. In addition, all scanners are equipped with peripherals necessary for functional imaging.

The Neuro Imaging Program is actively involved with the development of novel image analysis tools such as fiber tract analysis tools for DTI/DSI data as well as algorithms for resting state functional connectivity networks.

Our research portfolio includes Schizophrenia, ADHD, Mood disorders, PTSD, TBI, Autism, Alzheimers as well as normal brain anatomy and function with target species ranging from mice to human.

Cheuk Ying Tang, Ph.D.

Director Neurovascular Imaging Program
Assistant Professor of Radiology
Assistant Professor of Psychiatry

Nanomedicine Program

The mission of the Nanomedicine Program is to establish topnotch nanotechnology based approaches for medical imaging and therapeutics in cancer and cardiovascular disease. To this aim we have developed a range of multimodality nanoparticle platforms. All the platforms are based on assemblies of amphiphiles and functional materials. The main focus is on nanochemistry and novel nanoparticles as well as their application in experimental models of cardiovascular disease and cancer. Multimodal imaging is used to investigate the behavior of the new materials in vivo. The program involves close collaborations between the different research efforts within TMII.
Our nanoparticle platforms include liposomes, micelles, nanocrystal micelles, (nanocrystal) HDL, lipid-coated silica, nanoemulsions and different other structures composed of amphiphiles. Some selected (out of >50) key publications are listed below:

-Jarzyna PA et al. Iron oxide core oil-in-water emulsions as a multifunctional nanoparticle platform for tumor targeting and imaging. Biomaterials. 2009 Dec;30(36):6947-54
-Mulder WJM et al. Nanoparticulate assemblies of amphiphiles and diagnostically active materials for multimodality imaging. Acc Chem Res. 2009 Jul 21;42(7):904-14.
-Cormode DP et al. Nanocrystal core high-density lipoproteins: a multimodality contrast agent platform. Nano Lett. 2008 Nov;8(11):3715-23.
-van Schooneveld MM et al. Improved biocompatibility and pharmacokinetics of silica nanoparticles by means of a lipid coating. Nano Lett. 2008 Aug;8(8):2517-25.
-Mulder WJM et al. Quantum dots with a paramagnetic coating as a bimodal molecular imaging probe. Nano Lett. 2006 Jan;6(1):1-6.
Mulder WJM et al. MR molecular imaging and fluorescence microscopy for identification of activated tumor endothelium using a bimodal lipidic nanoparticle. FASEB J. 2005 Dec;19(14):2008-10.

Willem J.M. Mulder, Ph.D.

Director Nanomedicine Laboratory
Assistant Professor of Radiology
Assistant Professor of Gene and Cell Medicine

Program of Excellence in Nanotechnology (PEN) **NIH/NHLBI**

TMII is extremely proud to announce the success of our application "Translational Nanomedical Therapies for Cardiac & Vascular Diseases". This application aims to establish a unique multidisciplinary Program of Excellence in Nanotechnology (PEN) by integrating the cardiovascular medicine and imaging expertise of highly productive National Heart, Lung and Blood (NHLBI) funded investigators at Mount Sinai School of Medicine, New York University, and Columbia University, with the cutting-edge biomolecular and nanomedical engineering expertise of world-renowned pioneers at Massachusetts Institute of Technology and Brigham and Women's Hospital. The overarching long-term goal of this PEN application is to establish an innovative research and training program focused on developing translational nanomedical tools for the imaging-facilitated diagnosis and minimally-invasive treatment of vascular and cardiac diseases.

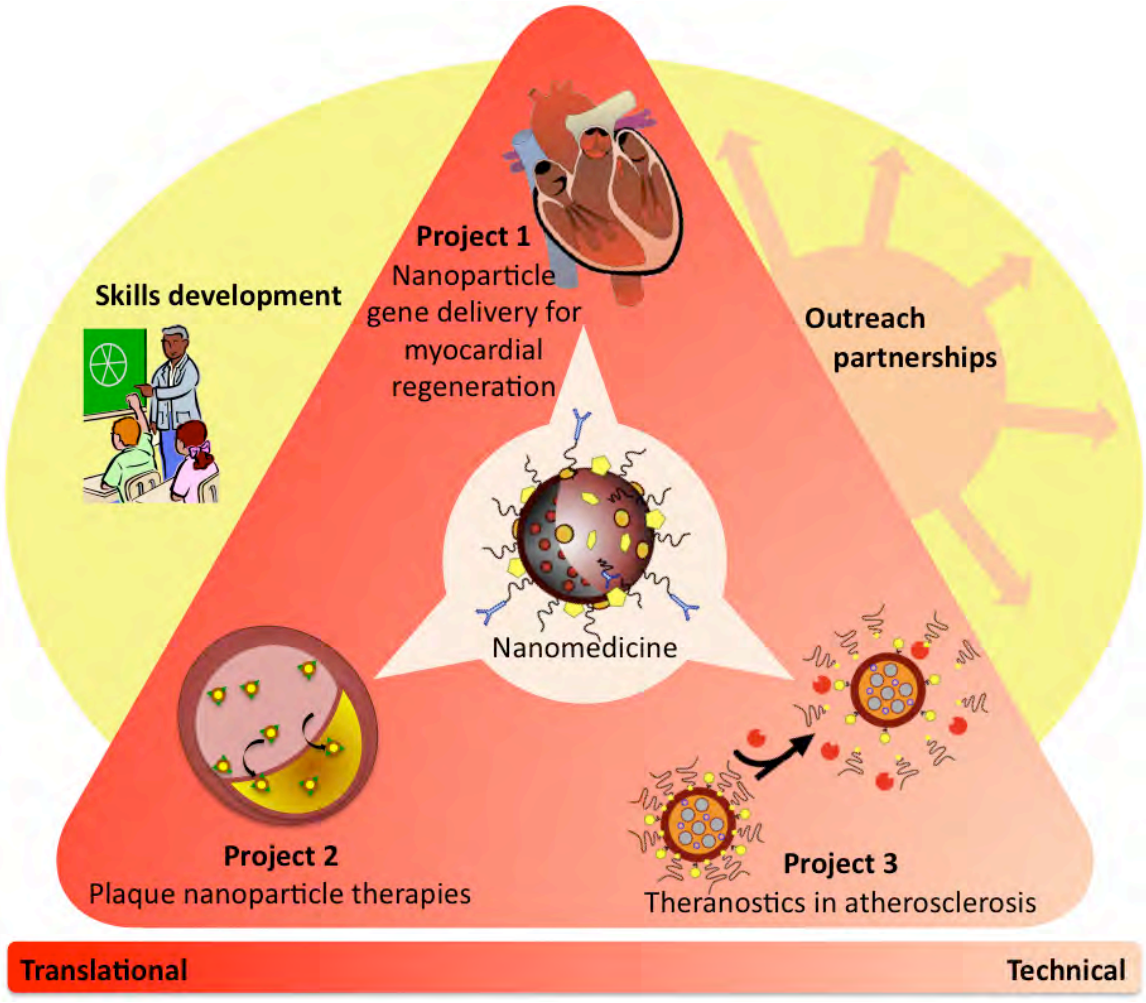

Directors: Zahi A. Fayad (MSSM) and Robert S. Langer (MIT)

Cell Tracking Core

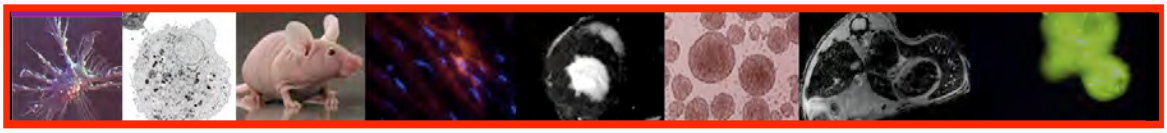

The mission of the Departmental Cell Tracking Core (DCTC) is to develop and provide novel technology to allow for non-invasive in vivo detection and tracking of transplanted cells. The program is designed to act as an active interface between the Departments of Radiology, Gene and Molecular Medicine, and Vascular Medicine. The specific aims of DCTC are as follows:

- To develop novel cell tracking probes/labels.
- To develop and validate pre-clinical diagnostic imaging methods to allow for accurate in vivo detection and longitudinal cell tracking.
- To provide consulting services to help investigators optimize cell labeling strategies.
- To perform comprehensive data analysis and aid in the interpretation of imaging results.
- To provide investigators with high quality data to allow for submission of new grant applications and/or support funded studies.

DCTC can provide the latest strategies for cell detection using Magnetic Resonance Imaging (MRI), Positron Emission Tomography (PET), and Computer Tomography (CT). The recent acquisition of a clinical hybrid time-of-flight PET/MR system allows for the combination of high sensitivity PET imaging with high-spatial resolution MRI. Novel cell labels are currently being constructed that combine MRI and PET tracers to take advantage of this exciting new technology.

Over the past year DCTC has been involved in the labeling, detection and tracking of a variety of cells for several indications. For example, antigen modified monocytes, Tcells, cardiac progenitor cells, hepatocytes and stem cells have been used to monitor novel immuno- therapeutics in mice and pigs. Activated labeled dendritic cells have been used to induce anti-tumor immunity that has proven effective in the fight against HIV and Lupus. The services provided by DCTC are open to all investigators on a fee for service. Summary of current publications submitted with DCTC support:

1) Adler ED et al., In vivo detection of embryonic stem cell-derived cardiovascular progenitor cells using Cy3-labeled Gadofluorine M in murine myocardium. JACC Cardiovasc Imaging. 2009 Sep;2(9):1114-22.

2) Mani V et al., Serial in vivo positive contrast MRI of iron oxide-labeled embryonic stem cell-derived cardiac precursor cells in a mouse model of myocardial infarction. Magn Reson Med. 2008 Jun 25;60(1):73-81.

3) Adler ED et al., The Cardiomyocyte Lineage is Critical for Optimization of Stem Cell Therapy in a Mouse Model of Myocardial Infarction. JACC Cardiovasc Imaging. 2009 Sep;2(9):1114-22.

Karen Briley-Saebo, Ph.D.

Instructor
Departments of Radiology and Gene and Cell Medicine
Mount Sinai School of Medicine

Translational and Molecular Imaging Institute

TMII

MSSM

Mount Sinai School of Medicine

The Translational and Molecular Imaging Institute (TMII) Seminar Series

"Looking Inside the Mouse: New Approaches using Magnetic Resonance and Ultrasound Micro-imaging"
February 19, 2010
Daniel H. Turnbull, PhD ,Associate Professor,Dept. of Radiology and Pathology, NYU School of Med.

"Biomimetic Lipid Nanoparticles for Imaging and Therapy"
March 26, 2010
Gang Zheng, PhD, Associate Professor, Department of Medical Biophysics, University of Toronto

"Title TBD"
May 21, 2010
Elazer Edelman MD, PhD, Director, Harvard-MIT Biomedical Engineering Center (BMEC)

"MRI Cell Tracking of New Neurons in the Rodent Brain"
May 28, 2010
Alan P. Koretsky, Ph.D, Director, MRI Research Facility, NIH

Hosted By:

Ehud Kaplan, PhD
Zahi Fayad, PhD

Contact: Sybil Price (212) 241-6858
sybil.price@mountsinai.org

All lectures, except where indicated, will be held from 10:30-11:30am in the Radiology Education Conference Room, MC Level of the Annenberg Building, Room AMC 330.

Directions: Enter 1468 Madison Avenue at 100th St. Proceed down the ramp, and turn left before the Security Office. Follow this hallway until it ends, then turn left. The door to the Education Center is the first door on your left after the vending machines.

Translational and Molecular Imaging Institute

TMII MSSM

Mount Sinai School of Medicine

MSICTS-TMII

CTSA TMII IMAGING PHYSICS, SCIENCE AND APPLICATION EDUCATIONAL SEMINAR SERIES

- ***Basic MRI Theory and Principles*** - David Carpenter, PhD, Director, Image Analysis Core, TMII
  January 22nd, 2010
- ***MR Relaxation Theory*** - Karen Saeboe, PhD, Instructor, Department of Radiology, TMII
  February 5th, 2010
- ***Principles and Quantitative Imaging with Dynamic Contrast Enhanced MR*** -Claudia Calcagno, MD, TMII
  February 12th, 2010
- ***Optical Imaging*** - Ehud Kaplan, PhD, Professor, Department of Neuroscience
  March 5, 201
- ***Principles of PET and Some Applications*** - Josef Machac , MD, Director, Nuclear Medicine
  March 19, 2010
- ***Computed Tomography*** - Don Werner, PhD, Siemens Healthcare
  April 23, 2010
- ***Contrast agents: MR, Optical, Nuclear and CT*** - David Cormode, PhD, Post-Doctoral Fellow, TMII
  May 14, 2010
- ***Molecular Imaging and Nanoparticle Targeting*** - Willem Mulder, PhD, Asst. Prof., Dept. of Radiology, TMII
  Date TBD (week of May 24, 2010)
- ***fMRI and DTI*** - Cheuk Tang, PhD, Assistant Professor, Department of Radiology, TMII
  June 11, 2010
- ***Image Analysis for Neuroimaging*** - David Carpenter, PhD, Director, Image Analysis Core, TMII
  June 25, 2010
- ***MRI for Detection of Liver Fibrosis & Cirrhosis***- Bachir Taouli, MD, Assoc. Prof. Radiology
  July 2, 2010 *LOCATION TBD*
- ***Atherosclerosis Imaging as Biomarker*** - Zahi A. Fayad, PhD, Director, TMII, Prof. Radiology/Medicine
  July 9, 2010
- **Cardiac Imaging – Applications** – Javier Sanz, MD, Director Cardiac MR/CT Program, Asst. Prof. Med. (Cardiology)
  TBD

All are Welcome to Attend

All lectures, except where indicated, will be held from 10:30-11:30am in the Radiology Education Conference Room, MC Level of the Annenberg Building, Room AMC 330.

Directions: Enter 1468 Madison Avenue at 100th St. Proceed down the ramp, and turn left before the Security Office. Follow this hallway until it ends, then turn left. The door to the Education Center is the first door on your left after the vending machines.

For further information, contact Dr. Zahi Fayad (Sybil Price) at (212) 241 6858; Sybil.Price@mssm.edu